Wireless Propagation Studies in Highly Resonant and Dynamic Environments

Mark Panitz M.Sci

GEORGE GREEN LIBRARY OF
SCIENCE AND ENGINEERING

Thesis submitted to The University of Nottingham

for the degree of Doctor of Philosophy

JULY 2011

Abstract

This thesis develops efficient tools for modelling wireless communications within highly resonant environments. The aim of these tools is to augment analysis of wireless systems inside closed metallic cavity environments. The primary application for these systems is within the aerospace industry where weight and space are restricted and robustness is critical. The use of ever-advancing wireless communication options would offer significant weight and cost savings and increase safety through supplementing or the replacement of wired systems. The use of a low power wireless system offers the greatest advantage in terms of flexibility and weight. Accordingly, the most suitable applications of the wireless systems are discussed in terms of existing avionic systems.

The electromagnetic properties of the aircraft environment and parameters to characterise both the properties of the environment and the wireless signal are introduced. Efficient models are then developed, which characterise the resonant and associated multipath nature of the cavity based on an equivalent circuit approach. The efficiency of these models permits the use of a statistical modelling approach, akin to reverberation chamber measurement techniques, in order to generalise the results for typically non-constant modal structures.

Finally, a fractional boundary placement model is developed to augment the

transmission line modelling method and permit boundary placement at non-integer positions within a structured mesh. The technique provides a semi-conformal capability with no deleterious impact on the modelling time step. This is then extended to a dynamic model for modelling structural variations during the simulation.

A subset of wireless communication approaches is presented and the effectiveness and suitability of such systems are discussed. The developed models are applied to characteristic environments and a selection of the wireless communication methodologies in order to provide examples of their use and an insight into the effect of these environments upon a wireless system.

Acknowledgements

Firstly, I would like to thank my supervisor Professor Christos Christopoulos for his unreserved guidance, support and encouragement throughout this project and beyond. I wish to thank my co-supervisor Professor Phillip Sewell and also Dr Chris Smartt for their early insights and discussions. In addition, I am grateful to Dr John Paul for his extended support and guidance whenever needed.

I would like to thank my colleagues at the George Green Institute of Electromagnetic Research (GGIEMR) for their support and friendship. I would also like to thank Dr Steve Greedy for his assistance during my time at the GGIEMR.

The work presented here was carried out as part of the Towards a Wireless Aircraft project within the wider FLAVIIR project supported by BAE Systems and EPSRC (GR/S71552/01). I extend my gratitude to the colleagues with whom I had the pleasure of collaborating, in particular David Hope and Dr John Dawson.

I wish to thank my family for their encouragement and support over the many years and helping me with my success.

Finally, I dedicate this thesis to Tamsin who has provided unremitting support, encouragement, understanding and immeasurable patience throughout my studies,

and especially during the writeup stage. Without you this work would not have been possible and I will be forever grateful for all that you have done for me.

List of Principal Symbols

Symbol	Definition
$\underline{E}$	Electric field strength
$\underline{H}$	Magnetic field strength
ε_0	Permittivity of free space
μ_0	Permeability of free space
η_0	Impedance of free space
Q	Q factor
α	Decay (attenuation) constant
$\overline{\mu}$	(Mean) excess delay
τ, τ_n	Continuous, discrete delay
T	Period of oscillation
ω_c, f_c	Carrier frequency
ω_B, f_B	Boundary oscillation frequency
$\phi(t)$, ϕ_n	Continuous, discrete amplitude
$g(f)$	Density of modes
M	Number of modes
T_b	Bit period
R_b	Bit rate
R_c	Chip rate
V	Voltage
I, i	Current, branch current
R	Resistance
L, L_d	Inductance, per-unit-length inductance
C, C_d	Capacitance, per-unit-length capacitance
C_m	Coupling capacitance
L_m	Coupling inductance
k_c	Coupling coefficient
Z	Impedance
Y	Admittance
Z_{TL}	Transmission line characteristic impedance
$F(k)$, $E(k)$	Full elliptic integral of the 1st and 2nd kind
λ, λ_g	Wavelength, guide-wavelength

Publications

Journal and conference papers authored or co-authored as part of the work contained in this thesis are as follows:

M. Panitz and C. Christopoulos. *An Internal Fractional Boundary Placement Model for the Transmission-line Modelling Method.* Proceedings of CEM 2011, Wroclaw, Poland, 1114 April, 2011

M. Panitz, C. Christopoulos, P. Sewell, D. C. Hope, J. F. Dawson, A. C. Marvin, T. Sato, E. Fearon, K. G. Watkins, G. Dearden, C. D. Harley and W. J. Crowther. *The Opportunities and Challenges Associated with Wireless Interconnects in Aircraft.* Journal of Aerospace Engineering, Proceedings of the Insitution of Mechanical Engineers, Part G. Vol 224, pp. 459-469, 2010.

M. Panitz, J. Paul and C. Christopoulos. *A fractional Boundary Placement Model Using the Transmission-Line Modeling (TLM) Method.* IEEE Transactions on Microwave Theory and Techniques, Vol 57(3), pp. 637-646, 2009.

J. F. Dawson, D. C. Hope, M. Panitz and C. Christopoulos. *Wireless Networks in Vehicles.* Invited paper in IET seminar on Electromagnetic Propagation in Structures and Buildings, London, 4 December, 2008.

J. F. Dawson, D. C. Hope, M. Panitz and C. Christopoulos, *Fly by wireless: Evaluation of the Zigbee Radio System for in Vehicle Connectivity.* EMC UK, Newbury, 14-15 October 2008.

M. Panitz , C. Christopoulos, P. Sewell, D. C. Hope, J. F. Dawson and A. C. Marvin. *Modelling Wireless Communication in Highly-multipath Low-loss Environments.* EMC Europe 2008, Hamburg, 8-12 September, 2008, pp. 709-714.

D. C. Hope, J. F. Dawson, A. C. Marvin, M. Panitz, C. Christopoulos and P. Sewell. *Assessing the Performance of ZigBee in a Reverberant Environment using a Mode Stirred Chamber.* IEEE International Symposium on Electromagnetic Compatibility, Detroit, 18-22 August, 2008.

M. Panitz, P. Sewell and P. Sewell. *Channel Characterization for Wireless Propagation in Reverberant Environments.* Proceedings of the 10th Anniversary International Conference on Transparent Optical Networks, ICTON 2008. Athens, 22-26 June, 2008. Vol.4. pp. 94-97.

M. Panitz, C. Christopoulos, P. Sewell and C. J. Smartt. *Electromagnetic Challenges in a Wireless Aircraft.* Proceedings of the UK National URSI Symposium 2007. University of Portsmouth, 2-3 July, 2007.

Contents

1 Introduction **1**

1.1 Advantages of Wireless 2

1.2 Practical Considerations 8

1.3 Possible Applications 10

1.3.1 Flight Control 11

1.3.2 Engine Control 11

1.3.3 Utilities 12

1.3.4 Health Monitoring 12

1.4 Scope of this Thesis and Contributions 13

1.5 Thesis Stucture 16

2 Parameter Definitions **19**

2.1 Representative Environments of Interest 20

2.1.1 Single Resonant Environment 20

2.1.2 Coupled Resonant Environment 22

2.1.3 Dynamically Varying Structures 22

2.2 Definition of Parameters 22

2.2.1 Quality Factor 23

2.2.2 Mean Excess Delay 26

2.2.3 Q Factor and Mean Excess Delay Relationship 27

2.2.4 Density of Modes 31

2.3 Bit/Packet Error ratio 34

3 Communication Systems of Interest **37**

3.1 System Requirements 38

3.2 Modulation Techniques 40

3.2.1 Amplitude Shift Keying (ASK) 40

3.2.2 Frequency Shift Keying (FSK) 41

3.2.3 Phase Shift Keying (PSK) 42
3.2.4 Quadrature Phase Shift Keying (QPSK) 43
3.2.5 Minimum Shift Keying (MSK) 46
3.2.6 Modulation Bandwidths 49
3.3 Spread Spectrum Techniques 51
3.3.1 DSSS 53
3.3.2 CDMA 56
3.3.3 FHSS 59
3.4 Complete Communication Systems 59
3.4.1 ZigBee 60
3.4.2 Bluetooth 61
3.4.3 Wireless LAN 62
3.4.4 Summary 62
3.4.5 References 63
4 Modelling of a Single Resonant Cavity **65**
4.1 Modelling Approach 67
4.2 Equivalent Circuit Model 69
4.3 Obtaining Circuit Parameters 76
4.3.1 Analytical 77
4.3.2 Data Fitting 81
4.4 A Statistical Approach to Channel Modelling 89
5 Modelling of Multiple Coupled Cavities **94**
5.1 Problem Description 95
5.2 Aperture Coupled Cavities 96
5.2.1 Two Slot-Coupled Cavities 96
5.2.2 Multiple Slot-Coupled Cavities 105
5.2.3 Effect of Slot Orientation 107
5.2.4 Analytical Coupling Coefficients 110
5.2.5 An Efficient Cavity Model 114
5.2.6 Validation 120
5.3 Waveguide Coupled Cavities 122
5.3.1 Waveguide Containing a Wire 126

6 Dynamic Models of Cavities **130**

6.1 Requirements 131

6.2 Existing Approaches 134

6.2.1 Graded Mesh 134

6.2.2 Stub Model 138

6.3 New Boundary Development 145

6.3.1 2D model 145

6.3.2 3D model 153

6.3.3 Validation 156

6.4 Non-PEC Boundaries 163

6.4.1 Magnetic Boundary 164

6.4.2 Lossy Boundary 166

6.5 Internal Boundaries 171

6.5.1 Validation 175

6.6 Time Varying Boundaries 178

6.6.1 Model Development 179

6.6.2 Validation 182

6.6.3 Model Stability 188

7 Propagation and Wireless Modelling Examples **192**

7.1 Model Summary 192

7.2 Resonant Cavity Problems 194

7.2.1 BPSK 194

7.2.2 Filtered BPSK 199

7.2.3 Bit Period 203

7.2.4 Summary 207

7.3 Fractional Boundary Problems 209

7.3.1 Practical Impact of Vibrations 214

7.4 Acute Angle Modelling 216

8 Conclusions **220**

8.1 Possible Wireless System Modelling 224

8.2 Concluding Remarks 225

A Sequences for Spread Spectrum Techniques **235**

A.1 Maximal-Length Sequences 235
A.2 Gold codes 238
B Cavity Resonance from Geometric Optics **241**
B.1 A Geometric Optics Approach 242
B.2 Example Problem 246
C TLM Stub Calculations **250**
C.1 Stub Calculation in 2D 250
C.2 Stub Calculation in 3D 252

Chapter 1

Introduction

The advancement of electronic technology over recent decades has gradually displaced mechanical systems with electronic devices. One area where this change is most noticeable is in the aerospace industry where, for example, aircraft control that previously has been purely mechanical has become electronic with typically mechanical input and output. Aircraft systems, for example, are coupled mainly by wires that form bundles and the total length of wiring in aircraft can be tens of kilometres. Other environments where the volume of electronic monitoring, control and hence wiring has increased include the automotive, nautical and locomotive industries.

The choice of wires as the coupling method is preferable in many cases due to the reliability, efficiency and low initial costs involved. Wires are typically used where there is no need for movement of the transmitter and receiver as the topology is fixed. However, in the area of communications and networking there has been a recent movement towards wireless systems to allow for flexibility and mobility. Most noticeable are the advancements in mobile telephony and local area networks

to facilitate the connection of portable computers to high speed networks.

The work in this thesis was carried out as part of the FLAVIIR project where there is an interest in moving towards a wirelessly networked, flapless aircraft [1]. It is hoped that the increase in weight and complexity associated with the large number of sensors and actuators necessary to control airflow over the wings of the aircraft could be offset by moving to a wireless based system. In replacing wired systems with an unguided wireless system an understanding of the impact of such an approach must be gained as safety-critical systems are involved.

The environment in which the wireless system must operate can be considered challenging from an electromagnetic perspective. Aircraft, cars, trains and ships are typically constructed such that they consist of a large number of small, metallic, cavity-like stuctures through which wires will normally pass. These cavities are highly resonant and low-loss so that energy is reflected from the cavity wall a very high number of times. Equivalently, it will be shown that the cavities form a highly multipath, low differential delay channel. In this thesis the electromagnetic propagation properties of these cavities are explored and efficient models for modelling them are developed. The models developed are computationally efficient and are applied to some commonly used wireless communication systems in order to assess their performance in the highly resonant and dynamically varying environments that can be encountered.

1.1 Advantages of Wireless

The use of wireless systems has a large number of advantages over wired systems within the application areas mentioned above. In this thesis the primary area of interest is aerospace, this is also the area where a wireless system is most

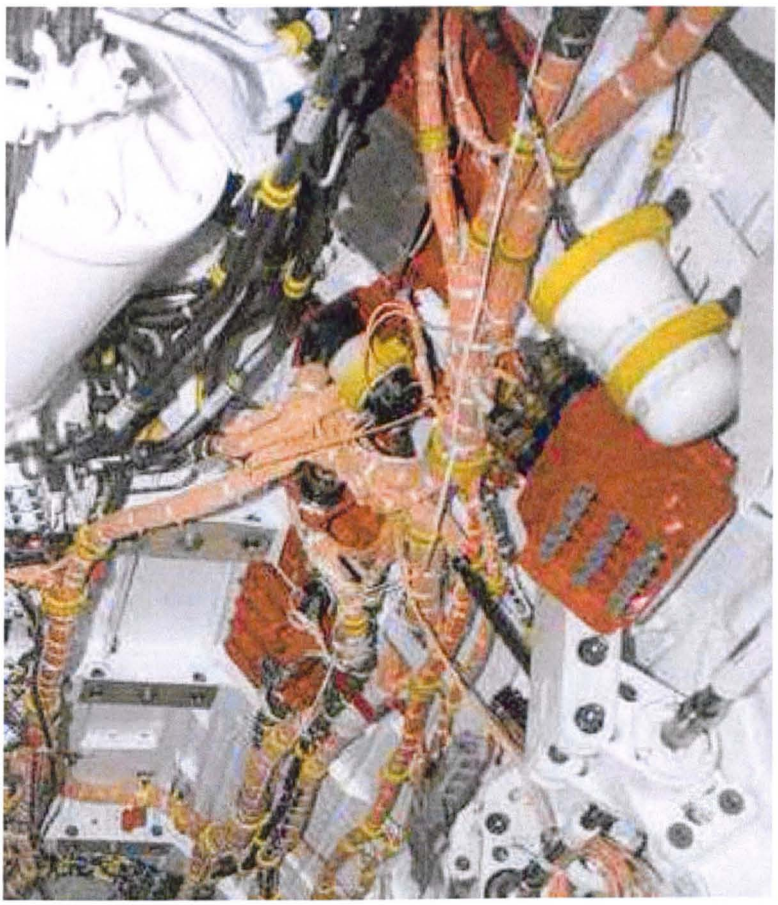

Figure 1.1.1: Equipment bay and wiring within the JSF [2]

advantageous, as weight, space and safety are highly significant factors in aerospace design. However, the models and findings herein are not limited to aerospace environments, they can be equally applied to any of the industry areas mentioned above, provided the environment of interest can be considered equivalent to those investigated in this thesis.

A reduction in the number of wires in an aircraft would have a number of benefits, the most obvious of which is a reduction in weight. A Boeing 747, for example, contains over 220,000 metres of wire weighing a total of 1,600 kilograms [4] and the Airbus A380 contains 500,000 metres of wiring [5]. An example of the

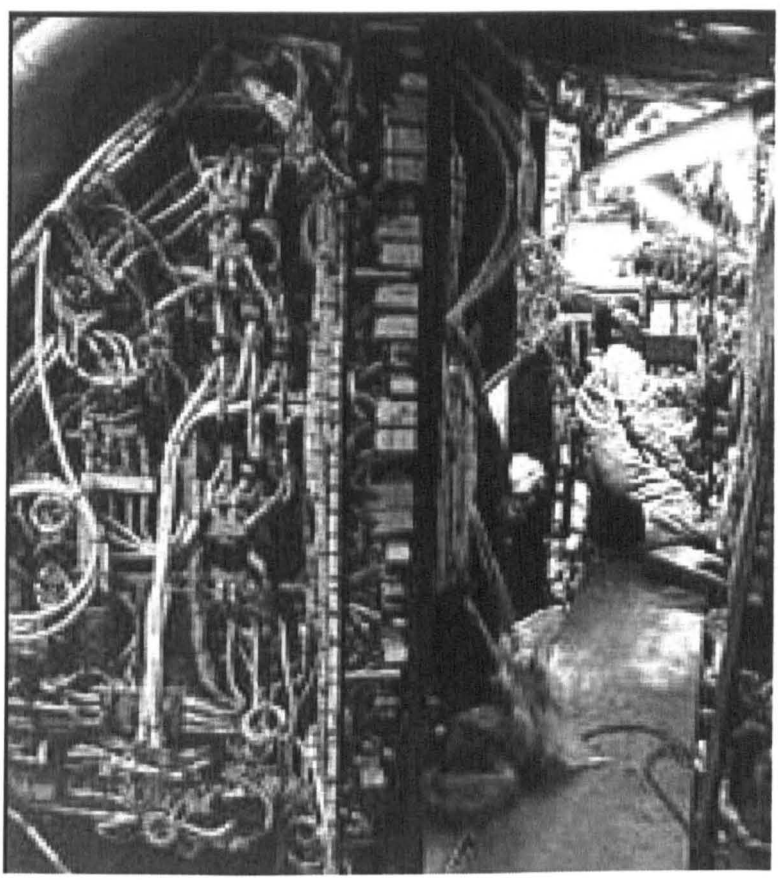

Figure 1.1.2: Wiring behind the forward bulkhead within Concorde [3]

amount and complexity of wiring within an aircraft can be seen in Figures 1.1.1 and 1.1.2. Figure 1.1.1 shows the complexity of the wiring within the Joint Strike Figher (JSF), which contains over 28 kilometres of wiring. Figure 1.1.2 shows the wiring behind the forward bulkhead of Concorde. The volume of wiring is not only a major contributor to the aircraft weight but also greatly increases the complexity of maintenance and repair of aircraft systems.

Airbus have been actively seeking to reduce wiring weights by replacing copper wiring with lighter aluminium wiring. Furthermore, the amount of point-to-point wiring is being reduced through the use of data buses such as the ARINC 429 and more recent ARINC 629[1] [6]-[7]. An increase in weight leads to greater fuel consumption and a reduction in manoeuvrability, it is therefore very desirable to reduce the weight within an aircraft.

Wires suffer fatigue and degrade over time due to bending, flexing, vibrations, chemicals and moisture and therefore need to be replaced periodically. Typically the wires are difficult to access and this maintenance task becomes costly; both financially and in terms of time. The breaking of wires will lead to intermittent or permanent failure and the degrading of insulation can lead to short circuits, interference, arcing and possibly fire as a result. Wiring failure has led to the loss of a number of aircraft including TWA flight number 800 from New York JFK in July 1996, due to arcing of fuel sensor wiring leading to a fuel tank explosion, and Swiss Air flight 111 from New York JFK in September 1998, due to a wiring failure leading to a cockpit fire [8]. Wiring complications also considerably delayed the delivery of the Airbus A380 [5].

[1]The ARINC 429 data bus is a digital half duplex, single source, multiple sink standard device that sends data at between 12 kbit/s and 100 kbit/s. This system is being replaced with a higher data rate ARINC 629, which also is a multiple source device, on modern aircraft including the Airbus A380 and Boeing 787. The modern data bus is based on an ethernet standard and can opertate at data rates of upto 100Mbit/s.

Wireless systems permit a far greater degree of flexibility than wired systems, as a large number of wireless nodes can be connected to a single control node. Furthermore, if it is desired that additional nodes be retrofitted it is far easier to add additional wireless nodes than it is to add wired systems. The route of the wiring through the airframe does not need to be considered when using a wireless system, this is advantageous because the routing of wired systems often becomes very complex and difficult as it is not considered in detail at the design phase.

Finally, a wireless system provides a more *distributed* system where much greater protection is guaranteed against single node failure. Using a wire as a coupling path presents a single mode of failure if the wire is broken at any point, a wireless system can only fail at the transmitter and receiver. Wireless systems could also theoretically re-route themselves through other nodes if a link is lost, creating a temporary communication path as a failsafe. The absence of a wire between the sensor or control device and the processing unit of the aircraft is advantageous in terms of lightning protection. There is no direct coupling path to the processing unit so a lightning strike would lead only to local failure and not a potential system-wide failure.

Optical fibres are commonly being used to reduce the number of wires and increase reliability and weight in aircraft [9][10], however these too suffer some of the disadvantages of wires. The fibres are still subject to structural failure and require routing through complex airframes and their flexibility is less than that of wires. A wireless system will also provide similar advantages over an optical fibre based system as a wired system.

Figure 1.2.3: Equipment bay within a small civilian aircraft

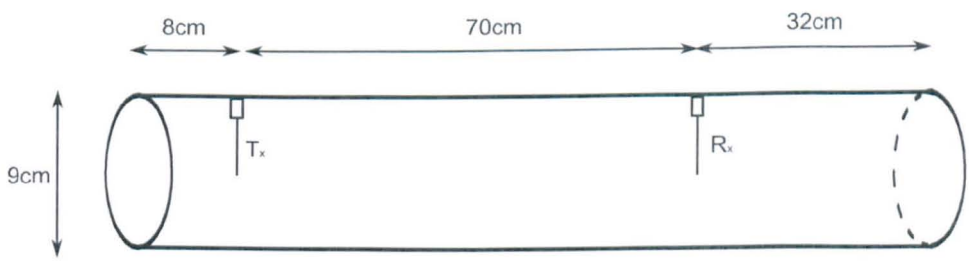

Figure 1.2.4: Schematic of a metallic cylinder containing a pair of antenna

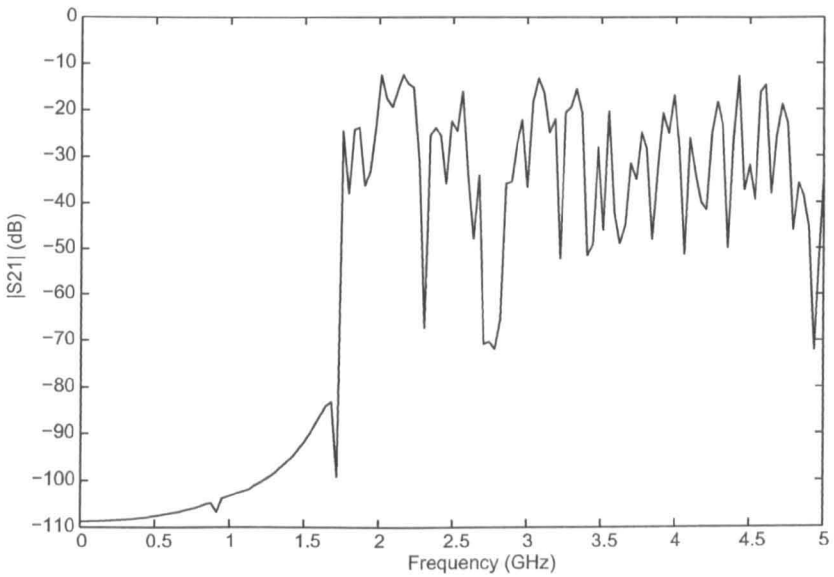

Figure 1.2.5: S21 response of the metallic cylinder calculated using the TLM method

1.2 Practical Considerations

There are a number of factors that must be considered in order to investigate suitable environments and suitable wireless systems. Most suitable, existing wireless network systems operate in the Industrial, Scientific and Medical (ISM) band around 2.45GHz, although some do operate in other bands such as 900MHz [11]. The wavelength in air at 2.45GHz is 12.2cm, which is smaller than many structural features inside the aircraft, for example avionic bays, apertures and bulkheads. Such an equipment bay within a small civilian aircraft can be seen in Figure 1.2.3.

It is therefore expected that the aircraft structure will have a strong influence, whether through reflections or absorption, on wave propagation in this environment. As an example, the frequency response of a cylindrical metal tube was simulated where a signal is propagated between a pair of antennae in the cylinder [12]. Both ends of the cylinder are closed and both antennae are connected to a

50Ω load. A schematic of the geometry can be seen in Figure 1.2.4 where dimensions are shown. The model was constructed using the transmission line modelling method [13] and the S21 response was calculated; the $|S21|$ magnitude response can be seen in Figure 1.2.5.

The response shows a number of features that are characteristic of the environments being considered here. There is a well defined cut-off where energy is dramatically attenuated and does not propagate below 1.788GHz [14]. If a wireless system was used in this environment, below this frequency, it is very unlikely that the system would function without a significant number of errors occurring. Furthermore, it is clear that the resonant behaviour of the channel leads to a large number of narrow and deep valleys in the spectrum. Again, it is unlikely that a wireless system would operate effectively in this region of the spectrum. If the system being used coincided with one of the valleys in the spectrum it is unlikely that the transmitted signal could be recovered. Furthermore, the position of the peaks and troughs are not guaranteed to be fixed as it is possible that vibrations and structural flexing will cause them to move in frequency. It is therefore very difficult to obtain a reasonable approximation of quality of the channel by directly modelling the environment. In this thesis approaches are developed to obtain a suitable estimate of the channel quality in terms of its effect on the physical layer of a wireless system.

In order for a system to be truly wireless it is necessary that the power usage of the nodes of the devices is as low as possible. In this way the power source for the devices can be provided by batteries or the scavenging of power from the vicinity of the device. Power could potentially be scavenged from heat, vibrations, fluid flow or direct mechanical means. In Chapter 3 some wireless systems are introduced along with their typical power usages where it is shown that higher data rates typically lead to higher power usage.

The safety and security of the wireless system is of great importance. For flight critical systems such as flight control, the legally required level of reliability established in FAR/JAR25.1309 is that the probability of catastrophic failure should be no greater than 1×10^{-9} per flight hour [10]. Furthermore, it must be ensured that the system is not affected by interference from external or internal means, whether intentional or not, by RADAR for example, or intercepted by any means.

1.3 Possible Applications

The advantages of moving from a wired system to a fully or partially wireless system have been described. However, there are a number of factors that must be considered that place limits on the applications of wireless systems within aircraft. There is a significant number of systems within an aircraft each with large numbers of interconnections [15]. Data rates available using wireless systems are typically far lower than those available using wired systems and high data rate wireless systems typically use a greater amount of power than lower data rate systems. Furthermore, wireless systems do not use fixed wires as guiding structures and instead use free space propagation. This makes the reliability and integrity of a wireless system dependent on, in addition to hardware and software factors, its surroundings. Therefore, flight critical systems that rely on very low communication error rates may not be suitable candidates for replacement with wireless systems.

In order to ascertain the requirements of a wireless system and where they could be adopted it is necessary to consider the types of systems usually present on aircraft. These avionic systems vary greatly in their application within the aircraft, however [16] categorises them as defined in the following sections.

1.3.1 Flight Control

Flight control encompassess the control and monitoring of a large number of aircraft components and systems. The role of the flight control system is to ensure that the aircraft responds firstly to input from the pilot or autopilot regarding altitude and heading, and secondly ensures the short term stability of the aircraft. In terms of sensing, the flight control system must monitor airspeeds, three-axis accelerations, roll, pitch, yaw, angle of attack and outside pressures. In terms of control, the control surfaces on an Airbus A320 include; 10 spoiler sections, 3 rudder sections, 4 aileron sections and 4 elevator sections. These control devices are managed through 7 control computers which must also provide information to the pilot, these are connected through an ARINC 429 data bus [6].

Based on data rates alone, it is feasible that digital communications that are typically taken care of by the ARINC 429 bus could be replaced by wireless links. However, the safety criticality of these systems means that it may not be possible to directly replace these systems [17]. In the case of higher data rate systems, such as those that use the ARINC 629 it is likely that these could only be replaced with wireless LAN based systems that typically have high power consumption and would make them unsuitable for wireless replacement.

1.3.2 Engine Control

Engine control is heavily dependent on a large number of sensors to monitor the status of the engine. In order to provide smooth engine operation it is necessary to monitor a number of engine parameters, these include fan speed, temperature, pressure, exhaust temperature, exhaust pressure and fuel intake. Furthermore, control of fuel intake, air valves and the engine start are all necessary. A wireless

system would be able to replace the links necessary between the engines and aircraft control computer. Engine control is typically at a lower data rate than flight control and requires a large amount of wiring to be placed within the wings of the aircraft.

1.3.3 Utilities

This category of avionic system incorporates many avionic systems not related to flight or engine control, including fuel management and level monitoring, temperature controls, brakes and hydraulics. Fuel management and monitoring, for example, includes a large number of sensors in order to record fuel density, temperature, water content and tank levels of the aircraft fuel. This data must be communicated to a fuel processing unit and involves a large number of low data rate, low duty cycle data signals. This sort of system is ideal for replacement using a wireless system. Use of a wireless system would reduce, if not eliminate, the number of wires that must pass close to and into the fuel tanks. In the Boeing 777 there are a total of 128 links to fuel tank sensors which typically operate through the ARINC 429 bus, as mentioned before this would be suitable for replacement with low power wireless systems.

1.3.4 Health Monitoring

Health and usage management systems (HUMS) involve monitoring the general properties of the aircraft not captured by the preceding categories. HUMS may include the monitoring of vibration levels, strains, general power levels, engine torques etc. It is common that such monitoring is both low data rate and low duty cycle and with utilities management would be ideal for replacement with a

wireless system.

1.4 Scope of this Thesis and Contributions

The possible applications of a wireless system within an aircraft have been considered. In utilising wireless systems in an aircraft, it has to be demonstrated that transmission inside the hull of an aircraft can be established and offer the very high levels of security and reliability necessary in a safety critical environment. It has been shown that the environment is highly resonant and multipath and electromagnetically challenging as a result. Such an environment will lead to a large amount of intersymbol interference due to the high number of reflections involved. Usually, where intersymbol interference is present, as in this case, analytic solutions do not exist for determining system performance and simulations or measurements must be employed. This work focusses on providing suitable computational models for assessment of the quality of propagation inside the highly resonant environment. This offers modelling advantages over and above those available using conventional multipath modelling tools that are used in large and high loss environments.

There exists a large amount of literature in the area of wireless communications in terms of both the methods used within the physical layer and in terms of signal transmission. A number of suitable references include [18] and [11] however all refer to wireless system use in office, home or urban environments with typically long path lengths and high losses. The use of wireless interconnections in aircraft is a new area but there has been some work done that has been published recently. In [19] health monitoring systems are brought out as a potentially suitable area for the deployments. Fragoulis, Tsagaris and Anastassopoulos have also looked at the use of ad-hoc sensor networks for health monitoring systems [20]. Coelho and Macelo looked at "A fly-by-wireless UAV platform based on a flexible and distributed

architecture" and demonstrated a simple distributed avionics system built around the Bluetooth standard [21]. GulfStream too have demonstrated wireless flight control to one actuator [16]. Furthermore, in 2007 there was a CANEUS/NASA workshop on "Fly-by-wireless for Aerospace Applications" where companies such as Honeywell and Bombardier presented [22]. Despite the interest in the area no literature has so far been found looking rigorously at how to build a reliable system from the physical communications layer upwards.

As power requirements limit the complexity of any system that is to be used to replace a traditional wired system the direct effects of the environment must be fully understood. This is a challenging area as the enviroments are highly complex and any suitable modelling tool must be efficient in modelling the environment whilst capturing all of the important features of that environment. The work herein provides a novel approach to directly modelling the physical layer in an efficient manner. In doing so there is the potential to provide significant cost savings in the design stage of any system. In this work efficient filter models are developed that are capable of modelling a genric environment efficiently in a statistical manner similar to that used in reverberation chamber measurements. In this approach measurable parameters of a general environment are taken to provide a statistically meaningful characterisation of the communication channel. Models are developed for both single and multiply-coupled cavities to provide a powerful tool, these models are then used to investigate commonly used wireless schemes. Whilst multipath models exist they focus on urban environments and only model a limited number of reflections, the models and approaches developed here contribute significantly to this area of research as they are capable of modelling any number of reflections and loss levels and scale linearly with respect to the number of modes considered.

In addition, a novel dynamic modelling tool is developed within a structured

time-domain full-field electromagnetic modelling technique, specifically the transmission line modelling (TLM) method. This model allows boundaries to be fractionally and dynamically positioned relative to a fixed regular grid without impact to the time discretisation used. Such a model was not previously available and any similar tools have significant drawbacks in that the simulation timestep must be reduced or the accuracy of the result is compromised. The model developed here suffers neither of these problems and provides an accurate and efficient full-field modelling tool. Furthermore, this model provides a means for modelling the impact of structural vibrations and flexing on a wireless system. This model is capable of modelling the impact of dynamic structures on the wireless channel and not simply static environments. Furthermore, the approach offers efficient modelling of acute angles that may be encountered for example in wings.

The filter models developed here are validated, where possible, against full-field models of simple canonical cavities where the full-field model is known to give an accurate result. The validation of the fractional boundary placement model is performed through comparison with standard TLM models and the analytical result for the cavity being modelled. In the case of dynamically varying structures, a simple case is considered where the analytical solution is known allowing the model to be validated. Through validation of the models based on the time and frequency domain results obtained for a $|S21|$ type simulation, the models are then used to assess the impact of the channels on the wireless signal types of interest. Validation based on simple numerical test cases and analytical structures gives confidence in the results obtained when assessing the impact of such channels on the error rates encountered in wireless communication.

1.5 Thesis Stucture

The structure of this thesis and the contents of each chapter are designed to demonstrate the development of a number of tools for electromagnetic modelling of wireless signal propagation in a resonant environment. Details are also given of specific wireless systems and schemes and the models are applied to the wireless systems to demonstrate the applicability of the models, also to give an insight into the effect of the resonant environments on wireless systems.

Chapter 2 introduces the types of environment that are of interest in this thesis and describes their properties. The parameters of interest in such an environment are introduced and defined, such as the quality factor, mean excess delay and modal density. The analogy between the electromagnetic concept of a quality factor and the communications concept of mean excess delay is derived. Finally some analysis techniques that are used later in the thesis are introduced.

Chapter 3 provides some background information and approaches to wireless communications. Initially, the application of a wireless system to an aircraft environment is introduced and the requirements of such a system are explored. Next, the most commonly used wireless communication modulation approaches are introduced and defined. Spread spectrum approaches are introduced as a means of increasing signal bandwidth or providing code based orthogonality to multiple wireless channels. Finally, complete communication systems are introduced and described. It is discussed which system is the most suitable for the applications defined in this thesis in order to capture any properties that may influence the wireless system with the models.

Chapter 4 describes the development of a novel model for modelling the effect of a highly resonant and multipath cavity environment. The rationale behind the

modelling approach is described and used to develop an efficient and flexible model for wireless communication modelling. The inputs for the model are introduced and a number of methods of obtaining the parameters are described. Parameters can be obtained analytically, through data fitting or using a statistical approach to modelling.

In Chapter 5 the effect of cavity coupling is introduced. The impact of coupling two of more cavities through apertures is of interest when considering the environments described in this thesis. Efficient models are introduced to model the effect of cavity coupling through the use of a coupling coefficient. An analytical approach to obtaining the coupling coefficent for a particular aperture shape is developed based upon the concept of transmission lines and waveguide modelling.

Chapter 6 describes the development of a dynamic fractional boundary placement model for the transmission line modelling method. The model is developed to allow external and internal boundaries to be positioned within a structured mesh but not coincide with mesh lines as is customary. The model is developed in 2D and 3D and can model perfect electric conducting, perfect magnetic conducting and first-order lossy boundaries. Furthermore, the model is extended to allow the boundaries to be moved dynamically during a simulation. This model is ideal for modelling the complex environments of interest and the effects of structural vibrations and flexing.

In Chapter 7 the tools developed in Chapters 4 to 6 are then applied to some example wireless communication problems. The environments and communication systems defined in Chapters 2 and 3 respectively are used to provide some examples of the effect of the highly resonant and dynamic environments on wireless signal propagation.

Finally, Chapter 8 concludes the thesis with a discussion of the models developed and the findings through use of the models. Other application areas for the developed models are also discussed with reference to the limitations and approximations made in the development stage. Possible areas of further development based on this work are also included to provide an insight into the many concepts and ideas that could be explored but were not possible in the scope of this thesis.

Chapter 2

Parameter Definitions

In order to understand and evaluate the effect of the aircraft environment on wireless propagation the properties of the environment and the wireless system must first be understood. There are a large number of resonant cavity environments that can be considered of interest in this thesis. Within any aircraft, or modular vehicle or structure, there is large variation in the internal cavity structure. Furthermore, the overlap of the disciplines of electromagnetic propagation and wireless communication introduce a number of similar, overlapping concepts, which are often defined in different ways.

This chapter starts by introducing the environments of interest in this thesis and the properties that are unique to each of them in this context. Next, the terms used throughout to describe the properties of the enviroments are introduced and defined. Finally some of the tools used to measure the effects of these environments on wireless propagation are introduced.

2.1 Representative Environments of Interest

The environments of interest herein can be divided into the catagories of single cavity resonant environments, multiple coupled resonant environments and dynamically varying resonant environments. In practice, the shape, size and properties of the cavities of interest vary considerably. Therefore, in order to quantify the effects of the environments in a meaningful way it is necessary to introduce structures that are representative of real structures. These structures should be simple, yet capture the physics of the real environments.

Figures 2.1.1-2.1.3 show schematics of representative environments of the types that will be considered herein. The unique properties of each are briefly described in the following subsections.

2.1.1 Single Resonant Environment

The single cavity resonant environment is characterised by the system shown in Figure 2.1.1. Here the environment is a closed metallic cavity with a transmitter (T_x) and receiver (R_x) within the same volume. The dimensions (l, w, h) of the cavity are time invariant constants.

Losses can be introduced in two ways; either through wall losses or through lossy materials within the volume. Wall losses are due to the skin effect, which reduces the magnitude of the surface reflection coefficent of the cavity walls, disippating electromagnetic energy as heat in the cavity walls. Lossy materials absorb the electromagnetic radiation within the volume of the cavity; typically such materials are likely to be found in the cavities. The effect of losses is to reduce the quality factor (Q factor) of the cavity, which will be defined in the next section.

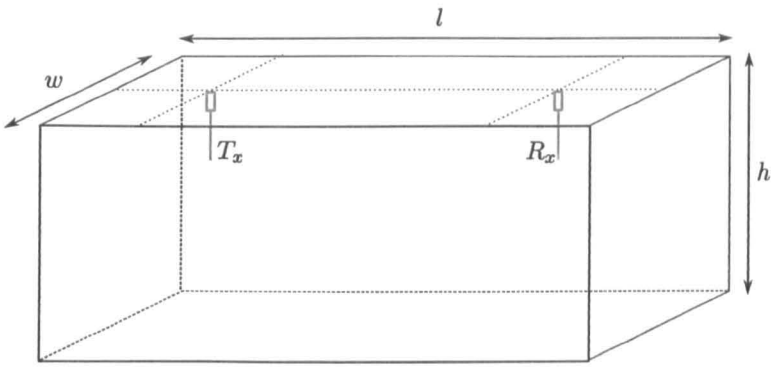

Figure 2.1.1: Schematic of a single cavity resonant environment

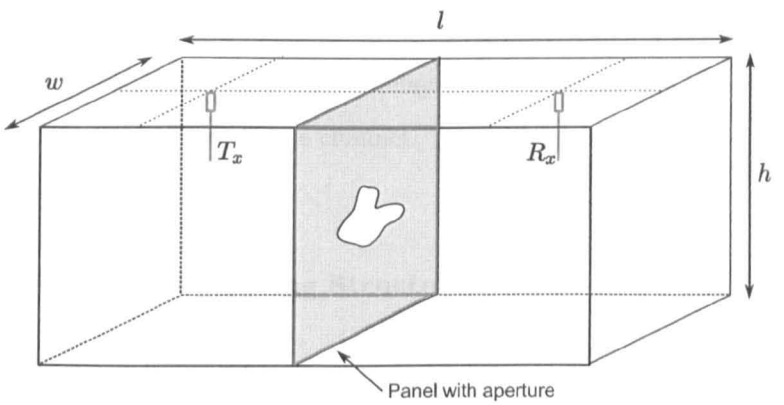

Figure 2.1.2: Schematic of a coupled cavity resonant environment

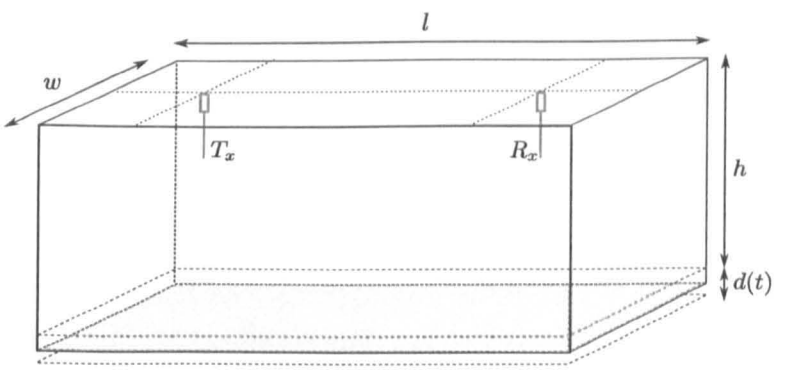

Figure 2.1.3: Schematic of a dynamically varying resonant environment

2.1.2 Coupled Resonant Environment

The coupled resonant environment can be seen in Figure 2.1.2. The properties of this type of system are the same as that of the single cavity except now there are two volumes seperated by a screen in which there is an aperture. The aperture could be of any shape or thickness and provides the coupling path between the two volumes.

Again, losses can be introduced via a surface loss or through lossy materials. The definition of a single Q factor cannot strictly be applied to a system of this kind as there is no longer a single cavity, both cavities will have its own Q factor. Instead, in this thesis the mean excess delay is introduced as the metric of choice for measuring energy decay in the channel.

2.1.3 Dynamically Varying Structures

Finally, a dynamically varying resonant cavity is considered in Figure 2.1.3. Here, the structure is no longer time invariant and varies with time. It has been discussed that such variation can be due to flexing, bending and vibrations. One or more of the surfaces that make up the cavity is able to move as represented by the time varying displacement $d(t)$ in Figure 2.1.3.

2.2 Definition of Parameters

This work is associated with both the electromagnetic behaviour of resonant environments and wireless communication systems. It will be shown in Chapter 4

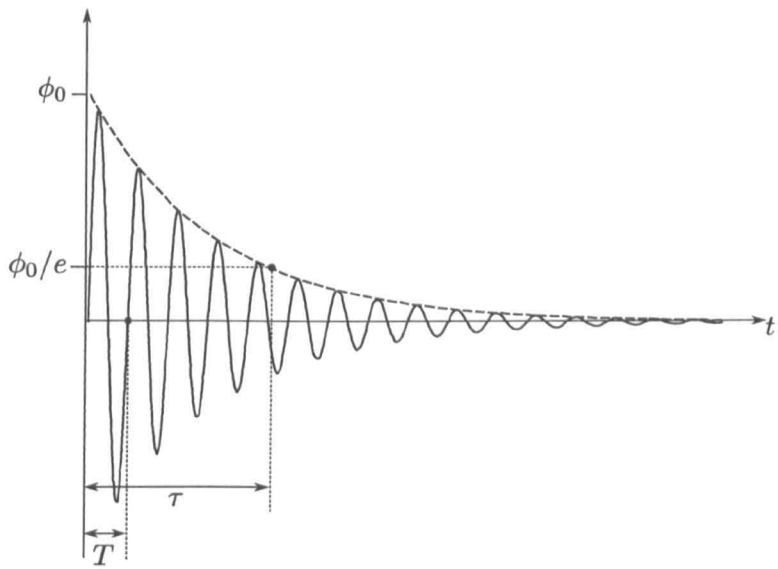

Figure 2.2.4: A damped sinusoid and its parameters

that the resonant environment can be considered to be a highly multipath, low loss communication channel. In order to provide background and present the link between the two fields, this section describes some of the parameters commonly associated with each field.

2.2.1 Quality Factor

The *quality factor* or Q factor is a quantity that is usually associated with resonant systems including resonant cavities. It is a dimensionless quantity that can be used to quantify the energy storage properties of a cavity. Being dimensionless, the Q factor is defined in a number of ways depending on its application and is usually frequency dependent. This frequency dependence arises from the fact that, in most situations, the losses within a system are dependent on frequency. For example, the resistive losses due to the frequency dependent skin effect inside a metallic cavity [14], [23].

The Q factor is defined for a resonant cavity in terms of the frequency of the energy oscillations within the cavity. In this thesis the Q factor is defined as [23]

$$Q = 2\pi \left(\frac{Energy\ Stored}{Energy\ Lost\ Per\ Cycle} \right) \tag{2.2.1}$$

The Q factor can be obtained from the time domain decay profile of a resonant decay or from the resonant peak width in the frequency domain. Consider the decaying sinusoid shown in Figure 2.2.4. The decaying sinusoid can be expressed in the form

$$\phi(t) = \phi_0 e^{j(\omega_0 + j\alpha)t} \tag{2.2.2}$$

where α is the decay constant and ϕ_0 is the initial amplitude. The decay constant is given by the reciprocal of the decay time, which is the time, τ, for the envelope to decay by an amount ϕ_0/e, so that $\alpha = 1/\tau$. The Fourier transform of the decaying sinusoid is given by

$$|\Phi(\omega)|^2 = \frac{1}{\alpha^2 + (\omega - \omega_0)^2} \tag{2.2.3}$$

It can be easily identified that at resonance ($\omega = \omega_0$) the maximum energy is given by $1/\alpha^2$ and hence the half maximum energy is reached at

$$\begin{aligned} \omega_+ &= \omega_0 + \alpha \\ \omega_- &= \omega_0 - \alpha \end{aligned} \tag{2.2.4}$$

so that the full width at half maximum (FWHM) is given by

$$\Delta\omega = \omega_+ - \omega_- = 2\alpha \tag{2.2.5}$$

The Q factor using (2.2.1) can be calulated by discretising time, t, in terms of the period, T, of the oscillations so that the decay profile is sampled every nT, where n is a positive integer. Hence, the Q factor can be expressed in terms of the

energy decay

$$Q = 2\pi \frac{e^{-2nT\alpha}}{e^{-2nT\alpha} - e^{-2(n+1)T\alpha}} = \frac{2\pi}{1 - e^{-2T\alpha}} \tag{2.2.6}$$

We consider only the limit of high Q factor cavities so that the decay time is long compared with the sinusoid period, hence, $T << \tau$ and $\alpha T << 1$. Therefore, the approximation

$$e^{-2\alpha T} \approx 1 - 2\alpha T \tag{2.2.7}$$

can be applied to yield

$$Q = \frac{\pi}{\alpha T} = \frac{\omega_0}{\Delta\omega} \tag{2.2.8}$$

with substitution of (2.2.5) and the angular frequency of the sinusoid. Inspection of (2.2.8) also shows that the Q factor is equal to 2π times the number of cycles in the decay time τ.

The higher the Q factor of the cavity the better it is at storing energy. The Q factors obtainable within an empty cavity can exceed 32,000, for example [23] and [24]. However, in this study the cavities of interest will have Q factors of 5,000 or less and typically of the order of 100-1,000 when loaded with equipment.

In practice the total energy stored and the total energy lost cannot be measured directly. As a result, the Q factor can be defined in terms of input and output power; this is an approach commonly taken in reverberation chamber studies [23] so that the Q factor is given by

$$Q = \frac{2V\omega^3}{\pi c^3} \left\langle \frac{\overline{P}_{Received}}{P_{Input}} \right\rangle \tag{2.2.9}$$

where V is the cavity volume and the bracketed terms is the ratio of the average received power, at a sufficient number of sample points, to the input power over one complete tuner/stirrer sequence [23].

A number of sample points must be taken as the Q factor can vary with position within the cavity as does the energy measured due to the resonant structure within the cavity. The approach taken in reverberation chamber studies is to use a mode stirrer instead of moving the sampling point. A simulation approach analogous to this will be used in Chapter 4 to efficiently characterise the properties of the resonant channel.

2.2.2 Mean Excess Delay

The term *mean excess delay* is usually associated with wireless propagation and mobile communications. The mean excess delay is a metric that can be used to characterise a multipath environment by providing information about the relative delay in the multiple received signals and is the first moment of the power delay profile.

In a multipath channel there will be a number of delayed and attenuated copies of the transmitted signal that arrive at the receiver. The trend observed in the received signal is that the delayed copies tend to be progressively weaker as they have travelled further and been reflected from more surfaces. Short-scale variation in the received signal can vary but the long term trend will be a decaying signal.

The *mean excess delay* is used to quantify the delay in a channel where a greater mean excess delay indicates a larger number of higher power reflections being received. The mean excess delay can be expressed in the following form [25]

$$\overline{\mu} = \frac{\int_0^\infty \tau \left|\phi(\tau)\right|^2 d\tau}{\int_0^\infty \left|\phi(\tau)\right|^2 d\tau} \tag{2.2.10}$$

where $\phi(\tau))$ is the amplitude of a received pulse that is delayed by time τ compared

with the first received pulse. The denominator is used to normalise the expression for received power so that the mean excess delay is independent of input power.

The mean excess delay can be considered to significantly affect the received signal if it approaches one-tenth of the transmitted bit period [11]. As the excess delay is increased it becomes more and more difficult to recover the sent bit and seperate it from previous bits. There are a number of references that define the errors of communication protocols in terms of the mean excess delay in the channel. Using these formulas it is possible to find the mean excess delay of a given channel and make a crude estimate of the errors that are likely in that channel for a given protocol.

2.2.3 Q Factor and Mean Excess Delay Relationship

It can be shown that, under special conditions, the mean excess delay is closely related to the Q-factor described previously and is a more useful representation of the resonant channel quality. In order to demonstrate the relationship between the mean excess delay and Q factor, consider again the decaying sinusoid shown in Figure 2.2.4. It has been shown that this sort of decay is typical for a resonant lossy system such as a resonant cavity. The oscillations in the received signal of Figure 2.2.4 can be considered representative of low-pass filtered impulses. This allows the rewriting of (2.2.10) in discrete form so that the integrals become sums over N received pulses, viz.

$$\overline{\mu} = \frac{\sum_{n=0}^{N} \tau_n |\phi_n|^2}{\sum_{n=0}^{N} |\phi_n|^2} \tag{2.2.11}$$

In (2.2.11), τ_n and ϕ_n are the discrete delay and amplitude equivalences respectively.

Consistent with the calculation of the Q factor the period of the decaying sinusoid is given by T and the envelope has an exponential form with a decay constant α. Therefore, sampling the peaks of the decaying oscillation gives a discrete decaying amplitude of

$$\phi_n = \phi_0 e^{-\alpha n T} \tag{2.2.12}$$

as the peaks are periodically separated in time for a single frequency. Inserting the squared modulus of (2.2.12) into (2.2.11) and assuming a periodic signal where $\tau_n = nT/2$, as the power peaks occur at twice the oscillation frequency, the mean excess delay is given by

$$\overline{\mu} = \frac{T}{2} \frac{\sum_{n=0}^{N} n e^{-2\alpha n T}}{\sum_{n=0}^{N} e^{-2\alpha n T}} \tag{2.2.13}$$

where the initial powers cancel as the mean excess delay is independent of this parameter.

From inspection of (2.2.13) it can be seen that the numerator is in the form of a geo-arithmetic series [26] so that

$$\sum_{n=0}^{N} n e^{-2\alpha n T} = \frac{1 - e^{-2N\alpha T}}{(1 - e^{-2\alpha T})^2} - \frac{(N-1)\, e^{-2N\alpha T}}{1 - e^{-2\alpha T}} \tag{2.2.14}$$

and the denominator is in the form of a geometric series so that

$$\sum_{n=0}^{N} e^{-2\alpha n T} = \frac{1 - e^{-2N\alpha T}}{1 - e^{-2\alpha T}} \tag{2.2.15}$$

Hence, in the limit that $N \to \infty$, the mean excess delay can be expressed as

$$\overline{\mu} \underset{N\to\infty}{=} \frac{T}{2} \frac{\left(\frac{1}{(1-e^{-2\alpha T})^2}\right)}{\left(\frac{1}{(1-e^{-2\alpha T})}\right)} = \frac{T}{2(1 - e^{-2\alpha T})} \tag{2.2.16}$$

Expanding the exponential as a Taylor series and again assuming that the decay time is much smaller than the period of oscillation yields

$$\overline{\mu} = \frac{T}{2} \cdot \frac{1}{2\alpha T} = \frac{1}{4\alpha} \tag{2.2.17}$$

which can in fact be seen to be equal to $\tau/4$ for the resonant cavity Q factor approach demonstrating the analogy between the two approaches in the small cavity, high Q factor limit. The amplitude decay constant α is related to the damping ratio ζ [27] for a particular frequency ω_0 and hence the Q factor through

$$\alpha = \zeta\omega_0 = \frac{\omega_0}{2Q} \tag{2.2.18}$$

Therefore, the mean excess delay for a decaying sinusoid is related to the Q factor through the expression

$$\overline{\mu} = \frac{Q}{2\omega_0} \tag{2.2.19}$$

The result in equation (2.2.19) is important in justifying some of the models described in the remainder of this thesis. The analogy between the Q factor, typically associated with resonant cavities, and the mean excess delay, typically associated with wireless communications, is clearly demonstrated. The resonant cavity can be considered as a highly multipath environment, as demonstrated through this expression. The consequences for modelling such a system is discussed in further detail in Chapter 4.

In deriving (2.2.19), some idealisations were made that would effect the result when considering a real or general environment. It can, however, be shown that the effect of these assumptions is negligible under the conditions being explored here. Given a general environment from a path based point of view, the received signal will not be exactly periodic as described here. Furthermore, a resonant

environment will have a transient period where the oscillation is not periodic until it reaches a steady state. However, if a large number of reflections are being considered, as here, it can be expected that over the full decay of the signal the *average* pulse separation is equivalent to the periodic decay case. The mean excess delay is an average quantity, hence given sufficent reflections, it can be assumed that the result will converge to the decaying sinusoid result for the resonant cavity case.

Furthermore, only a single frequency has been considered here. The Q factor definition used here is dependant on the decay of only a single frequency oscillation whereas the mean excess delay applies to pulses. The bandwidth of interest for a communication system is narrow compared to the carrier frequency and the damping effect on all frequencies can be assumed uniform, that is the Q factor is independent of frequency across the bandwidth of interest. Therefore, the average Q factor, for a narrow bandwidth, is consistent with the mean excess delay, as applied here, hence (2.2.18) is valid.

It has been demonstrated that the Q factor and the mean excess delay are equivalent measures for a highly multipath resonant environment. The definition of mean excess delay applies to any channel, that is the environment is not considered, whereas the Q factor, in this context, applies to cavity structures. The Q factor is related to the power stored and the power dissipated in a particular cavity, normally a simple cavity, and not normally directly related to the propagation path within the cavity. To conform to convention, both measures will be used herein. However, Q factor will be used solely to refer to the resonant environment's energy decay properties and the mean excess delay will be used to quantify the multipath effect on a signal transmitted within the environment.

2.2.4 Density of Modes

Another parameter of resonant cavities is the density of modes within the cavity, that is the number of modes in a defined bandwidth at a defined frequency. The density of modes tells us the density of peaks in the frequency spectrum of a cavity, and hence resonant channel response. The density of modes can be considered a macroscopic measure of the modal structure. For a well defined canonical system the actual modal structure for all frequencies can be calculated. However, due to the possible variation in the communication channel, and the possibility of non-canonical cavities, it is sensible to define an average, macroscopic measure of the modal structure.

In the theory of reverberation chambers the density of modes is defined in order to obtain a minimum frequency of operation [23]. The density of modes must be sufficient to allow, over one full stirrer rotation, the peak power at all points to be within 3dB of any other point.

In this study, the density of modes is defined to permit the use of a statistical representation of the modal structure within the channel. The resonant cavity environment can be decomposed into a discrete system if it is represented in terms of the electromagnetic modes that occupy its volume. The modes must satisfy the boundary conditions at the approximately perfectly conducting walls of the cavity, that is the electric field parallel to the wall must be zero. In this way, the volume, or cavity, can be imagined in the same way as a regular lattice structure; like that seen in a solid state crystal.

The amplitude of a particular mode in a 3D volume can be calculated at any

position using the function

$$\Psi_{mnp} = \sin(k_x x) + \sin(k_y y) + \sin(k_z z) \tag{2.2.20}$$

where the wave vectors, k, are given by

$$k_x = \frac{2\pi m}{X} \quad k_y = \frac{2\pi n}{Y} \quad k_z = \frac{2\pi p}{Z} \tag{2.2.21}$$

In (2.2.21) m, n and p are integers and X, Y and Z are the dimensions of the volume occupied by the wave function. Hence the magnitude of the of the wavenumber, in a vacuum, is given by

$$|k|^2 = \frac{\omega^2}{c^2} = k_x^2 + k_y^2 + k_z^2 \tag{2.2.22}$$

Each combination of wave vectors can be said to represent a particular *mode* in the volume with the wavenumber k.

In order to define the density of modes the system is consider in *k-space*, the reciprocal space to the wavelength, λ. The volume, V, of a given mode in k-space is

$$\frac{(2\pi)^3}{XYZ} = \frac{8\pi^3}{V} \tag{2.2.23}$$

The density of modes, $g(k)$, can therefore be defined as the number of modes, dN, in k-space, dk, so that

$$dN = g(k)dk \tag{2.2.24}$$

The volume of a spherical shell in k-space is given by

$$V = 4\pi k^2 dk \tag{2.2.25}$$

so that the number of modes in a given volume is given by the total volume,

(2.2.25), divided by the volume of one mode, (2.2.23), hence

$$g(k)dk = \frac{4\pi k^2 dk}{8\pi^3/V} = \frac{Vk^2}{2\pi^2}dk \tag{2.2.26}$$

In k-space there exist two modes for each $|k|$ as two waves may oscillate with the same wavelength but π-radians out of phase with each other. Therefore, the modal density, in k-space is given by

$$g(k) = \frac{Vk^2}{\pi^2} \tag{2.2.27}$$

The density of modes in terms of frequency is obtained using the chain rule and (2.2.24) with (2.2.26) so that

$$g(f) = \frac{dN}{df} = \frac{dN}{dk} \cdot \frac{dk}{df} = \frac{Vk^2}{\pi^2} \cdot \frac{2\pi}{c} \tag{2.2.28}$$

so that

$$g(f) = \frac{8\pi V f^2}{c^3} \tag{2.2.29}$$

The density of modes can be used in combination with the standard definition of the Q factor to determine the number of modes in a Q-bandwidth. Here, the Q-bandwith decribes the bandwith of modes excited by an excitation at the centre frequency, f_0, of the Q-bandwidth, Δf [23]. From (2.2.8), the Q factor is defined as

$$Q = \frac{f_0}{\Delta f} \tag{2.2.30}$$

and the number of modes in a Q-bandwith is given by

$$M_Q = g(f)\Delta f \tag{2.2.31}$$

Combining (2.2.29) and (2.2.30) through (2.2.31) gives an expression for the num-

ber modes in the Q-bandwidth

$$M_Q = \frac{8\pi V f^3}{c^3 Q} \tag{2.2.32}$$

This study is based upon the investigation of wireless systems in resonant environments. Therefore, it is possible to define the bandwidth of interest as it is known at which frequency the cavity will be excited, that is the bandwidth of the wireless system being used. If the wireless system has a bandwidth $\Delta f' = f_2 - f_1$, where f_2 and f_1 are the upper and lower frequency limits of the communication band respectively, then the number of modes in this bandwidth is given by

$$M = \int_{f_1}^{f_2} g(f)df = \frac{8\pi V}{3c^3}\left(f_2^3 - f_1^3\right) \tag{2.2.33}$$

2.3 Bit/Packet Error ratio

In order to quantify the effect of the propagation channel on a wireless transmission useful representations of the received signal or data are required to perform an analysis. Perhaps the most meaningful and useful quantity to obtain is the bit error ratio (BER) for a given configuration type. The bit error ratio, sometimes bit error rate, is a measure of the number of bits in error during transmission of a signal. If there are a total of N_{Tx} bits transmitted and a total of N_{Rx} are successfully recovered then the bit error ratio is given by

$$BER = 1 - \frac{N_{Rx}}{N_{Tx}} \tag{2.3.34}$$

where in this work the BER is expressed as a ratio.

Usually data is transferred as a *packet*, that is a sequence of bits, and error checking or decoding is usually performed on the whole packet so a packet error ratio (PER) becomes the measurable quantity. An approximate conversion between BER and PER can be made where

$$PER = 1 - (1 - BER)^{N_b} \tag{2.3.35}$$

and N_b is the number of bits in the packet. This expression is applicable when no forward error correction is used, that is one incorrect bit in a packet leads to the packet being incorrect. Error checking and correction can be used to minimise the packet errors due to individual bit errors. However, this would lead to higher power usage due to the additional processing required and reduced data rate due to the transmission of non-data carrying bits [28].

A BER of zero indicates that all bits were correctly received and the channel quality is very good. If the channel is poor and the transmitted signal cannot be recovered at the receiver the BER will increase. If the received signal is significantly distorted and can be considered random then the maximum BER will be 0.5. However, if data is sent as a symbol or packet (of 2 or more bits) then a poor channel will lead to a PER that tends towards 1.0 due to the power term in (2.3.35).

The acceptable BER and PER is an application dependent metric and a single acceptable value is not defined. For example, for low data rate systems, such as health monitoring, a BER of 1×10^{-3} may be acceptable especially if a number of transmissions are made and the duty cycle is low. However, for control applications an error rate of this magnitude would require significant resending of data and reduce the data rate unsatisfactorily. In this case the error rate would need to be as low as possible. Typically an error rate of less than 1×10^{-6} is required [10] for

a viable system.

The error rate is a metric often used when considering modulation schemes and specifically their immunity to noise. In this work, the BER will be used as a metric for the errors that occur due to the resonant and multipath properties. Whilst the desired limit is not well defined it is still possible to present the trends in BER encountered in the environments and draw the necessary conclusions from this data.

Chapter 3

Communication Systems of Interest

This chapter discusses some wireless communication protocols and systems that are of interest to the problem being considered in this thesis. Research and theory in the field of wireless communications is vast and it would be impossible to cover all of the possible wireless options available. The purpose of this chapter is to provide a background that is sufficient for the purposes of the work described herein. Should the reader wish to research further the information about these, and other communication systems then there are a number of references provided in Section 3.4.5. Wireless communication schemes that are suitable to the required application and meet limits in terms of power availability are investigated using the developed models. However, further schemes can be investigated using the models developed and the results shown here aim to demonstrate the effect of the highly resonant channel on a wireless system.

3.1 System Requirements

There are a number of requirements of the wireless systems that must be met in order to make the system feasible both practically and financially. Performance of a wireless system will be heavily dependent on the choice of radio technology. The resistance to interference, the robustness in heavily multi-path environments and the maximum obtainable data rates are all fixed by the choices made at the physical layer for the radio. The properties of the wireless system are interdependent and a compromise must be reached when choosing a suitable system. The properties of interest of the wireless system and the desired characteristics are as follows [8]:

Cost The wireless system should be low cost to purchase, install, operate and maintain. Furthermore, indirect costs due to the system must be kept low such as the extra fuel required to carry the weight of the technology.

Weight The weight must be kept to a minimum to take advantage of one of the main goals of moving to a wireless system. An increase in weight not only effects fuel consumption but also manoeuverability. The weight of the power source, battery or scavenging mechanism, must also be taken into account and kept to a minimum.

Power In order to keep the weight of the power source low and to eliminate the need of power cables to the systems its power requirements must be kept to a minimum. Ideally the systems should be battery operated and hence should use very little power so that the battery lifetime is comparable to the aircraft maintenance schedule. In order to keep the power low the onboard processing must be limited and efficient and the transmitter power be low.

Secure The system should be secure and not easily intercepted or interfered with. This must be done in an efficient manner to keep the power requirements down.

Robust As well as being secure against intentional threats the system must be robust to the aircraft environment. The environment is very challenging to a wireless system, being highly multipath and resonant, and the system must be able to efficiently operate in this environment.

Data rate The data rate must be sufficient for the application intended. The required data rate for a HUMS system is lower than that of a control system for example. However, the higher the data rate the higher the power usage and more affected by multipath propagation the system becomes.

Reconfigurable Another major advantage of the wireless system is its configurability. It should be simple to install extra sensors and interface them with the existing system in a quick and cost effective manner. The system should be able to support a variable number of nodes and the upper limit of the number of nodes should be large; some COTS systems only support a small number of nodes, such as Bluetooth, which supports eight nodes per master [29]. For many applications the number of required nodes may be larger than this either from the time of production or due to the installation of additional nodes at a later date.

In summary, the chosen systems should be such that cost, weight and power are reduced; security and robustness are increased and the data rate and reconfigurability are task dependent but should ideally be increased. In order to effectively meet these goals standard commercial off the shelf (COTS) technology will be con-

sidered from this point. COTS technology is commonly used in aircraft systems as it is state of the art, highly configurable and cost effective to do so. With this in mind, the common properties of the physical layer, which is the part of the system that interacts directly with the environment, will be introduced.

3.2 Modulation Techniques

With the proliferation of digital technology over recent decades there has been a shift towards the use of digital wireless communications. Such developments are most noticeable in television and radio broadcasting, mobile phone communications and with the emergence of wireless local area networks (LAN).

Traditional analogue systems commonly use amplitude modulation or frequency modulation where the signal is used to continually modulate the carrier wave. However, in digital communications the modulation is discrete and the concept of keying is used where the transmitted wave has constant states that represent the bit, or sequence of bits that are being transmitted. In its simplest form the digital communication system is used to send a sequence of binary bits represented as either 0 or 1. Usually these are voltage levels and bipolar encoding is used where a negative voltage, -1, represents a 0 bit in order to eliminate and DC buildup in the channel.

3.2.1 Amplitude Shift Keying (ASK)

Amplitude shift keying (ASK) is a digital form of amplitude modulation (AM) commonly used for radio communications and broadcasting [11], [30]. In this form of modulation the binary signal is used to control the amplitude of the carrier

signal. Let the data be a binary sequence, an amplitude is then applied to the two states, for example 0.5 and 1.0, such that the signal can be represented as a varying amplitude carrier with fixed frequency. The ASK modulated signal can be represented as

$$S(t) = A(t)\sin(\omega_c t) \tag{3.2.1}$$

where $A(t)$ is either 0.5 or 1.0 for a binary 0 or 1 and ω_c is the carrier frequency.

If modulating amplitudes of 0.0 and 1.0 are chosen, whereby a zero bit will transmit no carrier, then the modulation is called *on-off* keying (OOK). This kind of modulation is spectrally inefficient and only normally used for transmission of Morse-code [25]. The amplitude $A(t)$ can also be broken into 4 levels, for example 0.25, 0.50, 0.75 and 1.00, so that two data bits can be sent at once in a symbol formed from the binary pairs $\langle 0,0\rangle$, $\langle 0,1\rangle$, $\langle 1,0\rangle$ and $\langle 1,1\rangle$. These binary pairs, or symbols, can be transmitted with the same period as the normal binary system therefore doubling the data rate. ASK modulated signals are very vulnerable to amplitude changes due to interference as additive noise changes the amplitude and received value of the signal.

To avoid rapid changes in signal and hence high frequency components the signals are often bandlimited, where the pulses are shaped by a Gaussian envelope. However, the susceptibility to interference renders this modulation technique unsuitable for the wireless system.

3.2.2 Frequency Shift Keying (FSK)

Frequency shift keying is used to transmit data at a single amplitude where the data is used to change the frequency of the carrier. The amplitude of the transmitted signal does not contain any of the data so FSK modulated signals are less

susceptible to additive noise than ASK signals [31]. As with ASK, binary data is used to choose between one of two states where, in this case, the states are two different frequencies. A FSK signal can be represented as

$$S(t) = A\sin\left((\omega_c + \omega(t))t\right) \tag{3.2.2}$$

where A is a constant amplitude and $\omega(t)$ is assigned two values to represent either a binary 0 or 1.

FSK modulation is not very spectrally efficient as the signal contains a large number of sidebands. The bandwidth of a FSK limits the maximum data rate that can be used and the power consumption of FSK systems tends to be high compared with other modulation techniques. FSK is used at audio frequency in characteristically low data rate *dial-up* modems. The power and inefficient bandwidth usage of FSK modulation makes it unsuitable for low power high data rate wireless communications.

3.2.3 Phase Shift Keying (PSK)

The most commonly used modulation type in current wireless communications is phase shift keying (PSK). The signal is transmitted using a fixed amplitude and frequency and the binary data is used to invoke phase shifts in the carrier. Schemes of this type are used in modern wireless communications such as ZigBee, Bluetooth, Wireless LAN and mobile phone communications [25], [28]. The simplest form of phase shift keying is binary phase shift keying (BPSK). In this case two different phases of carrier wave are used to represent the 0 and 1 data bits, usually 0 and π. This offers advantages over standard ASK modulation as a change in phase is less susceptible to interference, however BPSK can be seen to be equal to ASK if

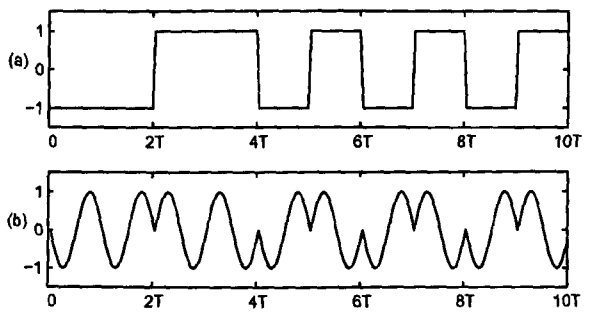

Figure 3.2.1: An input signal (a) and the modulated signal for transmission (b) using BPSK

bipolar coding is used, that is $1 \Rightarrow 1$ and $0 \Rightarrow -1$.

A BPSK signal can be represented in the form

$$S(t) = A \sin(\omega_c t + \theta(t)) \tag{3.2.3}$$

where $\theta(t)$ is either 0 or π for a binary 0 or 1, A is the signal amplitude and ω_c is the carrier frequency. Figure 3.2.1 shows the BPSK scheme applied to some binary data, the input data stream (a) is used to modulate a carrier to give the modulated signal (b).

BPSK is the simplest form of phase shift keying and is normally used for long distance communications such as communications with distant satellites due to its simplicity and low power requirements.

3.2.4 Quadrature Phase Shift Keying (QPSK)

Quadrature phase shift keying can be considered as an expansion of BPSK which makes use of the in-phase (I) and quadrature (Q) channels to transmit a pair

of data bits at once. The I and Q channels are sinusoidal carriers separated in phase by $\pi/2$, or equally a sinusoidal carrier and its co-sinusoidal carrier. The orthogonality of the two carriers means that the received signal can be separated into I and Q signals and decoded.

In QPSK the input is divided up alternately between the two channels so that an input data sequence $d(t) = d_0, d_1, d_2, \ldots$ becomes

$$\begin{aligned} d_I(t) &= d_0, d_2, d_4, \ldots \\ d_Q(t) &= d_1, d_3, d_5, \ldots \end{aligned} \tag{3.2.4}$$

These data sequences are then used to modulate the carrier waves in the following way

$$S(t) = \frac{1}{\sqrt{2}} d_I(t) \cos\left(\omega_c t + \frac{\pi}{4}\right) + \frac{1}{\sqrt{2}} d_Q(t) \sin\left(\omega_c t + \frac{\pi}{4}\right) \tag{3.2.5}$$

which using a well known trigometric identity [26] can also be written as

$$S(t) = A \cos\left(\omega_c t + \frac{\pi}{4} + \theta(t)\right) \tag{3.2.6}$$

In Equation (3.2.6) the phase $\theta(t)$ can take the values 0, $-\pi/2$, π and $\pi/2$ giving four possible phase variations where each represents a pair of binary bits. As there are two bits per symbol in a QPSK system it enable twice as much data to be transferred in the same bandwidth as BPSK [11]. The modulation of a data sequence using this scheme is shown in Figure 3.2.2.

In QPSK the binary signal is used to phase-shift a sinusoidal carrier as with BPSK but here a pair of carriers are used to transmit pairs of data bits so that a four level system is created and the data rate can be doubled. The problem with both BPSK and QPSK is that the modulated signal can contain an instantaneous phase shift of π. This abrupt phase shift introduces a number of sidebands into the signal spectrum which would be an undesired effect in such a frequency dependent

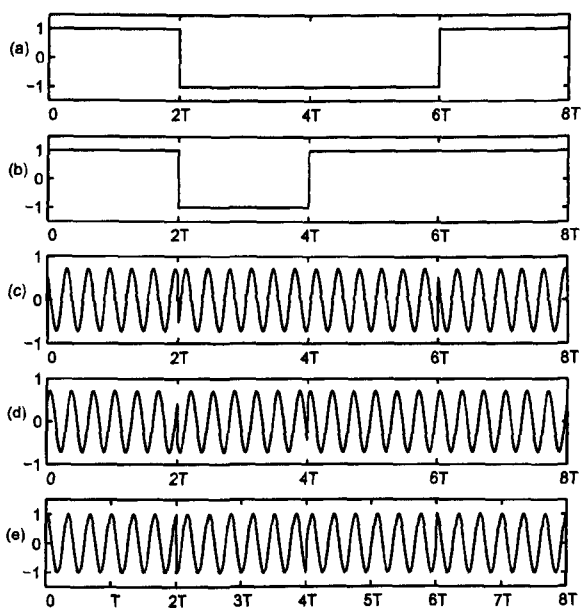

Figure 3.2.2: In-phase (a) and quadrature (b) data sequences used to modulate orthogonal carriers (c) and (d) and combined to form the transmitted QPSK signal (e).

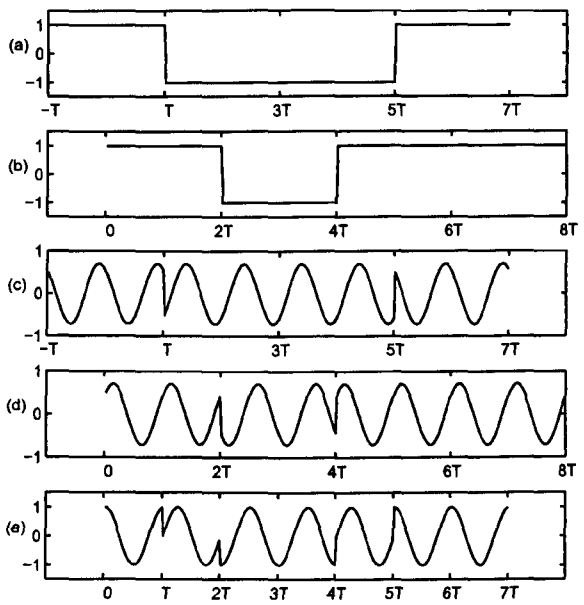

Figure 3.2.3: In-phase (a) and quadrature (b) data sequences used to modulate orthogonal carriers (c) and (d) and combined to form the transmitted OQPSK signal (e).

multipath environment. One option is to band limit the transmitted signal but this causes a loss of transmitted signal power at the phase transitions.

A further development is to offset one of the carriers used in QPSK by 1/2 a bit interval to create an offset-quadrature phase shift keying scheme (OQPSK) where the maximum phase shift encountered is reduced to $\pi/2$. The modulation of a data sequence using this scheme is shown in Figure 3.2.3.

3.2.5 Minimum Shift Keying (MSK)

Although the large phase shifts in the signal can be reduced by using OQPSK this technique is still not ideal as side bands are introduced into the signal's spectrum

by the $\pi/2$ phase shifts. Furthermore, a band limited version of the signal still results in the signal power being reduced at the phase transitions, though not as significantly as BPSK and QPSK. A solution to the side band or power loss problems that occur with BPSK, QPSK and OQPSK is the minimum shift keying scheme (MSK) [25]. It is this scheme that is used in ZigBee communications at frequencies of 2.45GHz.

Minimum shift keying can be thought of in two ways. Initially it is considered to be a relatively simple extension of OQPSK where the square pulses of the data sequence are first shaped to be a half cycle sinusoid per data bit. Mathematically this modulation can be expressed as

$$S(t) = d_I(t)\cos\left(\frac{\pi t}{2T_b}\right)\cos(\omega_c t) + d_Q(t)\sin\left(\frac{\pi t}{2T_b}\right)\sin(\omega_c t) \tag{3.2.7}$$

where T_b is the bit period.

The MSK modulation process is shown in Figure 3.2.4 where initially the signal is split into two carrier channels. The process of pulse shaping is then applied which makes the phase transitions linear over the whole bit period. The two carrier channels are then recombined to give a constant amplitude signal to be transmitted. This reduces the bandwidth of the transmitted signal and interchannel interference, hence more channels at higher data rates can be used.

Upon inspection of the transmitted signal it can be seen that the frequency of the signal changes. Therefore, as mentioned the MSK modulation can be described in another way, that is a Frequency shift keying where the frequency shift occurs uniformly over each bit period.

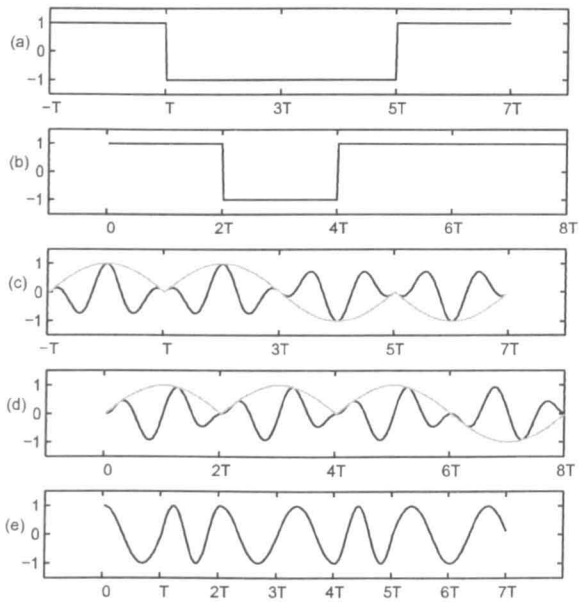

Figure 3.2.4: In-phase (a) and quadrature (b) data sequences pulse-shaped and used to modulate orthogonal carriers (c) and (d) and combined to form the transmitted MSK signal (e)

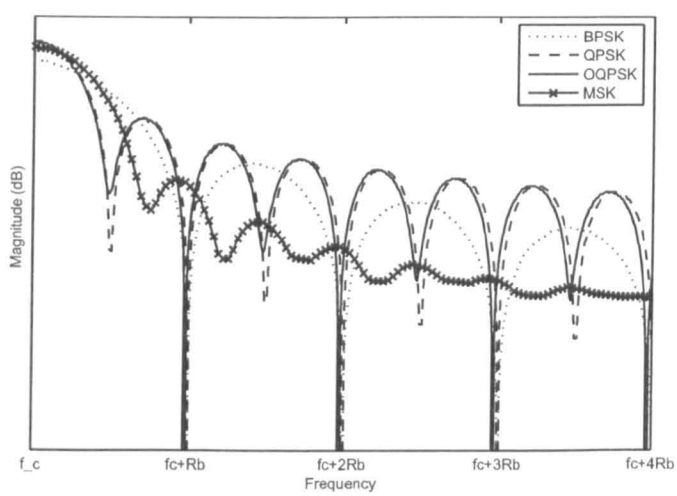

Figure 3.2.5: Bandwidth comparison of phase shift keying methods

3.2.6 Modulation Bandwidths

The bandwidth of each modulation scheme is important as ideally there should be only a limited amount of uncontrolled interchannel interference. The spectrum of each of the modulation schemes is shown in Figure 3.2.5 where the carrier frequency of each is f_c and the bit rate is R_b.

A number of the points discussed in the preceding subsections can be seen in Figure 3.2.5. BPSK has the widest bandwidth of all of the methods as shown by the broad lobes in the spectrum. Both QPSK and OQPSK have the same bandwidth, which is much smaller than that of the BPSK method, but both schemes have a large number of high power side lobes. It can be seen that MSK possesses a relatively narrow bandwidth and the side lobes rapidly decay in power away from the carrier frequency. MSK can be seen to be the best method to use if bandwidth limitation is a requirement. The ZigBee specification uses the MSK method due to its relatively low power requirements and the data rate advantage offered over BPSK [32].

The wireless communication channel, especially a channel within a cavity can be considered to be bandlimited. Therefore a square shaped input function will suffer dispersion within the channel and the received signal will be blurred and interchannel interference will occur. Wireless systems operating at 2.45GHz, for example, are typically allocated a bandwidth in which they operate. This bandwidth is then split into channels so that multiple systems can operate without interfering with each other. In the case of the ZigBee the bandwidth is contained between 2.405GHz and 2.49GHz and is split into 16 5MHz channels. Wide bandwidth pulses are undesirable for the mutual operation within a number of channels as interchannel interference will occur.

In order to limit interference pulse shaping can be used to reduce the bandwidth of the transmitted signal by avoiding high frequency steps in the transmitted signal. The use of a half sinusoid shaping in MSK has already been introduced however others are also used, the most common pulse shaping is the raised cosine. The raised cosine has a bandlimited frequency domain spectrum and its zero crossings can be set to coincide with subsequent bits such that there is no intersymbol interference at the bit sampling point and the pulse energy is contained within one channel bandwidth.

The raised cosine function is given by [33]

$$h(t) = \left(\frac{\cos(2\pi\alpha t)}{1-(4\alpha t)^2}\right) \text{sinc}\left(\frac{t}{T_b}\right) \tag{3.2.8}$$

where T_b is the bit period, α is the rolloff factor and sinc()) is the normalised sinc function

$$\text{sinc}\,(x) = \frac{\sin(\pi x)}{\pi x} \tag{3.2.9}$$

The raised cosine function is usually used with a rolloff factor of $\alpha = 0.5$ in digital communication pulse shaping. The function is non-causal in nature so that in practise the transmitter must store data in a buffer so that preceding bits are augmented with the leading tail of the most recently input cosine filtered bit. Typically, the pulse shaping of bit n is applied to bits $n+6$ to $n-6$ [11]. The bandwidth of a BPSK signal with and without pulse shaping can be seen in Figure 3.2.6 where a rolloff factor of 0.5 is used. The raised cosine filtered signal is of a far lower bandwidth than the unfiltered signal as the rapid variations in magnitude are filtered by the pulse shaping ensuring a smooth continuous signal is sent to the modulator.

Other pulse shapings can also be used in order to reduce the signal bandwidth. For example, Gaussian pulse shaping is used in combination with frequency shift

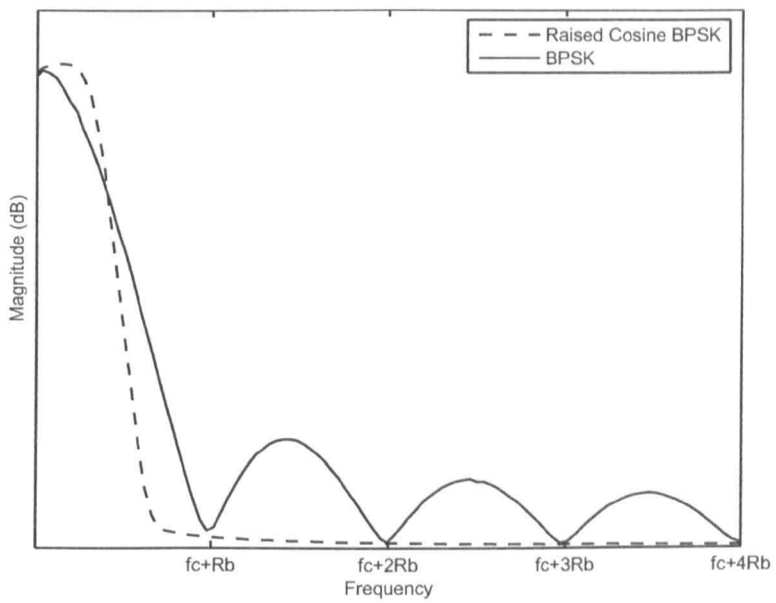

Figure 3.2.6: Frequency content of a BPSK signal with and without raised-cosine pulse shaping

keying in a Bluetooth system (GFSK). More details regarding pulse shaping can be found in [11].

3.3 Spread Spectrum Techniques

A transmitted signal has a centre frequency, f_c, and a bandwidth, Δf, determined by the signal modulation. Typically, for a given modulation approach, increasing the datarate of transmission will increase the bandwidth of the signal. To minimise interchannel interference the bandwidth of a signal is usually kept as low as possible through a reduced data rate or pulse shaping.

As with the Q factor the bandwidth of a signal is defined as the width of the frequency domain representation of the signal at which the power is greater than a particular threshold, normally where the amplitude is -3dB of the maximum. The

aim of a spread spectrum system is to intentionally increase the signal bandwidth. Spread spectrum approaches are used by many wireless systems including ZigBee, Bluetooth and Wireless LAN. They are of interest here as the aim is to operate a wireless system inside a highly resonant cavity. The rapidly fluctuating frequency response and potentionally time-varying channel with narrow peaks that could lead to a reduction in received power if a narrow bandwidth is used for data transmission. The use of a spread spectrum technique will widen the bandwidth of the transmitted signal and potentially minimise the power that falls into the troughs of the transmission spectrum.

There are number of spread spectrum schemes currently used in communications, some of these are outlined below [34]:

- Direct Sequence Systems (DSSS) - The transmitted signal is multiplied by a pseudo random wideband signal in order to spread the signal over the whole transmission bandwidth. This is done by sending data at a much higher rate than is necessary through the spreading. This system is used for ZigBee and 802.11 wireless LAN and is the basis for Code Division Multiple Access (CDMA) systems.

- Frequency Hopping (FHSS) - The signal is transmitted using a carrier which is switched through many frequencies using a pseudo random sequence. This system is used in Bluetooth and military use.

- Time Hopping - The transmitter is turned on and off at a higher rate than the data rate using a pseudo random sequence. This is usually combined with frequency hopping systems.

3.3.1 DSSS

The most commonly used frequency spreading scheme is direct sequence spread spectrum (DSSS). DSSS can be considered a multiplexing technique which is normally combined with phase-shift keying modulation in order to produce a broadband signal from a narrowband signal. DSSS is used in both the wireless LAN and ZigBee communication schemes [32].

DSSS works by multiplying a binary signal by a pseudo random sequence of 1 and -1 values which are at a much higher rate than the actual signal rate; this random sequence is called the spreading code. The rate at which the raw data bits are transmitted is given by the bit rate, R_b, the rate at which the spreading bits are transmitted is the chip rate, R_c, and the number of chips per data bit, R_c/R_b, is the expansion factor [35]. The result is a signal of higher data rate resembling noise where the original signal can be recovered at the receiver by multiplying by the spreading signal.

The signal used to spread the data signal must be carefully chosen to spread the signal efficiently and allow recovery of the signal at the receiver. In order to be wideband and resemble noise the spreading sequence must possess a well defined auto-correlation function with a single clear peak. A single auto-correlation peak allows despreading of the signal at the receiver and, through the discrete convolution theorem

$$Corr(g,h)_j \Leftrightarrow G_k H_k* \tag{3.3.10}$$

and hence

$$AutoCorr(g)_j \Leftrightarrow G_k G_k* \;=\; |G_k|^2 \tag{3.3.11}$$

can be seen to produce a wide and flat spectrum. The sequences with the best

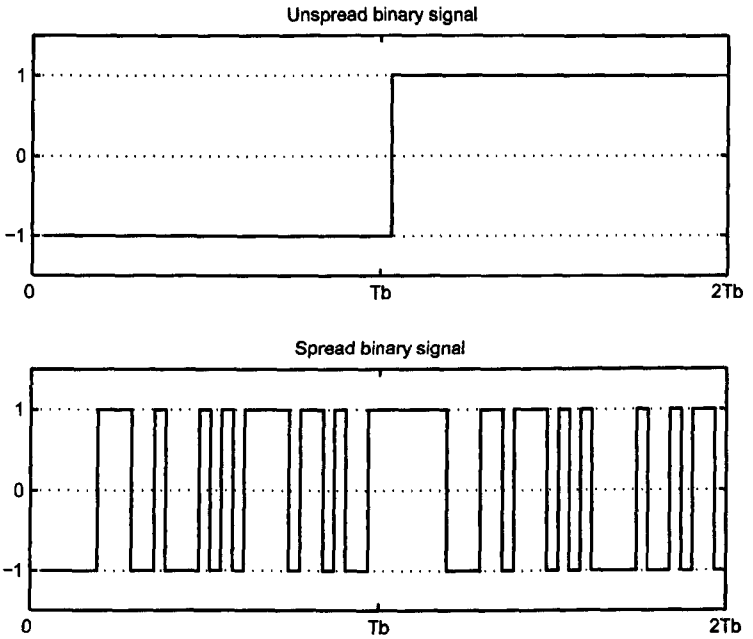

Figure 3.3.7: Spreading of a 100 bit sequence using DSSS. A pair of bits (top) spread using a 31 bit maximal length sequence (bottom)

auto-correlation properties for a given length are maximal length sequences[1], which have a two-level auto-correlation function with a single peak and hence the widest bandwidth available as shown by (3.3.11).

Figures 3.3.7 and 3.3.8 show the effect of DSSS on a binary digital signal without modulation. The first two bits of an input binary sequence are shown in 3.3.7 (top) and has amplitude which switches between -1 and 1. The frequency spectrum of this sequence is narrow as shown in Figure 3.3.8. Spreading of the sequence by a 31 bit maximal length sequence gives the spread signal shown in Figure 3.3.7 (bottom). It can be seen from the spread signal spectrum why this is advantageous; the spectrum is now much wider and flatter compared with the original spectrum. The spectrum of the spread signal falls at frequencies further away from the carrier frequency, but across the bandwidth of interest the signal

[1]Maximal length sequences are a sequence of chips obtained using a shift register system; they are descibed in more detail in Appendix A.1

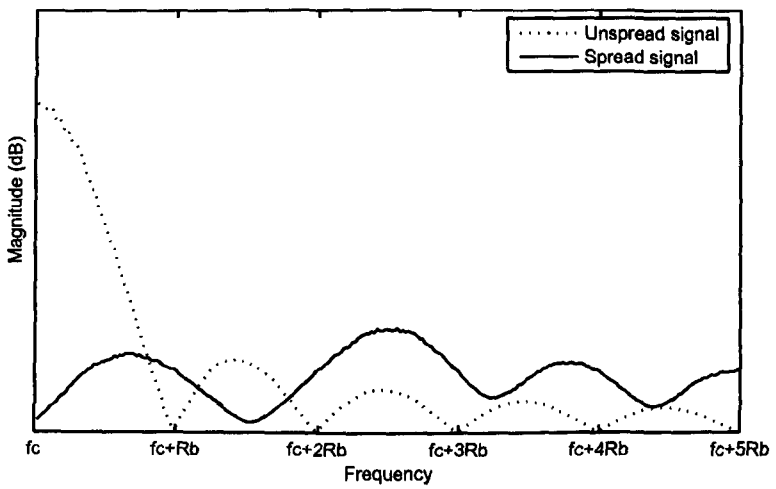

Figure 3.3.8: Frequency domain representation of the spread and unspread signal

spectrum is much flatter. This makes the spreading process suitable for combating the highly fluctuating transmission spectrum of the resonant cavity, as the risk of the signal power falling into a valley in the channel spectrum will be greatly reduced.

The spreading process produces the same effect when acting upon a sinusoidal modulated signal causing the desired widening of the signal spectrum. The higher the expansion factor the wider the spectrum of the transmitted signal. A pseudo-random code is used to spread the data so that the transmitter and receiver both have matching codes therefore the signal can be recovered. The advantages of using a DSSS approach are as follows:

Wide bandwidth As can be seen from Figure 3.3.8 the spectrum of a spread signal is very wide and spread across all frequencies. This wide spectrum is clearly advantageous, when compared with the transmission spectrum of the resonant environment. As the signal power is spread out across all of the peaks and troughs of the transmission spectrum there is no chance of the signal being lost in noise due to the fall in transmission as with a narrow band signal. This makes the system

less susceptible to interference whether intended or unintended [36].

Noise like appearance The signal has a noise-like appearance and the chip sequence is required to reconstruct the original signal. This makes the system more secure although further security would be required in sensitive situations.

Multi-path rejection Unless the de-spreading code and the received signal are synchronised, the signal cannot be extracted from the transmitted pseudo-random signal. Therefore, if the code and signal are synchronised any other signal will be ignored, even if it is a time delayed version of required signal. This is a direct consequence of the auto-correlation properties of the spreading sequence and allows delayed signals due to the multiple paths within the cavity can be rejected by the de-spreading process. The delayed signals are all captured, synchronised and combined to reproduce the signal. A consequence of the multipath nature of the channel is that the receiver will experience fast fading due to small structural changes in the environment leading to different paths arriving at the receiver. Fast fading occurs when the coherence time of the channel is much shorter than the packet or symbol period. The use of spread spectrum techniques provides some resistance to the fading and will minismise its impact on communications [34].

3.3.2 CDMA

As a concept related to DSSS the use of CDMA is briefly described here. The use of a pseudo-random chip sequence is the basis for CDMA systems. The received signal appears as noise and unless the chip sequence is known it cannot be de-spread. CDMA allows multiple signals to be transmitted at the same time in the same channel but using different pseudo random sequences. A particular signal

can be then separated from the random noise by using the chip sequence and all others ignored.

Unlike signals which are transmitted in a particular frequency or time slot CDMA signals share the whole of the time and frequency spectrum. This is the approach used by modern mobile phone networks when managing the bandwidth available to them and allows them to use fewer transmitters. The user limit of the CDMA system is said to be a soft limit and is determined by the expansion factor used. CDMA spreading codes must have good autocorrelation functions and well bounded cross-correlation functions. The major difficulty in de-spreading the signal is that the chip sequence and the received signal must be synchronised [34].

CDMA allows multiple users to use a single channel, which is ideal for use in wireless networks. It means that a single transmitter can be used to control and monitor all of the nodes simultaneously without having to change frequencies or use specific time slots. The multiplexing codes could be hard-wired into the sensors making the system relatively low power. It also avoids the hard user limit encountered with other systems.

In order to decode a multiplexed signal at the receiver the spreading code used must be synchronised with the received signal. To allow for good synchronisation the spreading codes must have good autocorrelation functions whereby there is a single definite correlation peak where the sequences are synchronised. To allow for CDMA we require a large number of equal length orthogonal codes with a well bounded cross-correlation function, but again good auto-correlation properties. Two types of codes are explored here; these are namely maximal length sequences and Gold codes.

Maximal length sequences (m-sequences) are named as such as they are the largest codes that can be generated by a shift register of a given length. M-sequences possess a number of properties that make them suitable for use in spread spectrum techniques. They possess a binary auto-correlation function with a well defined peak correlation, the sequences are spectrally flat due to their pseudo-random nature and codes can be created from simple shift register systems. Details of maximal-length sequences and the closely related Gold codes can be found in Appendix A.

CDMA, as a DSSS based system, is vulnerable to the near-far problem. This is a problem that is common in mobile telephone systems where a strong (nearby) signal arrives at the receiver making it impossible to recover a weaker (far away) signal. One of the main advantages of CDMA is the ability to share both time and frequency space. However, this leads to the near-far effect being a problem as the received signals occur at the same time and frequency and cannot be separated in that way. Although the receiver is capable of separating a large number of simultaneous signals, the strong signal leads to the receiver reducing its gain and the weaker signal falls below the noise floor [11].

The high Q factor, low loss nature of the cavities inside the aircraft is an advantage in the case of the near-far problem. Although the transmitters may be at different distances from the receiver, the low loss cavity leads to the received signals being of similar strength (for the same input power) as the energy propagates within the cavity rather than radiating isotropically into free space. Therefore, it is likely that the near-far problem will not impact the wireless system within the aircraft. If the problem is encountered then the power output of the transmitters can be modified so that similar power levels arrive at the receiver [25]; as the nodes will normally be fixed this is a power level that can be fixed. Conversely, in mobile telephony the power is adjusted dynamically as the transmitters are moving large

distances over time.

3.3.3 FHSS

Another method of spectrum enhancement is to periodically change the frequency at which the signal is transmitted around the chosen carrier frequency. The aim is to avoid complete loss of transmission due to low power propagation or interference. Typically the system will actively avoid the frequencies at which communication problems are encountered. This approach is called frequency hopping spread spectrum and is the method used by Bluetooth systems.

This method will not be discussed further here, but could be applied in the models developed in this thesis. Further references on such an approach can be found in [34].

3.4 Complete Communication Systems

The modulation and spreading schemes discussed so far form the basis of most modern wireless communication systems. This section considers some of the more common COTS wireless systems and describes their suitability to this work. Currently there are 3 wireless network technologies in common use. These are the ZigBee/802.15.4 [32], Bluetooth/802.15.1 [29] and 802.11 wireless LAN standards [37]. An overview of the communication system parameters are shown in Tables 3.4.1 and 3.4.2 and the systems are described in more detail in the following subsections.

3.4.1 ZigBee

ZigBee is a recent standard, specifically designed for wireless sensor networks and built on top of the IEEE802.15.4 standard which specifies the physical and MAC layers [32]. A ZigBee system is relatively low in complexity and data rate and therefore typically has low power requirements. In order to be a truly wireless system the power usage must be kept to a minimum so that power can be scavenged and/or provided by a battery. Based on current battery and energy scavenging technologies the most likely application of a wireless system is for low duty cycle, low data rate applications such as simple sensors, and health and utility monitoring. This makes ZigBee an ideal candidate for the system to use. Full details of the ZigBee specification can be found in considerable depth in [32], here the properties of the physical layer are presented for reference in later chapters.

There are a number of bands within which ZigBee operates, these are the ISM bands at 900MHz and 2.45GHz. The focus of this work is at the 2.45GHz band which is the most common wireless communication band. The transfer bit rate, R_b, in ZigBee is specified as 250kb/s which is the bit rate in the radio communication channel if we consider the radio and its channel to be a *blackbox*. This bit rate corresponds to a bit period of $4\mu s$ in the channel, however the data is not sent as individual bits. ZigBee uses a DSSS approach to bit spreading by assigning chip sequences to a particular sequence of input bits or symbols .

When data enters the radio a group of four bits is taken at a time, these four bits together form a symbol. This symbol is then used to choose one of sixteen thirty-two bit long spreading codes, this corresponds to a expansion factor of 8. The chip rate, R_c, at this point is therefore $250kb/s \times 8 = 2000kchips/s$ and the chip period is $0.5\mu s$. A MSK modulation is then used so that the sequence is separated into the two channels I and Q where chips 0,2,4,6... are used for the I

channel and chips 1,3,5... are used for the Q channel. As described previously one channel is then offset by half the chip period and the sequences are shaped with a half sine pulse shape; the data is then modulated onto the carrier in the normal way. As a result the 250kb/s data bit rate has been converted to a 62.5ksymbols/s transmitted rate. This corresponds to a symbol period of $16\mu s$ and a chip period of $1\mu s$. The data is transmitted in a ZigBee channel which has an available bandwidth of 5MHz.

3.4.2 Bluetooth

Bluetooth is primarily designed for a small number of nodes. It was designed with ad-hoc networks in mind for short range local connectivity between mobile phones and peripheral devices. Considered here is Bluetooth v1.2, which is ratified as the IEEE standard 802.15.1-2005 [29]. Recent generations provide higher data rates and greater reliability combined with higher power usage, though offer low power modes if the application permits. Power usage is higher than ZigBee due to a greater degree of complexity in the specification. This greater degree of complexity is due to increased security and error checking for example.

Typically Bluetooth is used for connecting 2 or 3 devices and has a limit of 8 active devices. In terms of data rate for comparible specifications, Bluetooth offers very little advantage over ZigBee and has a higher power usage. For the applications considered here Bluetooth occupies a niche between ZigBee and wireless LAN and is unable to support a large number of nodes. The modulations and schemes used by Bluetooth can be tested using the models developed in this thesis, however Bluetooth will not be considered further as it is felt that ZigBee is the most applicable system based on the criteria of Section 3.1. More details of Bluetooth can be found in references [29] and [31].

3.4.3 Wireless LAN

Wireless LAN encompases the various IEEE802.11 standards and has a number of subsets identified by the letters b, g and n [37]. The standard varies from the more established and older, low performance (11Mbit/s) 802.11b standard to the newer, 802.11n standard which achieved an order of magnitude increase in data rate at the expense of multiple antennae and enhanced signal processing [38]. Therefore the main difference between wireless LAN and ZigBee systems is that the former provides higher data rates at the expense of extra complexity, power consumption and cost.

Wireless LAN type systems might be required for high data rate applications like flight control functions or the transfer of video, radar and other data. For example a sensor that sampled at 100Hz and 16 bits would require a data bandwidth of 32kbit/s and video would require a bandwidth in the order of 10Mbit/s [6]. Therefore, if data rates in the order of megabits are needed then wireless LAN is the only option for a communication system. However, these standards are not considered in detail here due to their high power usage and signal processing complexity. Power usage is approximately 1W and it would not be possible to operate such a system without a sufficient power supply. The use of battery or scavenged power would not be a possibility for Wireless LAN.

3.4.4 Summary

In the remainder of this thesis the focus will be on the use of the fundamental modulation schemes used by systems such as ZigBee with only reference to the other systems. The modulation and spreading approaches used by wireless schemes will be used in the models developed to demonstrate examples of wireless

communication modelling and to provide insight into the performance of such a system in a highly resonant cavity environment.

Considering the application of wireless communications to aircraft systems ZigBee is currently the most applicable COTS system. Bluetooth and Wireless LAN are built upon similar methods but are not currently suited to the task being considered. Due to its power requirements Wireless LAN cannot be powered by battery or power scavenging. As it is likely that a large number of nodes will be required then Bluetooth is not suitable for this application. Furthermore, Bluetooth offers little data rate advantage over ZigBee with a greater power requirement.

3.4.5 References

The wireless concepts and systems that are related to this work have been introduced and defined. The methods described here are far from exhaustive and there exist far more approaches in the literature. Should the reader wish to research wireless methods and systems further there are a number of useful references. Rappaport [11] provides an excellent introduction to a large range of wireless communication concepts including examples of hardware implementations. In addition Laverghetta [30] and Tse [28] present a useful introduction to wireless communications with mobile phone communications as their main them. Finally, more rigorous and advanced texts discussing wireless communication systems, mobile telephony and the signal processing involved can be found in Proakis [18] and Stuber [25].

System	ZigBee	Bluetooth v1.2
Data rate (Mbps)	0.25	1.00
Power consumption	10-100mW	≈150mW
Modulation	MSK	GFSK
Spread spectrum	DSSS	FHSS
Number of nodes	65,000	8
Symbol period (μs)	16	1
Chip period (μs)	0.5	N/A

Table 3.4.1: Properties of commonly used wireless systems

System	802.11b	802.11g	802.11n
Data rate (Mbps)	11	54	150
Power consumption	1W	1W	1W
Modulation	DPSK	PSK/ASK	PSK/ASK
Spread spectrum	DSSS	OFDM	OFDM
Number of nodes	100,000	100,000	100,000
Symbol period (μs)	0.73-1	3.2	3.6
Chip period (μs)	0.09	N/A	N/A

Table 3.4.2: Properties of the wireless LAN systems

Chapter 4

Modelling of a Single Resonant Cavity

In Chapter 1 the frequency domain response of a simple cavity model was shown. This result was obtained using a full field 3D time domain solver, specifically an implementation of the Transmission Line Modelling (TLM) method. Details of such an approach can be found in the texts [13] and [39]. The model acts to solve Maxwell's curl equations over all discretised space in a time incrementing fashion. Discretisation of the magnetic and electric fields onto the structured node based mesh also implicitly ensures that Maxwell's divergence equations are satisfied. There are a number of advantages to using such a model. All of the field interactions are captured by the model and the only approximation is made at the discretisation stage. Given sufficient mesh density, computational resources and time, all of the geometric features can be captured by the model.

However, considered here are communication systems operating, for example,

in the 2.45GHz ISM band. As a rule of thumb, the requirements of such a full field model at this frequency would require a minimum cell size spacing of $\Delta l \leq \lambda/10 = 0.012$cm in order to sufficiently sample a wave in the model [13]. This leads to a time step $\Delta t = \Delta l/2c = 20ps$ which would require approximately 50,000 time steps to model a single transmitted bit of $1\mu s$ in duration.

The computational cost of such a model, when used for wireless communication modelling, is very high and if a general solution is sought this becomes quite limiting. A general solution is desired as the environment being modelled is not geometrically fixed. There will be small changes throughout the lifetime of the cavity and small changes between each manufactured cavity structure, even if the design is exactly the same.

Therefore, the response of a single cavity channel is not enough on its own to perform an assessment of the effectiveness of a wireless scheme. A number of cavities, with the same modal density and Q factor of the cavity, but different modal structures require modelling so that the average effect of the channel can be considered. To implement an approach of this type the model used to describe the channel must be efficient so that it can be readjusted and computed numerous times for each set of channel parameters. A task which full field models are capable of, but far from efficient at doing so.

This chapter describes the development of a model that is able to model the channel parameters of interest in an efficient, flexible and stable way. The model is a time domain filter based model derived from an equivalent circuit of the cavity.

4.1 Modelling Approach

In Chapter 2 the link between the concepts of mean excess delay and the resonant cavity Q factor were presented. Throughout, the assumption was made that the decay of the energy in the environment is sufficiently slow that the decay time, τ, is far greater than the carrier oscillation period, $T << \tau$. It will be shown that in highly resonant environments the propagation properties of the channel are dominated by the resonant behaviour and the environment can be considered highly multipath.

Consider a multipath approach to the wireless communication channel problem, as would often be applied in an urban environment. We assume that a transmitter transmits, at time $t = 0$, a top-hat function of width T_b. If the channel is multipath with infinite bandwidth so that the received signal will also be a top-hat followed by its delayed copies, an example of the received signal can be seen in Figure 4.1.1 (top)[1].

Here, we define the differential path delay to be the difference in arrival time between two paths. For two paths, one delayed by τ_1 and the other τ_2 the differential path delay is given by $\dot{\tau} = |\tau_2 - \tau_1|$. In 4.1.1 (top), we see that the differential path delay is large compared with the duration of the input function as we observe large uneven delays between the signals and clearly defined delayed pulse copies. This same argument is now applied to the resonant cavity environment.

The cavity can be considered much smaller than the environment producing the first response and a received signal of the type shown in 4.1.1 (bottom) will

[1]In the example of Figure 4.1.1 (top) the delays are assumed to be larger than the signal period. In reality a small number of the pulses may overlap depending on the number and length of paths in the environment. However, the pulses will be spread further apart in an urban environment than in the aircraft environment where there are a large number of similar length paths for propagation

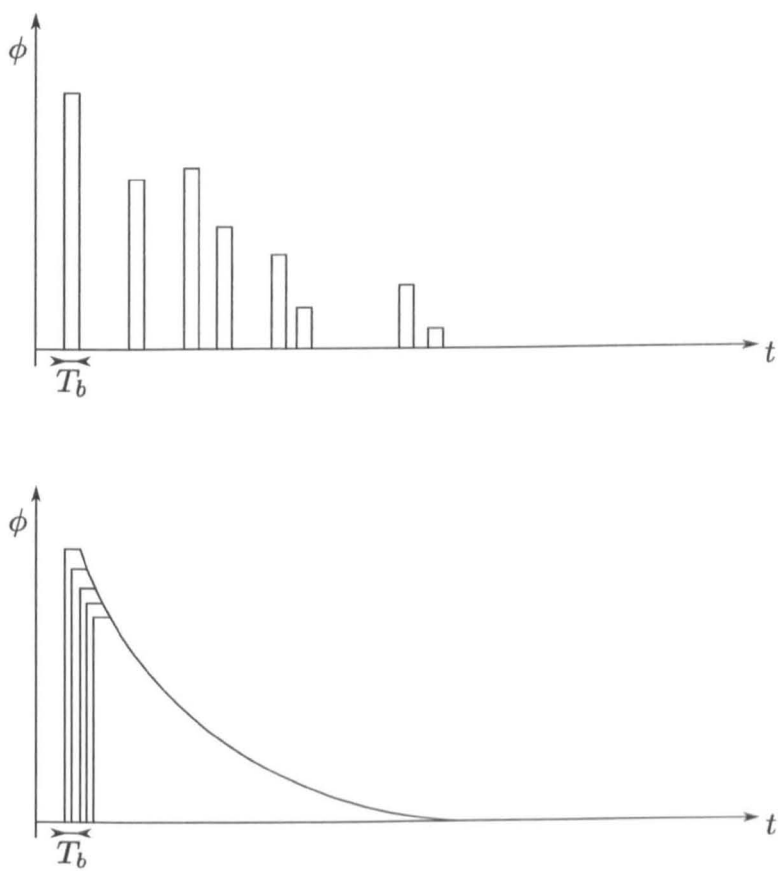

Figure 4.1.1: Representative time domain response of a multipath channel (top) and a resonant cavity channel (bottom)

be obtained. Here, the differential path delay is small and we see there are many overlapping duplicates of the transmitted signal. These signals also have a resonant decay associated with them due to the resonant nature of the channel. In this case the dominant effect is the resonant nature of the channel and interference of the carrier within the transmitted bit. We assume, therefore, that the properties of the channel are dominated by the resonant behaviour due to the multipath properties of the channel. A modelling approach derived from multipath propagation effects is described in Appendix B where the approach is shown to give results consistent with resonant behaviour when applied to a small highly reflective enclosed cavity.

Hence, the model to be developed is only required to efficiently model the resonant behaviour of the cavity, that is each of the resonant modes, and this model will implicitly model the multipath behaviour of the channel. It should be noted that the application of such a model to traditional communication will not correctly model the impact of the channel on wireless propagation and is restricted to highly resonant, small cavity systems. An equivalent model will be developed in the following sections that efficiently models the properties of this channel.

4.2 Equivalent Circuit Model

To model the resonant environment a continuous system that can be converted into a discrete form easily and in a computationally efficient manner can be used. A circuit analog that has the peaked resonant response behaviour of the resonant cavity is the resonant resistor, inductor, capacitor (RLC) circuit [14]. A resistor, inductor and capacitor in series connected to a voltage source, as shown in Figure 4.2.2(a), has a frequency response of the form shown in Figure 4.2.2(b). Here the

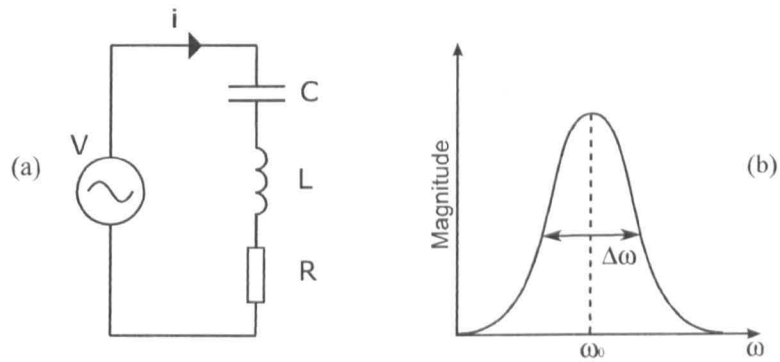

Figure 4.2.2: (a) A series RLC circuit with circuit parameters labelled and (b) an approximation of its frequency response function

current, i, is taken as the output of the circuit so that

$$\frac{i}{V} = \frac{1}{Z} = Y \tag{4.2.1}$$

where Z and Y are the impedance and admittance of the RLC circuit respectively.

The frequency response of the RLC circuit is due to the imaginary part of the circuit impedance, that is the frequency varying impedance of the capacitor and inductor in series. The real part of the impedance, owed to the resistor, acts as a loss in the circuit. These properties can be related to the size, hence resonant frequency and the loss, hence Q factor of the resonant environment.

Assuming the resistance of the circuit is zero it is simple to show that the impedance is given by

$$Z = \frac{1}{j\omega C} + j\omega L = \frac{1 - \omega^2 LC}{j\omega C} \tag{4.2.2}$$

Therefore, the circuit can be seen to be a short circuit when the numerator is zero, which occurs at the resonant frequency

$$\omega_0 = {}^{1}\Big/\sqrt{LC} \tag{4.2.3}$$

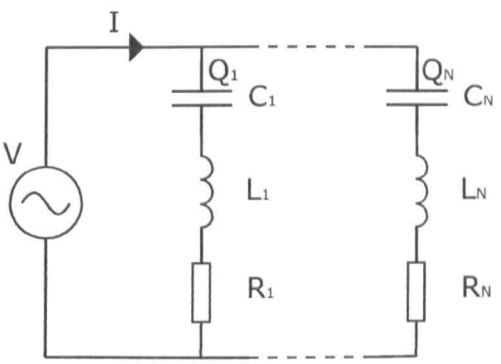

Figure 4.2.3: Parallel RLC circuits

where L and C are the inductance and capacitance of the circuit respectively. The circuit is therefore a band-pass circuit in the same way as the cavity being modelled. Equivalently, at the resonant frequency of the cavity the admittance of the frequency being propagated is infinite.

The real cavity has a number of resonances, not just the single resonance modelled by this circuit. In order to model the multi-peaked frequency response similar to that of the resonant cavity a number of RLC circuits can be connected in parallel with a variation of their circuit parameters as shown in Figure 4.2.3.

Each resonant branch sees the same voltage so the circuit can be separated into individual RLC circuits where the total current, I, is given by the sum of the currents in each of the branches. Therefore, the current transferred in the channel is represented by the common mode current of all the branches. In terms of charge flow, the total current is given by the time differential of the sum of the charges stored in the capacitor in each of the branches so that

$$i_n = \frac{dQ_n}{dt} \tag{4.2.4}$$

and hence

$$I = \frac{d}{dt}\sum_{n=1}^{N} Q_n = \sum_{n=1}^{N} \frac{dQ_n}{dt} \tag{4.2.5}$$

A time domain digital filter model can be produced by treating each branch of the circuit separately. The complex impedance of a single RLC branch is given by

$$Z = R + j\omega L + {}^{1}/_{j\omega C} \tag{4.2.6}$$

A digital filter can be constructed from the circuit represented by (4.2.6) in a number of ways. Approaches include representation of the differential terms of the reactive components using the trapesium rule or through conversion to a transmission line equivalent circuit. Here, the digital filter can be constructed using the bilinear Z-transform approach [40].

The bilinear transform is used to transform from continuous time to discrete time space [41]. The following equivalences can be imposed to transform into the Z-domain via the Laplace-domain (s)

$$j\omega \rightarrow \frac{\partial}{\partial t} \rightarrow s = \frac{\bar{s}}{\Delta t} \rightarrow \frac{2}{\Delta t}\left(\frac{1-z^{-1}}{1+z^{-1}}\right) \tag{4.2.7}$$

Here, s is the Laplace variable, z is the time-shift operator and Δt, is the sample time, that is the time step used by the discrete filter. The quanity z^{-1} corresponds to a negative time shift (delay) of Δt.

The transfer function of the RLC circuit can be represented by the ratio of an output quantity to an input quantity in terms of frequency. In this case the input is the voltage applied by the source and, in order to simplify the expansion in the derivation, the output is chosen to be the charge on the capacitor. Therefore, the

Laplace domain transfer function of the i^{th} branch is given by

$$H_i(s) = \frac{Q_i(s)}{V_i(s)} = \frac{\frac{1}{L_i}}{s^2 + s\frac{R_i}{L_i} + \frac{1}{L_i C_i}} \tag{4.2.8}$$

where V_i is the incident voltage applied to the branch by the voltage source and Q_i is the charge on the capacitor.

The right-hand term is then converted into the discrete time domain filter by substituting for s and expanding so that

$$H_i(z) = \frac{a_1 \Delta t^2}{z^{-2}(4 - 4a_2\Delta t + a_3) + z^{-1}(-8 + 2a_3) + (4 + 4a_2\Delta t + a_3)} \tag{4.2.9}$$

where, neglecting the subscript i, a_1, a_2 and a_3 are constants given by

$$a_1 = \frac{1}{L}; \quad a_2 = \frac{R}{2L}; \quad a_3 = \frac{1}{LC} \tag{4.2.10}$$

In (4.2.9) it can be seen that the transfer function is now expressed in terms of the present timestep and the two previous time steps, as would be expected for a second order filter of this type. Substituting for the input voltage, output charge and identifying that

$$z^{-n}A(T) = A(T - n) \tag{4.2.11}$$

where T is the discrete time variable, gives the charge stored in the capacitor at time step T

$$Q(T) = A_1 Q(T-1) + A_2 Q(T-2) + B_1 V_i(T) + 2B_1 V_i(T-1) + B_1 V_i(T-2) \tag{4.2.12}$$

where

$$A_1 = \frac{8 - 2\Delta t^2 c^2}{4 + 4b\Delta t + \Delta t^2 c^2} \tag{4.2.13}$$

$$A_2 = \frac{-4 + 4b\Delta t - \Delta t^2 c^2}{4 + 4b\Delta t + \Delta t^2 c^2} \tag{4.2.14}$$

$$B_1 = \frac{a\Delta t^2}{4 + 4b\Delta t + \Delta t^2 c^2} \tag{4.2.15}$$

The resonant properties of the branches are controlled by the values of L, C and R in each branch. These parameters affect the constants used in the filter as defined by (4.2.10). It can be seen from circuit theory that the constant a_3 represents the resonant frequency of the branch where $a_3 = \omega_0^2$. The Q-factor of the RLC circuit can be derived in the same way as that of the cavity and is given by

$$Q = \frac{\omega_0}{\Delta\omega} = \frac{f_0}{\Delta f} = \frac{1}{R}\sqrt{\frac{L}{C}} \tag{4.2.16}$$

Therefore, substituting for ω_0 in terms of L and C and solving for $\Delta\omega$ it can be seen that the bandwidth of the resonance is given by

$$\Delta\omega = \frac{R}{L} = 2a_2 \tag{4.2.17}$$

The peak amplitude is obtained when the source only sees the resistor value, therefore the peak amplitude is given by

$$A_0 = \frac{1}{R} \tag{4.2.18}$$

Hence, if the required resonance properites are known, i.e. the centre frequency w_0, bandwidth $\Delta\omega$ and peak amplitude A_0 then the complete set of circuit constants are given by

$$a_1 = \Delta\omega A_0 \tag{4.2.19}$$

$$a_2 = \Delta\omega/2 \tag{4.2.20}$$

$$a_3 = \omega_0^2 \tag{4.2.21}$$

Equations (4.2.19)-(4.2.21) provide the parameters that can be related directly to

the properties of the cavity being modelled and it will be shown how to obtain these values in the next section.

The output current can then be obtained as prescribed by (4.2.5) by replacing the derivative by a central difference approximation. The use of a time-domain digital filter avoids the use of convolutions with response functions. We need only store data values for the preceding two time steps instead of storing all the response data making a computationally efficient time-domain model. Also it produces a model that can be run in parallel or hybridised in a fully coupled manner with other time-domain modelling approaches. Furthermore, the model defined here is derived from passive components which are solved exactly. Therefore, given we provide positive, real values for the circuit components the filter will be unconditionally stable.

It is necessary that the sampling frequency be taken into consideration so that the signal is correctly represented by the filter [41]. In the case of this model the time step defined for this branch is the time step that must be used in all of the other branches to retain synchronisation. The maximum frequency in the pass band of the filter is $f_{max} = f_0 + \Delta f$, where f_0 is the centre frequency of the highest frequency mode in this context. Therefore, it can be easily shown that the maximum time step to accurately sample the transmitted wave is

$$\Delta t_{max} = \frac{Q}{10 f_0 (Q+1)} \approx \frac{1}{10 f_0} \tag{4.2.22}$$

as $Q >> 1$ in the case of a resonant cavity.

The model developed here represents the resonant channel as a parallel combination of RLC circuits. Assuming that there are no non-linear effects within the channel and that the channel is static, the system can be considered linear and

time-invarient (LTI). In the case of a LTI system it is possible to transform the frequency window that we are interested in. Therefore, in order to maximise the efficiency of the model it is possible to model the effect of the channel on a modulating signal using lower frequency carrier wave. By reducing the carrier frequency it is possbile to reduce the sampling rate and increase the model time step Δt.

For example, the carrier frequency of interest is given by f_c and a shift in frequency towards baseband of f_s is to be modelled. The carrier frequency used for modelling is then

$$f_c' = f_c - f_s \tag{4.2.23}$$

and the Q factor is frequency dependent so the new Q factor used within the model is

$$Q' = Q\frac{f_c'}{f_c} = Q\left(1 - \frac{f_s}{f_c}\right) \tag{4.2.24}$$

The sampling rate can then be increased to model the new frequency and significantly increase the efficiency of the model and reduce its CPU time.

4.3 Obtaining Circuit Parameters

It is important that the digital filter model can be used to represent a real communication channel. It has been demonstrated that the filter model is able to model general resonances where the properties of the resonances are known. The properties of the resonance can be obtained in a number of ways depending on the application of the model. This section explores some of the ways of defining the channel parameters. As an example consider the cavity shown in Figure 4.3.4 where the dimensions of the cavity are shown and the source and receiver are assumed to be isotropic and point-like. A loss is introduced in the form of a reflection coefficient on the cavity walls of $\Gamma = -0.995$. For reference, the simulated $|S_{21}|$

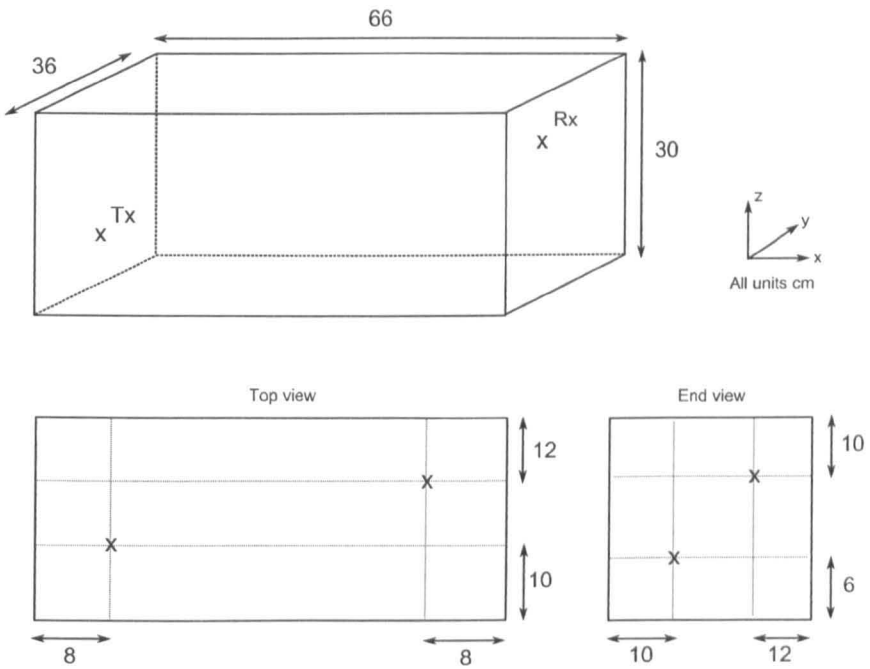

Figure 4.3.4: Example cavity schematic with measurements

response of the cavity is shown in Figure 4.3.5 where this was calculated using a full field TLM model.

4.3.1 Analytical

Perhaps the most straightfoward means of obtaining the circuit parameters is to calculate them analytically. For simple canonical cavities, a rectangular cavity for example, this will be a relativly simple procedure.

Let the cavity of interest be a simple rectangular cavity of the type shown in Figure 4.3.4. The cavity has dimensions l, w, h and is uniform in each dimension so that boundary conditions can be easily obtained. It is trivial to show that the

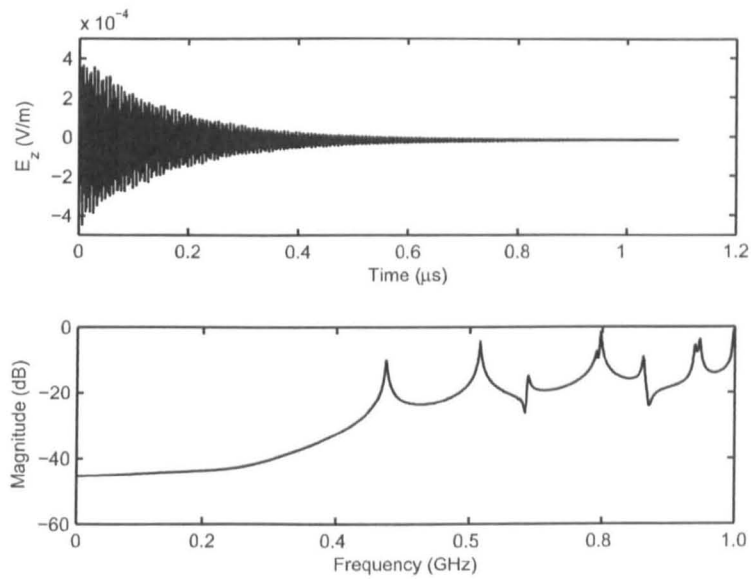

Figure 4.3.5: Time domain and frequency domain response of the cavity model

resonant frequency of the cavity is given by

$$f_{mnp} = \frac{c}{2}\sqrt{\left(\frac{m}{l}\right)^2 + \left(\frac{n}{w}\right)^2 + \left(\frac{p}{h}\right)^2} \tag{4.3.25}$$

where m, n and p are integers and the cavity volume is assumed to be free space. In 4.3.25 not more than one of the integers can be zero and for a given field polarization we find that the zero integer, if present, corresponds to that component of the field.

The Q factor of the cavity can be obtained from the losses of the cavity walls and from [27] or [14] is given by

$$Q = \frac{\pi\eta_0}{4R_s}\left[\frac{2w\left(l^2+h^2\right)^{3/2}}{lh\left(l^2+h^2\right)+2w\left(l^3+h^3\right)}\right] \tag{4.3.26}$$

where η is the impedance of free space and R_s is the surface material resistance.

The amplitude, A_0, of each resonant mode is dependent on the source used to

excite the cavity [42]. If the field is being sampled at a particular point then the received field amplitude will also depend on the receiver properties. Therefore, it is difficult to analytically define the amplitudes that will be received in the case of the system of Figure 4.3.4.

Equivalent resonant frequencies and Q factor definitions can be derived for other simple cavity shapes, including cylinders and spheres. However, for general cavities that may contain complex structures it is impossible to obtain boundary conditions in order to solve Maxwell's equations and find the variables needed for the filter model and other approaches are required.

Using the example shown in Figure 4.3.4 the resonant frequencies of the first 5 modes and losses were calculated and used in the filter model developed in this section. The relative amplitude of the modes effects the components that make up the received signal and a lack of agreement in the mode amplitudes will lead to the time domain solution diverging from that of the full field model. In order to match the amplitudes of the full field model the modes in the circuit model were simply tuned to those of the full field response. A comparison of the full field result and the filter model result can be seen in Figures 4.3.6 and 4.3.7. Good agreement can be seen between the filter model and the full field model, indicating that the filter model provides an efficient representation of the channel. In this case the run time of the full field model on a single processor was 436 seconds, the filter model completed in 3 seconds. The efficiency of the filter model makes it a very powerful modelling tool as it allows a large number of simulations to be performed in place of one full field simulation. This is necessary for a general cavity to be modelled for wireless applications.

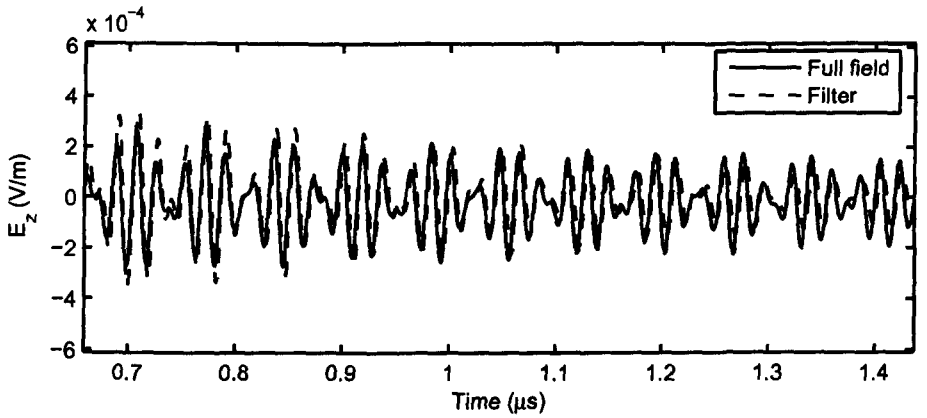

Figure 4.3.6: Time domain response of the full field and filter models

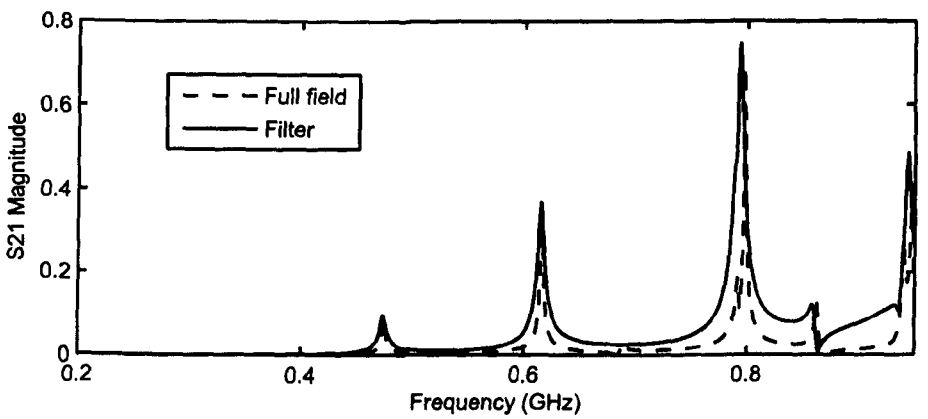

Figure 4.3.7: Frequency domain response of the full field and filter models

4.3.2 Data Fitting

To obtain the properties of complex cavities measurements of the response of the real cavity will have to be made, or the cavity be simulated using a full field model. The response of the channel need only be measured or simulated once and the data be analysed to extract the modal structure of the channel.

In order to use the filter model constructed here we require the frequency, bandwidth and amplitude of each resonant mode in the cavity. In many cases the channel will be relatively overmoded and the Q factor of the cavity less than 1000. This will lead to the modes blending and not being well defined. Inspection of the measured or simulated result will be insufficient and some other means must be adopted.

One method of extracting mode parameters from response data is the Prony method, this method yields a decomposition of the response function in terms of complex decaying exponentials [40]. The Prony method is particularly useful for modelling materials in TLM as the Padé coefficients are ideal for creating digital filters allowing the properties of materials such as Lorentz dielectrics to be modelled [40]. The method is usually applied to systems that only consist of a small number of poles, however here we seek to apply the method to the highly moded resonant cavity channel.

Assuming that the impulse response of a channel is constructed from all the resonant modes of the cavity, then it is expected that each mode will result in a damped exponential response where the damping is related to the width of the resonance. By representing the channel response as a linear superposition of

decaying sinusoidal functions of the form

$$f(t) = f(0)e^{-\alpha t}cos(\omega t) \tag{4.3.27}$$

it becomes a simple task to extract the model parameters; amplitude $f(0)$, centre frequency ω and decay constant α.

Generally, techniques such as the Prony technique are applied to systems that contain a low number of poles, such as representing the response of a frequency dependent material or a complex aperture grating for example. The usefulness of the approach is limited when a high number of poles are used to represent the data. The applicability of this technique is demonstrated here for systems with a high number of modes. The limitations in setting up a filter model to be a match of the real channel are described.

Given an impulse response $f(t)$ with NT equally spaced samples we can expand the response in terms of NP complex poles s_{pi} and residues C_i so that[40]

$$f(t) = f(N\Delta t) = f_{i=0,1,2...NT-1} = \sum_{i=0}^{NP-1} C_i e^{s_{pi}\Delta t N} \tag{4.3.28}$$

The parameters s_{pi} and C_i are found using a least-squares approximation to the signal samples f_i. In this case the functions are in the form of decaying sinusoidal functions as shown in (4.3.27) therefore, for each function, there will exist two poles. Hence, neglecting phase differences

$$f(0)_i e^{-\alpha_i t}cos(\omega_i t) = \frac{1}{2}\left[f(0)_i e^{-(\alpha_i + j\omega_i)t} + f(0)_i e^{-(\alpha_i - j\omega_i)t}\right] \tag{4.3.29}$$

Hence, the poles s_{pi} are related to the damping and frequency by

$$s_{pi} = \alpha_i \pm j\omega_i \tag{4.3.30}$$

where the damping is related to the Q factor of the cavity through (2.2.8).

Again the Z-transform is employed to convert continuous data into the discrete Z-domain. Given the Z-transform of an input signal $X(z)$ the channel output $Y(z)$ can be obtained through multiplication with the Z-domain transfer function of the channel $F(z)$ such that[43, 18, 41]

$$Y(z) = F(z)X(z) \tag{4.3.31}$$

In Equation (4.3.31) the transfer function $F(z)$ is related to the impulse response of the channel by

$$F(z) = \sum_{i=0}^{\infty} f_i z^{-i} \tag{4.3.32}$$

and can be approximated by the Padé fraction[44]

$$F(z) = \frac{B(z)}{A(z)} = \frac{\sum_{i=0}^{NP} a_i z^{-i}}{\sum_{i=0}^{NP} b_i z^{-i}} = \frac{b_0 + b_1 z^{-1} + b_2 z^{-2} + \ldots + b_{NP} z^{-NP}}{a_0 + a_1 z^{-1} + a_2 z^{-2} + \ldots + a_{NP} z^{-NP}} \tag{4.3.33}$$

where NP is the number of poles (or damped exponentials) in the system. The complex poles and residues can be obtained from the Padé coefficients a_i and b_i.

The first step in finding the Padé coefficients is to find the coefficients a_i and then use these values to obtain the coefficients b_i. The coefficients a_i are found using a least-squares minimisation over the region f_{NP+1} to f_{NT-1}[44]. Over this region the least-squares error is set to zero and the following difference equations

are constructed

$$\begin{bmatrix} f_{NP} & f_{NP-1} & f_{NP-2} & \cdots & f_1 \\ f_{NP+1} & f_{NP} & f_{NP-1} & \cdots & f_2 \\ f_{NP+2} & f_{NP+1} & f_{NP} & \cdots & f_3 \\ \vdots & \vdots & \vdots & \ddots & \vdots \\ f_{NT-2} & f_{NT-3} & f_{NT-4} & \cdots & f_{NT-NP-1} \end{bmatrix} \begin{bmatrix} a_1 \\ a_2 \\ a_3 \\ \vdots \\ a_{NP} \end{bmatrix} = - \begin{bmatrix} f_{NP+1} \\ f_{NP+2} \\ f_{NP+3} \\ \vdots \\ f_{NT-1} \end{bmatrix} \tag{4.3.34}$$

In the Padé form expansion the coefficient $a_0 = 1$. Using the notation of [40] equation (4.3.34) can be solved for the coefficients a_i by expressing the equation in the matrix form

$$\underline{\underline{f_2}}\,\underline{a} = -\underline{f_{21}} \tag{4.3.35}$$

This expression can then be solved by multiplying both sides by the transpose of $\underline{\underline{f_2}}$ giving

$$\left(\underline{\underline{f_2}}^T \underline{\underline{f_2}}\right) \underline{a} = -\underline{\underline{f_2}}^T \underline{f_{21}} \tag{4.3.36}$$

By defining the matrix $\underline{\underline{A}} = \underline{\underline{f_2}}^T \underline{\underline{f_2}}$ and vector $\underline{B} = \underline{\underline{f_2}}^T \underline{f_{21}}$, the coefficients can be found using

$$\underline{a} = -\underline{\underline{A}}^{-1} \underline{B} \tag{4.3.37}$$

Equation (4.3.37) can only be solved if the matrix $\underline{\underline{A}}$ is non-singular so it must be ensured that not too many poles NP are chosen in the estimation. However, if not enough poles are selected a poor approximation is obtained. In order to obtain the modal structure of an overmoded cavity it is difficult to estimate the number of modes needed. Through trial and error it is best to use the maximum number of poles possible such that $\underline{\underline{A}}$ remains invertable. The consequence of using a high number of poles is that spurious poles are obtained in the result. These can be discarded however if they exceed limits defined by the modeller.

Prony's method proceeds by obtaining the coefficients b_i by forcing

$$b_i = f_i + \sum_{k=1}^{NP} a_i f_{i-k} \qquad 0 \leq i \leq NP \tag{4.3.38}$$

resulting in an exact fit for the first NP values of the response function[44]. Here $f_i = 0$ for $i < 0$ as we assume a causal system.

Equation (4.3.38) can be rewritten in matrix form as

$$\begin{bmatrix} f_0 & 0 & 0 & \cdots & 0 \\ f_1 & f_0 & 0 & \cdots & 0 \\ f_2 & f_1 & f_0 & \cdots & 0 \\ \vdots & \vdots & \vdots & \ddots & \vdots \\ f_{NP} & f_{NP-1} & f_{NP-2} & \cdots & f_0 \end{bmatrix} \begin{bmatrix} 1 \\ a_1 \\ a_2 \\ \vdots \\ a_{NP} \end{bmatrix} = \begin{bmatrix} b_0 \\ b_1 \\ b_2 \\ \vdots \\ b_{NP} \end{bmatrix} \tag{4.3.39}$$

so that

$$\underline{\underline{f_1}}\,\underline{a} = \underline{b} \tag{4.3.40}$$

It can be seen from Equation (4.3.40) that the coefficients b_i can be easily found through multiplication of the vector $\underline{a}$ by the matrix $\underline{\underline{f_1}}$. The values of the Padé coefficients a_i and b_i found using this method provide a least-squares approximation of f_i over the region $i = 0, 1, ..., NP$ which can be now used to find the poles and residues of the system response. These can be found by substituting the Padé coefficients into Equation (4.3.33) and performing a partial fraction expansion on the resultant function to give[43]

$$\frac{B(z)}{A(z)} = \frac{C_1}{1 - \mu_1 z^{-1}} + \frac{C_2}{1 - \mu_2 z^{-1}} + \ldots + \frac{C_{NP}}{1 - \mu_{NP} z^{-1}} \tag{4.3.41}$$

In Equation (4.3.41) the values of μ_i are used to find the complex poles of the

system through $s_{pi} = \frac{1}{\Delta t}\log(\mu_i)$. The damping α and resonant frequency ω of each pole is then given by (4.3.30). Substituting the poles and residues into Equation (4.3.28) allows an approximation to the initial function to be formed[18].

Using the Prony fitting approach an approximation to the response of the cavity problem in Figure 4.3.4 can be made. Using a total of 18 poles (9 resonances) the Prony approximation shown in Figures 4.3.8 and 4.3.9 was obtained. Very good agreement can be seen between the full field data and the Prony approximation. The method can be seen to be effective at extracting the resonant information from a channel response. This information can then be used in the filter model to provide an efficient model that represents the channel. However, in this case the channel has a relatively low modal density, in this situation the Prony method works well, if the number of modes increases then the Prony approximation can fail due to the matrix in (4.3.34) becoming badly conditioned.

It is found that in practice the Prony method is not robust and often involves a degree of trial and error when choosing the number of poles to use and is sensitive to the input data used. A common problem with the Prony method, in particular for experimental measurements, is that any noise in the data often degrades the method. If simulated results are to be used as the input, from a full field model for example, then it must be ensured that no spurious data is introduced due to frequencies above the mesh limit being included. This can be ensured by passing the response data through a low pass filter, however in common practice the use of Gaussian input waveform effectively performs this before passing the data through the full field channel model.

In the cavity channels considered here the Q factor is high and the response will be long. In addition, the band of interest is localised around the bandwidth of the the communication protocol being used. ZigBee, for example, uses a total

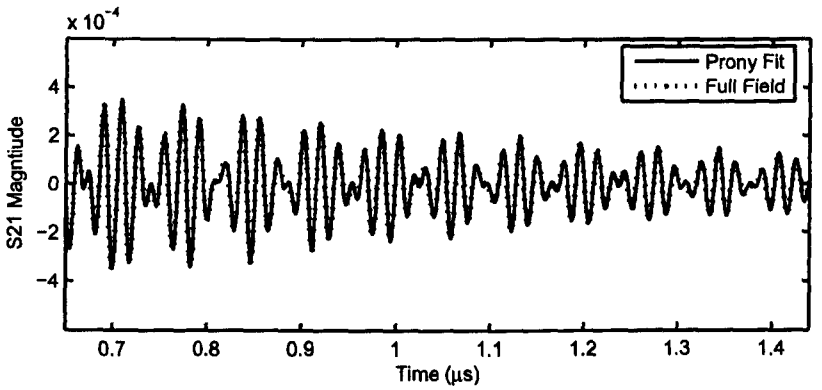

Figure 4.3.8: Time domain Prony approximation to the cavity response

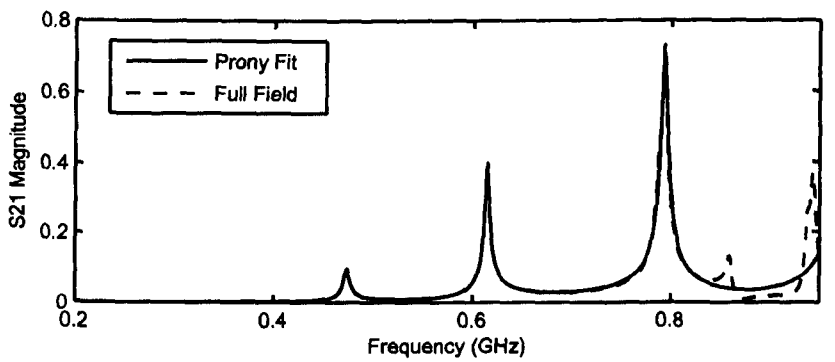

Figure 4.3.9: Frequency domain Prony approximation to the cavity response

frequency range of 2.405-2.485GHz and hence we are not interested in the response far outside this range. The Prony method requires the construction of the matrix as in Equation (4.3.34) in order to solve for the a_i coefficients; with a large number of data samples this matrix can quickly become unmanageable.

One option is to downsample and window the response in order to reduce the number of data points. Under most common circumstances this is proved a good approach and no loss of accuracy in results is incurred. However, in some cases the high frequency numerical noise can cause errors when the signal is downsampled as the underlying lower frequency response is not correctly sampled. Another approach is to window the data in order to reduce the number of data samples. However, the length of the decay means that if the window is too small then a lot of the frequency data is lost.

In order to reduce the number of data samples a bandpass approach has proven the most suitable where the band of interest is isolated and shifted to baseband to isolate the poles. Taking as an example a ZigBee scheme, the centre-frequency of the channels used by ZigBee are given by[32]

$$f_C = (2405 + 5 \times (k - 11))\text{MHz};\ k = 11, 12, ..., 26 \tag{4.3.42}$$

where the index k is referenced against the formal wireless channel number. Each ZigBee channel occupies less than 5MHz ($T_{decay} \approx 1\mu s$) of bandwidth around the centre frequency so it can be assumed that all ZigBee signal transmission is between f_{min} = 2.400GHz and f_{max} = 2.490GHz. Removing all frequency components outside this range from the response yields a response that only includes the modes of interest in the channel and any unnecessary modes are omitted.

The response of the ZigBee region can be shifted to baseband by a negative shift

in frequency equal to f_{min}. This process has the effect of removing the frequency domain shift due to the carrier frequency. The frequency of any response in the shifted function ω_s can be easily mapped to the frequency of the real system ω_r by $\omega_r = \omega_s + \omega_{min}$ so that the complex poles of the real system are given by

$$s_{pi} = \alpha + j\left(\omega_c + \omega_{min}\right) \tag{4.3.43}$$

where $\omega_c = 2\pi f_c$ and the poles are found from the time response data.

The elimination of the high frequency oscillations in the channel response allows downsampling to be performed on the data. The Prony approximation can then be performed on the frequency shifted and downsampled data without loss of information within the frequency band of interest. In addition it is necessary to remove any DC component of the response before a Prony approximation is attempted, this will yield the most accurate results for the Prony approximation.

4.4 A Statistical Approach to Channel Modelling

The approaches described above are specific to one particular geometry configuration. Using measurement and full-field simulation it is possible to calculate the response of any given cavity structure. However, as stated before, this response is only valid for this single configuration and does not provide a general representation of the cavity or channel. Even small changes can have large effects on the position of the resonant peaks and hence the properties of cavity. It is demonstrated in [45] that small variations in the structure lead to the shifting of resonant peaks in the channel. As the Q factor of the channel is high this leads to significant changes in the S_{21} transmission in the channel. Therefore, it is possible that for a high Q factor, low modal density channel the variation in BER for a

wireless system could vary between 0% and 100%.

Hence, calculating the effect of the channel on a wireless system will not be conclusive for a single channel as it cannot be guaranteed that the channel will not change over time or be exactly as modelled. Therefore, in order to assess the properties of the channel and how they will effect a wireless signal an averaging approach should be taken whereby the specific resonant peak positions are not specifically defined. It was shown in Chapter 2 that the channel can be characterised by two quantities, that is the density of modes (2.2.29) and the Q factor (2.2.1).

In this modelling apprach the channel is characterised by only these two parameters and the other parameters, the resonant frequencies and mode amplitudes, are varied in a random way. A channel can be defined so that the density of modes, at the centre frequency of interest, is used to obtain the number of modes, M, that will be randomly located within the channel bandwidth Δf. Furthermore, each peak resonance is assigned the average Q factor of the cavity across the same bandwidth. The amplitude of the modes can either be kept constant or randomly varied. As in a real resonant cavity it is allowed that modes overlap and become degenerate.

The effiency of the filter model developed here means that it is ideal for this approach to channel modelling, a large number of simulations can be performed in the same amount of time it would take to perform a single full-field simulation. Furthermore, the random definition of the channel parameters makes this model simple to apply to parallel or distributed computing approaches. The modelling process is as follows when using the statistical modelling approach.

1. The independent variables are set: modal density ($g(f)$), modelled band-

width ($\Delta f'$), Q factor (Q), spreading sequence ($b(t)$), carrier frequency (f_c), input sequence length (N)

2. The number of modes are calculated: ($M = g(f)\Delta f'$)
3. The random variables are calulated: modal amplitude ($A_0(1\ to\ M)$), mode centre frequency ($f_0(1\ to\ M)$)
4. The channel is constructed using the random and independent variables
5. A random sequence of N bits is produced, spread in frequency and modulated
6. The signal is passed through the channel
7. The signal is demodulated and despread and bit-summed
8. The bit error ratio (BER) is calculated
9. Process repeated from step 3 until the result converges sufficiently

This approach can be considered analogous to the approach taken in reverberation chamber measurements. The modes of the reverberation chamber are shifted between measurements through the use of the stirrer structure within the cavity. It is necessary at this point to consider the accuracy of the results derived from the reverberation chamber and hence this model when a statistical approach is taken to the resonant cavity problem. It must be ensured that enough simulations are performed, with differing modal structures, in order to obtain meaningful results. Equivalently enough simulations must be performed that the result converges sufficiently to ensure accuracy. In reverberation chamber measurements it is defined that "the field within the chamber is considered uniform if the standard deviation [of the maximum field strength] is within 3dB above 400 MHz, 4dB at 100 MHz decreasing linearly to 3 dB at 400 MHz, and within 4 dB below 100 MHz" [23]. The maximum field strength is recorded over a stirrer cycle. It is assumed that the wireless systems used will operate at greater than 400MHz, therefore, analogous

to this approach it is ensured that the average response obtained for all repeated simulation runs be uniform to within 3dB.

An estimation of the number of simulations necessary to model an average channel can be arrived at using the frequency domain representation of a resonance (2.2.3). Let the total bandwidth being modelled be occupied by equally spaced modes such that their spacing is the average of the spacing, $\Delta\omega_n$, of the modes surrounding a centre frequency ω_c. Recalling the density of modes, g, defined in Chapter 2, the average spacing is given by

$$\langle \Delta\omega_n \rangle = \frac{1}{g(\omega_c)} \tag{4.4.44}$$

Assuming the modes to be equally spaced the resonant peak magnitude in the frequency domain can be given by the magnitude of a given peak plus the contribution from all neighbouring peaks so that

$$|\phi(\omega_0)|^2 = \frac{1}{\alpha^2} + \sum_{n=1}^{\infty} \frac{1}{\alpha^2 + (n/g)^2} = \frac{\pi g}{\alpha} \coth(\pi g \alpha) \tag{4.4.45}$$

In a similar manner the magnitude at the minumum between neighbouring peaks is given by

$$\left|\phi(\omega_0 + \frac{1}{2g})\right|^2 = \sum_{n=1}^{\infty} \frac{1}{\alpha^2 + ((2n-1)/g)^2} = \frac{\pi g}{\alpha} \tanh(\pi g \alpha) \tag{4.4.46}$$

Hence, the peak to trough magnitude ratio is given by

$$\Phi = \tanh^2(\pi g \alpha) = \tanh^2\left(\frac{\pi^2 f_0 g}{Q}\right) \tag{4.4.47}$$

and can be seen to be dependent on the density of modes and the width of the modes. As a rule of thumb we can define a minimum number of simulations that will be required so that the average response of the channel is within 3dB across

the bandwidth of interest. For a given Q factor it is possible to find the density of modes that will allow the average peak ratio of the transfer spectrum to be within 3dB by rearranging (4.4.47) for g. Hence for an actual density of modes the number of repeats necessary to obtain the equivalent density of modes necessary to ensure the channel can be considered flat on average. As the modes are to be randomly positioned and not evenly spaced, it will be necessary to add a factor to the number of simulations to perform. From numerical experiment it was found that doubling the estimated number for a uniform modal structure is more than sufficient.

In modelling the wireless channel the bit error ratio is of interest in order to quantify the quality of the channel. Through the statistical approach described here it is possible to obtain the average error for a given channel as well as the variance in the error rates. As seen in reverberation studies it is possible to define two modal structures both with the same modal density and Q factor where one will lead to very high BERs and the other to very low BERs [45]. It has been shown that this model is efficient and is able to model the properties of the channel using a direct or statistical approach. This approach to modelling the errors in communication in the channel is used in Chapter 7 to demonstrate the application of the model to a BPSK signal in the highly reverberant environment.

Chapter 5

Modelling of Multiple Coupled Cavities

The model developed in Chapter 4 provides an efficient means of modelling the propagation effects within a single resonant cavity environment. It was shown that the model can be easily adapted to model a general cavity using a statistical approach to error rate modelling. The model is suitable for complex cavities as it only considers the propagating modes within the cavity and is not specific to one particular geometrical configuration.

Consider the aircraft environment as an example where it is necessary to propagate a wireless signal from one cavity to another. Aircraft have a modular structure which consists of a number of adjacent cavities each with the resonant behavior described in Chapter 4. In some cases the cavities will be completely isolated, in which case some kind of coupling device will be needed. Alternatively the cavities are connected with small apertures in their common wall. In existing aircraft these

small apertures are used for wire routing and weight reduction. Perhaps the most prominant of examples is the structure within the aircraft wing, which usually consists of a ribbed structure that is covered by the surface of the wing.

The behaviour of wireless propagation through these resonant coupled cavities is of interest, in particular the effect of aperture coupling. This chapter investigates the effects of cavity coupling and develops efficient models for the modelling of the cavity coupling.

5.1 Problem Description

An attempt to propagate electromagnetic radiation through small apertures leads to a number of interesting effects including diffraction and frequency cutoff [42]. The aircraft structure contains a large number of apertures that are small, that is compared with the wavelength at 2.45GHz, which are used for weight reduction and cable routing. The aircraft can contain apertures that are large with respect to the wavelenth and in this case the aperture has little impact on the propagation properties of the environment. Here, only small apertures are considered as these will have the most impact on the wireless propagation characteristics of the channel.

The theory of electromagnetic fields propagating through an aperture is described in papers by Bethe [46], Wheeler [47] and McDonald [48]. One approach to modelling aperture coupling is to treat the aperture as a dipole at the aperture centre and the coupling is related to the *effective volume* of the coupling hole [47]. Other cavities may be coupled by waveguiding structures where there is a long (compared to the wavelength) coupling waveguide between the cavities with a smaller cross section than cavity. This could also be considered to be the case

where the aperture has a large thickness, such that cutoff modes are significantly attenuated by the coupling aperture.

In order to use a wireless communication system in the coupled environment it is necessary to maximise the coupling between the two cavities and minimise errors in commmunication. It has been shown that in order to minimise errors in a given size of cavity we should aim to reduce the excess delay. In order to do this the loss of the cavity can be reduced, however this will affect the power coupled in the cavities. The following sections develop an efficient model of the coupled resonant cavity environment to demonstrate the effect of the environment on wireless propagation.

5.2 Aperture Coupled Cavities

The simplest case to be considered for cavity coupling is the case of two identical cavities coupled by an aperture in their common wall. Let the aperture be a slot that extends the full height of the cavity so that the problem can be reduced to that of a 2D cavity problem. A schematic of the simplified cavity is shown in Figure 5.2.1a. In the first instance the common wall of the cavities is assumed to be thin and all cavity walls are perfect conductors so that losses are neglected.

5.2.1 Two Slot-Coupled Cavities

If we assume that the walls of the cavity exhibit resonant behaviour with energy stored in magnetic and electric fields we can model the first resonance of the cavity using the LC resonant circuit shown in Figure 5.2.1b where the current source represents the field excitation. The coupling of the two cavities is provided

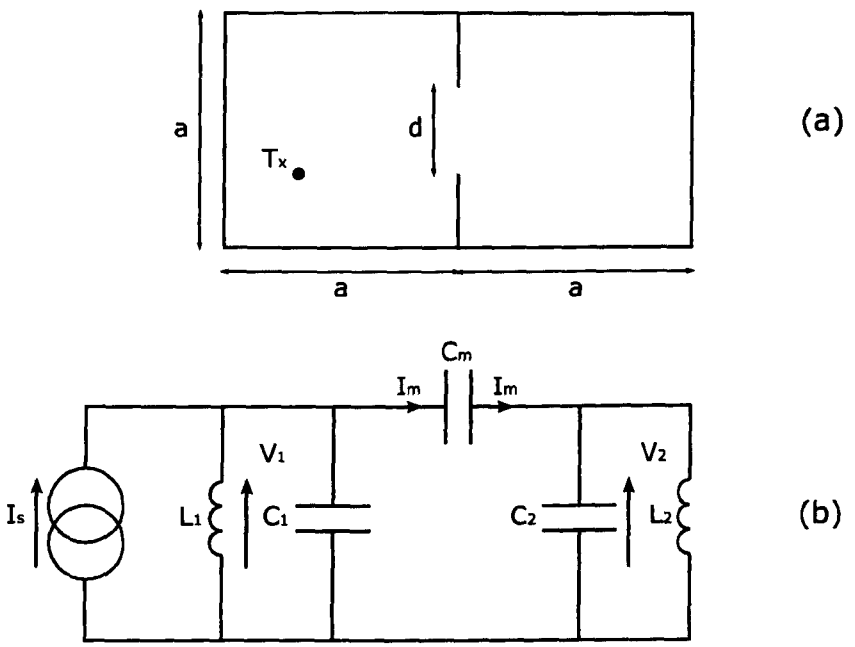

Figure 5.2.1: Coupled cavities and an equivalent circuit model

through a frequency dependent coupling. The choice of the coupling component is determined by the geometry of the coupled cavity system, which will be discussed in Section 5.2.4. In this case the coupling is modelled by a mutual capacitance C_m for reasons that will be explained.

The electric field is stored in the capacitance C and the magnetic field is stored in the inductance L. This circuit model can be analysed to ascertain the effect of the coupling on the resonant behaviour of the cavities. As the two cavities are identical in size and hence have the same resonant frequency as individual cavities the circuit model can be simplified with $C = C_1 = C_2$ and $L = L_1 = L_2$.

Referring to Figure 5.2.1b, the current in the source side of the circuit is given by

$$I_s - I_m = \frac{V_1}{sL} + sCV_1 \tag{5.2.1}$$

and the current in the coupled side is given by

$$I_m = \frac{V_2}{sL} + sCV_2 \tag{5.2.2}$$

where the Laplace variable $s = -j\omega$ in the lossless system. The voltage across the coupling is dependent on the coupling capacitance and is given by

$$V_1 - V_2 = \frac{I_m}{sC_m} \tag{5.2.3}$$

Expressing the circuit equations (5.2.1)-(5.2.3) in an admittance matrix of the form

$$\underline{I} = \underline{\underline{Y}}\underline{V} \tag{5.2.4}$$

yields

$$\begin{bmatrix} I_s \\ 0 \end{bmatrix} = \begin{bmatrix} 1/sL + sC & 1/sL + sC \\ -sC_m & 1/sL + sC + sC_m \end{bmatrix} \begin{bmatrix} V_1 \\ V_2 \end{bmatrix} \tag{5.2.5}$$

The resonant frequencies of the circuit can be obtained by requiring that the determinant of the complex admittance vanishes [26], [27]

$$\det \underline{\underline{Y}} = 0 \tag{5.2.6}$$

In finding the resonant frequency of the circuit we make the common substitution

$$\omega_0 = \frac{1}{\sqrt{LC}} \tag{5.2.7}$$

Here, we introduce the dimensionless coupling coefficient k_c which parametises the coupling of the two resonant cavities through the coupling capacitance where

$$k_c = \frac{C_m}{C} \tag{5.2.8}$$

We see that in the limit $C_m \rightarrow 0$ the coupling coefficient $k_c \rightarrow 0$ and the resonance of only the single cavity is modelled by the circuit as the right-hand-side circuit is isolated from the left-hand-side.

Substituting (5.2.8) and (5.2.7) into (5.2.6) and rearranging yields the quadratic equation

$$0 = \omega_0^4 + 2s^2\omega_0^2(k_c + 1) + s^4(2k_c + 1) \tag{5.2.9}$$

Solving (5.2.9) for $s^2 = -\omega^2$ we obtain the resonant frequencies of the circuit in Figure 5.2.1

$$\omega_1 = \omega_0; \quad \omega_2 = \frac{\omega_0}{\sqrt{2k_c + 1}} \tag{5.2.10}$$

It can be seen from (5.2.10) that the circuit possesses two resonances, one at the resonant frequency of the LC circuit and another shifted to a lower frequency by the coupling dependent term. These equations allow the coupling coefficient, k_c, to be obtained for a cavity configuration if the resonant frequencies are known. From inspection of (5.2.8) and (5.2.10) the negative shift of the aperture resonance can be seen to increase with increasing coupling capacitance, hence coupling coefficient. When the slot width is equal to the width of the cavity it is trivial to show that the coupling coefficient for the configuration described here is equal to

$$k_c = \frac{1}{2}\left[\left(\frac{\omega_0}{\omega_2}\right)^2 - 1\right] = \frac{1}{2}\left[\left(\frac{8}{5}\right) - 1\right] = 0.3 \tag{5.2.11}$$

where the factor 8/5 comes from a pair of cavities with side length a and $2a$.

To validate this model a full-field TLM model was constructed of a cavity structure where $a = 21$cm and two slot widths are chosen, $d = 7$cm and $d = 11$cm. The model was created using a $\Delta l = 1$cm mesh and iterated for a total of 32,768 time steps. The transmitter, or source, cavity was excited using a Gaussian pulse of width 0.3ns so that energy was excited at below the maximum mesh frequency

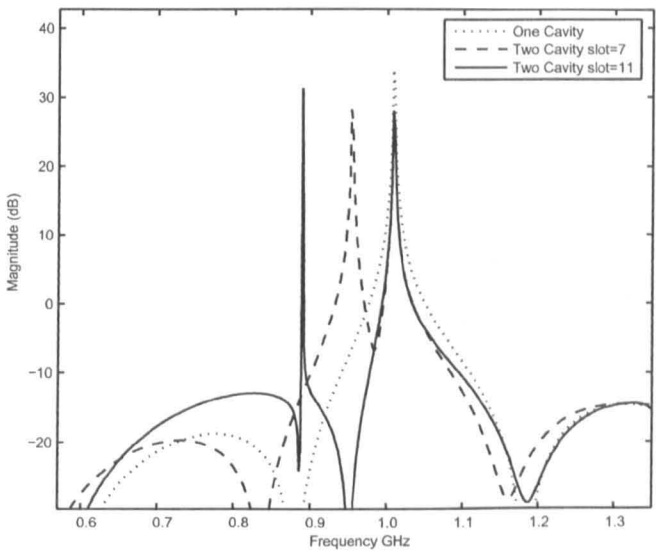

Figure 5.2.2: TE_{110} resonance of a single cavity and coupled cavities through a 7cm and 11cm slot

[13]. The un-normalised received power at the first half cavity resonance, $TE_{110} = 1.0095$GHz, is shown in Figure 5.2.2. Note that the resonant frequency of the combined cavity without the aperture is $TE_{110} = 0.7981$GHz.

It can be seen that the coupling of the resonant cavities through an aperture leads to a splitting of the first resonance $\mathrm{TE}_{(110)}$ of the cavity. The resonance of the single cavity does not move but the split resonance is shifted by an amount dependent on the aperture size and hence k_c. As the slot width increases the split resonance, the cavity-aperture resonance, shifts towards that of the complete double cavity. Using the shifted resonant frequencies and the normal mode the coupling coefficient can be obtained from (5.2.10). Hence, for a slot width of $d = 7$cm, $k_c = 0.059$ and for a slot of width $d = 11$cm, $k_c = 0.142$, for example.

The stucture of the modes that account for the resonances can be identified in order to isolate the effect of the coupling. The normal resonance and the split reso-

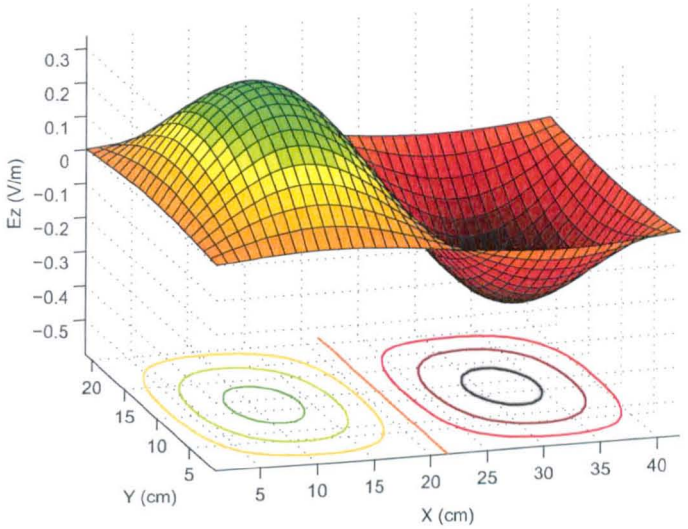

Figure 5.2.3: Out of phase electric field oscillations of coupled cavities (Normal mode)

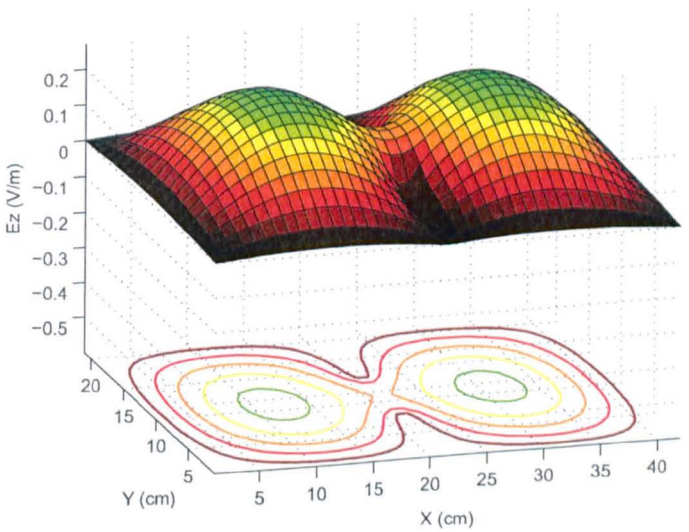

Figure 5.2.4: In-phase electric field oscillations of coupled cavities (Split mode)

nance were individually excited using a narrow band input. A Gaussian enveloped sinusoidal field excitation was used in each case so that the centre frequency corresponed to the mode of interest and the bandwidth only contained the single mode. The field produced for each mode excitation is shown in Figures 5.2.3 and 5.2.4.

It can be seen that the un-shifted mode is a mode where the fields oscillate π radians out of phase in the two cavities, whereas the shifted mode occurs due to an in-phase field oscillation. In the former case the field at the aperture can be seen to be zero at all times as there is a natural node in the resonance at that point. In the latter case there is coupling across the aperture such that the aperture field is non-zero, the field magntitude at the centre of the aperture increases with aperture width. This is as expected because rearranging (5.2.3) for the coupling current yields

$$I_m = sC_m (V_1 - V_2) \tag{5.2.12}$$

Therefore, in the limit that the slot width is zero the coupling current $I_m = 0$ as no field can penetrate the aperture. Increasing the slot width increases the coupling capacitance from zero, hence the coupling current also increases with slot width, for a given frequency. The coupling capacitance models the field coupling across the aperture between the two cavities and can be imagined as the coupling between the charges on the walls of the two halves of the structure. The coupling current can be imagined as the magnetic field at the aperture that can be created by an equivalent source in place of the aperture which is exciting the half space looking into the cavity.

Equivalently, consider the fully coupled $a \times 2a$ cavity with no central aperture region. The first mode of resonance in such a structure is the case where the maximum field is at the centre of the cavity; the second is that where the maximum field occurs at $0.5a$ and $1.5a$. In the first case the inclusion of a coupling boundary influences this field oscillation as it is positioned at the point of maximum field

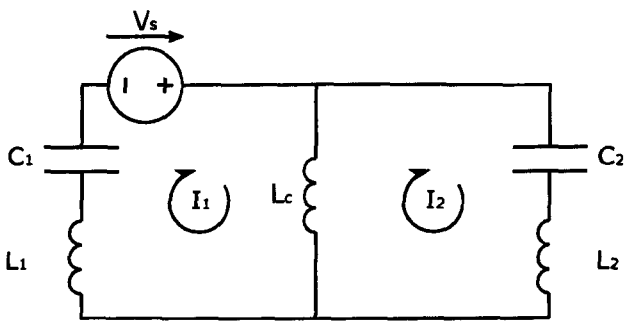

Figure 5.2.5: Coupled cavities and an equivalent circuit model

displacement. In the latter case the position of boundary is at a null in the field oscillation and hence the mode is not affected.

5.2.1.1 An Alternative Dual Model

The circuit model described in the previous section is based on capacitive coupling between the two cavities and it was shown that the resonances of the circuit could be found. An alternative circuit representation is to assume inductive coupling as shown in Figure 5.2.5 where the source is provided by a voltage in this case.

In the same manner that was adopted for the capacitively coupled model it is possible to analytically solve for the resonant frequencies of the circuit. As previously done for the capacitive model the resonances are found by relating the circuit currents and voltages. The coupling this time is applied through the common voltage on both sides of the coupling inductor, rather than the coupling current through the capacitor. The voltage on the source side is given by

$$V_s - V = I_1 sL + \frac{I_1}{sC} \tag{5.2.13}$$

and the voltage on the coupled side is given by

$$V = I_2 sL + \frac{I_2}{sC} \tag{5.2.14}$$

The currents on either side of the coupling are related by the coupling inductance such that

$$I_1 - I_2 = \frac{V}{sL_c} \tag{5.2.15}$$

Hence, using the matrix form to obtain the resonant frequencies of the circuit

$$\begin{bmatrix} V_s \\ 0 \end{bmatrix} = \begin{bmatrix} sL_c + sL + 1/sC & -sL_c \\ -sL_c & sL_c + sL + 1/sC \end{bmatrix} \begin{bmatrix} I_1 \\ I_2 \end{bmatrix} \tag{5.2.16}$$

and solving for the determinant set to zero yields the resonance condition

$$0 = \omega_0^4 + 2s^2\omega_0^2 (k_c + 1) + s^4 (2k_c + 1) \tag{5.2.17}$$

In (5.2.17) the inductive form of the coupling coefficient is used where

$$k_c = \frac{L_c}{L} \tag{5.2.18}$$

From inspection it is clear that (5.2.17) is identical to (5.2.10) and hence the two circuit models are analogous to each other.

The choice of which model to use depends on the fields that are to be modelled. The resonant frequency of the two models are the same for a given aperture width and cavity size so the choice of model is not important for a resonant frequency study. However, if fields are of interest then it can be seen that the inductive model is derived in terms of the magnetic field within the cavities and the capacitive model is in terms of the electric field within the cavities.

5.2.2 Multiple Slot-Coupled Cavities

In some cases a number of cavities may be coupled through apertures. In such a case the methodology described above can be followed for numerous coupled cavities. Let the cavities be modelled using the capacitively coupled approach. Relating the current and voltages of the equivalent cavity circuits yields a coupling matrix for three cavities of the form

$$\begin{bmatrix} I_s \\ 0 \\ 0 \end{bmatrix} = \begin{bmatrix} Y_0 & Y_1 & 0 \\ Y_1 & Y_2 & Y_1 \\ 0 & Y_1 & Y_0 \end{bmatrix} \begin{bmatrix} V_1 \\ V_2 \\ V_3 \end{bmatrix} \tag{5.2.19}$$

where

$$\begin{aligned} Y_0 &= \tfrac{1}{sL} + sC + sC_m \\ Y_1 &= -sC_m \\ Y_2 &= Y_0 - Y_1 = \tfrac{1}{sL} + sC + 2sC_m \end{aligned} \tag{5.2.20}$$

The admittances in (5.2.20) can be considered in the following manner: Y_0 is the admittance of a cavity when an aperture is on a single face, Y_1 is the admittance of the coupling aperture between two cavities and Y_2 is the admittance of a cavity with an aperture on two of its faces.

Assuming that all cavities are identical in size and coupled through identically sized slots leads to the following expressions. For three cavities the resonances are given by

$$\omega_1 = \omega_0; \quad \omega_2 = \frac{\omega_0}{\sqrt{k_c + 1}}; \quad \omega_3 = \frac{\omega_0}{\sqrt{3k_c + 1}} \tag{5.2.21}$$

For four cavities the matrix in (5.2.19) can be expanded to account for the extra

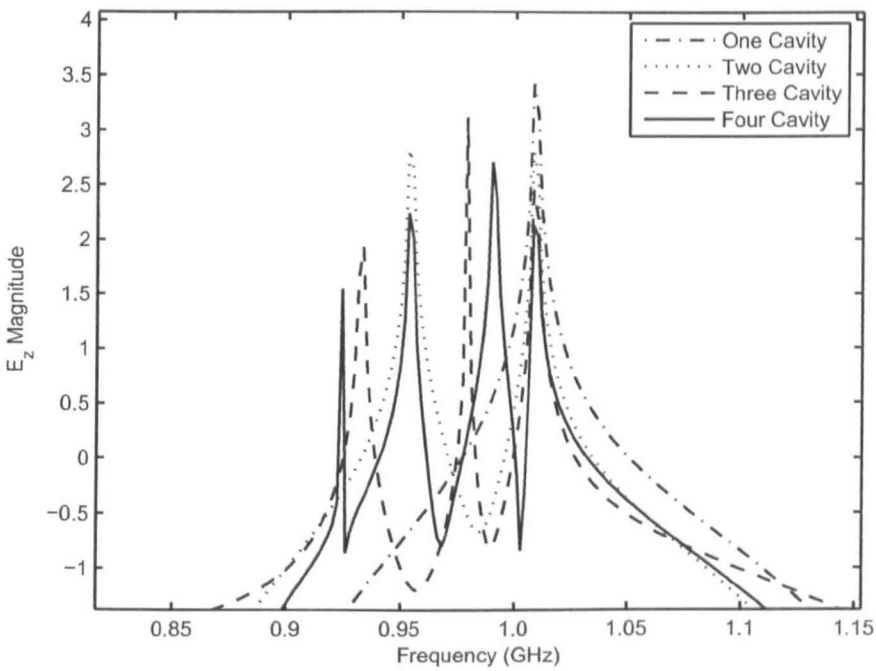

Figure 5.2.6: TE_{100} resonances of multiple linked cavities

cavities. The resonant frequencies in this case are given by

$$\omega_1 = \omega_0; \quad \omega_2 = \frac{\omega_0}{\sqrt{2k_c+1}}; \quad \omega_3 = \omega_0\sqrt{\frac{2k_c+1-\sqrt{2}k_c}{2k_c^2+4k_c+1}}; \quad \omega_4 = \omega_0\sqrt{\frac{2k_c+1+\sqrt{2}k_c}{2k_c^2+4k_c+1}} \tag{5.2.22}$$

This methodology may be expanded for any number of identical coupled cavities as there are only ever the three coupling admittances defined in (5.2.19).

Using a TLM model of the cavities the result shown in Figure 5.2.6 was obtained where all cavities are 21cm sided squares coupled through a 7cm slot. It has been found that the expressions in (5.2.21) and (5.2.22) agree with the simulation results where the coupling coefficent, $k_c = 0.059$, was obtained previously for the two cavity case.

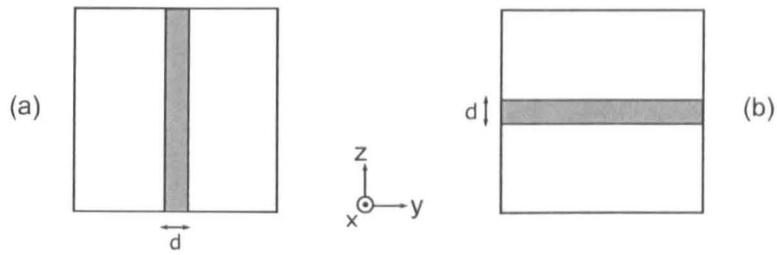

Figure 5.2.7: Slot orientations for cavity coupling where the field is polarised in the z direction

5.2.3 Effect of Slot Orientation

The previous sections have described the effect of a vertically oriented slot on the coupling coefficent of the cavity. It was shown that for a 2D representation of the arrangement, where the aperture is a slot extending the full height of the cavity, a circuit analogue could be derived. The circuit analogue had the form of a pair of resonant parallel or serial LC circuits coupled by either a capacitive or an inductive component. The result of the coupling on the resonant nature of the cavity was a mode splitting and shifting where the degree of shifting was shown to be determined by the coupling coefficient.

In this section the slot is again considered to be the full height of the cavity, however the orientation of the slot will be varied to be either parallel or perpendicular to the orientation of the field of interest as shown in Figure 5.2.7

In order to investigate the effect of the slot orientation on the cavity coupling the two orientations shown in Figure 5.2.7 were modelled using a full field TLM model as before. The cavity size, a, used is 21cm and the spacestep in the model is 1cm. The slot width is chosen to be 5cm and was positioned parallel and perpendicular to the wavevector of the source excitation. The source cavity is excited using a Gaussian excitation in the E_z field. The un-normalised received power in the second cavity is shown in the frequency domain in Figure 5.2.8 as

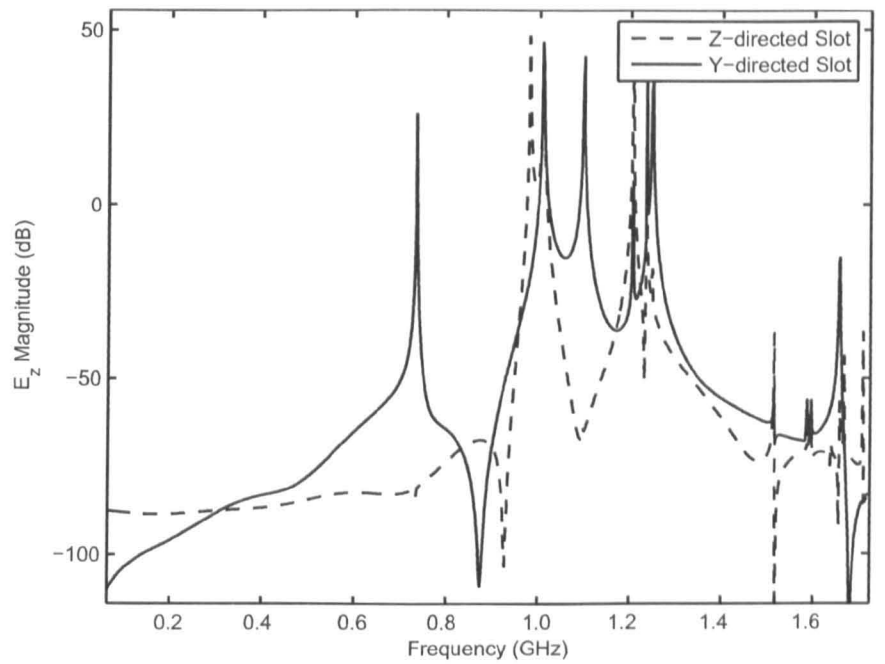

Figure 5.2.8: Received E_z field for the two slot orientations

modelled by the full field approach.

Results of the two slot orientations show that the field is not dramatically attenuated due to the slot for either orientation. This is most likely due to the aperture being thin so that there is no attenuation of cutoff modes. Furthermore, the apertures are connected to resonant cavities on either side where the decay time in either cavity is much longer than the time required for the energy in either cavity to become balanced. Hence, the energy in the system is able to reach an equilibrium between the two cavities before it is attenuated by losses in the source cavity.

The vertical z-directed slot behaviour was shown to be consistent with a capacitive coupling between two resonant circuits. It can be seen here that for the case of the y-directed slot there is still the resonance of the half cavity at 1.0095GHz. The low frequency resonance for the y-directed slot occurs at the resonant fre-

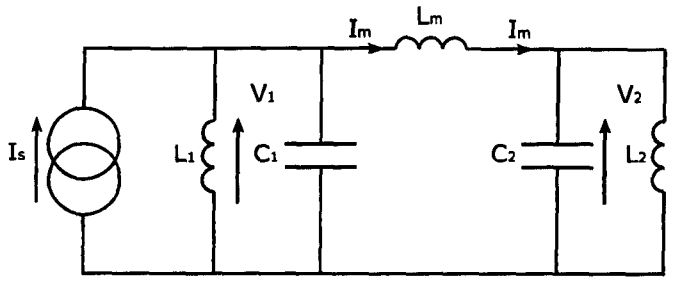

Figure 5.2.9: Inductive cavity coupling circuit

quency of the cavity with dimensions $2a \times a \times a$. The additional modes are in different locations to that of the capacitive coupling, for the same slot width. In fact, referring to Figure 5.2.8 it can be seen that the shift for the y-directed slot appears to be positive in frequency.

These resonances can be modelled in the same way as in the previous section by use of resonant circuits. The coupling in this case takes the form of an inductive coupling as shown in Figure 5.2.9. As shown previously the circuit can be analysed to obtain the resonant frequencies by constructing the matrix

$$\begin{bmatrix} I_s \\ 0 \end{bmatrix} = \begin{bmatrix} 1/sL + sC & 1/sL + sC \\ -1/sL_m & 1/sL + sC + 1/sL_m \end{bmatrix} \begin{bmatrix} V_1 \\ V_2 \end{bmatrix} \tag{5.2.23}$$

Then substituting for ω_0 and the coupling coefficient, which is related to the slot width d,

$$k_c = \frac{L}{L_m} \tag{5.2.24}$$

and solving for the determinant set to zero yields the resonances

$$\omega_1 = \omega_0 \quad \omega_2 = \omega_0\sqrt{2k_c + 1} \tag{5.2.25}$$

It can be seen from (5.2.25) how the slot orientation leads to the resonances shown in Figure 5.2.8 as the coupling coefficient leads to a positive shift in this case. In the case of a vertical slot the coupling coefficient has been shown to be capacitive and in

the case of a horizontal slot it has been shown to be inductive. Therefore, in order to model a general aperture the coupling can be considered to be a combination of these two effects. Therefore, we can replace the reactive coupling component by the general component jX where X is to be determined.

In reality it can be expected that the operating frequency of ZigBee, or other 2.45GHz systems, will be much higher than the fundamental resonance of the cavity. Such a cavity, if uniform would have side lengths of only 8.7cm. Realistic cavities that are encountered would likely be highly moded at a frequency of 2.45GHz, hence propagation through an aperture will be possible with the extra resonances excited. Referring to [38] it can be seen that if the width of the coupling aperture, or waveguide, is sufficient then a significant number of modes are propagated. The result is that the structure displays the same propagation behaviour in terms of field amplitude received as a single resonant environment. However, it has been shown that the aperture leads to mode splitting, hence for a given cavity volume a higher density of modes will occur.

5.2.4 Analytical Coupling Coefficients

It is desirable to be able to obtain the coupling coefficient for a given configuration analytically to allow modelling without the need of full field simulations. In Wheeler [47] it is suggested that the coupling coefficient varies with the square of the aperture width d. Wheeler proposed that the coupling coefficient could be estimated based on the equivalent volume, or area, of the cavity and the aperture. In the example described previously the equivalent area of one cavity is given by

$$A_c = \frac{1}{4}a^2 \tag{5.2.26}$$

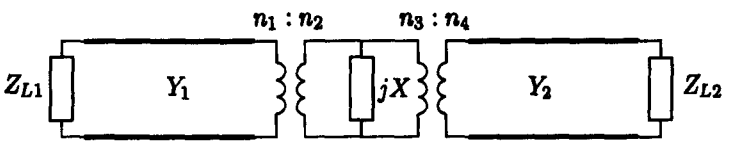

Figure 5.2.10: Equivalent coupled cavity transmission line circuit

and the equivalent area of the aperture is

$$A_a = \frac{\pi}{4} d^2 \tag{5.2.27}$$

where d is the slot width [47]. Hence, for cases where $d/a \ll 1$ the coupling coefficent can be approximated by

$$k_c = \frac{A_a}{4A_c} = \frac{\pi}{8}\left(\frac{d}{a}\right)^2 \tag{5.2.28}$$

This approximation is valid for small slot widths to cavity dimension ratios. However, if we consider the case of an aperture in an overmoded cavity, as is being considered here, this approximation becomes poor. In calculating the coupling coefficent for the environments of interest here a more accurate estimation of the coupling coefficent is required.

In order to obtain a more accurate and general figure for the coupling coefficient a waveguide approach is adopted. Consider the two cavity model described in Section 5.2.1, we can represent this in terms of the equivalent circuit model shown in Figure 5.2.10 where the two cavities are modelled as transmission lines terminated by loads Z_{L1} and Z_{L2}. The transmission lines are coupled to the aperture circuit through ideal transformers with turn ratios $n_1 : n_2$ and $n_3 : n_4$. This turns ratio characterises the coupling efficiency of a mode in one cavity to the mode in the other cavity. As there are cavities on both sides of the aperture the incident field is resonant with a slow decay time. This is in contrast to a plane wave illumination of a one sided cavity aperture where the incident wave has a component that is reflected and the coupling turns ratio must be modified according to the area of

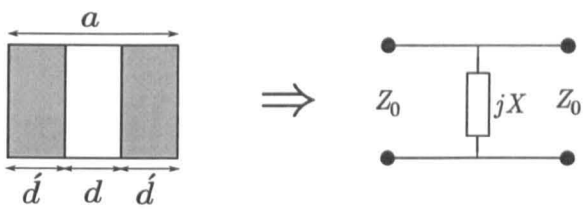

Figure 5.2.11: Waveguide slot aperture and its equivalent circuit [50]

the aperture [49].

We assume the cavities are lossless such that the the transmission line loads are $Z_{L1} = Z_{L2} = 0$ and the input impedance of the transmission lines are given by

$$Z_{in} = jZ_0 \tan(\beta_\lambda l) = jZ_0 \tan\left(\frac{\omega l}{c}\right) \tag{5.2.29}$$

In (5.2.29) l is the distance from the load, which is equal to the length of the cavity in this case, and Z_0 is the characteristic impedance of the transmission line. The input impedance will be a periodic function of frequency and models the impedance of each mode within the length of the cavity. Let the decay time of the cavity be long so that the turn ratios of the coupling transformers are equal to 1:1. This implies that all of the field in the source cavity will be incident upon the aperture at some point and excite the field in the receiver cavity. In the case of an open source cavity, where any field that is not incident upon the cavity is reflected into freespace, this ratio must be reduced accordingly [49]. In this way the voltage and currents on both sides of the coupling will be equal.

The aperture coupling circuit is shown in Figure 5.2.11. The coupling coefficient for the vertical slot can be obtained using a variational approach. Using the

result of [50] the impedance ratio at the aperture is given by

$$\frac{X}{Z_0} = \frac{a}{\lambda_g}\tan^2\left(\frac{\pi d}{2a}\right)\left[1 + \frac{3}{4}\left(\frac{1}{\sqrt{1-\left(\frac{2a}{3\lambda}\right)^2}} - 1\right)\sin^2\left(\frac{\pi d}{a}\right) + 2\left(\frac{a}{\lambda}\right)^2\left(1 - \frac{4}{\pi}\frac{E(k_\alpha)-k_\beta^2 F(k_\alpha)}{k_\alpha^2}\cdot\frac{E(k_\beta)-k_\alpha^2 F(k_\beta)}{k_\beta^2} - \frac{1}{12}\sin^2\left(\frac{\pi d}{a}\right)\right)\right] \tag{5.2.30}$$

where

$$\begin{aligned} k_\alpha &= \sin\left(\frac{\pi d}{2a}\right) \\ k_\beta &= \cos\left(\frac{\pi d}{2a}\right) \end{aligned} \tag{5.2.31}$$

The functions $F(k)$ and $E(k)$ are the full elliptic integrals of the first and second kind respectively, they are defined here as

$$\begin{aligned} F(k) &= \int_0^{\frac{\pi}{2}} \frac{d\theta}{\sqrt{1-k^2\sin^2\theta}} \\ E(k) &= \int_0^{\frac{\pi}{2}} \sqrt{1-k^2\sin^2\theta}\, d\theta \end{aligned} \tag{5.2.32}$$

The guide wavelength in equation (5.2.30) is defined in the usual way so that

$$\lambda_g = \frac{\lambda}{\sqrt{1-\left(\frac{\lambda}{2a}\right)^2}} \tag{5.2.33}$$

The coupling circuit provides the source of the cavities and the impedance Z_0 is taken to be the impedance of free space, η_0, so that (5.2.29) may be used to obtain the total circuit impedance for the circuit in Figure 5.2.10, viz.

$$Z = \frac{jXZ_{in}}{2jX + Z_{in}} = j\left(\frac{X}{2j\frac{X}{Z_{in}} + 1}\right) \tag{5.2.34}$$

which provides a means of obtaining the coupling coefficient of the cavity system analytically. From inspection of (5.2.34) it can be seen that the impedance of the circuit is always imaginary as we have assumed no loss in this case and the circuit is purely reactive. A plot of the magnitude of (5.2.34) can be seen in Figure 5.2.12. There exists a zero when $Z_{in} = 0$ which corresponds to the uncoupled resonance of the cavity and a pole when $Z_{in} = -2jX$ which corresponds to the coupled

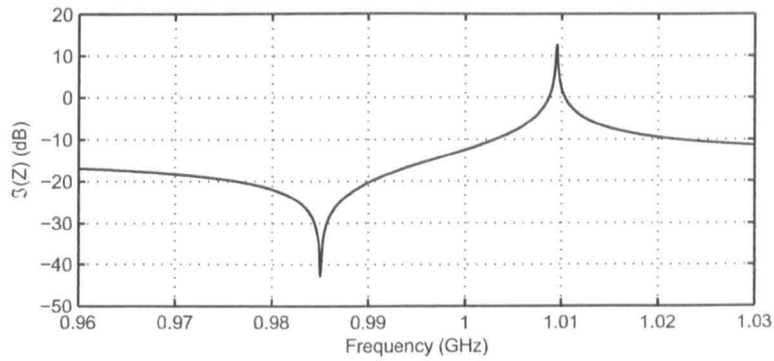

Figure 5.2.12: Imaginary impedance of the coupled cavity circuit

aperture-cavity resonance. Relating the positions of these values through (5.2.10) allows the coupling coefficent to be obtained.

A plot of the coupling coefficient obtained using full field simulation, the approximation of [47] and the method described here is shown in Figure 5.2.13 where good agreement with the full field result can be seen. This shows that this is an accurate approach to obtaining the coupling coefficent of a number of apertures where the properties can be obtained from the extensive examples defined in [50], [27] or other texts and applied in the same way as the slot coupling modelled here.

5.2.5 An Efficient Cavity Model

In order to model the propagation of a wireless signal using the equivalent model developed here it is necessary to produce a discrete time domain representation of the model. Starting from the equivalent circuit model in Figure 5.2.1 it is possible to derive such a model. In contrast to the model of Figure 5.2.1, let the coupling be represented by a variable circuit component combination of inductive and capacitive terms.

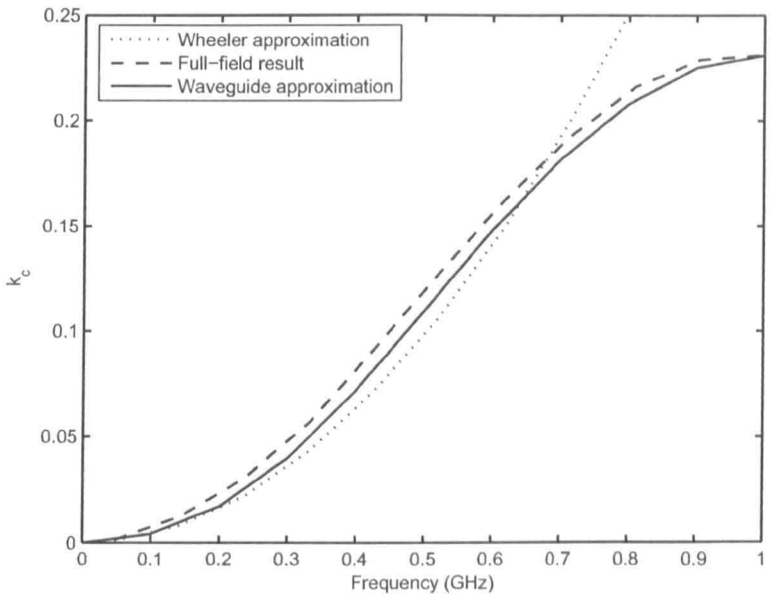

Figure 5.2.13: Coupling coefficient from approximations and full-field results

Discretisation will be carried out using the tranmission line modelling method [13] which permits the modelling of passive components as transmission lines and in turn provides an unconditionally stable discrete time-domain model. The capacitor and inductor components of Figure 5.2.1 are modelled using transmission line stubs. The capacitor is modelled as a open circuit stub where the capacitance to be modelled is given by

$$C = C_d \Delta l \tag{5.2.35}$$

where C_d is the per unit length capacitance, Δl is chosen to be

$$\Delta l = \frac{c\Delta t}{2} \tag{5.2.36}$$

and Δt is the time taken for a pulse to propagate into the stub and back. Hence, the capacitor can be modelled using a transmission line stub with characteristic impedance

$$Z_C = \sqrt{\frac{L_d}{C_d}} = \frac{\Delta t}{2C} \tag{5.2.37}$$

where L_d is obtained from the propagation speed c such that

$$L_d = \frac{1}{c^2 C_d} \tag{5.2.38}$$

Following the same arguments, the characteristic impedance of a short circuited transmission line representation of an inductor is given by

$$Z_L = \frac{2L}{\Delta t} \tag{5.2.39}$$

More details regarding the approach to modelling inductors and capacitors in the transmission line modelling apprach can be found in [13], or in terms of an equivalent Z-transform approach in [40].

Through modelling the components as transmission lines the model of Figure 5.2.1 is converted into its transmission line Thevenin equivalent circuit as shown in Figure 5.2.14a. The coupling circuit is modelled by the stubs shown in Figure 5.2.14b which is tuned to the coupling coefficent obtained for the cavity problem being considered.

A time domain solution is obtained by modelling the circuit in the form of Figure 5.2.14c where the incident voltage and impedance in the left-hand-side cavity are given by

$$V_1^i = \frac{\frac{2V_{C1}^i}{Z_{C1}} + \frac{2V_{L1}^i}{Z_{L1}} + I_s}{\frac{1}{Z_{C1}} + \frac{1}{Z_{L1}}} \tag{5.2.40}$$

and

$$Z_1 = \frac{Z_{C1} Z_{L1}}{Z_{C1} + Z_{L1}} \tag{5.2.41}$$

Equivalent expressions exist for the right-hand-side cavity and the coupling circuit. Therefore, the current in the circuit of Figure 5.2.14c is given by

$$I = \frac{V_1^i + V_m^i - V_2^i}{Z_2 + Z_1 + Z_m} \tag{5.2.42}$$

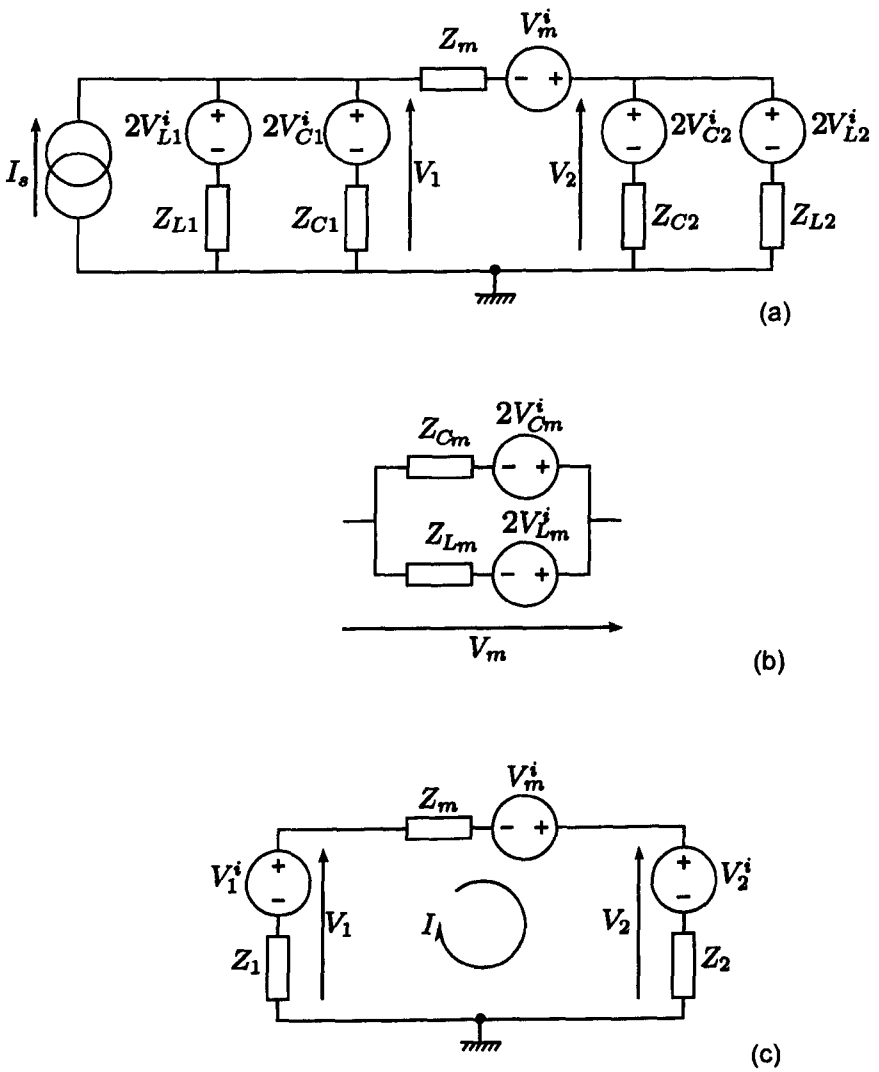

Figure 5.2.14: Thevenin equivalent circuit of the coupled cavity model (a), the coupling circuit (b) and a simplified circuit form (c)

The update for the next timestep proceeds by calculating the voltage across each of the ports of the equivalent circuit. The voltages are obtained using the expressions

$$\begin{aligned} V_1 &= V_1^i - IZ_1 \\ V_2 &= V_2^i + IZ_2 \\ V_m &= V_m^i - IZ_m \end{aligned} \tag{5.2.43}$$

for each of ports. The reflected voltages into each of the stubs can then be calculated by refering back to Figure 5.2.14a. For example, the reflected voltage at this time step, k, and hence the incident voltage at the next time step, $k+1$, for the inductor of cavity 1 is given by

$${}_{k+1}V_{L1}^r = {}_kV_{L1}^r = -\left(V_1 - V_{L1}^i\right) \tag{5.2.44}$$

The negative sign is due to the stub being short circuited. Equivalently the update for the capacitive stub is given by

$${}_{k+1}V_{C1}^r = {}_kV_{C1}^r = \left(V_1 - V_{C1}^i\right) \tag{5.2.45}$$

The calculations can now be performed iteratively until a solution is reached. The input for the circuit is the current source in cavity 1, I_s. and the output is obtained from the voltage of cavity 2, V_2/Z_2. This model can be extended to include cavity and aperture losses by introducing a resistive element in parallel with the corresponding circuit element. In this way (5.2.40) becomes

$$V_1^i = \frac{\frac{2V_{C1}^i}{Z_{C1}} + \frac{2V_{L1}^i}{Z_{L1}} + I_s}{\frac{1}{Z_{C1}} + \frac{1}{Z_{L1}} + \frac{1}{R_1}} \tag{5.2.46}$$

and (5.2.41) becomes

$$Z_1 = \frac{1}{\frac{1}{Z_{C1}} + \frac{1}{Z_{L1}} + \frac{1}{R}} \tag{5.2.47}$$

where R is a loss term related to Q factor and hence modal width by

$$R = \frac{1}{2\pi C \Delta f} \tag{5.2.48}$$

and C is the capacitance used in the cavity model.

The model developed here considers the fundamental mode within the cavities and the coupling of those modes through the aperture. The thin aperture leads to efficient coupling between the two cavities and a splitting of modes at low frequencies. The low order modes of the cavities are influenced in the same manner as the fundamental mode and possess the same coupling coefficient. High frequency resonances corresponding to the higher order modes are influenced predominantly by the resonant nature of the two cavites rather than the aperture and see a cavity governed susceptance due to the higher order modes within the coupled cavity [14], [49]. If the frequency of interest is sufficient that the modal density of the cavity is high then the filter model of Chapter 4, using the generalised approach to channel modelling, will provide suitable results for the cavity channel characteristics. At low frequency the aperture properties must be taken into account and the model developed here can be used to model the lower order resonances in the cavities.

The model demonstrated applies to only a single mode in the cavities and the coupling mode between the two cavities. In practise more modes will be of interest in the same way as the filter model of Chapter 4 was used. To model more resonances a number of models of this type can be connected in parallel where each one represents a cavity mode and its coupling mode. The model can then be tuned to represent a known cavity structure or can be applied in a statistical way as before where the variables parameters are used to tune the resonances of the cavities that are coupling through the aperture.

5.2.6 Validation

The model developed in the previous section has been applied to the coupled cavity problem in Section 5.2.3 for the two slot orientations in a 21 × 21cm cavity with a 5cm slot aperture. The resonant frequencies of the individual cavities are obtained analytically using

$$f_{mnp} = c\sqrt{\left(\frac{m}{2a}\right)^2 + \left(\frac{n}{2b}\right)^2 + \left(\frac{p}{2d}\right)^2} \tag{5.2.49}$$

to give a resonant frequency of 1.0095GHz for the TE_{110} mode within the cavity. This is consistent with the full field modelling previously. The coupling coefficient is obtained using the approach described in Section 5.2.4. The expressions shown in Section 5.2.4 are used for the vertical slot and the horizontal slot is obtained using a similar approach based on the waveguide aperture approach where the aperture properties are obtained from [50]. The susceptance of the horizontal aperture is obtained in the same manner as the vertical aperture starting from the expression

$$\frac{B}{Y_0} = \frac{4a}{\lambda_g}\left[\ln\left(\frac{1}{k_\alpha}\right) + \frac{Q_2 k_\beta^4}{1+Q_2 k_\alpha^4} + \frac{1}{16}\left(\frac{a}{\lambda_g}\right)^2 \left(1-3k_\alpha^2\right)^2 k_\beta^4\right] \tag{5.2.50}$$

where

$$Q_2 = \frac{1}{\sqrt{1-\left(\frac{b}{\lambda_g}\right)^2}} - 1 \tag{5.2.51}$$

and

$$\begin{aligned} k_\alpha &= \sin\left(\tfrac{\pi d}{2a}\right) \\ k_\beta &= \cos\left(\tfrac{\pi d}{2a}\right) \end{aligned} \tag{5.2.52}$$

Using the analytical approach the coupling coeffients for a 5cm slot are $k_c = 0.030$ in the vertical slot case and $k_c = 0.093$ in the horizontal slot case. Using these parameters in the transmission line model yields the results shown in Figures 5.2.15 and 5.2.16.

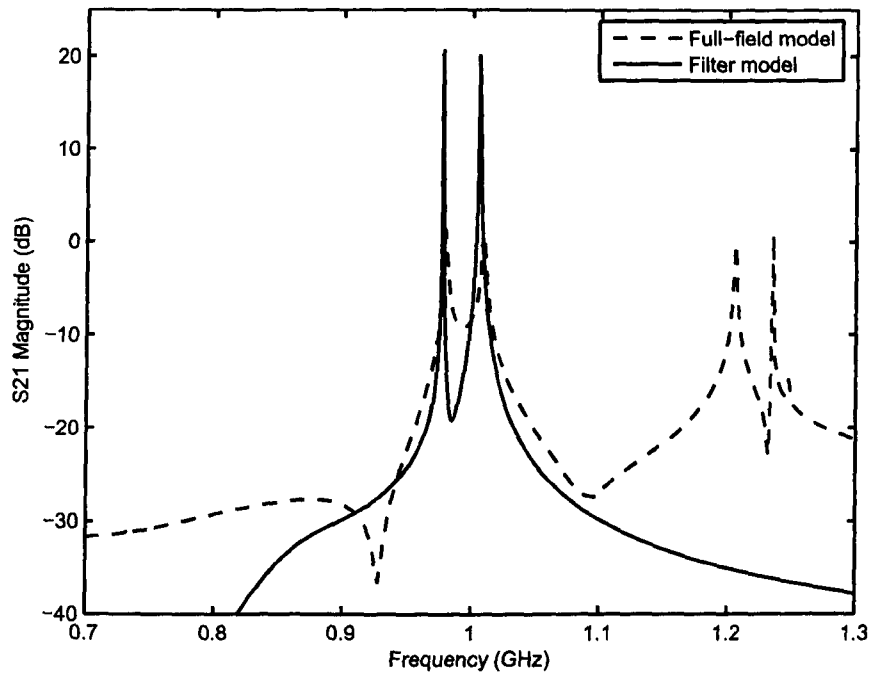

Figure 5.2.15: Cavity response due to vertical slot coupling (capacitive)

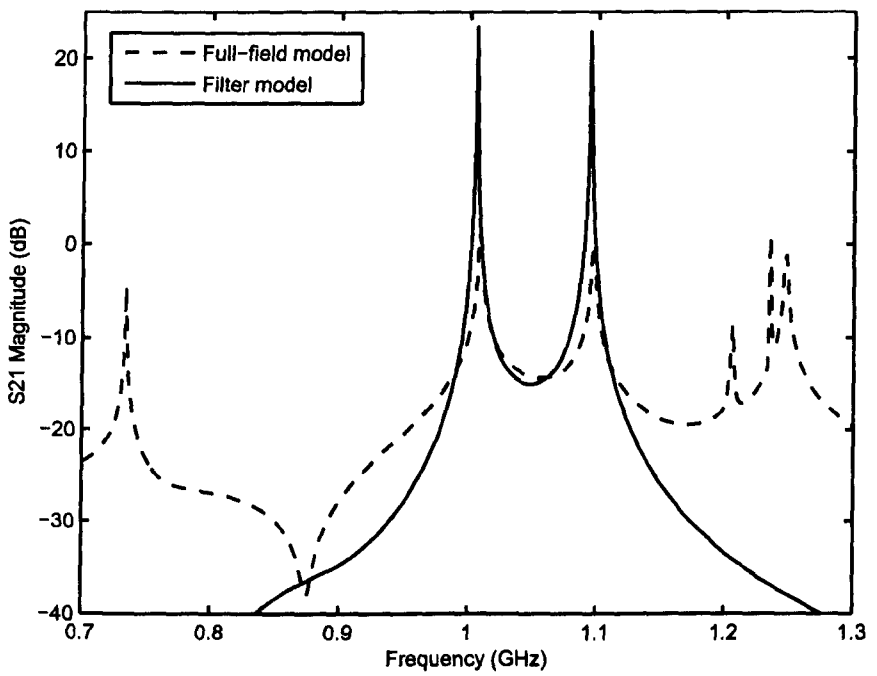

Figure 5.2.16: Cavity response due to horizontal slot coupling (inductive)

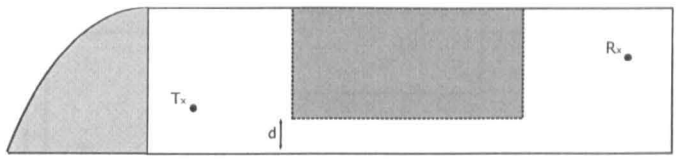

Figure 5.3.17: Possible internal layout leading to the creation of a waveguide arrangement

The results are shown with the results from a full field simulation of the same problem. Good agreement can be seen in the position of the resonant frequencies obtained however the applitude of the modes are not as accurate. The most likely cause of this difference in resonant mode amplitude is that the full field model is excited and sampled at single points and the filter model does not directly take into account the coupling efficiency of these points to each of the modes in the cavity.

5.3 Waveguide Coupled Cavities

In addition to the aperture coupled cavities described here it is possible that the aperture may have significant thickness that its cutoff properties need to be considered. An example of the arrangement of interest is where there is a transmitter and receiver in a resonant cavity within an aircraft wing. Also inside the wing there may be a fuel tank or some kind of support structure which, for a significant distance, limits the width of the transmission space. A diagram illustrating such a situation is shown in Figure 5.3.17.

In order to simplify the system a structure with equal sized cavities connected by a waveguide at their centres will be considered in this section. A schematic of the system is shown in Figure 5.3.18. The size of the cavities are $a \times a \times a$, the cross-sectional area of the waveguide is $d \times d$. In all cases it is assumed that

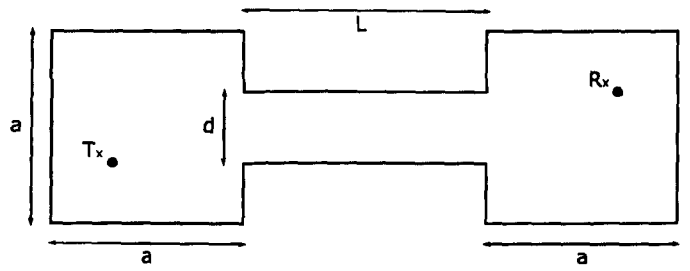

Figure 5.3.18: A simplified schematic of cavities coupled by a waveguide

the cross-sectional area of the waveguide is much smaller than that of the cavity itself. Therefore, the resonant frequencies of the cavity with wavelengths close to dimensions of the cavity will not be propagated down the waveguide. Taking the TE_{110} resonance of a 30 × 30 × 30cm cavity, for example, we find that this has a frequency given by

$$f_{mnp} = c\sqrt{\left(\frac{m}{2a}\right)^2 + \left(\frac{n}{2b}\right)^2 + \left(\frac{p}{2d}\right)^2} \tag{5.3.53}$$

and equal to 0.707GHz. In (5.3.53) a, b and d are the cavity dimensions and m, n and p are integers where not more than one integer can be zero.

For the waveguide the first propagating transverse electric mode TE_{10} has a cutoff frequency given by

$$f^c_{mnp} = c\sqrt{\left(\frac{m}{2a}\right)^2 + \left(\frac{n}{2b}\right)^2} \tag{5.3.54}$$

The cutoff frequency for this mode in a waveguide of dimensions $10 \times 10\text{cm}^2 = a/3$, for example is 1.5GHz. Therefore, the mode corresponding to the first resonance of the cavity, and any frequency up to the waveguide cut-off frequency may be attenuated by the waveguide and not reach the second cavity. The commonly used ISM frequency [32] is 2.45GHz and is much higher than the 1.5GHz cut off of this example. In this case a wireless system attempting to communicate in the channel will be able to propagate through the waveguide as this frequency

corresponds to a high density of modes in the cavity and waveguide as the density of modes is related to the square of the frequency. In this particular case the density of modes can be approximated using the expression derived in Chapter 2

$$g(f) = \frac{8\pi V f^2}{c^3} \tag{5.3.55}$$

leading to a modal density of 1.51×10^{-4} modes/Hz.

The dimension of the waveguide that will lead to the TE_{01} mode cutoff being at a frequency of 2.45GHz can be calculated using (5.3.54) to be 0.0612m $\approx$ 6cm. Should the waveguide be of a sufficient length then this value provides a lower limit for the dimensions of the waveguide in order to allow propagation into the second cavity. For a frequency below cutoff the attenuation constant of the propagating wave in the waveguide has the value

$$\alpha = k_{c,mn}\sqrt{1-\left(\frac{f}{f_{c,mn}}\right)^2} \tag{5.3.56}$$

where $k_{c,mn}$ is the cutoff wavenumber [14]. The propagating wave is then attenuated according to $e^{-\alpha z}$. Therefore, it is expected that for the structure shown in 5.3.18 the low frequency received field will be attenuated with increasing waveguide length. In order to investigate this possibility, a number of 3D full field models were constructed using the transmission line modelling technique where the length L of the waveguide was extended and the transmitted signal between the source cavity and receiver cavity was calculated. The lengths of the waveguide used were 0, 20, 40 and 60cm. The S21 response was calculated for each waveguide length and is shown in Figure 5.3.19.

The waveguide dimension in this case was $d = 10cm$ and the cavity dimensions were $a = 30cm$. The waveguide dimensions lead to a cut-off frequency of 1.5GHz. It can be seen that the received field in all cases is greatly reduced below this

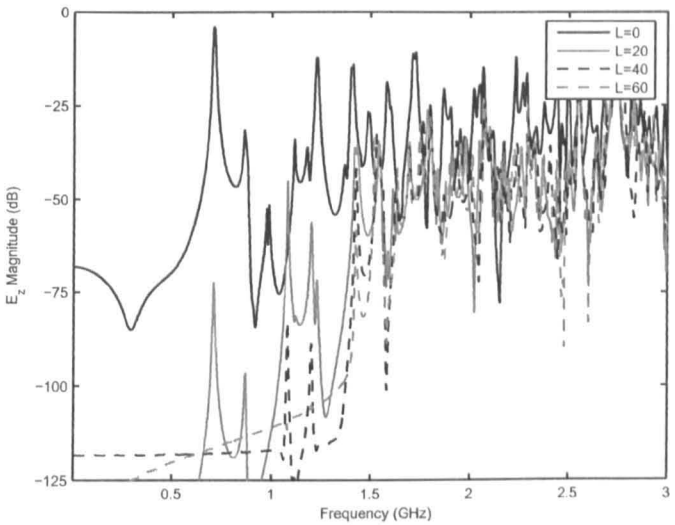

Figure 5.3.19: Received field magnitude for varied length waveguides using a 3D TLM model

frequency as the field is attenuated by the waveguide, which acts as a high-pass filter. In addition it can be seen that the length of the waveguide affects the degree of attenuation below this frequency as was predicted by (5.3.56). The attenuation below the cutoff is significant, it can be seen to be up to 50dB which, if the waveguide had dimensions close to those that would limit ZigBee frequencies, would likely make communication impossible.

The results shown show a number of resonances as would be expected. The fields of the two cavities are resonant, these are then linked by what is effectively a high-pass filter which has its own frequency response. The field in the source cavity couples to the waveguide modes as shown in [38] which are propagated down the waveguide, providing they are above cutoff. At the end of the waveguide a virtual antenna array is formed radiating power into the second cavity with the frequency content of the first cavity and waveguide. This leads to the resonant and attenuated responses shown in Figure 5.3.19. In situations where the frequency of the wireless system is below that of the cut off frequency of the waveguide coupling

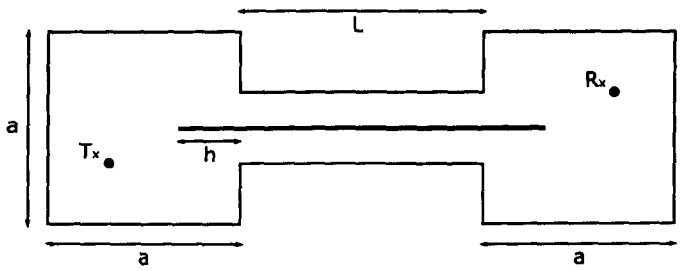

Figure 5.3.20: Cavities coupled by a waveguide with a line inside the waveguide

will be poor. In such a case it is desirable to increase the coupling between the two cavities so that wireless communication can take place. In order to remove the cut off properties of the waveguide it is possible to insert a thin wire down the centre of the waveguide to form a coaxial structure. This will then allow a TEM mode to propagate down the waveguide and not be cut off.

5.3.1 Waveguide Containing a Wire

If the waveguide coupling two cavities has a small cross-section the coupling into the second cavity will be poor. To overcome this problem a conducting line can be passed through the centre of the waveguide as shown in Figure 5.3.20.

The motivation for this is that the waveguide and conducting line form a coaxial transmission line which does not act as a high pass filter in the way the waveguide does. The coaxial transmission line created will propagate energy as a TEM mode and the end of the line will act as a monopole radiator or receiver [14]. The use of what is effectively a wire in a wireless communication system seems somewhat counterintuitive. However, any metal structure that may already be present in the environment would create such an arrangement. This may include an alternative wired system or pipework for example.

To investigate whether the inclusion of an extra line within the waveguide provides the necessary coupling a number of tests have been performed. As the extension of the line into the cavities acts as monopole radiator, the length h in 5.3.20 is likely to affect the coupling efficiency.

In each case the length of the line is modified in both the transmitter and receiver cavities. The parameters for the investigation are as in the previous section, the protruding line lengths used are 6cm 10cm and 14cm where 14cm corresponds to the $\lambda/4$ monopole antenna length for the TE_{110} resonant cavity mode. The transmitted responses are shown in Figures 5.3.21 and 5.3.22 for each line length. In addition the response is shown for the system without the extra line for reference. The results show the effect of varying the length of the antenna on the transmission behaviour.

These results show that frequencies below the cutoff of the waveguide, which were shown not to propagate before, now do propagate down the waveguide structure. The line provides a coaxial transmission line structure allowing the transmission of a signal through the waveguide that would not normally be possible. The problem is reduced to that of the basic aperture coupled problem through the inclusion of the wire as the waveguide no longer attenuates the wireless signal.

Furthermore, the results of Figures 5.3.21 and 5.3.22 show that the length of the wire protruding into the cavity does not have a significant effect on the transmitted power. The most likely reason for this is that the resonant nature of the cavity coupling to the waveguide means that the wave propagates enough into the waveguide that it is able to couple to the wire in an efficient manner. This is similar to the effect seen for the aperture coupled cavities as the cutoff mode propagates into the second cavity and excites resonance therein.

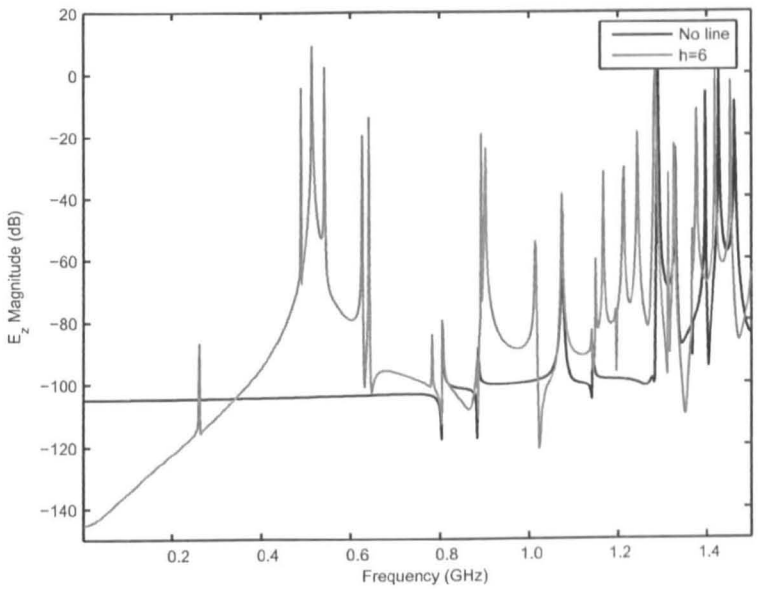

Figure 5.3.21: Received field magnitude using an additional line within the waveguide

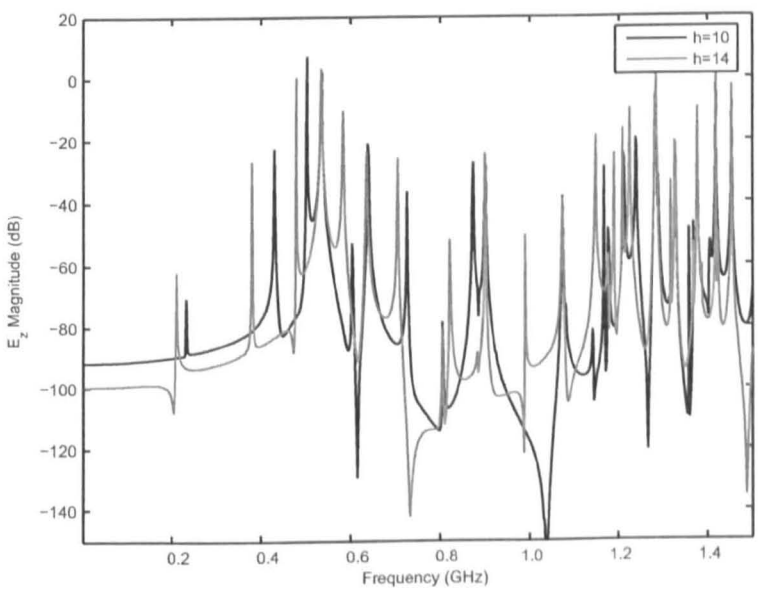

Figure 5.3.22: Received field magnitude using an additional line within the waveguide

The line itself causes more resonances to appear in the received spectrum. Notably, there are resonances close to 0.2GHz for each of the cases where the line is present. It can be seen that these vary with the length of the line and it has been found that they correspond to standing waves on the transmission lines. Further resonances also appear at high frequencies due to higher order modes on the line although these are insignificicant as the cavities contain a significnat number more modes.

Chapter 6

Dynamic Models of Cavities

In previous chapters, suitable computationally efficient models have been developed to represent highly resonant multipath environments. This chapter investigates resonant cavities whose structure is time-varying, or dynamic, due to low frequency structural vibrations or flexing. The physics of such a cavity is of interest as one might consider an aircraft where the engines, normally contained within nacelles fixed to the wings, may induce vibrations in the panels of the aircraft with frequencies of the order of kHz.

Considering the ZigBee specification, the bandwidth of the transmitted signal is 5MHz so there is a possibility that the vibrations in the panels of the aircraft may effect the signal transmission as the vibrations exist within the bandwidth of Zigbee. Although the carrier frequency is far greater than the frequency of vibration the information is contained within a bandwidth that is directly influenced by the physical size of the resonant cavity.

In order to investigate the effect of these cavity wall vibrations the time vary-

ing effects of vibrations and flexing must be somehow included in a model of a resonant cavity. Previous chapters have explored asymptotic models of cavities where the problem space is reduced to only the physical parameters that will affect wireless communications within the cavity, that is the effect of mode density, mode splitting, and mode bandwidth or Q-factor.

The effect of cavity variations on wireless propagation is not well understood. Perturbation theory could be used for simple problems where variations in the cavity structure are added as a small perturbation to a known analytical solution. Such an approach is suitable for simple problems but is not a robust or general approach. In the case of a complex cavity problem it is often not possible to obtain an analytical solution or predict how a perturbation will effect the solution.

Full-field models that solve Maxwell's equations directly, though considered inefficient, capture all of the electromagnetic physics of the problem, provided sufficient regard is given to the discretisation being used. In order to investigate the properties of a dynamic environment this chapter develops an approach to augment a full field TLM model so that dynamic systems can be efficiently modelled.

6.1 Requirements

The Transmission Line Modelling method, or Matrix method, (TLM) in its simplest and most efficient form requires space to be discretised into uniform discrete cells with equal size. Furthermore, the time step is chosen to allow synchronisation throughout the mesh where pulses propagate at the speed of light. The electromagnetic properties of individual cells can be modified to allow modelling of a multitude of materials, including dielectrics, metals and frequency dependent materials. Perfectly conducting, resistive or frequency dependent boundaries are

normally positioned at the edge of cells within the mesh and as a result their positioning is limited by the mesh spacing chosen.

Full field models are not ideal for modelling communications due to the differences in the time scales being considered. In the case of ZigBee we observe a carrier wave period of $0.416ns$ and a bit period of $1\mu s$ and therefore we require the most efficient model possible as sampling of the carrier with a time step of $\Delta t = \lambda/10$ requires a total of approximately 24,000 timesteps per bit. In order to implement such a scheme the goal is to produce a model that consists of efficient structured cells with boundaries positioned at their true position without the need for fine meshes throughout.

In order to model structural features that do not coincide with the chosen mesh, it is required that the boundaries are positioned at non-integer space steps whilst not adjusting the structure of the rest of the mesh. Due to the finite resolution $\Delta\ell$ of the mesh there are a number of less than satisfactory options available to the modeller.

- The modelled boundary can be positioned at the closest node to its actual position. This is not ideal as the position of the boundary could be up to $0.5\Delta\ell$ in error, which also leads to coarse staircasing errors.
- The resolution of the mesh can be increased to accommodate the boundary which, as discussed, is not acceptable as it leads to a large increase in the required computational overheads and time.
- A multigrid mesh could be used where the space step, Δl, is reduced where required. However, a small timestep and stubs in the main region of the simulation would be required. These stubs are not ideal as they reduce the timestep that can be used and lead to dispersion in the mesh and, therefore,

must be handled carefully [13].

Another goal is that a model that is capable of modelling a dynamic, time-varying, environment is required and that it must be possible to move specific features within the mesh. The positioning of a boundary followed by running a simulation is a trivial task, but the movement of a boundary during a numerical simulation is much more challenging. There are a number of factors that must be considered when attempting this:

- The model must conserve energy as the boundary is moved
- Small boundary movements ($< \Delta l$) must be modelled in the discrete mesh
- Ideally we would like to maintain a large mesh spacing to minimise the computational overhead

These constraints limit the way in which the boundary can be moved in the model. The simplest way to change a boundary position would be to adjust the number of cells in the model mesh as the simulation proceeds. However, in order to model small movements in a regular mesh a very small mesh spacing would be required which is not ideal. Most importantly, energy conservation would be difficult if the grid is increased or decreased by one cell. For a one cell increase the field values in the new cell must be calculated in some way. Equally it would be difficult to determine what to do with the field values if the mesh is reduced by one cell.

Taking these requirements and limitations into consideration the following sections explore some existing techniques for modelling such a system and develop a novel and efficient modelling technique that fulfils the aforementioned requirements.

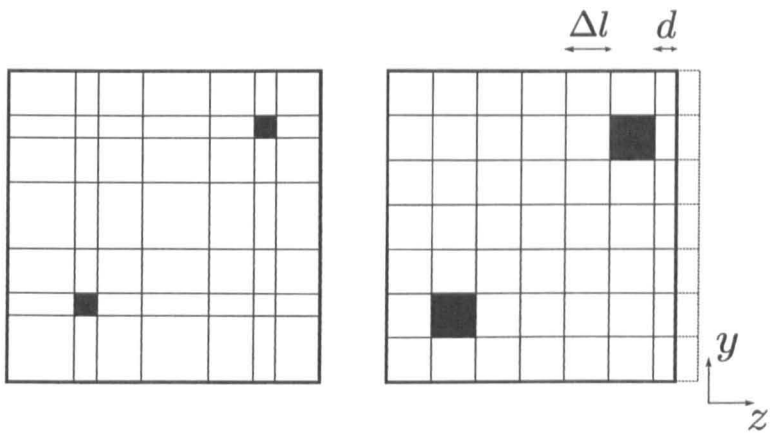

Figure 6.2.1: A graded mesh (left) and grading close to the external boundary (right)

6.2 Existing Approaches

There are a number of existing approaches to boundary placement within structured grids. However, these approaches suffer from a number of limitations that make them unsuitable for application to the problems being modelled here. This section describes the principles of the existing models and their limitations prior to a novel fractional boundary placement model being derived.

6.2.1 Graded Mesh

A well known solution to the requirement for localised detail within a structured mesh is the variable, or graded, mesh. The graded mesh allows the modeller to explicitly model small features in a coarse mesh by locally reducing the mesh spacing in one or more dimensions. An example of such a mesh is shown in Figure 6.2.1

This approach allows the mesh to be distributed so that the cell edges coincide with the features being modelled. It can be seen that synchronisation of the mesh

requires that the neighbouring cell must have the same edge length as the cell it connects to. The consequence of this restriction is that a 3D mesh is graded in planes as shown.

It is a requirement here that the model developed should be able to perform comparable conformality at the external boundaries, and possibly internal boundaries, where the grading can be varied dynamically. It is only the boundaries that are time varying in position and the rest of the mesh must be kept the same throughout the model.

Considered here are cases such as that shown in Figure 6.2.1 where it is desirable to keep the *internal* mesh constant whilst only varying the boundary cells. An approach of this type can be implemented using a graded mesh, however the grading of the structured mesh introduces an undesirable limitation on the simulation time step. Other published works are based on what is termed the *tensor node* [51] which, although being a more efficient algorithm, suffers the same limitation as the graded mesh.

The limitation of the graded mesh approach can be demonstrated using the example shown in Figure 6.2.1. It is required that the region of the mesh adjacent to the boundary has a thickness of d in the z direction where $d << \Delta l$. The remainder of the mesh is modelled using a regular structured symmetrically condensed node (SCN) grid, as in this region the structure remains static throughout the simulation. This structured region has a transmission line impedance of

$$Z_0 = \eta_0 = \sqrt{\frac{\mu_0}{\varepsilon_0}} \tag{6.2.1}$$

The region of space modelled adjacent to the boundary has a z-directed capac-

itance associated with it of

$$C_z = \frac{\varepsilon_0 \Delta l \Delta l}{d} \tag{6.2.2}$$

which must be modelled by the modified cell.

The SCN cell already has a capacitance associated with it in this direction due to the four associated link lines equal to

$$C_{SCN} = 4C_{link} = \frac{2\Delta t}{Z_0} \tag{6.2.3}$$

We therefore introduce a stub capacitance C_z^s [13] to model the missing capacitance of the SCN cell so that the total required capacitance (6.2.2) is modelled, where

$$C_z = C_{SCN} + C_z^s \tag{6.2.4}$$

Represented as a characteristic admittance, the stub capacitance is given in the typical form

$$Y_z = \frac{2C_z^s}{\Delta t} = 2\frac{\varepsilon_0 \Delta l \Delta l}{d\Delta t} - \frac{4}{Z_0} \tag{6.2.5}$$

Normalising the expression with respect to free space, as is customary [13]

$$\widehat{Y_z} = Y_z Z_0 = \frac{2}{c\Delta t}\frac{\Delta l^2}{d} - 4 \tag{6.2.6}$$

Following the same procedure for the other two dimensions, where

$$C_x = C_y = \frac{\varepsilon_0 \Delta l d}{\Delta l}, \tag{6.2.7}$$

equivalent expressions for the stub admittance can be obtained

$$\widehat{Y_x} = \widehat{Y_y} = \frac{2}{c\Delta t}d - 4 \tag{6.2.8}$$

Further expressions can be obtained for the stub impedances to model the correct cell inductance in the same way as described here.

The limitation of the graded mesh approach to a fractional boundary placement model is apparent in (6.2.6) and (6.2.8). The admittance of the stub must be positive to maintain stability and physical meaning. In order to ensure this criteria is satisfied the inequalities

$$\frac{2}{c\Delta t}\frac{\Delta l^2}{d} \geq 4 \tag{6.2.9}$$

and

$$\frac{2}{c\Delta t}d \geq 4 \tag{6.2.10}$$

must be satisfied for the three dimensions.

It can be seen that in the limit $d \rightarrow \Delta l$ both equations reduce to being equal where the maximum TLM timestep is being used

$$\Delta t = \frac{\Delta l}{2c} \tag{6.2.11}$$

That is, the case where the cell is equivalent to the unmodified SCN and requires no modification.

However, in the limit that $d \rightarrow 0$ the left hand side of (6.2.10) tends to zero and the timestep, to satisfy the inequality, must also tend to zero. In fact, in the limit of $d = 0$, the simulation must be infinitely long to model any physical time period at all. Therefore, in order to compensate for reducing d, the timestep used in the simulation must be reduced where it must be ensured that, from (6.2.10),

$$\Delta t \leq \frac{d}{2c} \tag{6.2.12}$$

A reduction in the time step throughout the mesh leads to much longer runtime and requires stubs to be introduced throughout the mesh. In addition, if the boundary extension is applied by making the boundary cells larger so that they are $\Delta l + d$ in length then stubs must also be added to the bulk mesh to maintain mesh synchronisation. The introduction of stubs increases dispersion errors in the model [13]. It is clear that neither of these two outcomes are desirable and considerably affect the displacement range, d, that can be realistically and practically modelled using the graded mesh boundary. For the reasons outlined above it can be seen that the graded mesh model would be limited and inefficient for modelling the systems of interest here and another model must be sought.

6.2.2 Stub Model

In order to avoid the problems associated with the graded mesh model there has been previous work based on a specific boundary model, not based on the SCN. The approach described here uses inductive stubs to model an arbitrarily placed perfect electric conductor (PEC) boundary. Such techniques can be found in references [52, 53] and the references listed therein. This section describes a method based on this approach and shows the limitations of the method under certain critical conditions.

It has been demonstrated that in order to model delays in a structured TLM mesh the speed of propagation can be changed within the cell through the use of inductive and capacitive stubs. Equivalences between the Telegrapher's and Maxwell's equations show that an inductive stub can be modelled by a short circuited transmission line. This section describes the simple inductive stub model which can be used to greater effect for simple 1D problems. It will be shown that its application to higher dimension problems is not straight forward and leads to

numerical errors.

The conventional inductive stub boundary for modelling fractional boundary placements proceeds by modelling a cell of length $\Delta\ell + d$ by a normal TLM cell of length $\Delta\ell$ and an additional segment of length d, as indicated in Figure 6.2.2. To maintain synchronism in the scattering and connection processes, the round trip time of the additional segment must be equal to the computational time step, Δt, of the mesh.

The normalised input reactance of a transmission line of length d terminated by an electric boundary is given by [52, 53]

$$Z_i = Z_0 \tanh\left(\frac{j\omega d}{c}\right) \tag{6.2.13}$$

where, for a one dimensional (1D) TLM model, the transmission line impedance is equal to the free space impedance $Z_0 = \eta_0$. Providing the transmission line extension is much less than the wavelength of interest, which is assumed true as $d < \Delta\ell \ll \lambda_{min}$, the approximation $\tanh(x) \approx x$ for $x \ll 1$ can be used, so that

$$Z_i = Z_0\left(\frac{j\omega d}{c}\right) = j\omega L \tag{6.2.14}$$

where

$$L = \frac{Z_0 d}{c} = \mu_0 d \tag{6.2.15}$$

In (6.2.15) μ_0 is the permeability of free space. The boundary extension can therefore be modelled as shown in Figure 6.2.2 by an inductive transmission line stub with characteristic impedance

$$Z_L = \frac{2L}{\Delta t} = 2\eta_0\left(\frac{d}{\Delta\ell}\right) \tag{6.2.16}$$

where for a 1D TLM model $\Delta\ell/\Delta t = c$.

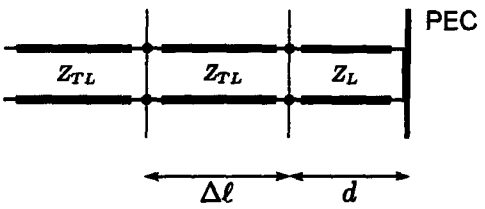

Figure 6.2.2: 1D inductive stub model

This model can be used to extend the boundary of a two dimensional (2D) and three dimensional (3D) mesh where the stub is attached to the appropriate ports of the boundary node [53]. The transmission line impedance of the stub in each case is

$$Z_{L(2D)} = 2\sqrt{2}\eta_0 \left(\frac{d}{\Delta\ell}\right), \quad Z_{L(3D)} = 4\eta_0 \left(\frac{d}{\Delta\ell}\right) \tag{6.2.17}$$

where for the 2D case $\Delta\ell/\Delta t = \sqrt{2}c$ and for the 3D case $\Delta\ell/\Delta t = 2c$. An equivalent model can be created using a capacitive stub to represent a magnetic boundary, and a general boundary can be modelled using a resistor and inductor or capacitor combination. It can be shown that the boundary extension produced using this technique is very accurate when considering normal incidence on the boundary.

The additional length added to the line should cause a reflected pulse to be time delayed by an amount dependent on the extension added to a 1D transmission line. Figure 6.2.3 shows the incident and reflected pulses from the boundary with varying extensions produced using the inductive stub. The delays are shown for extensions up to Δl. The figure also shows the delay when an additional TLM cell is added to the transmission line (dotted).

It can be seen that the delay produced by the $d = \Delta l$ stub agrees well with the result for an additional cell. The extensions of $d < \Delta l$ also show the expected delay in the reflected pulse, increasing with increasing d. There is only a very small error in the resulting delay, this is likely due to the stray capacitance error in the

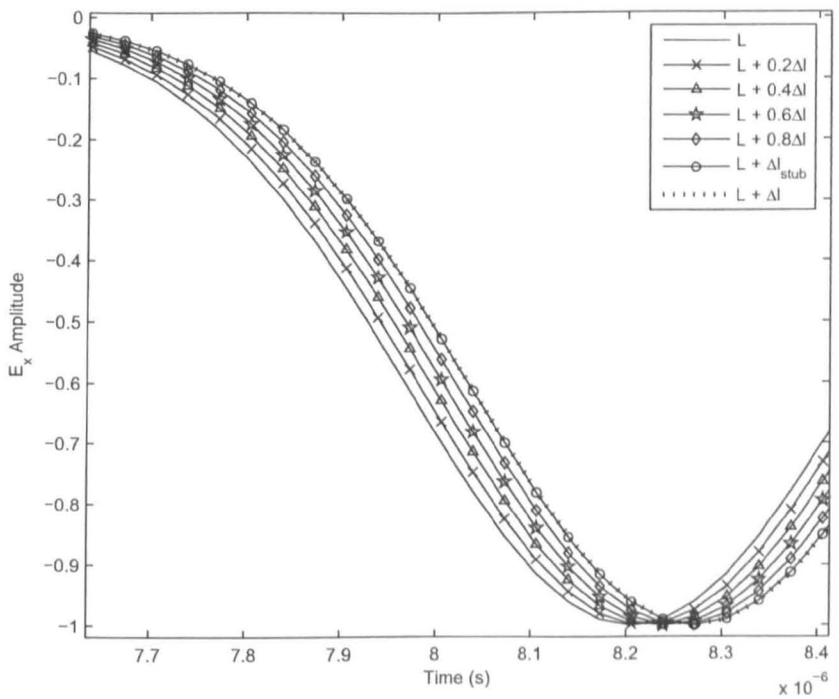

Figure 6.2.3: Reflected pulse from a boundary with varying displacement in a 1D model

inductive stub.

The model described in [52] and [53] can be used to accurately simulate a metal cavity with boundaries positioned at non-integer space steps provided; (a) the field of interest is polarised normal to the modified boundary or (b) the dimension of the cavity to be modified is long compared with the other two dimensions. However, the model becomes very limited if we are to apply it to the kind of problems in this thesis as demonstrated here.

The response of a $20 \times 20 \times 21$ m metal cavity to a pulse excitation is shown in Figure 6.2.4 where the E_z field is excited and measured. The results shown were obtained using a space step of $\Delta\ell = 1$ m, the maximum time step for the 3D model and a Gaussian excitation with a half width of $\sigma = 50\Delta t$ and a delay of $150\Delta t$ from $t = 0$. The result shown was obtained for an inductive stub boundary extension used to extend the cavity in the z-dimension from 20 to 21 m by adding to the Z_{max} boundary, so that $d = \Delta\ell$. Also shown is the response obtained by adding a normal TLM cell to the Z_{max} boundary. Electric boundary conditions are imposed on all boundaries. This particular example was chosen as it violates the two conditions outlined above in order to demonstrate the failure of the inductive stub model.

It can be seen in Figure 6.2.4 that the stub model response shows a non-physical resonance at ≈ 12.36 MHz which is not present using a normal TLM node, nor is it an analytically predicted resonance. This result is for the maximum boundary extension the modeller would wish to use and the displacement of this peak from 12.78 MHz reduces with decreasing boundary extension. Nonetheless, the peak is present for all boundary extensions which would lead to erroneous results.

Further non-physical peaks are present in the response and they increase in

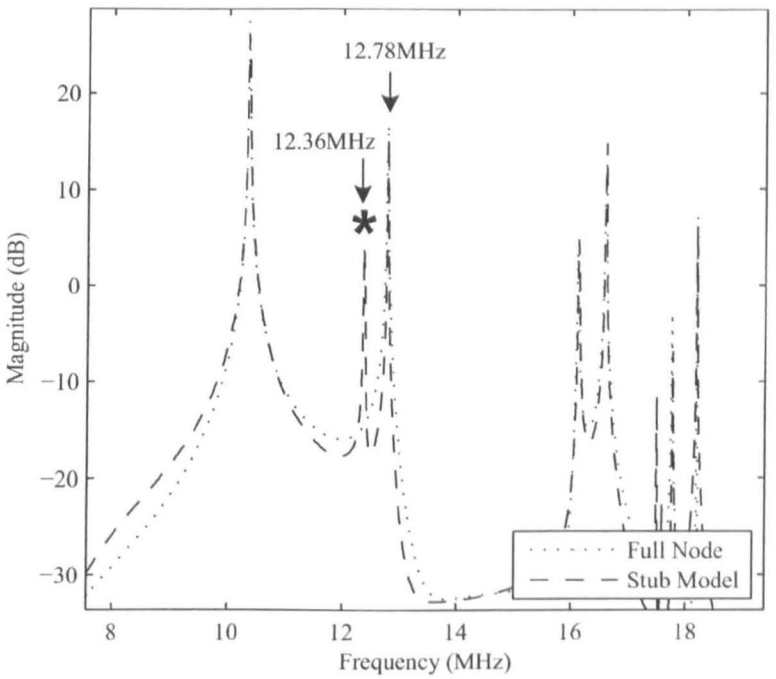

Figure 6.2.4: E_x field response of a $20 \times 20 \times 21$ m cavity. The spurious resonance is indicated with $*$

number with increasing modal density at higher frequencies. Similar results for the other wave polarisations reveal multiple non-physical resonances with varying degrees of magnitude and will have a significant impact on predictions as the model produces modes which do not exist in reality. The undesired effect of this boundary is to increase the density of modes in the cavity, the increase with density of modes increases further as frequency increases. In the overmoded cavities of interest this will have a significant effect on the results obtained for error rate analysis. It will be shown in Chapter 7 that the density of modes directly effects the error rates if a wireless system is used in the resonant environment and this model would not be suitable for wireless propagation studies.

The errors in the boundary can be theorised to occur due to the loss of directionality at the boundary. A horizontally polarised wave incident normal to the boundary will be reflected from it in the usual way. A wave incident at an angle

to the boundary region is transferred to a 1D domain within the boundary region and loss of propagation information occurs. The component which was parrallel to the boundary is no longer modelled. The result is that we lose information relating to the magnetic field parallel to the boundary.

The limiting case is a wave propagating parallel to the boundary. As stubs are used to extend the boundary there is no direct communication modelled between the stubs in adjacent nodes, so in order to propagate along the boundary the wave must pass in a zig-zag path through the ordinary nodes of the mesh. The result is that the wave velocity parallel to the boundary is less than the speed of light. This effect and the errors described in the previous section are estimated below.

The propagation velocity along a boundary extension d from the bulk mesh, where the boundary is modelled using the inductive stub to extend fractionally the boundary of a 2D mesh, is u_b. The 2D series TLM node is shown in Figure 6.3.5. The capacitance seen by the electric field in the 2D series node is

$$C_d = \varepsilon_0 \Delta\ell \tag{6.2.18}$$

where ε_0 is the permittivity of free space. The current loop at the node centre sees an inductance from each of the vertically and horizontally directed lines equal to

$$L_d = \mu_0 \Delta\ell/2 \tag{6.2.19}$$

The stub added to one of the transmission line ports effectively adds an inductance equal to (6.2.15) so that the total modelled inductance is

$$L_{d(tot)} = \frac{\mu_0 \Delta\ell}{2} + \frac{\mu_0 \Delta\ell}{2} + \mu_0 d = \mu_0 \Delta\ell \left(1 + \frac{d}{\Delta\ell}\right) \tag{6.2.20}$$

Therefore, the propagation velocity along the boundary is

$$u_b = \frac{\Delta\ell}{\sqrt{L_{d(tot)}C_d}} = \frac{c}{\sqrt{1+\frac{d}{\Delta\ell}}} \tag{6.2.21}$$

Equation (6.2.21) shows that u_b is a function of d and the larger the boundary extension the lower the velocity of propagation along the boundary. Ideally, propagation velocity should be independent of d to ensure that a wave always propagates at the speed of light along the boundary. In order to correctly model the fractionally positioned boundary the communication between boundary stubs must be included in the model.

6.3 New Boundary Development

In order to model the connection between the boundary nodes the boundary can be considered to be a regular wire lattice as opposed to a solid metallic structure. This wire mesh can in turn be modelled using a transmission line model where the free space solution couples to the wire mesh boundary. The properties of the free space region between the edge of the main mesh and the boundary mesh can then be modelled through the wire mesh properties and the coupling parameters.

6.3.1 2D model

The boundary model is developed in 2D through the model shown in Figure 6.3.6. The standard modelling procedure using series nodes can be found in [13], [39] or [40] so will not be discussed here. The transmission line impedance of a 2D series

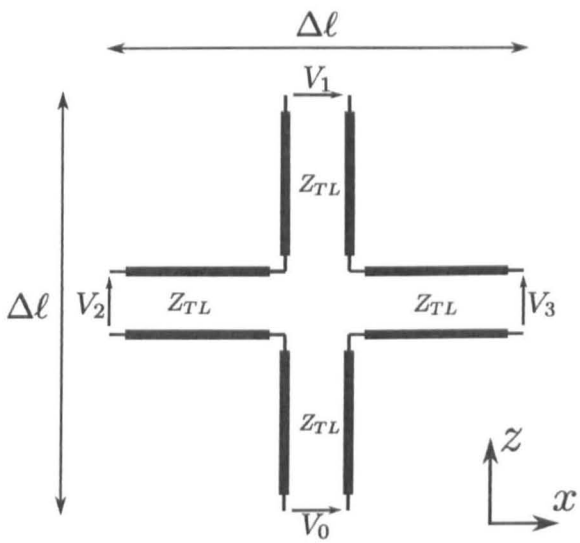

Figure 6.3.5: 2D series TLM node

TLM node is

$$Z_{TL} = \frac{\eta_0}{\sqrt{2}} \tag{6.3.22}$$

and the velocity of propagation is

$$\frac{\Delta\ell}{\Delta t} = \sqrt{2}c \tag{6.3.23}$$

It can be seen that in a 2D mesh the boundary is modelled as a 1D line running the length of the boundary, Figure 6.3.6b. The field node and the line boundary model are coupled through V_0. The properties of the PEC boundary are implicitly contained in the parameters of the line and there is no need to modify TLM nodes terminated with a fractionally placed boundary. The properties of the line representing the boundary are chosen to obtain the correct propagation velocity normal and parallel to the boundary.

Initially the case for a 2D series mesh terminated by a fractionally placed PEC boundary will be developed. The series mesh is assumed to be in the x-z plane, so that it models the E_x, E_z and H_y fields. The mesh is terminated by an x-directed

boundary corresponding to $z = Z_{min}$ and $x = 0$ to $x = X_{max}$. The Telegrapher's equations describing the x-directed line are

$$-\Delta x \frac{\partial V_b}{\partial x} = L \frac{\partial I_{bx}}{\partial t} - V_0 \tag{6.3.24}$$

$$-\Delta x \frac{\partial I_{bx}}{\partial x} = C \frac{\partial V_b}{\partial t} \tag{6.3.25}$$

The voltage representing the field coupling into the boundary is represented by V_0 in (6.3.24). The capacitance and inductance of the line is chosen so that it models the boundary and the extension d to the regular Cartesian field mesh. The region of free space with dimensions $\Delta\ell \times \Delta\ell \times d$ to be modelled by the line is shown in Figure 6.3.6a. The capacitance and inductance of this region are given by

$$C = \frac{\varepsilon_0 (\Delta\ell)^2}{d} \tag{6.3.26}$$

$$L = \frac{\mu_0 \Delta\ell\, d}{\Delta\ell} = \mu_0 d \tag{6.3.27}$$

The per-unit length capacitance and inductance modelled by the boundary wire are given by

$$C_b = \frac{C}{\Delta\ell} \tag{6.3.28}$$

$$L_b = \frac{L}{\Delta\ell} \tag{6.3.29}$$

The characteristic impedance of the volume of space and hence the impedance to be modelled by the line is

$$Z_b = \sqrt{L_b / C_b} = \eta_0 \left(\frac{d}{\Delta\ell} \right) \tag{6.3.30}$$

The velocity of propagation parallel to the boundary is

$$u = \frac{\Delta\ell}{\sqrt{LC}} \tag{6.3.31}$$

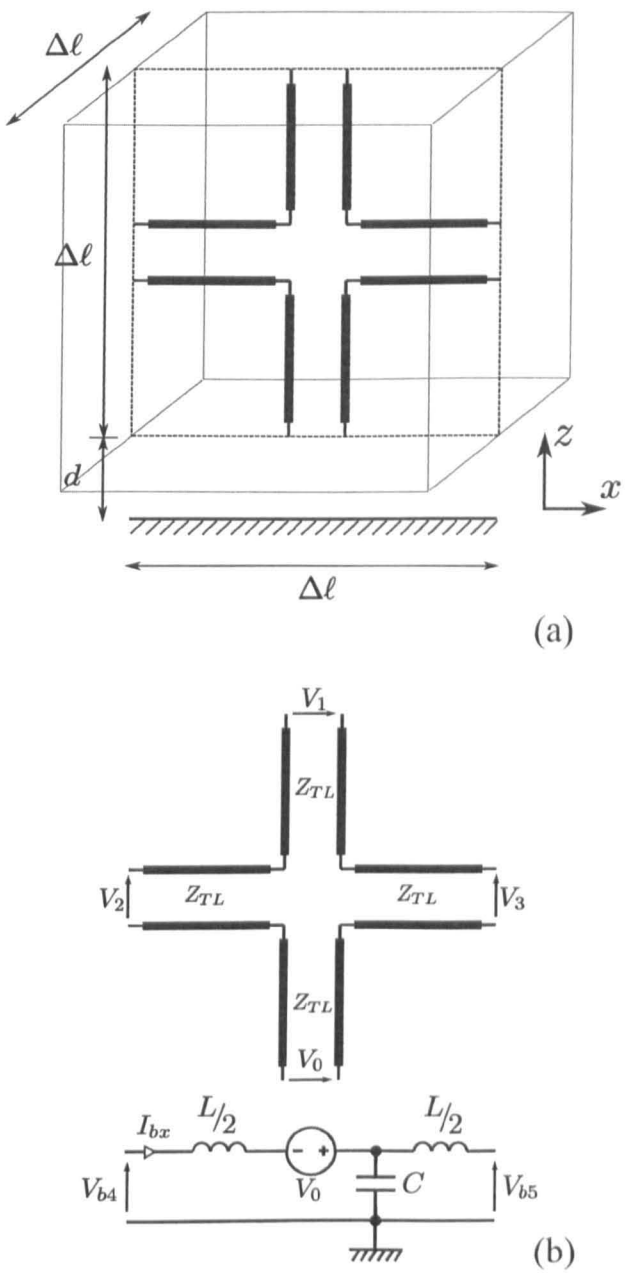

Figure 6.3.6: Fractional boundary placement in 2D, (a) schematic, (b) TLM model

It can be seen from (6.3.23) and (6.3.31) that the velocity of propagation in the line is not the same as that in the bulk mesh. The speed of propagation in the line is to be adjusted using stubs. The calculation of the stub impedances and the derivation of the TLM equivalent circuit model proceed as follows.

The boundary current is normalised [40] with respect to the boundary impedance using

$$I_{bx} = {}^{i_{bx}}/_{Z_b} \tag{6.3.32}$$

where the normalised current i_{bx} has the units of Volts. The temporal and spatial derivatives are normalised with respect to the space step and time step using

$$\frac{\partial}{\partial x} = \left(\frac{1}{\Delta \ell}\right)\frac{\partial}{\partial X}, \quad \frac{\partial}{\partial t} = \left(\frac{1}{\Delta t}\right)\frac{\partial}{\partial T}. \tag{6.3.33}$$

Normalising (6.3.24) and (6.3.25) using (6.3.32) and substituting (6.3.23), (6.3.28), (6.3.29) and (6.3.30) yields the normalised Telegrapher's equations

$$-\frac{\partial V_b}{\partial X} = \sqrt{2}\frac{\partial i_{bx}}{\partial T} - V_0 \tag{6.3.34}$$

$$-\frac{\partial i_{bx}}{\partial X} = \sqrt{2}\frac{\partial V_b}{\partial T} \tag{6.3.35}$$

These expressions are converted to a travelling wave format [54], [55] using

$$-\frac{\partial V_b}{\partial X} - \frac{\partial i_{bx}}{\partial T} = 2V_{b4}^i - 2V_{b5}^i - 2i_{bx} \tag{6.3.36}$$

$$-\frac{\partial i_{bx}}{\partial X} - \frac{\partial V_b}{\partial T} = 2V_{b4}^i + 2V_{b5}^i - 2V_b \tag{6.3.37}$$

where V_{b4}^i and V_{b5}^i are the incident voltage pulses from the left and right of the line segment in Figure 6.3.6b. The remaining differential voltage and current terms are converted to a stub format [54] as shown in Appendix C.1 to give

$$\left(\sqrt{2}-1\right)\frac{\partial i_{bx}}{\partial T} = 2V_{bLx}^i + 2\left(\sqrt{2}-1\right)i_{bx} \tag{6.3.38}$$

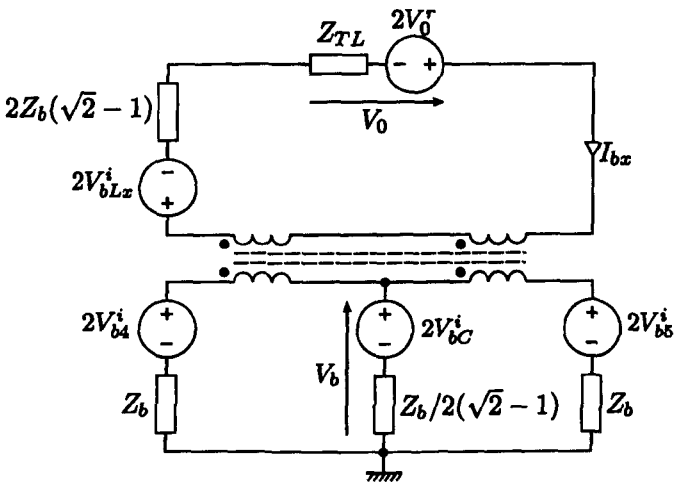

Figure 6.3.7: TLM equivalent circuit for fractional boundary placement in 2D

$$\left(\sqrt{2}-1\right)\frac{\partial V_b}{\partial T} = 2\left(\sqrt{2}-1\right)V_b - 4\left(\sqrt{2}-1\right)V_{bC}^i \tag{6.3.39}$$

The voltages V_{bLx}^i and V_{bC}^i are the incident voltages on the inductive and capacitive stubs respectively.

Substituting (6.3.36)-(6.3.39) into (6.3.34) and (6.3.35) yields the normalised boundary voltage and current

$$i_{bx} = \frac{2V_{b4}^i - 2V_{b5}^i - 2V_{bLx}^i + V_0}{2\sqrt{2}} \tag{6.3.40}$$

$$V_b = \frac{2V_{b4}^i + 2V_{b5}^i + 4(\sqrt{2}-1)V_{bC}^i}{2\sqrt{2}}. \tag{6.3.41}$$

Equations (6.3.40) and (6.3.41) can be interpreted as the circuit representation of the magnetic and electric field in the boundary region and the surface current on the boundary is implicitly included in the boundary model. These expressions can be used to construct the TLM equivalent circuit shown in Figure 6.3.7 where the coupling transformers are ideal with a 1:1 turns ratio.

In (6.3.40) the voltage V_0 is obtained from the reflected voltage of the neigh-

bouring 2D series node as shown in Figure 6.3.5 and is given by

$$V_0 = 2V_0^r - i_{bx}y_0 \tag{6.3.42}$$

where y_0 is the normalised boundary admittance

$$y_0 = Z_{TL}/Z_b \tag{6.3.43}$$

The incident voltage on the inductive and capacitive stubs are obtained in the usual way, so that

$${}_{k+1}V_{bLx}^i = -{}_kV_{bLx}^r = -\left({}_kV_{bLx}^i + 2\left(\sqrt{2}-1\right){}_ki_{bx}\right) \tag{6.3.44}$$

$${}_{k+1}V_{bC}^i = {}_kV_{bC}^r = {}_kV_b - {}_kV_{bC}^i \tag{6.3.45}$$

where k is the iteration index.

The reflected boundary voltages in the $+x$ and $-x$ directions are given by

$$V_{b4}^r = V_b - i_{bx} - V_{b5}^i \tag{6.3.46}$$

$$V_{b5}^r = V_b + i_{bx} - V_{b4}^i \tag{6.3.47}$$

The incident voltage on the 2D series node adjacent to the boundary is calculated using

$${}_{k+1}V_0^i = {}_kV_0^r - {}_ki_{bx}y_0 \tag{6.3.48}$$

If the model is used to replace the final node at the end of a boundary V_{b4}^i and V_{b5}^i are replaced with PEC boundaries so that the modelled boundary reduces to

only the inductive stub with impedance

$$Z = 2(\sqrt{2}-1)Z_b + 2Z_b = 2\sqrt{2}\eta_0\left(\frac{d}{\Delta\ell}\right) \tag{6.3.49}$$

which can be seen to be identical to (6.2.17) for the stub model discussed in Section 6.2.2.

6.3.1.1 Connection

The connection of the boundary ports V_{b4} and V_{b5} for a fixed boundary thickness is performed by passing voltages between the adjacent nodes. However, the boundary model developed here enables the boundary displacement to vary with position so that the boundary impedance becomes dependent on the node being considered $Z_b \Rightarrow Z_b(n)$. Therefore, the connection process is modified to account for this possibility.

The total voltage at the connection of the nodes n and $n+1$ is given by

$$V_{b4,5} = \frac{2V_{b5}^r(n)Z_b(n+1) + 2V_{b4}^r(n+1)Z_b(n)}{Z_b(n+1) + Z_b(n)} \tag{6.3.50}$$

The voltages incident on the ports of nodes n and $n+1$ at the next time step are subsequently calculated using

$$_{k+1}V_{b5}^i(n) = {}_kV_{b4,5} - {}_kV_{b5}^r(n) \tag{6.3.51}$$

$$_{k+1}V_{b4}^i(n+1) = {}_kV_{b4,5} - {}_kV_{b4}^r(n+1) \tag{6.3.52}$$

It can be seen from (6.3.50)-(6.3.52) that if $Z_b(n) = Z_b(n+1)$ the node connection

reduces to the normal 1D connection algorithm

$$ {}_{k+1}V^i_{b4}(n+1) = {}_kV^r_{b5}(n) \tag{6.3.53} $$

$$ {}_{k+1}V^i_{b5}(n) = {}_kV^r_{b4}(n+1) \tag{6.3.54} $$

In a region where the boundary displacement $d = 0$ then $Z_b(n+1) = 0$ and the connection algorithm can be seen to reduce to the electric boundary condition

$$ {}_{k+1}V^i_{b5}(n) = -{}_kV^r_{b5}(n) \tag{6.3.55} $$

as required.

6.3.2 3D model

The development of a boundary for the 3D SCN mesh proceeds in the same way as the 2D case. The configuration is shown in Figure 6.3.8 where the fractional space next to the boundary is occupied by the shunt node. Voltage sources are introduced into the shunt node to effect coupling with the field 3D node. The boundary derived here is to be positioned on the Z_{min} boundary of the mesh and therefore extends in the x-y plane. Equivalent models can be derived for the other boundaries of the mesh. The differential equations describing an x and y directed current flow in the boundary region are given by

$$ -\Delta x \frac{\partial V_b}{\partial x} = L_x \frac{\partial I_{bx}}{\partial t} - V_0 \tag{6.3.56} $$

$$ -\Delta y \frac{\partial V_b}{\partial y} = L_y \frac{\partial I_{by}}{\partial t} - V_6 \tag{6.3.57} $$

$$ -\Delta x \frac{\partial I_{bx}}{\partial x} - \Delta y \frac{\partial I_{by}}{\partial y} = C \frac{\partial V_b}{\partial t} \tag{6.3.58} $$

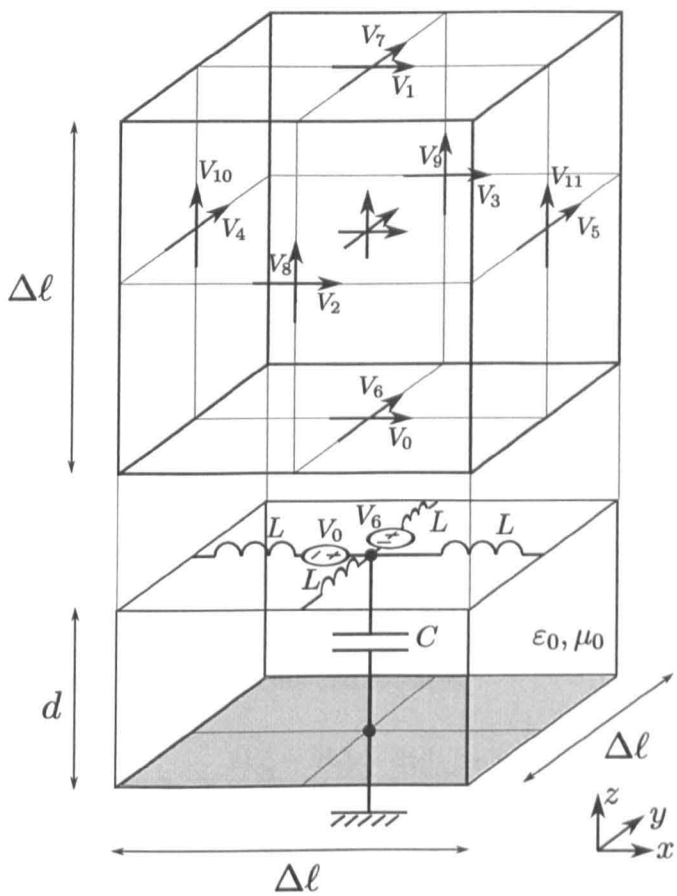

Figure 6.3.8: Coupling of the SCN field node to the boundary shunt node

where the port numbers are taken from Figure 6.3.8 so that V_0 and V_6 couple to the x and y directed ports respectively. The boundary impedance is assumed to be equal for both polarisations and equal to (6.3.30) so that $Z_{bx} = Z_{by} = Z_b$.

Normalising (6.3.56), (6.3.57) and (6.3.58) using the 3D time step

$$\frac{\Delta\ell}{\Delta t} = 2c \tag{6.3.59}$$

yields

$$-\frac{\partial V_b}{\partial X} = 2\frac{\partial i_{bx}}{\partial T} - V_0 \tag{6.3.60}$$

$$-\frac{\partial V_b}{\partial Y} = 2\frac{\partial i_{by}}{\partial T} - V_6 \tag{6.3.61}$$

$$-\frac{\partial i_{bx}}{\partial X} - \frac{\partial i_{by}}{\partial Y} = 2\frac{\partial V_b}{\partial T} \tag{6.3.62}$$

Converting to travelling wave format using equivalent expressions to (6.3.36) and (6.3.37) and converting the derivative terms to stub formats using

$$\frac{\partial i_{bx}}{\partial T} = 2V^i_{bLx} + 2i_{bx} \tag{6.3.63}$$

yields the expressions for the currents and voltages

$$i_{bx} = \frac{2V^i_{b4} - 2V^i_{b5} - 2V^i_{bLx} + V_0}{4} \tag{6.3.64}$$

$$i_{by} = \frac{2V^i_{b2} - 2V^i_{b3} - 2V^i_{bLy} + V_6}{4} \tag{6.3.65}$$

$$V_b = \frac{2V^i_{b2} + 2V^i_{b3} + 2V^i_{b4} + 2V^i_{b5}}{4} \tag{6.3.66}$$

These expressions can be unnormalised and used to construct the TLM equivalent circuit shown in Figure 6.3.9. Conveniently there is no need for a capacitive stub in this case, assuming that the model is used at the maximum time step (6.3.59). Should a lower time step be used then the capacitive stub needs to be included

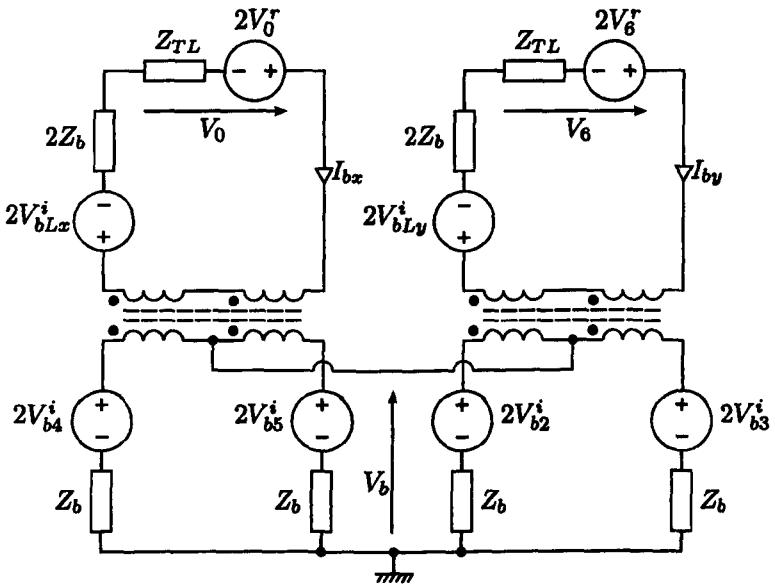

Figure 6.3.9: TLM equivalent circuit for fractional boundary placement in 3D

in parallel with the boundary voltages. This is shown in more detail in Appendix C.2.

6.3.3 Validation

In order to calculate the modelled boundary displacement and propagation velocity characteristics the domain considered consists of a 1000×1×1 cell TLM mesh bounded by PEC boundaries at Z_{min} and Z_{max} and PMC boundaries at Y_{min} and Y_{max}. Exciting ports 8, 9, 10 and 11 in this case yields a y-polarised plane wave propagating in the x-direction for these boundary conditions. The boundary displacement can be calculated where the fractional boundary is applied to the X_{max} boundary, therefore normal incidence is ensured. The propagation velocity can be calculated where the fractional boundary is applied to the Z_{min} boundary, ensuring a field polarisation perpendicular to the boundary and propagation along the length of the boundary.

Table 6.3.1: Error in boundary displacement with normal incidence in 2D mesh

Extension ($\Delta\ell$)	Modelled Extension ($\Delta\ell$)	Error (%)
0	0	0
0.2	0.19999	0.196×10^{-3}
0.4	0.39999	1.156×10^{-3}
0.6	0.59998	2.951×10^{-3}
0.8	0.79996	5.195×10^{-3}
1.0	0.99992	8.115×10^{-3}

Table 6.3.2: Error in boundary displacement with normal incidence in 3D mesh

Extension ($\Delta\ell$)	Modelled Extension ($\Delta\ell$)	Error (%)
0	0	0
0.2	0.19999	0.514×10^{-3}
0.4	0.39999	1.527×10^{-3}
0.6	0.59997	4.929×10^{-3}
0.8	0.79992	9.397×10^{-3}
1.0	0.99985	15.40×10^{-3}

6.3.3.1 Boundary Displacement

The boundary extension modelled using the developed model can be compared with the desired boundary extension to calculate the error in the model. To maintain synchronisation in the TLM mesh a pulse propagates $\Delta\ell$ every Δt (assuming the maximum time step is used), therefore, the delay resulting from a boundary extension of less than $\Delta\ell$ will be less than Δt. Under these conditions the precise time domain propagation delay of a reflected Gaussian pulse, for example, would be difficult to resolve and would require the use of an inaccurate curve-fitting approach. Therefore, the time delay due to a reflection from the displaced wall is calculated in the frequency domain where a phase shift θ is related to a time domain delay through

$$j\theta = -\ln\left[\frac{\mathcal{F}\{f(t-t_1)\}}{\mathcal{F}\{f(t-t_0)\}}\right] \tag{6.3.67}$$

$$= -\ln\left[\exp\left(-j\omega(t_1-t_0)\right)\right] = j\omega(t_1-t_0) \tag{6.3.68}$$

where $\mathcal{F}\{f(t)\}$ represents the Fourier transform of the function $f(t)$. Therefore, the gradient of the function $\Im(j\theta) = \omega\tau$ is equal to the time delay between the two signals where

$$\tau = t_1 - t_0 \tag{6.3.69}$$

The modelled boundary extension, compared with an extension of $d = 0$, can be calculated by comparing the time difference between the pulses from either boundary using

$$d' = \frac{c\tau}{2} \tag{6.3.70}$$

where propagation velocity is assumed to be c.

The errors in the boundary extension on a 1D line using the 2D model and the 3D model are calculated using this method and are shown in Tables 6.3.1 and 6.3.2. The results shown were obtained using a space step of $\Delta\ell = 10$ m, the maximum time step for each model and a Gaussian excitation with a half width of $\sigma = 50\Delta t$ and a delay of $150\Delta t$ from $t = 0$. The boundary extension was added to the Z_{min} boundary in both cases and suitable boundary conditions were chosen for the other directions.

It can be seen that the propagation delay modelled by the boundary for normal incidence is very accurate; errors are typically less than the order of $10^{-3}\%$.

6.3.3.2 Propagation Velocity

The failure of the original stub model was due to the fact that the propagation of a wave along the boundary is slowed considerably leading to non-physical modes. The propagation speed along a boundary using the model developed here has been calculated. Using a 1D line a boundary extension was modelled along the length

Table 6.3.3: Error in boundary propagation velocity in 2D mesh

Extension ($\Delta\ell$)	Propagation Velocity Error (%)
0	3.163×10^{-4}
0.2	2.681×10^{-4}
0.4	3.087×10^{-4}
0.6	2.232×10^{-4}
0.8	2.452×10^{-4}
1.0	1.935×10^{-4}

Table 6.3.4: Error in boundary propagation velocity in 3D mesh

Extension ($\Delta\ell$)	Propagation Velocity Error (%)
0	2.854×10^{-5}
0.2	2.806×10^{-5}
0.4	3.551×10^{-5}
0.6	2.734×10^{-5}
0.8	5.793×10^{-5}
1.0	3.020×10^{-5}

of the line using both 2D and 3D nodes. The line is excited using a Gaussian pulse with a half width of $\sigma = 50\Delta t$ and a delay of $150\Delta t$ from $t = 0$, the maximum time step was used in each case for a space step of $\Delta\ell = 10$ m. The velocity of propagation is calculated by measuring the field at two nodes along the line n_0 and n_1 and the delay τ calculated in the Fourier domain using the method described above, the velocity of propagation is given by

$$u = \frac{\Delta\ell\,(n_1 - n_0)}{\tau} \tag{6.3.71}$$

The values of $n_1 - n_0$ was chosen to be 10 so that the measurement nodes are separated by 100 m. The propagation velocity error for the 2D and 3D model are shown in Tables 6.3.3 and 6.3.4.

It can be seen that the propagation velocity obtained using the new boundary model is very accurate and almost exactly equal to the speed of light.

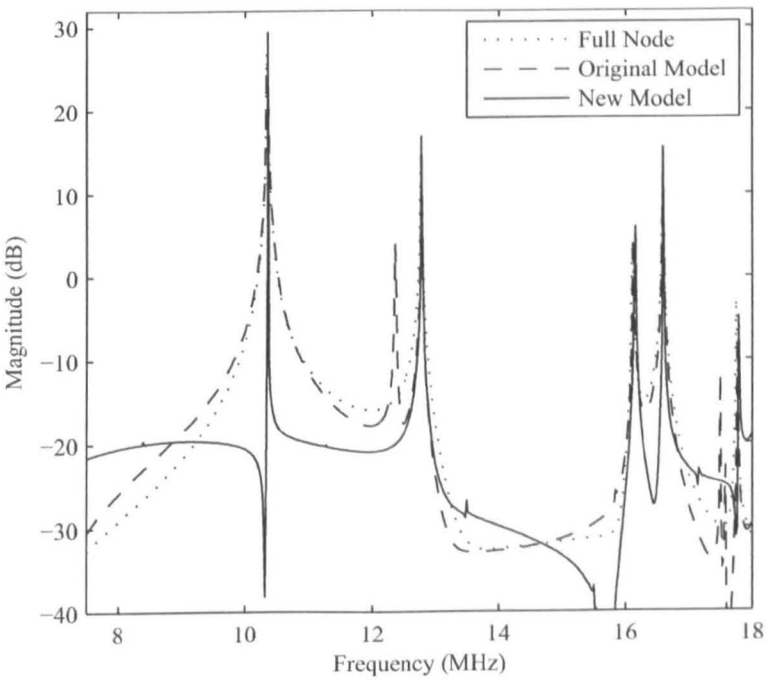

Figure 6.3.10: E_x field of a cavity with a $d = \Delta\ell$ boundary extension

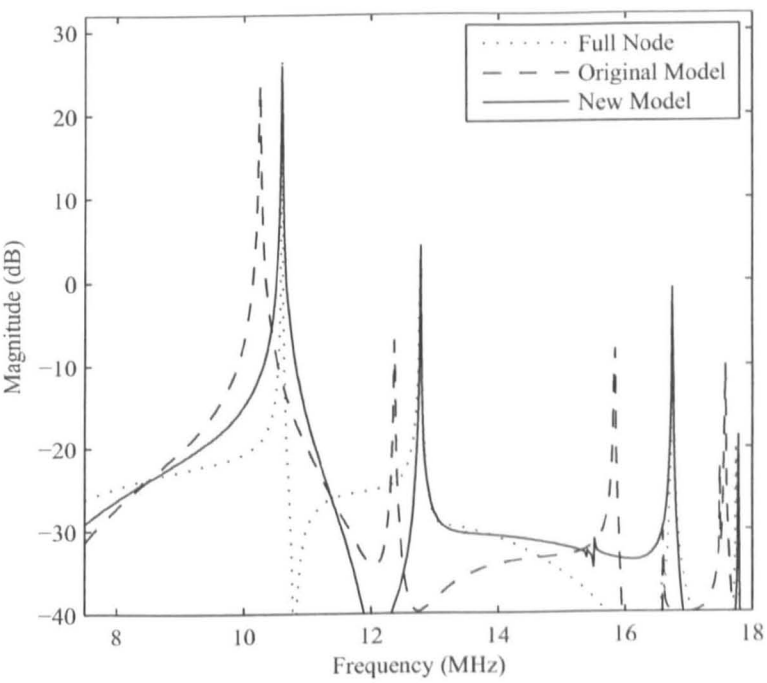

Figure 6.3.11: E_y field of a cavity with a $d = \Delta\ell$ boundary extension

Table 6.3.5: Error in 3D cavity resonant frequency of the first 10 modes

Mode	Analytical (MHz)	Model (MHz)	Error (%)
TE_{101}	10.3501	10.3566	0.0628
TE_{110}	10.5994	10.5899	0.0896
TE_{111}	12.7788	12.7673	0.0900
TE_{012}	16.1238	16.1525	0.1780
TE_{021}	16.6025	16.5962	0.0379
TE_{210}	16.7591	16.7380	0.1259
TE_{112}	17.7806	17.7855	0.0276
TE_{211}	18.2159	18.1835	0.1779
TE_{022}	20.7002	20.6949	0.0256
TE_{122}	22.0152	21.9895	0.1167

6.3.3.3 Rectangular Cavity Resonance

The new boundary has been used to model the resonances of a 20×20×21 m box using a step size of 1m as discussed in Section 6.2.2. The boundary extension has been used to model a boundary thickness of $d = \Delta\ell$ on the Z_{min} boundary. This extension was chosen so that results can be compared to that of a regular SCN TLM cell. The response to a Gaussian excitation is shown in Figures 6.3.10 - 6.3.12 for fields E_x, E_y and E_z. The figures also show the response obtained using the conventional stub model.

It can be seen from Figures 6.3.10 - 6.3.12 that the new boundary model produces the correct resonances without the non-physical resonances produced in the original stub method. The resonant modes can be seen to agree well with those obtained using a normal TLM node. The first ten resonances of the cavity are compared with the analytical resonances for the cavity in Table 6.3.5. It can be seen that the error in the resonant frequencies are small and less than 0.18% in all cases. The model can be used to model a cavity with dimensions that do not coincide with the space step. The TE_{110} resonance of a $20 \times 20 \times (20 + d)$ m cavity for $d = 0.00, 0.15, 0.50, 0.75, 1.00\Delta\ell$ obtained using the 3D model is shown in Figure 6.3.13. The analytical resonances are shown (dotted) and it

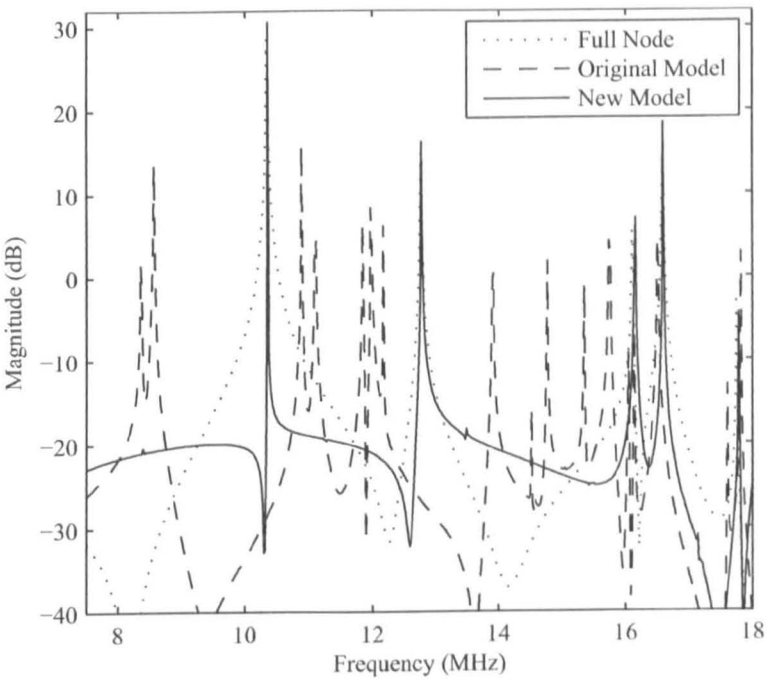

Figure 6.3.12: E_z field of a cavity with a $d = \Delta\ell$ boundary extension

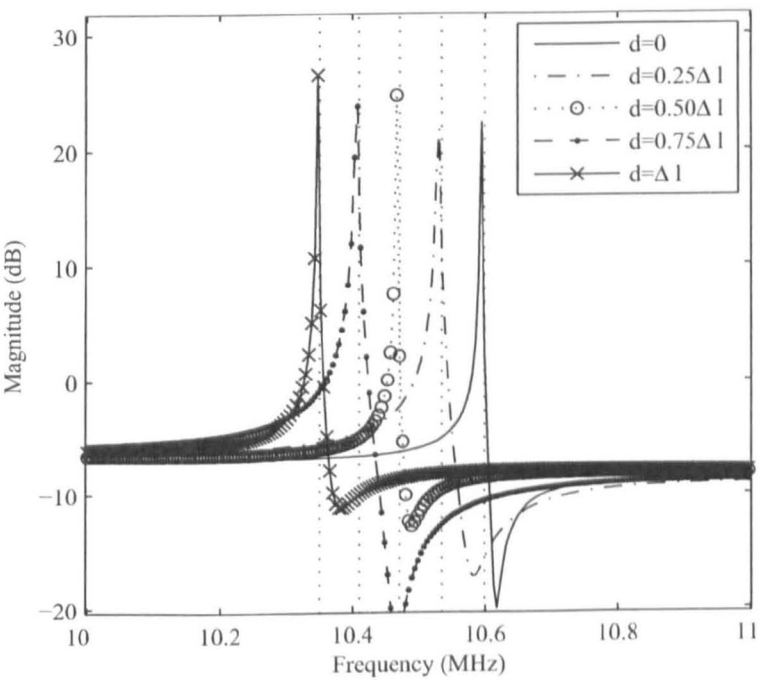

Figure 6.3.13: E_y field for fractional boundary placement of Z_{min} boundary

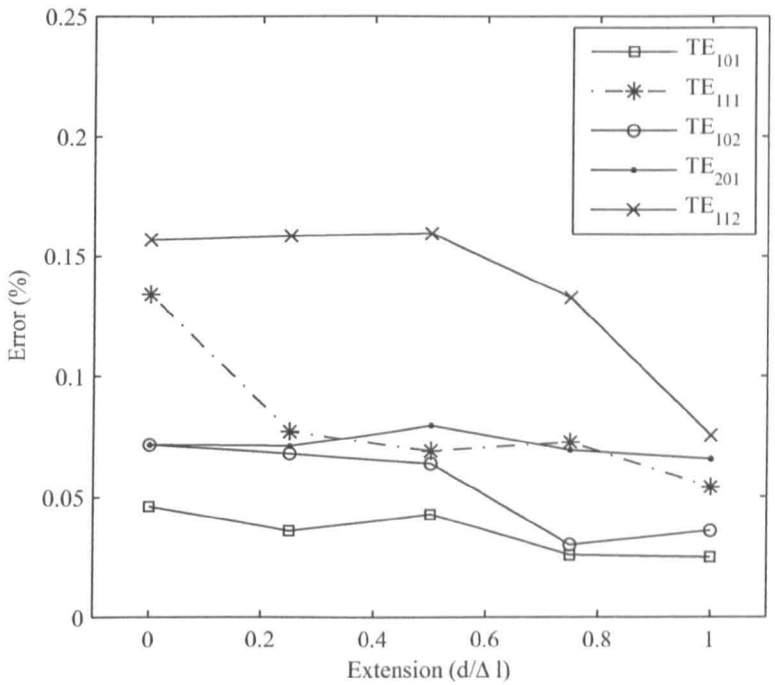

Figure 6.3.14: Error in 3D cavity resonant frequency for a number of fractional extensions

can be seen that the model accurately models the resonances of the cavity with fractional boundary placements. The error in the resonant frequency for a number of modes and boundary extensions is shown in Figure 6.3.14. It can be seen that the modelled resonances are accurate to within about 0.05% for the first cavity mode and the errors increase as the mode frequency approaches the mesh limit. The resonance error remains small and comparable to that of a regular SCN TLM mesh approaching its maximum usable frequency.

6.4 Non-PEC Boundaries

The model developed so far deals with a PEC boundary connected to the bulk mesh. This boundary is suitable for most cases that we are likely to encounter.

However, there are instances where an alternate boundary condition may be required, for example lossy or magnetic boundary properties. The following subsections describe the modifications necessary to model such boundaries.

6.4.1 Magnetic Boundary

A perfect magnetic conductor (PMC) boundary, that is a boundary with a reflection coefficient equal to 1, may be required in some instances. Such a boundary is required for terminating models that may have a structural periodicity, for example a cascade of cavities or a purely symmetrical cavity. The PMC boundary allows the modeller to reduce the modelling space by assuming that the behaviour within the imaginary domain on the other side of the boundary is exactly the same as the domain terminated by that boundary. Another, and perhaps more applicable, use of the PMC boundary is to terminate the 2D shunt mesh. The shunt mesh can be considered to be the dual of the series mesh. In cases where the modeller would terminate the series mesh with the PEC condition, the shunt mesh requires termination with a PMC condition [13].

The boundary model developed so far can be used to model a PMC boundary if the discrete representation of a gyrator is introduced between the incident voltage from the bulk mesh and the boundary model. A gyrator is physically realised as a device constructed using an operational amplifier circuit, which converts voltages to currents and currents to voltages respectively.

Computationally, the gyrator can be realised as a simple passive modelling device. Modelling proceeds whereby V_1 and I_1 are the voltage and current on the input side of the gyrator. V_2, I_2 are the voltage and current on the output side of the gyrator and R_g is the gyrator *resistance*. The transfer matrix for a gyrator is

given by

$$\begin{bmatrix} V_2 \\ I_2 \end{bmatrix} = \begin{bmatrix} 0 & R_g \\ 1/R_g & 0 \end{bmatrix} \begin{bmatrix} V_1 \\ I_1 \end{bmatrix} \tag{6.4.72}$$

In TLM the field-circuit equivalences are

$$\underline{E} = -\underline{V}/\Delta\ell, \quad \underline{H} = -\underline{I}/\Delta\ell \tag{6.4.73}$$

Therefore, the properties of the gyrator allow the existing boundary to represent a magnetic boundary as the conversion between voltage and current is equivalent to a conversion between electric and magnetic fields. The incident voltages on the boundary, V_0 and V_6, are coupled through gyrators into the boundary model, so that a short circuit modelled in the boundary is seen as an open circuit in the bulk mesh.

To correctly model the magnetic boundary we set the gyrator resistance equal to the transmission line impedance so that

$$R_g = Z_{TL} \tag{6.4.74}$$

By expanding the gyrator transfer matrix we obtain the new voltage and impedance coupling into the boundary line. It can be shown that the voltage is given by

$$\widehat{2V_0^r} = 2V_0^r \left(\frac{R_g}{Z_{TL}} \right) \tag{6.4.75}$$

and the impedance by

$$\widehat{Z_{TL}} = \frac{R_g^2}{Z_{TL}} \tag{6.4.76}$$

Substituting for R_g we find that these are equal to $2V_0^r$ and Z_{TL} respectively, which can be seen to be the same as for the PEC boundary values. The new incident

voltage on the field node equivalent to that of (6.3.48) is given by

$$ {}_{k+1}V_0^i = {}_k i_{bx}\left(\frac{R_g^2}{Z_b}\right) - {}_k V_0^r = -\left({}_k V_0^r - {}_k i_{bx} y_0\right) \tag{6.4.77} $$

The new incident voltage obtained through (6.4.77) has the opposite sign to that of (6.3.48) as is required for modelling of a magnetic boundary.

6.4.2 Lossy Boundary

Due to the skin effect it is not accurate to model the boundary using the PEC boundary condition. Except for a superconducting boundary, there will be a small amount of loss associated with the boundary and the corresponding reflection coefficient will not be exactly equal to -1 for the metallic boundary.

In order to include the loss associated with the walls of the structures being modelled, a modified reflection coefficient can be used on all walls of the cavity. For accuracy it is therefore desired that some loss be included in the boundary model to model such situations. It will be shown that a loss can be easily included in the boundary model by the addition of a loss into the circuit represention of the boundary.

The fractional boundary model is able to take advantage of the boundary condition at a PEC boundary by enforcing

$$ \hat{n} \times \underline{E} = 0 \tag{6.4.78} $$

$$ \hat{n} \cdot \underline{H} = 0 \tag{6.4.79} $$

Hence, for a boundary in the x-y plane we are able to assume that at the field

components E_x, E_y and H_z are all zero. However, if the boundary is lossy and no longer PEC then Equations (6.4.78) and (6.4.79) are no longer satisfied. It can be seen that if the boundary cell containing the skin loss does not satisfy the condition for zero tangential electric field and zero perpendicular magnetic field then there will be some error associated with it. It can also be shown that this error varies with both loss and boundary displacement.

The modelling of a lossy boundary in 2D proceeds by modifying (6.3.40) with a normalised loss term r_b so that

$$i_{bx} = \frac{2V_{b4}^i - 2V_{b5}^i - 2V_{bLx}^i + V_0}{2\sqrt{2} + r_b} \tag{6.4.80}$$

and equivalently in 3D the boundary current terms are modified to be

$$i_{bx} = \frac{2V_{b4}^i - 2V_{b5}^i - 2V_{bLx}^i + V_0}{4 + r_b} \tag{6.4.81}$$

$$i_{by} = \frac{2V_{b2}^i - 2V_{b3}^i - 2V_{bLy}^i + V_6}{4 + r_b} \tag{6.4.82}$$

where the normalised loss term is given by

$$r_b = \frac{R}{\eta_0} \tag{6.4.83}$$

The boundary voltage calculation remains unchanged through the inclusion of the loss. Applying a loss in this way is equivalent to terminating the mesh by an impedance in the same manner as the first-order boundary condition applied in standard TLM. However, in the limit that the boundary extension is zero it can be seen that (6.4.80) reduces to that of a simple lumped impedance. The value of R chosen is dependent on the loss being modelled, for a PEC material with no surface impedance the value of R will be zero and increases with increasing boundary impedance.

The loss impedance R in the boundary is applied within the boundary region only. Therefore, the impedance is applied to a 1D transmission line in a 2D model and to a 2D transmission line in a 3D model. The matched boundary condition for the 2D model requires an impedance of η_0 and in 2D we require an impedance of $\eta_0/\sqrt{2}$. If a matched boundary is to be used it is apparent that the boundary extension is not required as we could simply terminate the mesh at the edge of the bulk mesh.

The error in the lossy boundary is measured by simulating the return loss of a pulse reflected from the lossy boundary applied to the end of a 800 cell long 2D transmission line. The transmission line is terminated tangentially to the pulse propagation by PEC boundaries to model a plane wave. The return loss from the lossy boundary is shown in Figures 6.4.15-6.4.17. The dotted line shows the analytical return loss from the condition being modelled where

$$RL(dB) = 20log\left(\frac{V_r}{V_i}\right) = -20log\left(|\Gamma|\right) \tag{6.4.84}$$

The results are shown from 6 cells per wavelength to 30 cells per wavelength, typically a full field TLM model will use a minimum of 10 cells per wavelength to reduce dispersion and numerical sampling error. It is immediately clear that the boundary becomes more accurate for higher cell to wavelength ratios. The spatial field variations at low wavelengths are far more rapid than at high wavelength. Therefore, the required field variation across the boundary cell is higher at low wavelength, hence the enforcement of (6.4.78) and (6.4.79) becomes more inaccurate if a loss is included in the boundary.

It can be seen that the error in the boundary loss increases with boundary displacement and increases as the required loss of the boundary increases. This

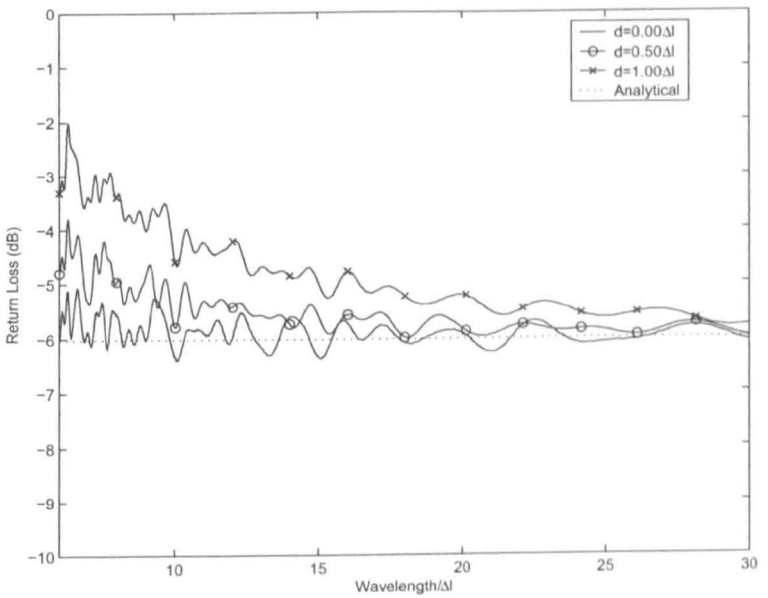

Figure 6.4.15: Return loss from a boundary with a reflection coefficient of -0.25

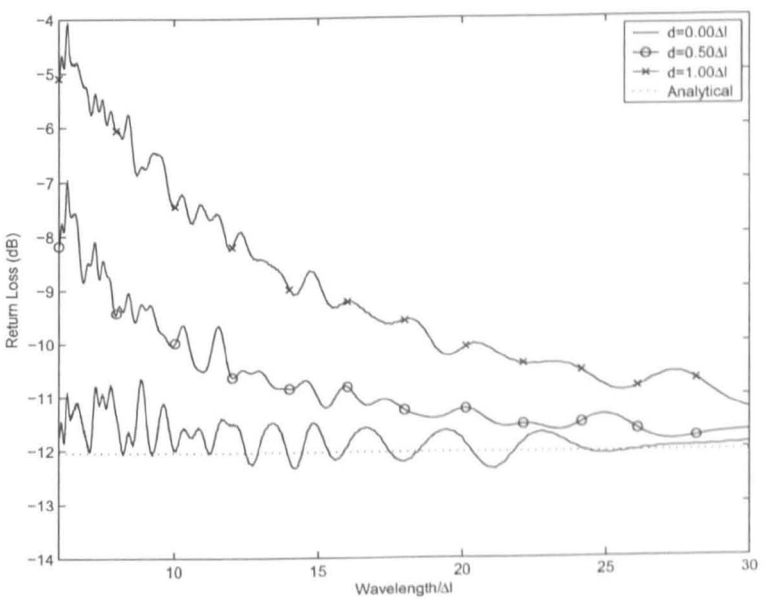

Figure 6.4.16: Return loss from a boundary with a reflection coefficient of -0.50

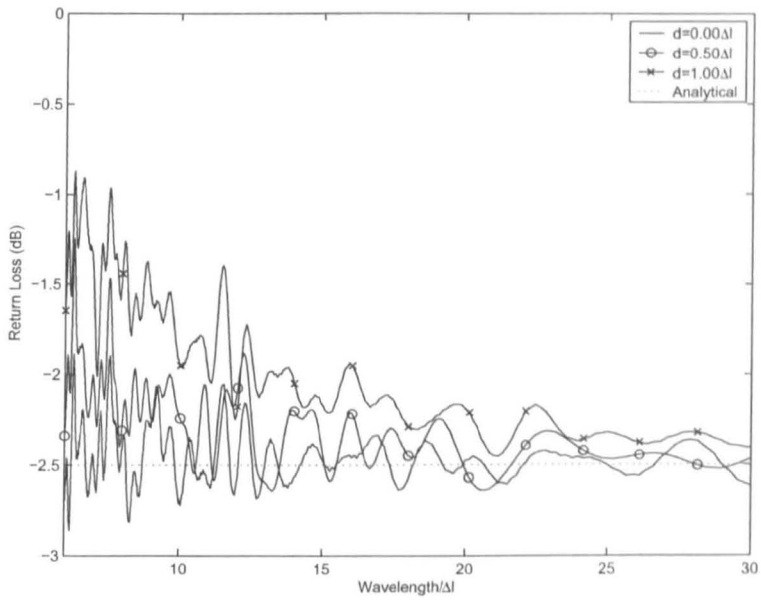

Figure 6.4.17: Return loss from a boundary with a reflection coefficient of -0.75

error effect is due to the same considerations as for the discussion of the effect of modelling resolution on the return loss. In most instances the boundary material will be metallic in nature and have a reflection coefficient of close to -1. Therefore, the error seen in the boundary will be minimal and should not greatly influence the result as shown in Figure 6.4.17.

As the boundary modelled here is only a first-order boundary condition, if a lossy boundary is modelled the accuracy of the boundary is only assured for normal incidence of plane waves. In the same manner as the regular TLM approach to boundary modelling it is found that the accuracy of the boundary reduces as the angle of incidence moves away from being normal to boundary [39], . Therefore, the accuracy of the boundary will be reduced for higher order modes within the cavity however, the error in results and the accuracy of the boundary is consistent with the standard TLM approach [13]. In this work the accuracy will be high and can be considered acceptable as the reflection coefficient is close to -1 for metallic surfaces as are being modelled here.

6.5 Internal Boundaries

The model discussed so far can be used to accurately model external boundaries, i.e. boundaries on the outer edges of the mesh. Chapter 5 discussed coupled cavity systems where an internal metallic boundary is present in the physical systems. So that coupled systems may be modelled and internal features be accurately positioned it is required that the boundary be extended to internal boundaries also.

This section discusses a procedure that allows the modelling of internal boundaries within the TLM mesh. Here we consider only those cases where the skin depth is small compared to the boundary thickness so that there is no propagation across the boundary. As an example, at 2.45Ghz the skin depth of copper is $1.32\mu m$ and Aluminium is $1.66\mu m$. Therefore, the skin depth of most metallic structures is sufficiently small that this approximation holds for any physical thickness that is likely to be encountered. For the sake of simpicity, the model presented here is the 2D internal boundary node, however the development of the 3D node is straightforward and follows the same development as before. The starting point for this model is the fractional boundary node as shown in Figure 6.3.6 and its TLM equivalent circuit as shown in Figure 6.3.7.

The model developed here is designed to represent the region of space shown in Figure 6.5.18 where the boundary can be oriented long either axis. As this model is positioned within the bulk mesh it is necessary that the edge dimensions of the internal boundary cell are equal to those of the bulk mesh, Δl. Therefore, there are two regions of space modelled adjacent to the internal boundary, these are differentiated using the subscript p and n representing the region on the positive and negative sides of the boundary in terms of the coordinate system. The thickness

of the boundary is given by h so that

$$d_p + d_n + h = \Delta l \tag{6.5.85}$$

Hence, the impedances of the boundary model are given by

$$Z_{bp} = \eta_0 \left(\frac{d_p}{\Delta \ell} \right) \tag{6.5.86}$$

and

$$Z_{bn} = \eta_0 \left(\frac{d_n}{\Delta \ell} \right) \tag{6.5.87}$$

Notice that the port numberings within the internal boundary node have been made consistent with those of the normal SCN node. This convention is useful as the internal boundary cell occupies a region in the mesh that would normally contain a SCN cell.

The equivalent circuit for the internal boundary cell is derived in the same way as the external boundary models. However, the TLM model represents the configuration shown in Figure 6.5.18 where the orientation of the voltage and current in the two regions are chosen to be consistent either side of the boundary. For the case of the external boundary coupling to the bulk mesh only took place through the voltage given by V_0. In order to model a general internal boundary, it is necessary to couple to the full field node in the same direction as the boundary orientation.

The internal boundary cell is updated during the connection process in the same manner as the external boundary model. Hence the boundary model is updated using the expressions of equations (6.3.40)-(6.3.47). Connection within the length of the boundary occurs as described in Section 6.3.1.1. Connection of the internal boundary model to the bulk mesh can take place in two ways; either

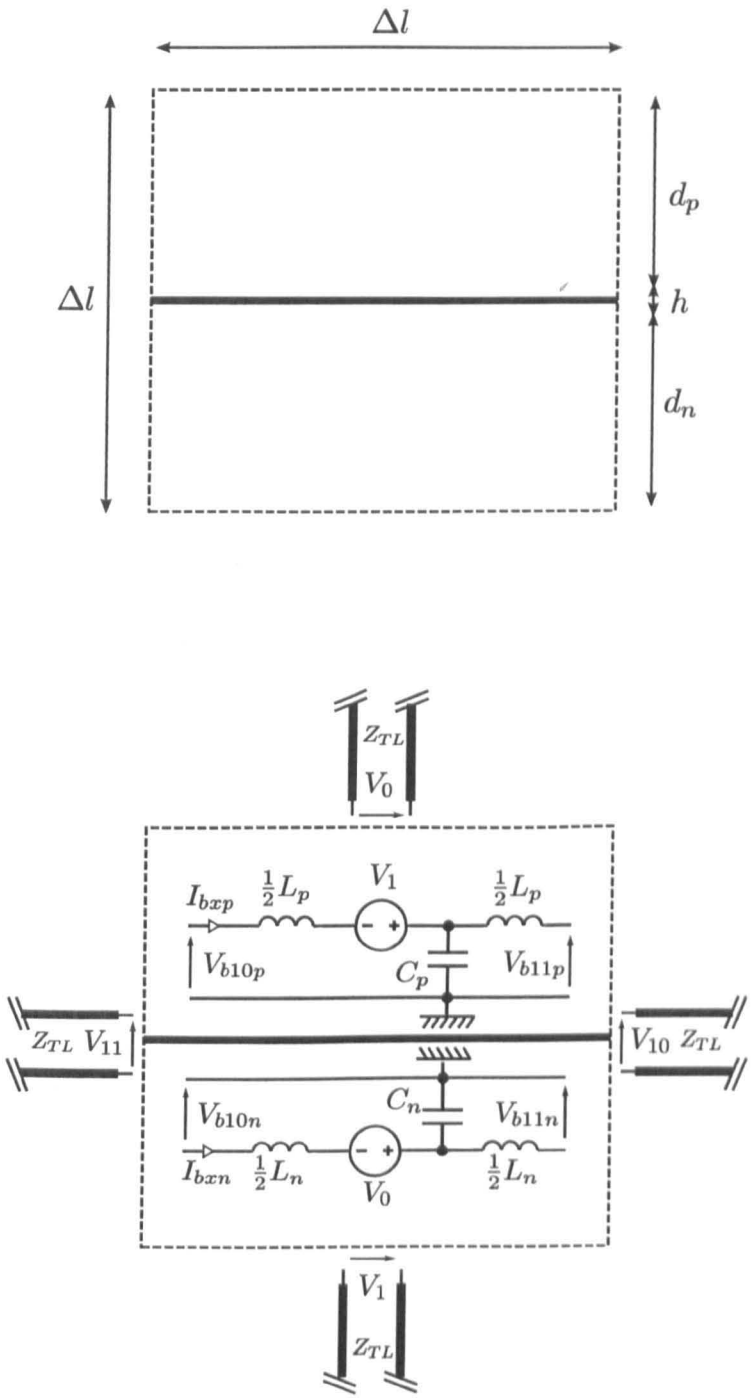

Figure 6.5.18: Internal fractional boundary and its equivalent circuit

normal to the boundary or perpendicular to the end of the boundary as shown in 6.5.18. Connection normal to the boundary is performed in the same way as for the regular 2D fractional boundary model, in the case shown that is through the expressions

$$_{k+1}V_0^i = _k V_0^r - _k I_{bxp} Z_{bxp} \tag{6.5.88}$$

$$_{k+1}V_1^i = _k V_1^r - _k I_{bxn} Z_{bxn} \tag{6.5.89}$$

where the subscripts correspond to the boundary impedance (b), in the x-direction (x) on the positive (p) or negative (n) side of the boundary. Connection to the end of the internal boundary from the bulk mesh takes place as follows. The reflected boundary voltages are calculated as part of the boundary update, then the total voltage at the end of the boundary is calculated where it interfaces with the bulk mesh. The total voltages at either end of the boundary are

$$_kV_{b10,11} = \frac{\left(2_kV_{b10p}^r + 2_kV_{b10n}^r\right) Z_{TL} + 2_kV_{11}^r \left(Z_{bp} + Z_{bn}\right)}{Z_{TL} + Z_{bp} + Z_{bn}} \tag{6.5.90}$$

and

$$_kV_{b11,10} = \frac{\left(2_kV_{b11p}^r + 2_kV_{b11n}^r\right) Z_{TL} + 2_kV_{10}^r \left(Z_{bp} + Z_{bn}\right)}{Z_{TL} + Z_{bp} + Z_{bn}} \tag{6.5.91}$$

where, for example, $V_{b10,11}$ corresponds to the voltage at boundary port 10 and mesh port 11. Hence, the new incident voltages at the bulk mesh ports are given by

$$_{k+1}V_{11}^i = _kV_{b10,11} - _kV_{11}^r \tag{6.5.92}$$

and the boundary ports by

$$_{k+1}V_{b10n}^i = \left(\frac{Z_{bn}}{Z_{bp} + Z_{bn}}\right) _kV_{b10,11} - _kV_{b10n}^r \tag{6.5.93}$$

$$_{k+1}V_{b10p}^i = \left(\frac{Z_{bp}}{Z_{bp} + Z_{bn}}\right) _kV_{b10,11} - _kV_{b10p}^r \tag{6.5.94}$$

The opposite end of the boundary is calculated in the same way as (6.5.92)-(6.5.94)

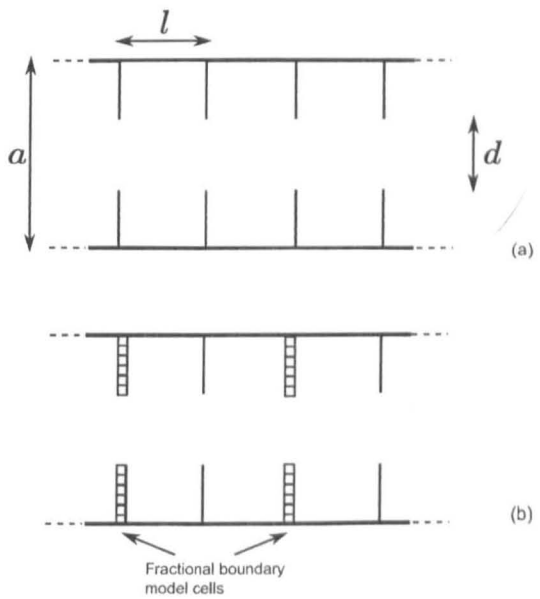

Figure 6.5.19: Bandpass waveguide overhead view (a) with fractional boundary placement cells (b)

by swapping the subscripts 11 and 10.

6.5.1 Validation

In order to validate the internal boundary modelling technique described above, a model of a waveguide band-pass filter was constructed. The filter consists of four diaphragm inductive apertures in the waveguide with periodic displacement between them. A schematic of the structure can be seen in Figure 6.5.19 where the waveguide width is a, the aperture seperation is l and the aperture width is d.

The admittance of each of the apertures is given by the inductive aperture expression in [50]

$$\frac{Y}{Y_0} = -\frac{j\lambda_g}{a}\cot^2\left(\frac{\pi d}{2a}\right) \tag{6.5.95}$$

The multiple aperture structure can be combined to give reflection coeffient of [14]

$$\cosh(\Gamma) = \cos\left(\frac{2\pi l}{\lambda_g}\right) + \frac{\lambda_g}{2a}\cot^2\left(\frac{\pi d}{2a}\right)\sin\left(\frac{2\pi l}{\lambda_g}\right) \tag{6.5.96}$$

where in the passband $|\Gamma| < 1$ and the reflection coefficent has no real part.

The waveguide modelled had a width $a = 7.11mm = 11\Delta l$ and the aperture width was $d = 1.94mm = 6\Delta l$. The separation of the apertures was set to $20\Delta l$ and 19Δ to permit modelling using only the conventional face based TLM boundary approach. The S21 response of the waveguide filter was then simulated by propagating the H_{10} down the waveguide and recording the field value at a point after the filter when the filter was and was not inserted.

The internal boundary model developed in this chapter was then used to model the condition where $l = 19.5\Delta l$ so that the boundary displacement is set to $0.5\Delta l$. In order to model this seperation two of the apertures had to be modelled using the internal boundary model. The S21 response of the two conventional boundary results and the new internal fractional boundary model can be seen in Figure 6.5.20. The analytical centre frequency of the pass bands calculated using (6.5.96) are also shown by the vertical lines.

The response for the internal boundary case is positioned in between the two conventional approaches indicating that the model is able to accurately model an internal boundary displacement. The centre frequency of the pass bands also agree well with the analytical result for the structure. In this case the fractional nature of the model is validated as well as the boundary end to SCN coupling. The fractional boundary model has been shown to be able to model both internal and external boundaries accurately and is suitable for fine tuning applications that might be encountered in waveguide modelling for example.

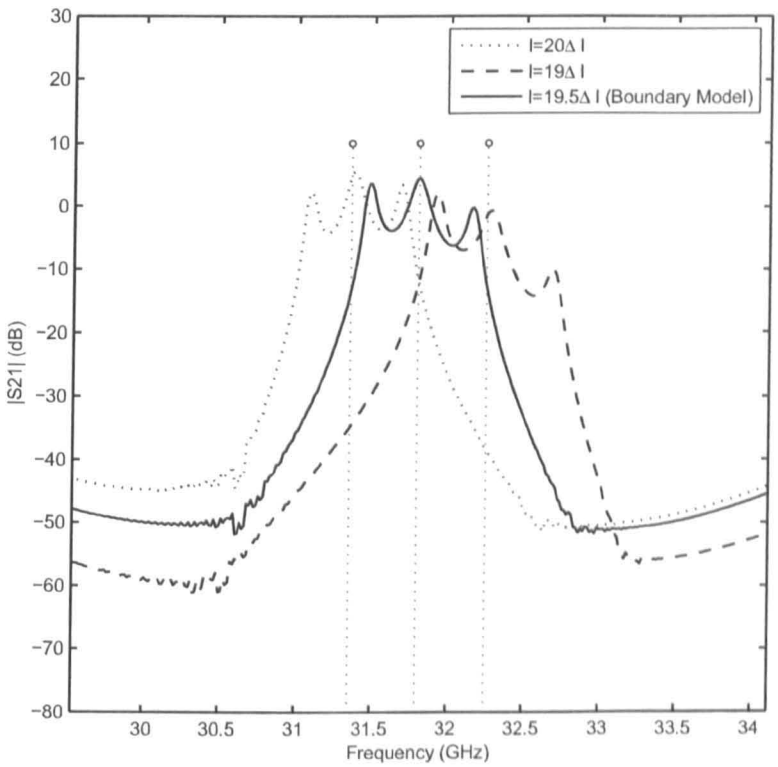

Figure 6.5.20: $|S21|$ response of the waveguide filter using varied aperture seperations

6.6 Time Varying Boundaries

The metallic cavity structures within aircraft often vary dynamically due to stresses, vibrations and structural movement. It is of interest to explore the impact vibrations may have on communications within the aircraft as small boundary changes can have a signifnicant effect on the channel, as seen in reverberation chambers. It has been shown in [45] that even a 1mm change in the periphery of a reverberation chamber stirrer can lead to a dramatic change in received power and errors in wireless communication systems.

Time varying boundaries are studied regularly in the field of acoustics as it is often the physical movement of a structure that excites a sound wave. Analytical solutions exist to simple problems with time varying boundaries where the wave equation for the domain with moving boundary is transformed into a form-invariant wave equation in a domain where the boundary is fixed [56]. Akin to the method of characteristics the partial differential equation which has the time varying boundary condition has been transformed into a solvable ordinary differential equation restricted to a line of charactistics [26]. The solution to canonical problems can be found in such a way however as with previous models they cannot be extended to complex geometries or arbitrary shaped cavities that cannot be solved analytically. Therefore, we seek a discretised full-field approach to modelling moving boundaries based on the TLM method using the model developed in this chapter.

One approach to modelling dynamic changes to structure in a simulation would be to adopt what could be considered a mode tuned approach. The methodology here would be to perform a number of simulations with the boundaries of the model kept static. Between each simulation the boundaries are moved by a small amount. Superposition of these results may give an insight into the effects of cavity

vibrations. The assumption must be made however that the variations in boundary position are slow so that the differential effects of the boundary movement can be ignored. From such a methodology we would be able to obtain results for any boundary variation from a large number of simulations.

Another approach is to vary the boundary position during the simulation so that the differential effect of the boundary position is taken into account in the model. An approach of this type would be able to capture Doppler type effects due to the time variation of the boundary. This is important for rapid variation in boundary position, that is, compared with the communication frequency or the channel bandwidth. This approach could be considered a mode stirred approach and would allow one to obtain the effect on a complete signal for one variation profile.

The model developed in this chapter is ideally placed to perform the first methodology, however some modifications must be made in order to allow dynamic boundary positioning. This section describes the steps needed to modify the boundary model for such a scheme and produce a general dynamic boundary model.

6.6.1 Model Development

Theoretically, in order to implement a moving boundary in the TLM method the impedance of the inductive stub boundary in Section 6.2.2 could be changed with each time step to model the movement of the boundary. As there is no change in the number of mesh cells using this technique some of the energy conservation concerns are avoided. In the first instance the boundary variation is limited to displacements of less than the global cell spacing so that $d < \Delta l$. Furthermore, we

apply the usual restriction that the boundary vibration frequency is much lower than the frequency limit of the mesh, that is $\lambda/\Delta l > 6$ and preferably $\lambda/\Delta l > 10$.

Starting from a 1D viewpoint we can revert back to the simple inductor only model used to extend a 1D line. Recalling that a boundary extension can be modelled using an inductive stub with impedance

$$Z_L = 2\eta_0 \left(\frac{d}{\Delta l}\right) \tag{6.6.97}$$

The voltage at the boundary node is given by

$$V = \frac{\frac{2V_0^i}{Z_0} + \frac{2VL_b^i}{Z_L}}{\frac{1}{Z_0} + \frac{1}{Z_L}} \tag{6.6.98}$$

where we can see that the contribution from the inductive stub is dependent on Z_L. The aim is to vary Z_L between time steps so that the incident voltage contribution from the inductive stub will also change between time steps.

In order to correctly conserve energy a per-unit-inductance, derived from those used to model a current dependant inductor [13], can be used. In order to model the time varying inductor the incident stub voltage, VL_b^i, is replaced by its per-unit equivalent $VL_{Ub}^i \times Z_L(t)$ where $Z_L(t)$ is the time varying impedance of the stub which is updated at each timestep and VL_{Ub}^i is the per-unit voltage on the inductive stub and has units of Amperes. Therefore, the voltage at the boundary node is now given by

$$V = \frac{\frac{2V_0^i}{Z_0} + 2VL_{Ub}^i}{\frac{1}{Z_0} + \frac{1}{Z_L(t)}} \tag{6.6.99}$$

where V_0^i is obtained from the bulk mesh and VL_{Ub}^i is known from the previous iteration and has been normalised with respect to the boundary displacement.

The reflected voltages are calculted in the usual way so that the reflected line

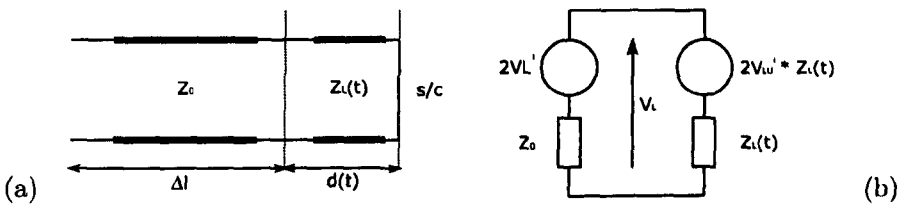

Figure 6.6.21: (a) Transmission line termination at moving PEC boundary and (b) its Thevenin equivalent

voltage is given by

$$V_0^r = V - V_0^i \tag{6.6.100}$$

and the reflected stub voltage is given by

$$VL_{Ub}^r = \frac{V}{Z_L(t)} - VL_{Ub}^i \tag{6.6.101}$$

or, in per-unit-voltage terms, by

$$VL_{Ub}^r Z_L(t) = V - VL_{Ub}^i Z_L(t) \tag{6.6.102}$$

The transmission line model of these equations are shown in Figure 6.6.21(a) alongside the Thevenin equivalent circuit in Figure 6.6.21(b).

It can be easily shown that the use of this model with a fixed boundary position, $\dot{Z_L}(t) = 0$, produces the same result as for the normal stub shown previously in this chapter. Furthermore, this model can be easily extended to 2D and 3D. In order to implement this the parameters dependent on boundary position, that is the boundary port and stub voltages, are replaced with their per-unit-stub equivalent in the same manner as demonstrated here. A 3D implemention of the time varying boundary model is used in Chapter 7 to demonstrate the effect of cavity wall vibrations on the resonant nature of the cavity.

6.6.2 Validation

The model developed here allows the modelling of a time varying boundary velocity directly within the mesh. In order to validate the model the response of the transmission line terminated by a vibrating wall can be measured. A sinusoidally varying voltage is applied to the line and the received voltage after a reflection from the vibrating wall is measured. One would expect to observe a Doppler shift due to the moving wall in the reflected voltage.

Assuming the boundary moves in a sinusoidal motion with maximum displacement d_0, the time varying distance d(t) to be modelled is given by

$$d(t) = \frac{d_0}{2}\left(1 + \sin(\omega_B t)\right) \tag{6.6.103}$$

Hence, the time varying impedance of the additional transmission line is given by

$$z_L(t) = \frac{z_0 d_0}{\Delta l}\left(1 + \sin(\omega_B t)\right) \tag{6.6.104}$$

It is ensured in (6.6.103) that the displacement does not fall below zero as this would lead to a negative inductance on the transmission line and the model would become non-causal and unstable [40].

An analytical solution can be derived for this particular simulation so confirm its validity. The Doppler shift of an electromagnetic wave with velocity c due to a source moving away from a receiver with velocity v is given by [57]

$$\omega = \omega_0 \gamma \left(1 - \frac{v}{c}\right)^{-1} \tag{6.6.105}$$

where ω is the measured frequency, ω_0 is the source frequency and γ is the time

dilation parameter given by

$$\gamma = \frac{1}{\sqrt{1 - v^2/c^2}} \tag{6.6.106}$$

In (6.6.106) the velocity of the source in the vibrating wall case is given by the velocity of the wall. The velocity of the wall is very small compared to the speed of light ($v \ll c$) so $\gamma \approx 1$. Both the source and the receiver are to the left of the boundary in Figure 6.6.21(a) so the image of the source appears to move at twice the wall velocity. Using a Taylor expansion (6.6.105) can be approximated, where we assume $v/c \ll 1$, to give

$$\omega \approx \omega_0 \left(1 + \frac{2\dot{d}}{c}\right) \tag{6.6.107}$$

Substituting for the boundary displacement yields

$$\omega(t) = \omega_0 \left(1 - \frac{\omega_B d_0}{c} \cos(\omega_B t)\right) \tag{6.6.108}$$

A sinusoidal wave of frequency ω_0 is applied to the transmission line incident toward the vibrating wall such that

$$V_{in}(t) = \cos(\omega_0 t) \tag{6.6.109}$$

The received reflected wave is given by

$$V_{out}(t) = \cos\left(\theta(t)\right) \tag{6.6.110}$$

where $\theta(t)$ is the instantaneous phase of the received wave when

$$\omega(t) = \frac{d\theta(t)}{dt} \tag{6.6.111}$$

Therefore, substituting for $\omega(t)$ from (6.6.108) and integrating yields

$$\theta(t) = \omega_0 t + \frac{d_0 \omega_B \omega_0}{c\omega_B} \sin(\omega_B t) \tag{6.6.112}$$

A useful substitution can be made at this stage by considering the maximum value of ω in (6.6.108). This occurs when $\cos(\omega_B t) = 1$ so the maximum frequency is given by

$$\omega_{\max} = \omega_0 \left(1 + \frac{d_0 \omega_B}{c}\right) \tag{6.6.113}$$

and the maximum frequency deviation from the input frequency is given by

$$\Delta\omega = |\omega_0 - \omega_{\max}| = \frac{d_0 \omega_B \omega_0}{c} \tag{6.6.114}$$

Substituting (6.6.114) in (6.6.112) allows the instantaneous phase to be written in the form

$$\theta(t) = \omega_0 t + \frac{\Delta\omega}{\omega_B} \sin(\omega_B t) \tag{6.6.115}$$

The output voltage is then given by

$$V_{out}(t) = \cos\left(\omega_0 t + m \sin(\omega_B t)\right) \tag{6.6.116}$$

where we define

$$m = \frac{\Delta\omega}{\omega_B} \tag{6.6.117}$$

It can be seen that (6.6.116) has exactly the same form as a frequency modulated (FM) wave, where m is the *modulation index* and determines the bandwidth of the modulated signal. The spectrum of an FM signal has a centre carrier frequency ω_0 and numerous sidebands which extend off to infinity with spacing equal to the modulating frequency, (ω_B in this case).

The spectrum of the reflected signal can be obtained by expressing (6.6.116)

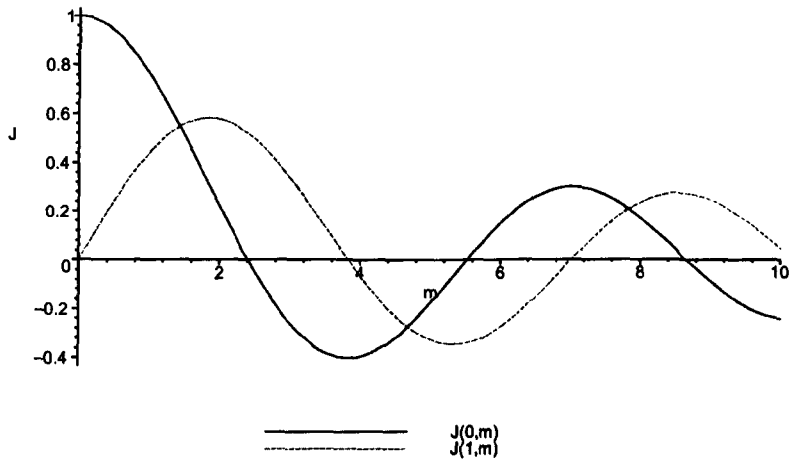

Figure 6.6.22: Bessel functions of the first kind for $J_0(m)$ and $J_1(m)$

in terms of Bessel functions [58] so that

$$\begin{aligned} V_{out}(t) &= J_0(m)\cos(\omega_0 t) \\ &+ \sum_{k=1}^{\infty} J_{2k}(m)\left[\sin\left((\omega_0 + 2k\omega_B)\,t\right) + \sin\left((\omega_0 - 2k\omega_B)\,t\right)\right] \\ &+ \sum_{k=0}^{\infty} J_{(2k+1)}(m)\left[\cos\left((\omega_0 + (2k+1)\omega_B)\,t\right) + \sin\left((\omega_0 - (2k+1)\omega_B)\,t\right)\right] \end{aligned} \tag{6.6.118}$$

Therefore the reflected signal in (6.6.118) consists of the carrier at a frequency of ω_0 and pairs of side bands that occur at integer multiples of ω_B on either side of the carrier frequency. The spacing of the sidebands is independent of the modulation index m, which determines the relative amplitudes of the carrier and sidebands. For low values of m the sidebands rapidly reduce in amplitude and normally only one or two sidebands are seen around the carrier frequency. The magnitude of each can be found from a plot of the Bessel functions as shown in Figure 6.6.22. The centre frequency magnitude is found at the value of $J_0(m)$, the first sideband at $J_1(m)$ and the n^{th} sideband at $J_n(m)$. Generally the bandwidth of the FM signal is taken to be $B_T = 2(\Delta\omega + \omega_B)$ or, substituting (6.6.117), the number of sidebands with significant power n is given by $n = 2(m + 1)$.

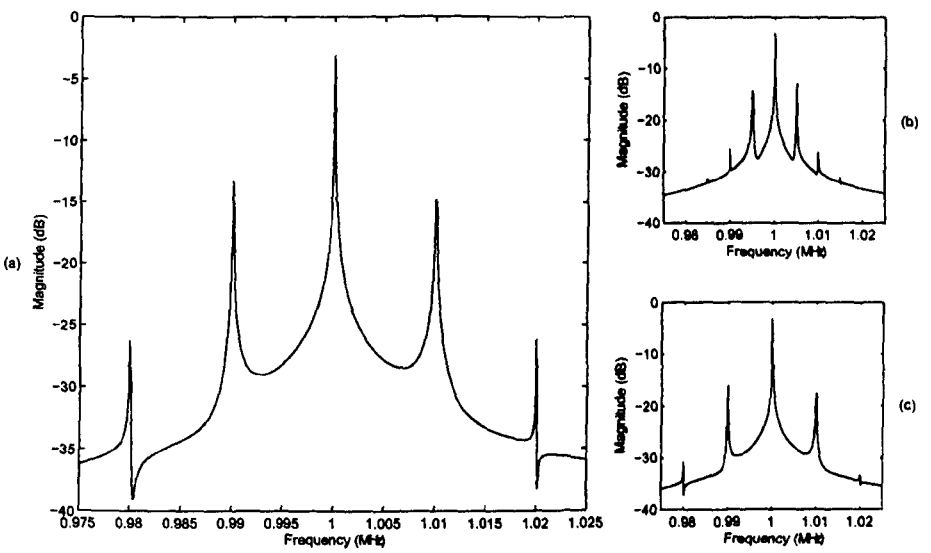

Figure 6.6.23: Frequency of received signal from a wall vibration where (a) $d_0 = 10m$ and $\omega_B = 10kHz$, (b) a change in oscillation frequency, $\omega_B = 5kHz$ and (c) a change in oscillation amplitude, $d_0 = 5m$.

In order to validate the model a sinusoid of frequency $\omega_0 = 2\pi \times 1MHz$ is applied to the line with a boundary vibrating with frequency $\omega_B = 2\pi \times 10kHz$ and amplitude 10m. Using (6.6.117) the modulation index of this system will be

$$m = \frac{d_0\omega_0}{c} = 0.209 \tag{6.6.119}$$

There should therefore be one significant sideband pair and using Bessel functions as described above the ratio of magnitudes of the carrier and first sideband is

$$\frac{J_1(0.209)}{J_0(0.209)} = 0.105 \tag{6.6.120}$$

The simulation result for this test is shown in Figure 6.6.23(a) and the ratio calculated from the result is 0.102. This shows good agreement with the analytical value expected. If the boundary frequency is reduced to 5kHz the result of Figure

6.6.23(b) is obtained. It can be seen that the sidebands have shifted closer to the carrier peak as would be expected from (6.6.118). The modulation index is independent of ω_B so the ratio of sideband to carrier magnitude should not change. Calculating this value from the simulation gives a ratio of 0.104 indicating that the ratio has not changed and is still equal to the analytical value.

Reducing the amplitude of the boundary oscillation will change the modulation index m and hence the ratio of the sideband to carrier. The result of reducing the boundary oscillation amplitude to 5m can be seen in Figure 6.6.23(c). As expected the sidebands have not shifted in frequency but changed in magnitude. The magnitude ratio from Figure 6.6.23(c) is 0.493 showing good agreement with the analytical ratio of 0.523.

It can be seen from the results above that the vibrating boundary will cause sidebands to be introduced around the carrier frequency of the signal. It has been shown that these will be positioned at integer multiples of the boundary oscillation frequency around the carrier frequency. Structual vibrations therefore not only vary the modal structure within the cavity, akin to the stirrer in a reverberation chamber but also act to increase the density of modes in the cavity.

In an aircraft environment we would not expect to see vibrations with frequencies above the order of a few kilohertz. A wireless system that is used in the cavity will have a bandwidth associated with its channel. ZigBee, for example has a channel bandwidth of 5MHz. Therefore all of the significant sidebands will occur within the ZigBee bandwidth and therefore it is likely that they will have an impact on the signal transmission.

6.6.3 Model Stability

The time varying boundary has been developed such that it conserves energy, however a number of difficulties can be encountered during modelling. It has been found that in a resonant cavity, in the absence of significant loss, where the boundary vibration oscillates to a minimum displacement close to zero an instability can occur. It is not clear at the time of writing where the instability arises from but has been found to be highly sensitive to the minimum extension of the boundary. The instability appears after a large number of iterations in the form of a high frequency oscillation, which grows and saturates the data of interest in the model.

From experimentation the instability appears to be dependant on the minimum extension of the boundary and not the peak-to-peak amplitude of the boundary it is felt that stability issues are due to numerical instabilities. Experimentation using a peak-to-peak amplitude of $0.9\Delta l$ and a minimum displacement of 0.01 and 0.1 revealed that the former would become unstable whereas the latter would not. It is possible that there are other sources of the instability such as incorrect conservation of energy in boundary however this taken into account by using per-unit stubs to model the boundary. Further work would be required to ascertain whether the steps taken to conserve energy in the TLM model are sufficient for such problems. Further investigation into the energy conservation of model were not possible in this work.

The most likely cause of the instability is numerical noise. The resonant nature of the environment of interest, and the boundary extension, lead to a periodic amplification of rounding error. It can be seen from (6.6.101) that as the boundary extension approaches zero that the current in the boundary approaches a large number and the voltage a small number. As the boundary is extended during the

simulation any rounding error is amplified through the term $2V_b^i Z_L(t)$. It has been found that stopping the boundary oscillation at any point ceases the growth of the instability. Through thorough numerical experimentation a number of possible solutions to the problem have been identified. These are given below in the order of merit in terms of modelling flexibility and resulting modelling error.

Introduce a loss within the boundary By introducing a loss in the boundary we can ensure that energy is dissipated and not able to grow and cause an instability. This approach is not ideal however as we may be required to model a loss far greater than we would wish to and model an incorrect Q factor.

Limit the minimum boundary displacement If possible, limiting the minimum displacement of the boundary has been shown to prevent the instability. It has been found that by ensuring that $d \geq 0.1\Delta l$ the model does not become unstable within a large number of timesteps. Limiting the boundary displacement may not be ideal as we may wish to model the maximum possible displacement of Δl.

Introduce filtering within the boundary Finally, the most elegant method of preventing the instability is to introduce filtering into the boundary so that only high frequency noise, that is the frequency of the instability, is filtered out. The modelling approach for the 1D stub is as follows and can be easily expanded to 2D and 3D by modifying the capacitive and inductive stubs in the model.

The reflected voltage in the unmodified 1D inductive stub is given by (6.6.121)

$$_kV^r_{bLx} =_k V -_k V^i_{bLx} \tag{6.6.121}$$

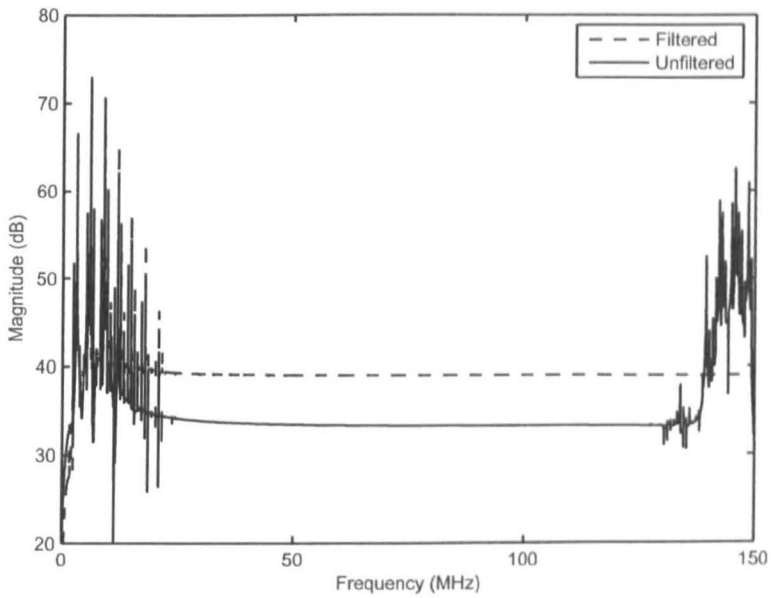

Figure 6.6.24: Vibrating cavity response with and without filtering (full frequency range)

Through introduction of a filtering factor α the filtered reflected voltage is given by

$$ {}_kV^r_{bLx} = \alpha {}_kV + (1-\alpha) {}_{k-1}V - {}_k V^i_{bLx} \tag{6.6.122} $$

or more compactly

$$ {}_kV^r_{bLx} = {}_k V - {}_k V^i_{bLx} + V_{alpha} \tag{6.6.123} $$

where $V_{alpha} = \alpha \left({}_{k-1}V - {}_k V \right)$ and can be considered to be the modification due to the filtering. If $\alpha = 0$ then the model reduces to the unmodified model condition in (6.6.121).

Through experimentation it has been found that a choice of $\alpha = 0.01$ is sufficient to ensure that the model is stable for minimum boundary displacements of $0.0001 \Delta l$. The effect on the result is negligible as can be shown by the example in Figures 6.6.24 and 6.6.25 where the filtered and unfiltered results can be seen. Here the example problem was a simple cavity test case consisting of a single vibrating wall.

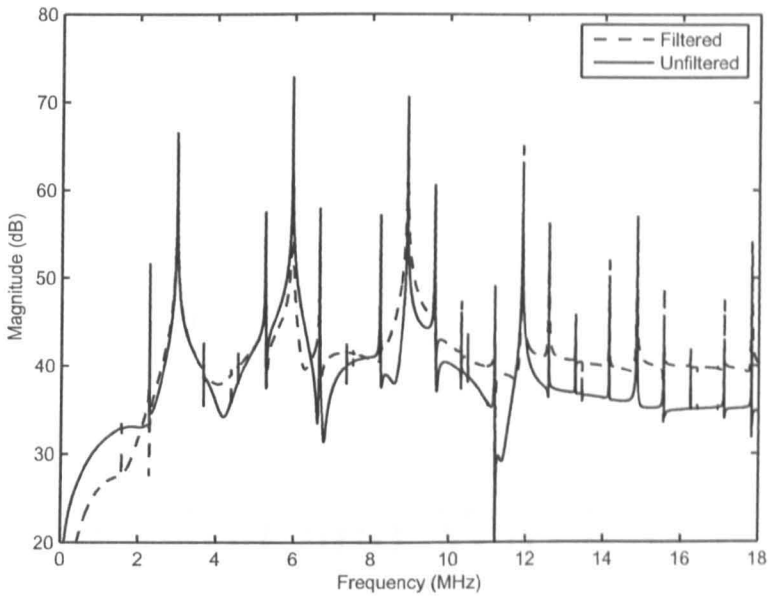

Figure 6.6.25: Vibrating cavity response with and without filtering

The peak-to-peak vibration amplitude was set to $0.998\Delta l$ with a frequency of 700kHz, the simulation was run for a total of 131072 timesteps. In the filtered case a filtering coefficient of $\alpha = 0.01$ was used. The unfiltered result becomes unstable as the high frequency components in Figure 6.6.24 continue to grow. The introduction of the filtering term has been shown to not significantly effect the model results but removes the instability issue. Whilst filtering is not ideal it is often necessary when modelling systems that are very sensitive to numerical noise and rounding errors [59], [39]. In this case the use of filtering is not detremental to the accuracy of the results obtained so is a satisfactory solution to the instabilities that can occur if this model is used rigourously.

Chapter 7

Propagation and Wireless Modelling Examples

The models developed in Chapters 4 to 6 are capable of the modelling the environments that are likely to be encountered if a wireless system were to be operated inside an aircraft structure or similar. This chapter demonstrates the use of these models to some of the environments and scenarios described in Chapter 2. In this way, it is possible to demonstrate some of the important effects of the environment on signal propagation within the structure.

7.1 Model Summary

The intended application of the models and tools developed here was to provide a modelling approach and channel characterisation for use within an aircraft environment. This application formed the basis of the collaborative research project

Towards a Wireless Aircraft [8] as part of the wider FLAVIIR project [1]. The physics and characteristics of the environments of interest are described in this thesis in order to derive the models.

As suggested in Chapter 1, the models can be applied to any environment that possesses the properties of the environments being considered here. The model developed in Chapter 4 is valid when the differential propagation delay is small compared with the bit period. This implies that the cavity must be small, that is of dimensions of approximately ten wavelengths or less, and low loss such that the quality factor of the cavity is high.

The coupled cavity model developed in Chapter 5 is suited to the same environments as the single cavity model. The model is valid in low loss environments and is most accurate when considering the lower order modes of the cavity. This limits the validity of the model to small cavities relative to wavelength again in the same way as the single cavity model. Both models are very efficient and can be used for thorough analysis of the environments of interest.

The third model developed in Chapter 6 is an extension to the transmission line modelling method. This is a full field time domain model that solves Maxwell's equations in all regions of modelled space. The approach developed here is designed to augment an efficient symmetrically condensed node mesh with a fractionally positionable boundary. Therefore the model is not limited to the domain of validity of the previous two models and is a more general modelling tool. The model is suitable for any common field modelling application and problem size given sufficient resources. The model is accurate for PEC and PMC boundary modelling with errors increasing if a significant loss is required in the boundary as shown in Chapter 6.

The model also enables the modelling of dynamic systems where the structure varies during the simulation. This make this model a powerful tool for any scenario where a boundary needs to be adjusted or where vibrations, for example, cause the structure to vary in time. The model offers significant advantages over the graded mesh approach as the simulation time step does not need to be reduced with reducing cell size. Such a model is also ideal for optimisation problems, in resonators or waveguides for example as the mesh spacing and time step can remain fixed for all simulations of a given structure.

7.2 Resonant Cavity Problems

The model developed in Chapter 4 can be used to model the effect of a characteristic channel on some of the wireless modulation and processing approaches that were described in Chapter 3. In this section some results produced using this model are presented so that an assessment can be made on the wireless systems and their effectiveness within the cavity model.

7.2.1 BPSK

In the first instance the robustness of a standard BPSK signal is simulated in the channel model. Here a statistical approach is used to set up the parameters of the channel model so that the average effect of the channel on the wireless signal can be assessed. The variables of interest in this study are the Q factor of the cavity and the density of modes within the cavity. The Q factors used are 500, 1000, 2000 and 5000 where the upper limit is chosen as in the cavities of interest it is unlikely that Q factors will exceed this value. In laboratory based reverberation chamber studies much higher Q factors can be achieved [23], [45].

The frequency of interest is centred around 2.45GHz to correspond to that used in the majority of currently available wireless systems. The density of modes was chosen to vary between 0.1 and 1 mode per megahertz. Therefore, using (2.2.29), this can be seen to correspond to a single cavity volume of $0.018 - 0.18m^3$ or a cubic side length of $0.26 - 0.56m$. These parameters are used to set up the model so that a BPSK modulated signal may be passed through it. As described in Section 4.4 the density of modes was used to define the number of randomly positioned modes across the bandwidth of interest. In this case, due to the wide bandwidth of the unfiltered BPSK signal the modelled bandwidth was chosen to be $f_c \pm 0.1 f_c$. The Q factor was used to set the width of each mode within the channel model. In this case the amplitude of the modes was chosen to have a Gaussian distribution with a mean $\mu = 0.5$ and a variance of $\sigma^2 = 1$ truncated at 0.0 and 1.0.

The bit error ratio BER for the BPSK modulation approach is shown in Figure 7.2.1. The Q factor can be seen to have a significant effect on the BER. For example, at a modal density of 0.6 modes/MHz there is an increase in BER of two orders of magnitude with an increase in Q factor of 1000 to 2000. Then, a further order of magnitude increase in BER with an increase in Q factor to 5000 can be observed.

Furthermore, the BER can be seen to decrease with an increase in modal density. This trend is consistent for all Q factors however an increase in gradient can be observed at lower Q factors. This suggests that in a high Q factor cavity the BER is less dependent on modal density than in a low Q factor cavity.

The dependency of the BER on the Q factor can be understood by referring to the arguments of Chapter 2. Consider the signal is propagating through the channel constructed using resonant poles as it has been developed here. Using (2.2.8) the higher the Q factor then the narrower the resonant peak in the channel

response. Furthermore, increasing the Q factor has been shown to increase the mean excess delay, that is the decay time, of the resonant oscillation that coincides with the signal power being applied to the channel.

The dependancy of the BER on the density of modes can be considered in terms of the ability of the channel to transmit the energy of the signal. At low modal densities the number of resonant peaks in a given bandwidth is low and hence the troughs between the peaks will be wider. The width of the troughs also increases with increasing Q factor as the peaks themselves are narrower. Therefore, the probability of signal power coinciding with a trough, where energy does not propagate efficiently, is increased with both increasing Q factor and decreasing modal density.

In order to reduce the probability of error within a channel there are a number of possible solutions. It is clear that reducing the Q factor will reduce the number of errors. This could be achieved by increasing the loss within the cavity, perhaps by adding a lossy material to the cavity. This would have a number of disadvantages however, adding lossy material to the cavity will add weight to the cavity which may not be desirable, especially in an aircraft. Furthermore, adding loss to the cavity will also absorb the energy of the signal that we are trying to propagate. In some cases the received power could already be low and reducing this further could lead to more errors and increase the susceptibility of the system to noise and interference.

Alternatively the density of modes within the cavity could be increased. Referring to (2.2.29), this can be done by increasing the volume of the cavity or increasing the frequency being used. It would be difficult to increase the volume of the cavity due to physical restrictions. Increasing the frequency of the signal may also not be possible as the power requirements of the system would increase,

this would also require modification to cost effective COTS systems.

7.2.1.1 Use of DSSS

An alternative solution is to modify the signal itself so that it is not as influenced by the bandlimiting nature of the channel. In Chapter 3 the direct sequence spread spectrum (DSSS) method is presented as a means of increasing the useful bandwidth of the signal [34]. A method of this type is also used in many of the COTS systems mentioned. Increasing the bandwidth of the signal through such an approach may reduce the number of errors as the signal is spread over a number of peaks within the channel.

In order to assess the impact of a DSSS on the BER obtained in the channel the same modelling approach was performed as previously. However, this time the signal is spread using DSSS before being sent through the channel. The modulation used remains the same as before, an unfiltered BPSK modulation, and the errors calculated in the same manner.

The spreading codes used are maximal-length sequences obtained using shift-registers as described in Appendix A. Three different lengths of code were investigated; a 7 bit code

$$b(t) = \{1, 1, 1, 0, 0, 1, 0\} \tag{7.2.1}$$

a 15 bit code

$$b(t) = \{1, 1, 1, 1, 0, 0, 0, 1, 0, 0, 1, 1, 0, 1, 0\} \tag{7.2.2}$$

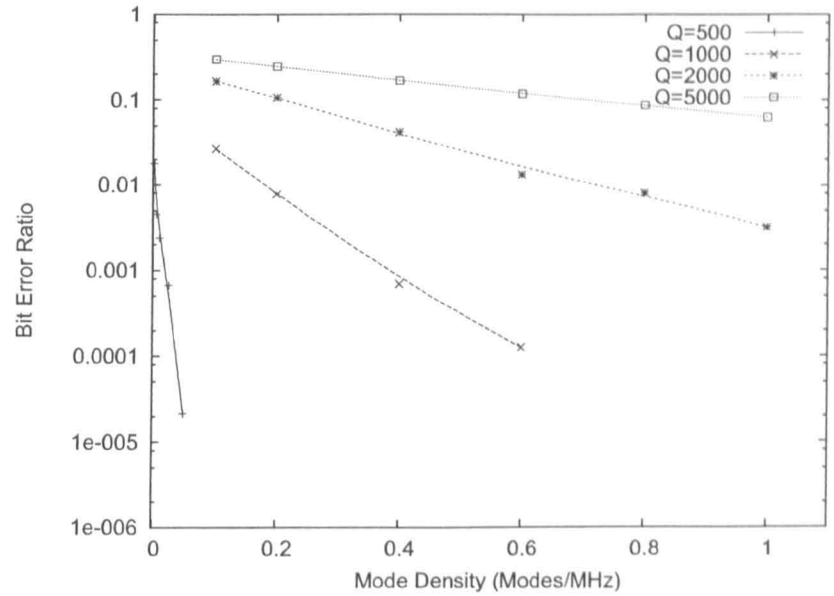

Figure 7.2.1: BER variation with Q factor and modal density using BPSK modulation

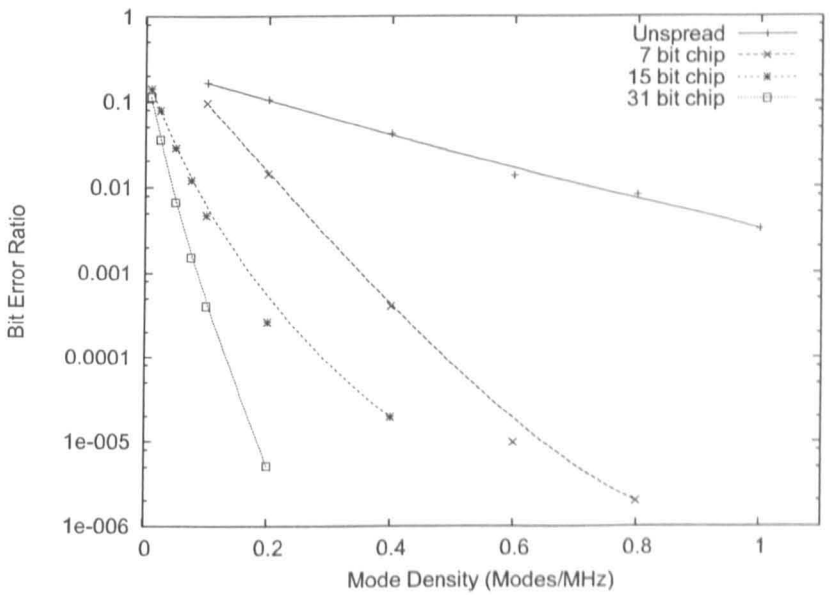

Figure 7.2.2: BER variation with modal density in a Q=2000 channel using DSSS with a number of expansion factors

and a 31 bit code

$$b(t) = \{1,1,1,1,1,0,0,0,1,1,0,1,1,1,0,1,0,1,0,0,0,0,1,0,0,1,0,1,1,0,0\} \tag{7.2.3}$$

Figure 7.2.2 shows the error rates for a Q factor of 2000 using the various lengths of spreading code.

The error rate has been reduced considerably by using a DSSS approach prior to modulation in order to increase the bandwidth of the signal. At a modal density of 0.2 modes/MHz a five order of magnitude reduction in error rate has been achieved when using a 31 bit spreading sequence. This shows that the DSSS used in systems such as ZigBee is efficient in reducing the number of errors in a highly resonant channel [32].

Figures 7.2.3 and 7.2.4 show the error rate variation with an expansion factor, or chip length, of 7 and 15. An increase in the expansion factor from 7 bits to 15 bits can be seen to reduce the BER by on average one order of magnitude. This is very useful as the DSSS method is low power and can be implemented using a hardware based system rather than complex software based systems, like for example the OFDM system used in wireless LAN [37].

7.2.2 Filtered BPSK

In Chapter 3 the use of filtering or pulse shaping was introduced as a means of limiting the bandwidth of a wireless signal. Filtering is normally applied to reduce interchannel interference between the discrete bandwidth channels. Specific pulse shaping is used to minimise intersymbol interference by carefully selecting zero crossings that coincide with adjacent bits.

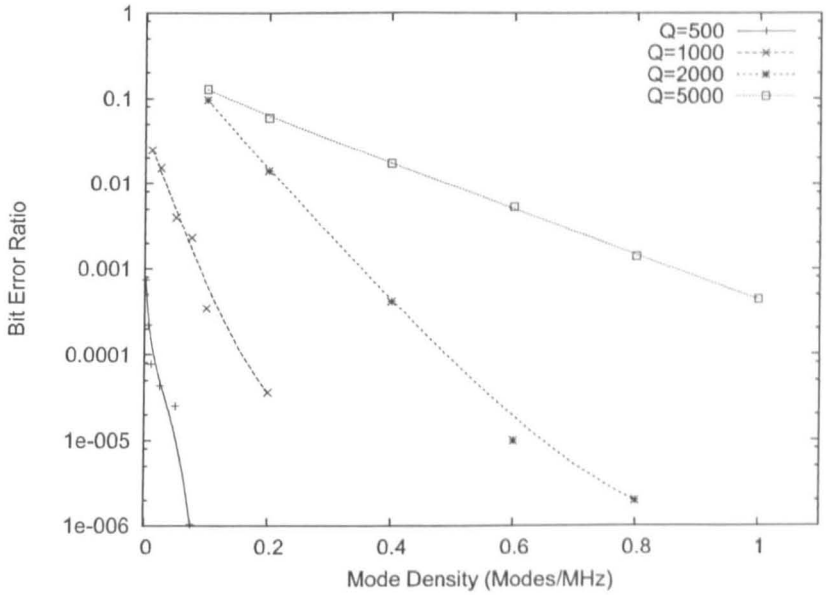

Figure 7.2.3: BER variation with modal density using DSSS with an expansion factor of 7 prior to modulation

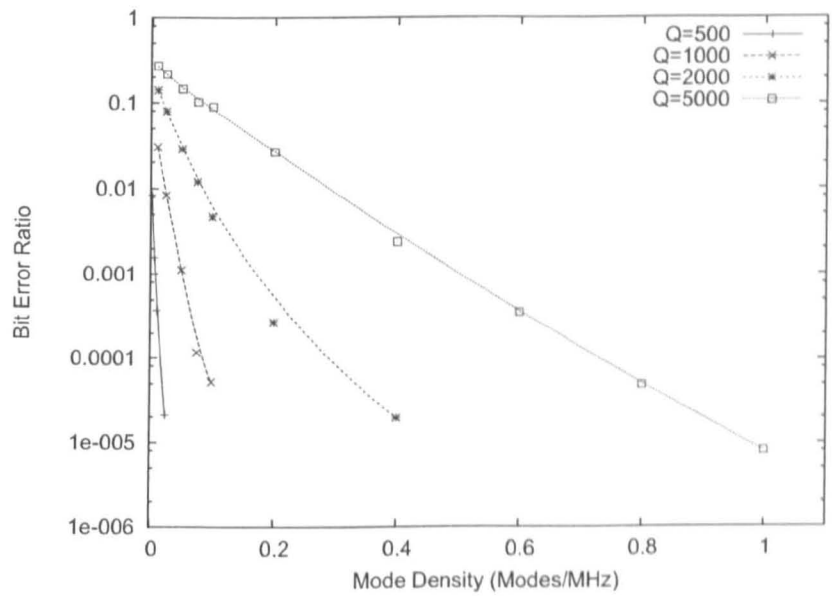

Figure 7.2.4: BER variation with modal density using DSSS with an expansion factor of 15 prior to modulation

In order to assess the effect of using pulse shaping in the highly resonant environments being considered here the raised cosine pulse shaping is applied to the signal used in the previous example. The error rate is then assessed and compared to the equivalent BPSK system without pulse shaping. A flow chart of the modelling process can be seen in 7.2.5 where the pulse shaping is shown to take place after the spread spectrum process. The pulse shaping is performed on bits between $n \pm 6$ to take account of the non-causal nature of the raised cosine function.

At a Q factor of 1000 the BER using raised cosine filtering can be seen in Figure 7.2.6. The error rate for the equivalent unfiltered signal can also be seen in the figure for comparison. It is clear that the filtering of the BPSK signal using the raised cosine pulse shaping, as is common when using BPSK [11], increases the BER in the resonant channel. The rate of increase in BER when compared to the unfiltered result also increases with increasing modal density.

It is clear that reducing the bandwidth of the wireless signal increases the BER in the resonant channel. The probability of the signal falling into a trough in cavity response spectrum is greatly increased by reducing the bandwidth of the signal. Furthermore, as the signal is narrow in frequency the BER reduction effect of increasing modal density is not as great as for a wider band signal. By covering a wider bandwidth the unfiltered signal is affected by a greater number of modes than the filtered signal for a given modal density. Therefore, we do not observe a linear relationship between the filtered and unfiltered signal with varying modal density.

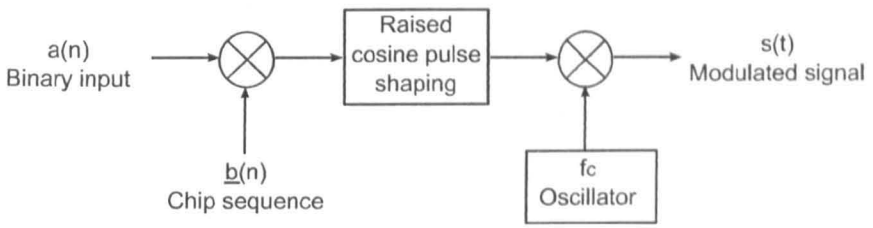

Figure 7.2.5: Raised cosine shaped BPSK modulation process

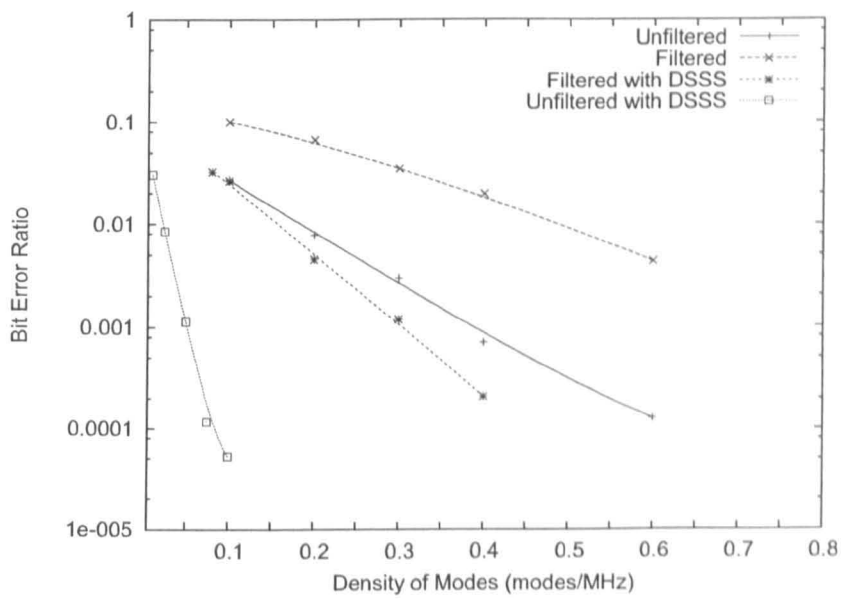

Figure 7.2.6: Effect of raised cosine filtering on the BER of a BPSK signal (Q=1000)

7.2.3 Bit Period

The resonant decay behaviour of the cavity that is parameterised by the Q factor or mean excess delay is a significant factor in the error rates seen when attempting to communicate in the cavity. In Section 7.2.1 it was shown that the increasing Q factor leads to an increasing number of errors.

The density of modes and the modal structure determine the *shape* of the data that is transmitted through the channel. The Q factor impacts the signal by adding reflections after its transmission that will impact subsequent bits that are transmitted. The greater the Q factor the greater the degree of bit blurring that occurs due to these reflections. In order to minimise the impact of a previous bit on the current bit being transmitted the bit period can be increased. This allows more time for the previous bit's energy to decay within the cavity.

The Q factor or mean excess delay and the bit length are therefore related in terms of the resultant BER that will occur. In order to assess the effect of the bit length on the BER a number of simulations were performed using the model developed in this chapter. Using three different Q factors the BER of an unfiltered BPSK signal was simulated in the channel model. The results can be seen in Figures 7.2.7-7.2.9 where in each case three modal densities were used and the length of the bit was varied.

The effect of increasing the bit length is to reduce the BER for the signal transmission in all cases. This is as expected as increasing the bit length means that each bit is less influenced by its predecessor. The effect of increasing the modal density is common to all Q factors tested, in all cases the effect of increasing the modal density is to reduce the BER.

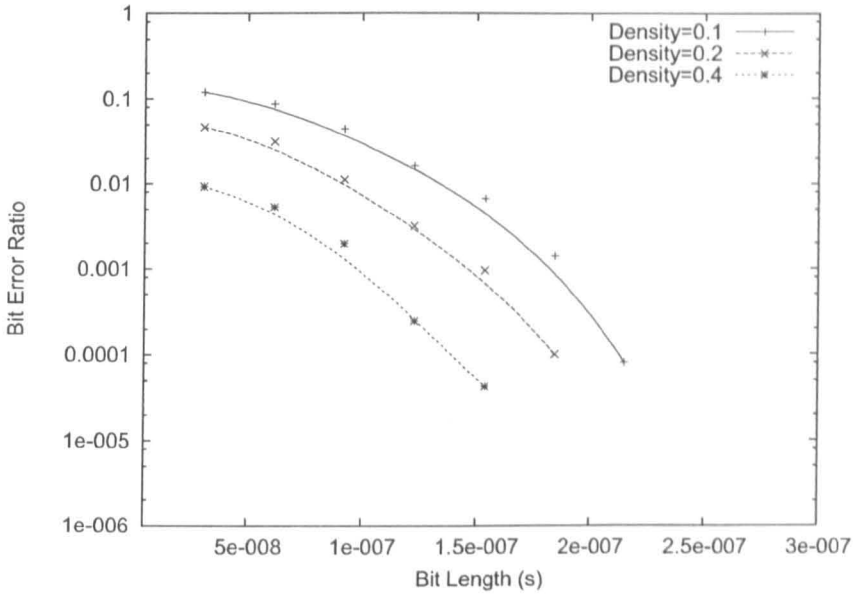

Figure 7.2.7: Impact of the bit period of a BPSK signal on the BER (Q=1000)

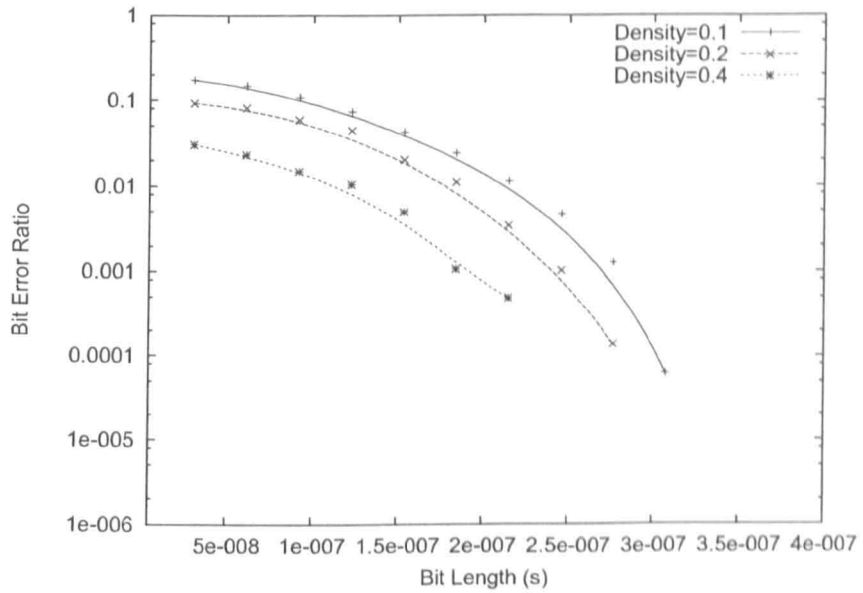

Figure 7.2.8: Impact of the bit period of a BPSK signal on the BER (Q=1500)

It was shown in Chapter 2 how the Q factor and the mean excess delay are related. It is possible to investigate the relationship between the mean excess delay in the resonant cavity and the BER. In order to demonstrate the link between the mean excess delay and the BER the Q factors can be converted into a mean excess delay using the result in (2.2.19), that is

$$\overline{\mu} = \frac{Q}{2\omega_0} = \frac{Q}{4\pi f_0} \tag{7.2.4}$$

Recalling that this expression is valid for the single high Q cavity means that it can be used in this case to obtain an equivalent mean excess delay for the cavity problem.

The ratio of the calculated mean excess delay to the bit period can then be used as the independent variable in order to assess whether the Q factor and bit period are related in this manner in the resonant channel. The modelled variable is the bit period and in each case the Q factor is kept constant. The result for three Q factor values can be seen in Figure 7.2.10 where there is very good agreement between the result for each Q factor. The modal density used in this example was 0.1modes/MHz corresponding, for example, to a cubic cavity with 25cm edge lengths.

Equally the relationship between the bit period to mean excess delay ratio and to the BER can be demonstrated by keeping the Q bit period fixed and varying the Q factor of the cavity. In the same way as before the Q factor used was converted into a mean excess delay, the result is shown in Figure 7.2.11. Again, the modal density used was 0.1 modes/MHz. A result obtained using the bit period as the independent variable is also shown for comparison. Good agreement can be seen between the two approaches indicating that the factor which governs the BER is the ratio of the mean delay (related to the Q factor) to the bit period for a fixed

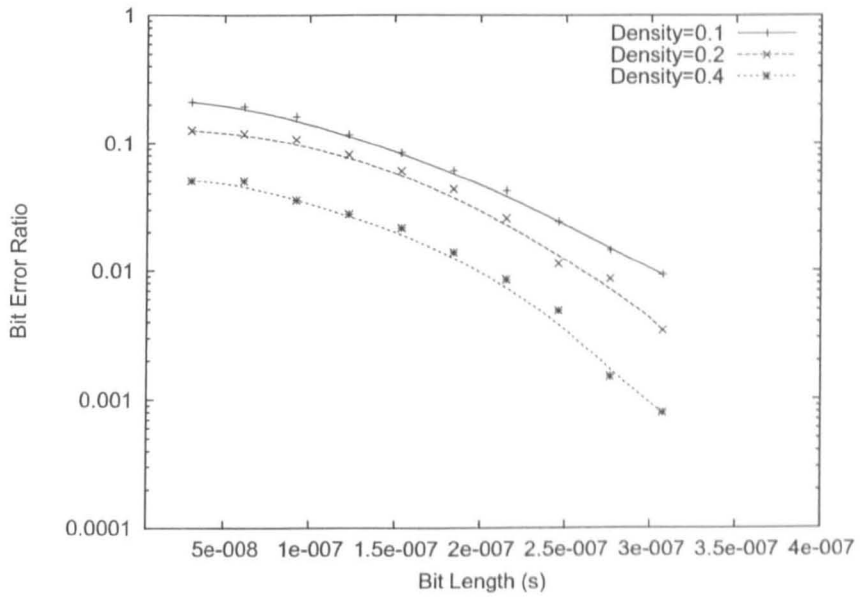

Figure 7.2.9: Impact of the bit period of a BPSK signal on the BER (Q=2000)

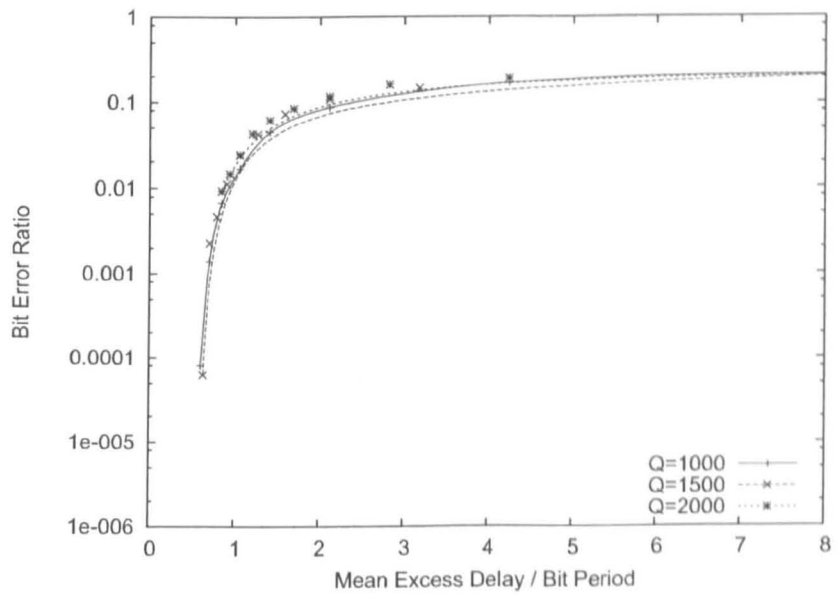

Figure 7.2.10: Effect of the bit period/mean delay ratio of a BPSK signal on the BER at three different Q factors

modal density.

This result is important as it provides a means of estimating the error for a given bit period to mean excess delay ratio. This allows the number of simulations that must be performed to be reduced as the bit period and mean excess delay variables are seen to be coupled. The model developed in this chapter can also be used in a similar manner to obtain the same relationship for other modulation schemes or modal densities.

7.2.4 Summary

The results of this section indicate that the BPSK signal, which is the basis of the suitable wireless systems in this thesis, is effected by the modal density and Q factor of the cavity. The BER of a BPSK signal increases with increasing Q factor due to the increasing bandlimiting nature of the channel. Furthermore, the BER reduces with increasing modal density as the number of modes in the channel increases and the probability of the signal coinciding with a trough in the transmission spectrum is reduced.

Increasing the bit period used in communication increases the bit period to mean excess delay ratio. This reduces the BER in the same manner as reducing the Q factor does as the Q factor is linked to the mean excess delay as defined in Chapter 2.

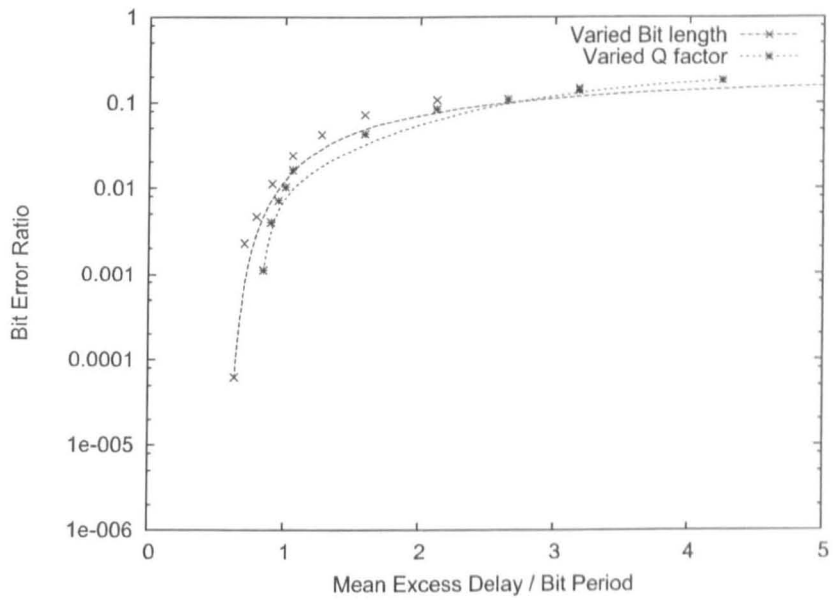

Figure 7.2.11: Effect of the bit period/mean delay ratio of a BPSK signal on the BER calculated using varied bit length or varied mean excess delay

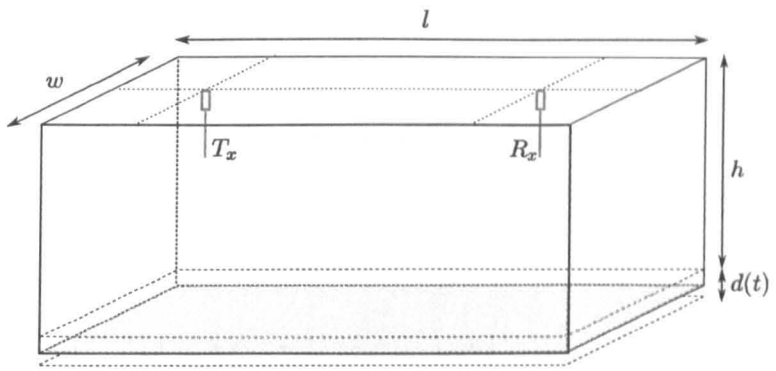

Figure 7.3.12: Schematic of a dynamically varying resonant environment

7.3 Fractional Boundary Problems

Vibrations and time varying structural changes are common in aircraft and other applications considered here, for example in the rail industry. The BER when communicating inside a highly resonant environment has been shown to be highly dependent on the modal structure and density inside the cavity. Sources of time varying structural changes may include:

1. The slow bending of the structure due to forces applied during a change of direction for example.
2. Vibrations due to the natural resonance of the structure excited by external sources such as airflow over a structure.
3. Vibrations due to engine rotation or other sources of high frequency oscillation.

Using the fractional boundary placement model developed in Chapter 6 it is possible to model the effect of structural changes and vibrations. Here, as an example, the effect of structural vibrations on the properties of the cavity will be shown. The model used is based on the simple structure defined in Chapter 2 as

shown in Figure 7.3.12. As an example the static case is that where the metal cavity has dimensions of $l = 30.00cm$, $w = 23.00cm$ and $h = 20.45cm$ so that the cavity supports a large number of modes. The surface that will be vibrating is labelled with the time varying displacement $d(t)$. In this case the peak-to-peak displacement used is 0.9cm.

The cell size used is $\Delta l = 1cm$ giving results accurate to 3GHz and a mesh size of $30 \times 23 \times 20$ cells with a fractional boundary placed on the Z_{min} boundary. The response of the static case was simulated and shown in 7.3.13. The analytical S21 response of a box with these dimensions has been calculated in the usual way and can be seen using the stem plot overlaid onto Figure 7.3.13. The reflection coefficient of the cavity walls were set to a value of -0.998 so that some loss is included in the cavity. The excitation source used was a point source excitation of the E_x field.

Well defined narrow resonances can be seen in addition to deep troughs in the transmission spectrum. Using the boundary placement model the position of the boundary is now varied during the simulation according to the function

$$d(t) = \Delta l + \frac{d_0}{2}(1 + sin(\omega_B t)) \tag{7.3.5}$$

where d_0 is the peak to peak oscillation amplitude (0.9cm) and ω_0 is the oscillation frequency. The boundary oscillation frequency was chosen to be 100kHz in this example. The S21 response of the cavity was calculated in the same manner as before and can be seen in Figure 7.3.14.

The impact of the vibrating boundary is to introduce multiple sidebands into the response around the natural resonances of the static case. This effect is the same as that shown for the 1D transmission line validation problem in Chapter

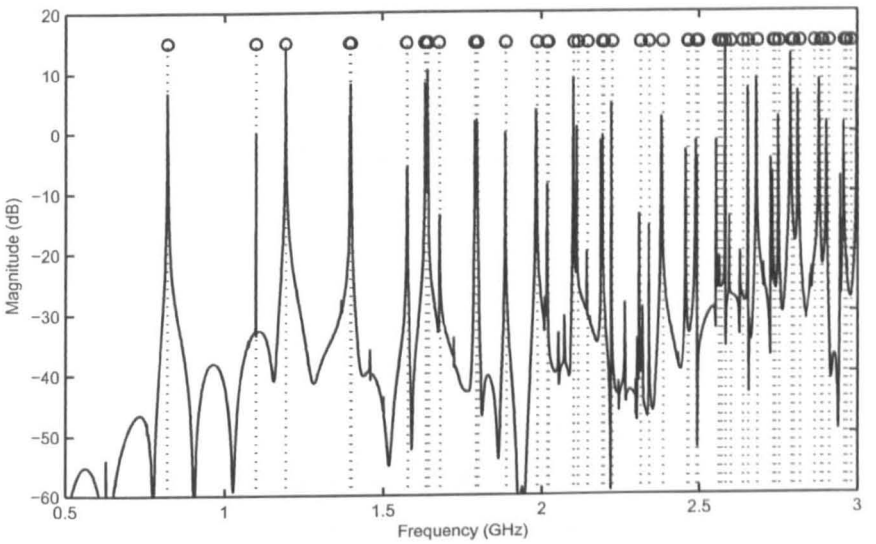

Figure 7.3.13: Response of the static cavity with analytical resonances labelled

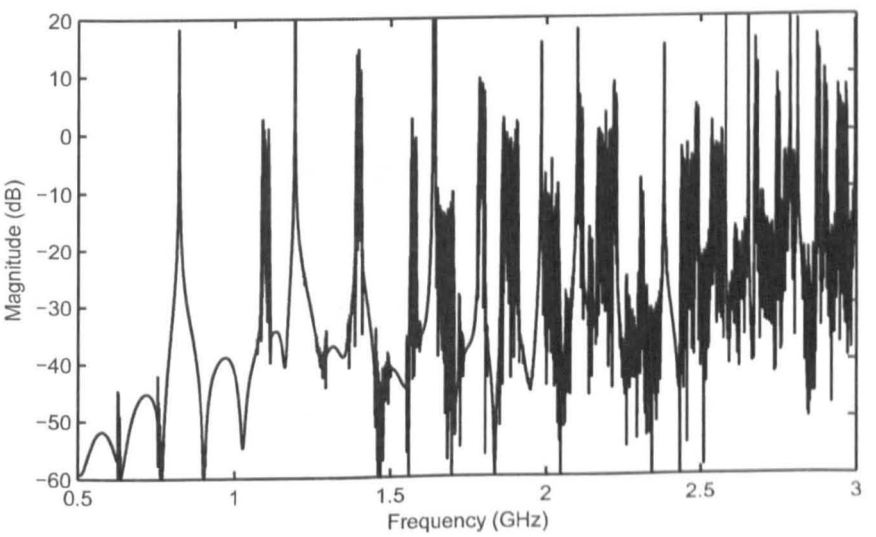

Figure 7.3.14: Response of the cavity with a 100kHz boundary oscillation

6. However, in the example of Chapter 6 the input signal was a single frequency continuous wave with a predefined frequency. In this case the pulse excitation excites all of the modes in the cavity and leads to the resonances seen in the static case. It was shown in Chapters 2 and 4 that the cavity response can be decomposed into exponentially decaying sinusoids which form the peaks seen in the frequency domain. These sinusoids are those that are now modulated by the boundary oscillation.

Furthermore, in this case a signal will be incident on a vibrating boundary a number of times as it propagates within the environment. Therefore, the sidebands formed due to the oscillating boundary have a magnitude that tends towards a magnitude of the centre frequency. This effect can be seen in 7.3.15 where the figure is windowed around the resonance at 1.1GHz.

The vibrating boundary appears to spread the resonant peak out into a number of resonances located around the natural resonance. With each subsequent reflection from the moving boundary power will be transferred to the sidebands and their sidebands in turn. Note that some of the resonances can be seen to not have any sidebands, which are those modes that do not depend on the dimension with the moving boundary. Assuming the time varying $e^{j\omega t}$ term the E_x field of the resonances can be written as

$$E_x = A\cos\left(\frac{m\pi x}{l}\right)\sin\left(\frac{n\pi y}{w}\right)\sin\left(\frac{p\pi z}{h}\right) \tag{7.3.6}$$

Therefore, for a boundary extension in the z dimension and modes where $p = 0$ there is no change to the fields.

Referring to the results of Figure 7.3.14 it can be seen that the spreading in the resonant peaks is independent of their centre frequency. This is most noticable

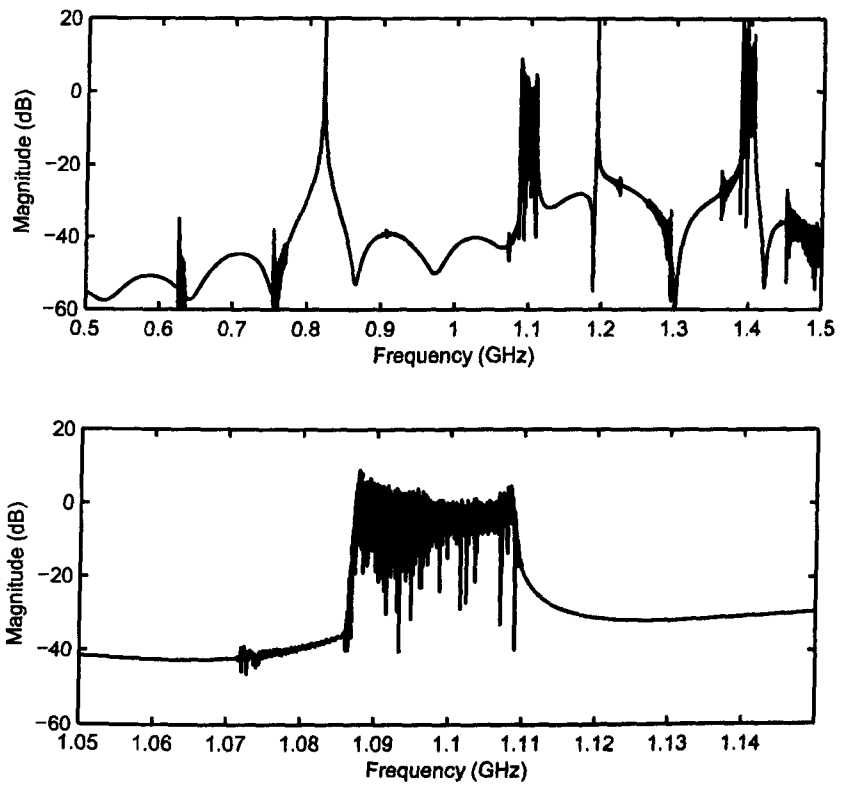

Figure 7.3.15: Response of the cavity with a 100kHz boundary oscillation (windowed regions)

around the isolated resonances close to 1.1GHz, 1.4GHz, 1.6GHz and 1.75GHz This is consistent with the frequency modulating effect described in Chapter 6. It was seen that the effect of increasing boundary oscillation frequency is to increase the spacing between the carrier frequency and its sidebands, as determined by (6.6.118). The same result is expected in the 3D resonant cavity model as the oscillation acts to frequency modulate the resonant nature of the channel. As an example of this effect, the boundary oscillation frequency is increased to 10MHz, which is significantly higher than would be expected in the environments being considered. The new response can be seen in Figures 7.3.16 and 7.3.17. The results demonstrate that the effect of the boundary oscillation frequency is to increase the sideband spacing as a much larger spacing can be seen between the sidebands in this case. As before, the spacing is independent of the resonant frequency.

7.3.1 Practical Impact of Vibrations

The ability to model vibrations during a simulation is significant as it provides a means of modelling variations dynamically. Such an approach was not possible previously without spurious errors or modifying the simulation time step. In the environments being considered the vibrations due to engines and structural resonances would occur at maximum frequencies of 10-100kHz [60]. At a frequency of 100kHz the period of oscillation is $10\mu s$, which as an example, is 10 times that of the ZigBee transmitted bit period [32].

Furthermore, equating the oscillation frequency to the mean excess delay in the cavity and using (2.2.19) gives a Q factor value at 2.45GHz of 77,000. This indicates that the Q factor would have to be at least 7,700 in the cavity for the vibration to effect one tenth of the bit decay. In practical environments it is unlikely that the Q factor will be as high as this, though in the laboratory this is

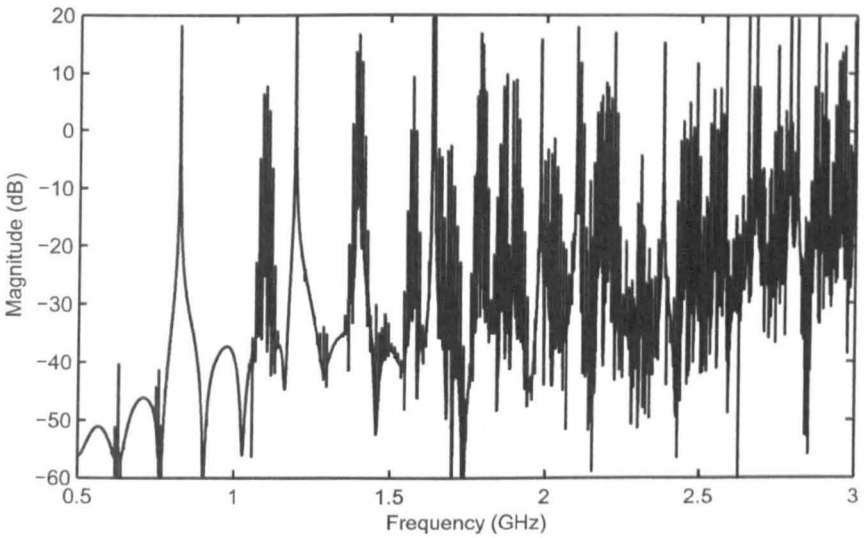

Figure 7.3.16: Response of the cavity with a 10MHz boundary oscillation

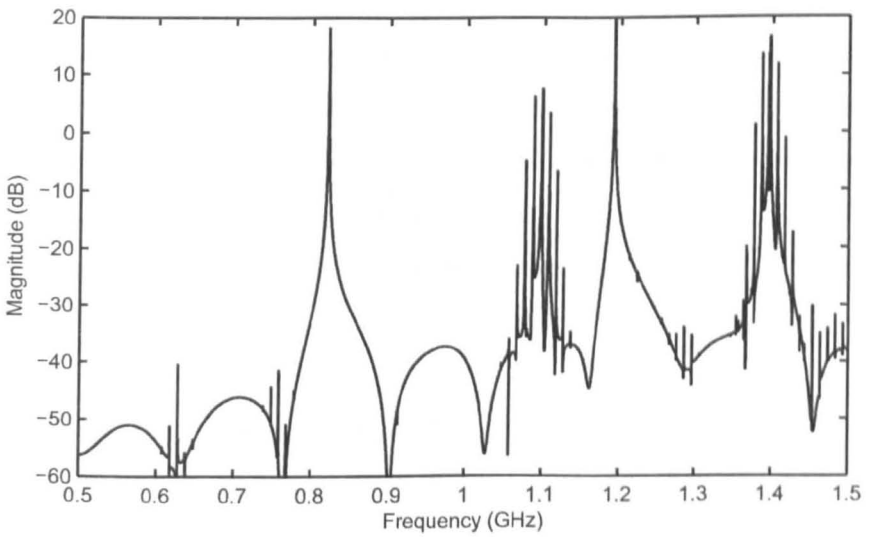

Figure 7.3.17: Response of the cavity with a 10MHz boundary oscillation (windowed region)

achievable [23]. In reality the dominant effect of cavity vibrations and flexing will be the movement of the modes in the cavity that lead to the shifting of modes in the way that is modelled using the filter model of Chapter 4. These long timescale variations can still be modelled using the full-field tool, however it would be more efficient to use the full-field tool to characterise the channel and then use a more efficient filter model to investigate the effect of the channel on a wireless signal. It would be of significant interest to directly simulate the effect of vibrations on the BER of a signal within the cavity. The model developed here would permit such modelling and allow an assessment based on the magnitude, frequency and shape of the structural oscillations. It was not possible to do such modelling within the scope of this work and this would form part of an interesting study in the future using the tools developed here.

7.4 Acute Angle Modelling

The fractional boundary model developed in this work provides a powerful tool when modelling small structural features within the environments of interest. An example of such an environment is an aircraft wing where the internal structure forms an acute angle. An example of such a situation can be seen in Figure 7.4.18 where the structure is seen to form a small angle as might be expected inside the wing.

Consider the case where it is desirable to model the internal structure of the wing using a full-field model in order to investigate the resonant behaviour of the cavity. The structure is large so that in order to model the structure as efficiently as possible a large space step should be used. In the case of a structured TLM approach based on SCN cells the maximum space step should be less than or equal to a tenth of the wavelength of interest in the model. In order to model sloping

surfaces in the mesh it is common to use stair-casing where the sloped surface is used to determine which edges of the square cells form the boundary [13]. The accuracy of this approach is normally sufficient for most applications.

When modelling the example shown in Figure 7.4.18 the space step of the cells is chosen to be Δl. Therefore, it can be seen that in modelling the wedge shaped structure the ratio of horizontal cells to vertical cells is

$$\alpha = \frac{\Delta l}{\Delta l \tan(\theta)} = \frac{\Delta l}{\Delta l \tan(9.614)} \approx 5.9 \tag{7.4.7}$$

If the frequency of interest is that of a wireless system operating at 2.45GHz then the space step that is chosen should be close to $\lambda/10 = 0.012 \approx 1cm$. A 2D model of the triangular cross-section structure was modelled using the fully structured TLM method. A derivative gaussian pulse was then used to excite the cavity close to the vertical edge. The pulse then propagates towards the termination at the wing point and increases in field strength as the wing seperation reduces. As the pulse propagates it excites the fields shown in figure 7.4.19.

It can be seen that there are a large number of high energy spurious resonances that are excited by the pulse excitation. The stair-casing of the structure has led to resonances with a wavelength/Δl equal to 2α. This is due to an artificial mismatch in the impedance of the structure at the steps in the stair-casing of the boundary. In this case the wavelength of these oscillations is consistent with the wavelength of interest in the cavity. Therefore, any results obtained using this mesh structure would contain spurious artefacts due to the stair-casing. The fractional boundary placement model can be applied to such a structure so that the boundary variation is stepped at every cell along the sloping boundary. Connection takes place between boundary cells with different displacements in the manner defined in Chapter 6. The response of the structure was again simulated and is shown in

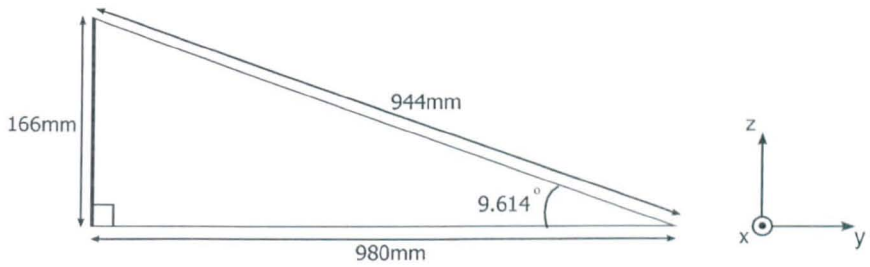

Figure 7.4.18: Small angle created inside an aircraft wing

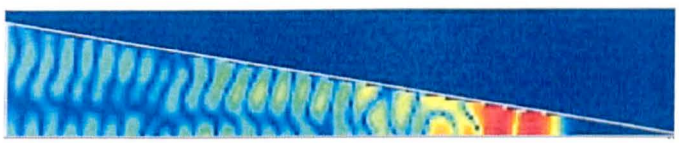

Figure 7.4.19: Pulse propagation in wing structure using stair-casing

Figure 7.4.20: Pulse propagation in wing structure using fraction boundary placement model

Figure 7.4.20. It can be seen that the spurious resonances have been removed by using the fractional boundary placement model.

The effect of the mesh spacing used when modelling resonant structures has been shown to be important. In the case demonstrated here the full field model gave spurious results due to the stair-casing being equal to the wavelength of interest in the cavity. The fractional boundary placement model developed here has been shown to improve the accuracy of results for resonant cavity problems in Chapter 6 and here in the case of modelling structures with acute angles. The significant advantage of this approach over the graded mesh approach, for example, is that the modification is limited only to the boundary region and there is no negative impact on the time step that can be used in the simulation.

Chapter 8

Conclusions

Following the development of the modelling tools and the findings of this thesis, this chapter provides a summary of the models and discusses their possible applications. The models developed in this thesis have been validated and applied to a sample of wireless communication modelling problems. The focus of this work was the development of tools which are efficient and general in such a way that they can be applied to wireless communication modelling.

Wireless communication systems typically operate in the ISM band at around 2.45GHz corresponding to a wavelength of 0.12m. It is desirable to use wireless systems within environments such as the inside of an aircraft where they would not normally be applied. The use of wireless systems in such environments has been discussed to show that they are rapidly becoming a cost effective and efficient alternative or addition to wired systems. The structures in which the wireless system will be used provide a unique electromagnetic environment due to its highly resonant and multipath nature. Often the cavities and small features within them will be close in size to the wavelength used for wireless communication and produce

interesting effects within the channel.

In order to model the impact of a highly resonant environment on a wireless communication system it is necessary to produce highly efficient models. Due to the highly resonant nature of the cavity it has been shown that the BER in wireless communication is very dependent on the modal structure within the cavity. It has been demonstrated that the electromagnetic parameters of the cavity can be quantified by the Q factor and the density of modes within the cavity. An efficient and robust filter model based on an equivalent circuit has been developed that uses these parameters to provide a statistical representation of the channel. In this way an average BER or PER can be calculated for a wireless system rather than a single estimate. This approach removes the effect of structural variations and inaccuracy in modelling or construction. Unlike full field modelling of a single cavity system a wide range of simulations can be performed to generalise the impact of the cavity on a wireless system using orders of magnitude less time and computing resources.

Coupled cavity systems have been modelled and the electromagnetic properties of the those systems have been represented using an efficent circuit analog so that a filter model can be created. The parameters of the model can be determined from an accurate analytical representation of the coupling apertures based on waveguide theory. It has been shown that the coupling coefficients obtained analytically agree well with values obtained from full-field simulation. The coupling coefficent can then be used in the efficient coupled cavity model in order to investigate the impact of coupled resonant cavity systems on wireless communications.

Furthermore, it was shown that if the aperture has thickness then the propagation of fields through the aperture is dependent on its cut-off properties and its length. However, it was demonstrated that if a wire is passed down the centre of the waveguide the field is able to propagate. In most applications it is likely that

existing structure will already provide such a coupling path. However, a coupling wire can be easily installed if necessary to provide the coupling path. The physical extension of the coupling wire into the resonant cavities has been shown to have little impact on the coupling efficiency.

The efficiency of the filter models is further enhanced through the ability to operate them at close to baseband frequencies when considering a band-limited wireless signal. This avoids the need to operate the model at the carrier frequency, as it necessary for full field models that aim to capture all of the geometry of the environment. Although the filter models developed here are very efficient, if they are used to calculate bit error rates directly then the error in the BER estimation is inversely proportional to the number of bits passed through the channel model. For example, if a channel leads to a BER of 1×10^{-6} then for a 1 bit packet signal on average at least 1×10^{6} bits must be passed through the channel in order to record a bit error. The accuracy of the result can only be assured if orders of magitude more bits are passed through the channel and the result converges to within a satisfactory error. An estimate of the number of simulations required to provide a statistically flat channel has been provided. In practise the convergence of the result can be easily observed for each modal structure iteration.

A novel fractional boundary placement model has been developed that is capable of positioning boundaries at non-integer space steps to provide a semi-conformal enhancement to the TLM method without loss of efficiency. Unlike existing models this model preserves speed of light propagation along the boundary whilst modelling the correct boundary position. The technique ensures fields normally incident to the boundary are modelled with the correct delay and fields travelling parallel to the boundary propagate with the correct velocity. The model separates the boundary region from the bulk mesh and the boundary is considered in the connection stage of the simulation rather than during scattering.

Validation of the fractional boundary model has shown that the position of the boundary can be modelled accurately to within 0.015%, the propagation velocity parallel to the boundary can be modelled to within 0.00003% and the resonant frequency of a cavity to approximately 0.1%. The approach presented here enables the modelling of a number of scenarios. The placement of boundaries at the edge of the simulated domain with arbitrary positions reduces modelling errors. A sloped or non-uniform boundary where displacement varies with position can be modelled. The position of the boundary can be modified dynamically during the simulation without affecting the time step. A short circuit electric, open circuit magnetic boundary and a first-order lossy boundary can be easily described.

A number of difficulties with the stability of the boundary model have been described when applied to moving boundary problems. It was not clear at the time of writing what the cause of the instabilities were, however a number of mitigation strategies were explored including filtering and limiting the model to set of limits to ensure that it did not become unstable. It was found that ensuring the minimum extension of the boundary did not become too small then the boundary would remain stable. Although energy conservation has been considered, it is possible that the cause of the instability could be due to incorrectly taking this into account in the model. This remains an area of further work as it is desirable to ensure the unconditional stability of the model. There is a considerable amount of work in the area of acoustics as moving boundary problems are common [56]. Applying the knowledge in this area to the problems described here would provide an interesting future study.

8.1 Possible Wireless System Modelling

In the scope of this work it was only possible to carry out tests using a limited number of wireless systems that are typically used. The models developed provide a numerical representation of the propagation channel in which wireless systems can be numerically tested and are not specific to the systems discussed here. In addition to the studies carried out in this thesis, this section discusses some further investigations that would be necessary to fully assess the suitability of a wireless system for operation in the highly resonant environments.

The wireless systems investigated were tested in a noiseless channel so that the errors measured here were due only to the physical properties of the environment. The impact of noise on wireless modulation and coding techniques is well understood and recorded. References [11] and [58] provide analytical solutions to the errors that occur due to additive white Gaussian noise (AWGN) being present in the channel. The aircraft environment will contain a large amount of equipment that will add noise to the communication channel; sources include electronics, cabling, radar equipment, electrostatic discharge. Hence, noise levels will fluctuate and occur at a wide range of frequencies and an AWGN model may not be the most appropriate approach to modelling noise. One approach would be to directly measure and characterise the noise that occurs in an aircraft. This noise can then be used to model the effects directly in the channel models developed here. This can be easily performed by simply adding the noise to the signal once it has passed through the model. The impact of such noise on the signal will be most significant when the bit decision is close to the threshold for a particular wireless system. For example, close to the zero crossing of the inphase channel axis for BPSK modulation. Research into the type and effect of noise in a aircraft could potentially form a large amount of future work in the area of wireless communications for aircraft environments.

In Chapter 3 the concept of code division multiple access (CDMA) was mentioned as an extension of the direct sequence spread spectrum approach in order to allow for mutual operation of multiple code based channels. Given the applications of interest in this thesis there will likely be a large number of wireless devices operating simultaneously. In a highly resonant environment time division and frequency division approaches are not ideal.

A time division based approach would introduce delays into often critical systems, which is undesirable. Furthermore, due to the resonant nature of the environment there must also be an additional delay to allow the energy of a previous communication to decay. Due to the peaked frequency response of the channel it has been shown that narrowband signals are subject to significant error in the channel. The use of wider band signals averages the channel response and reduces errors but at the expense of interchannel interference. This means that frequency division based systems, which are limited to a defined frequency and bandwidth are subject to the poor propagation characteristics of the channel at some frequencies. Therefore, a CDMA approach which allows simultaneous communication of multiple wideband signals [25] would theoretically be the best approach to such a problem. Further work could use the models developed here to assess the cooperability of multiple systems to explore the effect of the channel on their functionality.

8.2 Concluding Remarks

This thesis has described the development of some efficient and general channel models for wireless communication simulation and testing. The effects of the channel on some wireless systems have been provided as an example but are by no means exhaustive. The models developed here provide a valuable simulation tool for use in the design and testing phase of a system's development. Coupled with

measurements it is possible to rapidly test wireless systems in a generalised characterisation of the resonant channel environment. The filter models developed have applications most notably in the aerospace, rail, naval, shipping and automotive industries.

The advantages of replacing wires with wireless systems are perhaps not as great in industries other than aerospace as weight and space limitation may not be as great. The use of wireless systems can provide other benefits such as flexibility that may make them desirable. Wireless systems do not need a physical connection in the way that a wire or fibre optic system might. Nodes can therefore be easily integrated into a wireless system without manual intervention. Such applications could be found in the rail industry where it may be desirable to provide connections between carriages or containers. Other applications may be found in the naval or shipping industry where the environment is again a modular metallic cavity environment. Wireless systems could be used purely for local communications or could include personal computer networks within the environment. These models would provide a valuable tool in addition to commonly used urban and office modelling tools.

Finally, considering the principal intended application of this work, it has been highlighted where wireless systems are most applicable and advantageous. Areas such as system monitoring and HUMS are the most immediately suitable systems. The source of power for the wireless system is a significant factor. In order to be truly wireless the nodes of the system must be able to operate with minimal power requirements so that the system can operate from battery power or locally scavenged power from heat or vibrations. At present the power available through scavenging techniques is limited, and hence the applications of fully wireless systems remain limited to low data rate systems.

In other application areas the power requirements may not be an issue and higher power systems such as wireless LAN could be adopted. The models developed here are ideal for such modelling as they can be used with any input signal and can provide a general figure for the reliability that may be encountered in a particular environment based on only a small number of measurements or estimations.

Bibliography

[1] FLAVIIR Programme, "Special issue on the flapless air vehicle integrated industrial research FLAVIIR programme in aeronautical engineering," *Proceedings of the Institution of Mechanical Engineers. Part G, Journal of Aerospace Engineering, Vol 224*, 2010.

[2] F-35 Joint Strike Fighter, http://www.jsf.mil, 2010.

[3] BBC, "In pictures: Inside Concorde," http://news.bbc.co.uk/1/hi/magazine/inpictures/3168820.stm, 2003.

[4] C. Furse and R. Haupt, "Down to the wire," *IEEE Spectrum*, pp. 34 39, 2001, 38(2).

[5] J. Prendergast, "Airbus Industries - caught between several rocks and a hard place," pp. 14–18, 2007, 14(3).

[6] I. Moir and A. Seabridge, *Civil Avionics Systems*. New York: Wiley, 2006.

[7] Society of Automobile Engineers (SAE), "ARP4761, Guidlines and methods for conducting the safety assessment process on civil airbourne systems,"

[8] M. Panitz, D. C. Hope, T. Sato, C. D. Harley, C. Christopoulos, P. Sewell, J. F. Dawson, A. C. Marvin, E. Fearon, K. G. Watkins, G. Dearden, and W. J. Crowther, "The opportunities and challenges associated with wireless interconnects in aircraft," *Proceedings of the Institution of Mechanical Engineers*,

Part G, Journal of Aerospace Engineering - Special Issue on the Flapless Air Vehicle Integrated Industrial Research (FLAVIIR) Programme in Aeronautical Engineering , Vol 224, pp. 459–469, 2010.

[9] I. Moir and A. Seabridge, *Military Avionics Systems.* New York: John Wiley and Sons, 2006.

[10] I. Moir, *Aircraft Systems: mechanical, electrical and avionic subsystems integration.* John Wiley and Sons Ltd, 3 ed., 2008.

[11] T. S. Rappaport, *Wireless Communications Principles and Practice.* Prentice Hall, 1996.

[12] J. F. Dawson and I. D. Flintoft, "York test cylinder," January 2007. Courtesy of J. F. Dawson, University of York.

[13] C. Christopoulos, *The Transmission-Line Modelling Method.* Piscataway, NJ: IEEE Press, 1995.

[14] S. Ramo, J. R. Whinnery, and T. V. Duzer, *Fields and Waves in Communication Electronics.* New York: John Wiley & Sons, 3rd ed., 1994.

[15] D. H. Middleton, editor, *Avionic Systems.* Longman Scientific and Technical, 1989.

[16] GulfStream, "Gulfstream demonstrates fly-by-wireless aircraft control system, available from: http://www.gulfstream.com/news/releases/2008/101408.htm.," Oct. 2008.

[17] Society of Automobile Engineers (SAE), "ARP4754, Certification considerations for highly-integrated or complex aircraft systems.," 1996.

[18] J. G. Proakis and D. G. Manolakis, *Digital Signal Processing.* Pearson Prentice Hall, 4th ed., 2007.

[19] J. P. Daniel, "Fly-by-wirless airbus end-user viewpoint," *Technical report, Airbus*, March 2007.

[20] N. Fragoulis, V. Tsagaris, and V. Anastassopoulos, "Information fusion in ad hoc wireless sensor networks for aircraft health monitoring, in: Engineering against fracture," *Springer Verlag*, 2009.

[21] T. E. Coelho et.al., "Fly-by-wireless UAV platform based on a flexible and distributed architecture," *IEEE International Conference on Industrial Technology*, pp. 2359–2364.

[22] CANEUS/NASA, "Proceedings of the fly-by-wireless workshop, grapevine, texas, march 27-28, 2007," 2007.

[23] International Electrotechnical Commission IEC, "Electromagnetic compatibility, part 4, section 21: Reverberation chamber test methods, 61000-4-21," tech. rep., International Electrotechnical Commission, IEC, 2000.

[24] J. F. Dawson, "Lecture notes: Principles of reverberation chambers," 2006.

[25] G. L. Stuber, *Principles of Mobile Communication.* Boston, Ma: Kluwer Academic Publishers, 2nd ed., 2002.

[26] K. F. Riley, M. P. Hobson, and S. J. Bence, *Mathematical Methods for Physics and Engineering.* Cambridge, UK: Cambridge University Press, 2nd ed., 2004.

[27] M. Sucher and J. Fox, eds., *Handbook of Microwave Measurements*, vol. 2. Polytechnic Press, 3rd ed., 1963.

[28] D. Tse and P. Viswanath, *Fundamentals of Wireless Communication.* Cambridge, UK: Cambridge University Press, 2005.

[29] IEEE-SA, "IEEE Std 802.15.1-2005 IEEE standard for information technology telecommunications and information exchange between systems local and metropolitan area networks specific requirements part 15.1: Wireless

medium access control (MAC) and physical layer (PHY) specifications for wireless personal area networks (WPANs)," 2005.

[30] T. S. Laverghetta, *Microwaves and Wireless Simplified.* Boston, MA: Artech House, INC, 2nd ed., 2005.

[31] A. Bensky, *Short-Range Wireless Communication.* Oxford, UK: Newnes, 2nd ed., 2004.

[32] ZigBee Alliance, "ZigBee specification," June 2005.

[33] W. H. Press, S. A. Teukolsky, W. T. Vetterling, and B. P. Flannery, *Numerical Recipes in C++.* Cambridge University Press, 2nd ed., 2002.

[34] R. C. Dixon, *Spread Spectrum Systems.* New York: John Wiley & Sons, 2nd ed., 1984.

[35] P. T. Trakadas et. al., "Computation of transmission-line immunity level in the presense of a direct-sequence spread-spectrum electromagnetic signal by using CE-FDTD method," *IEEE Transactions on Electromagnetic Compatibility*, vol. 45, no. 1, pp. 2–9, 2003.

[36] R. L. Pickholtz et. al., "Theory of spread-spectrum communications - a tutorial," *IEEE Transactions on Communications*, vol. COM-30, no. 5, pp. 855 884, 1982.

[37] IEEE-SA, "IEEE 802.11 - wireless lan medium access control (MAC) and physical layer (PHY) specifications," June 2007.

[38] O. Delangre, P. D. Doncker, M. Lienard, and P. Degauque, "Adaptable measurement testbed for wireless systems applied to mimo channel modeling," *Wireless Communications and Networking Conference, 2006*, vol. 2, pp. 940 945, 2006.

[39] J. L. Herring, *Developments in the Transmission-Line Modelling Method for Electromagnetic Compatibility Studies.* PhD thesis, School of Electrical and Electronic Engineering, The University of Nottingham, May 1993.

[40] J. Paul, *Modelling of General Electromagnetic Material Properties in TLM.* PhD thesis, School of Electrical and Electronic Engineering, The University of Nottingham, October 1998.

[41] J. M. De Freitas, *Digital Filter Design Solutions.* Artech House, 2005.

[42] C. Christopoulos, *Principles and Techniques of Electromagnetic Compatibility.* CRC Press, 1995.

[43] A. V. Oppenheim and R. W. Schafer, *Digital Signal Processing.* Prentice-Hall, NJ, 1975.

[44] R. S. Barbosa, J. A. T. Machado, and M. F. Silva, "Time domain design of fractional differintegrators using least-squares," *Signal Processing*, vol. 86, pp. 2567–2581, 2006.

[45] D. Hope, J. Dawson, A. Marvin, M. Panitz, C. Christopoulos, and P. Sewell, "Assessing the performance of zigbee in a reverberant environment using a mode stirred chamber," *IEEE International Symposium on Electromagnetic Compatibility, Detroit*, Aug. 2008.

[46] H. A. Bethe, "Theory of diffraction by small holes," *The Physical Review*, vol. 66, pp. 163–182, October 1944.

[47] H. A. Wheeler, "Coupling holes between resonant cavities or waveguides evaluated in terms of volume ratios," *IEEE Transactions on Microwave Theory and Techniques*, pp. 231–244, March 1964.

[48] N. A. McDonald, "Electric and magnetic coupling through small apertures in shield walls of any thickness," *IEEE Transactions on Microwave Theory and Techniques*, vol. 20, pp. 689–695, October 1972.

[49] C. H. Liang and D. K. Cheng, "Electromagnetic fields coupled into a cavity with a slot-aperture under resonant conditions," *IEEE Transactions on Antennas and Propagation*, vol. AP-30, pp. 664–672, July 1982.

[50] N. Marcovitz, *Waveguide Handbook*. New York: New York Dover Publications, Inc., 1st ed., 1951.

[51] H. Du, P. So, and W. J. R. Hoefer, "Cells with tensor properties for conformal TLM boundary modeling," *2006 IEEE MTT-S Int. Microwave Symp. Dig.*, pp. 157–160, 2006.

[52] U. Mueller, A. Beyer, and W. J. R. Hoefer, "The implementation of smoothly moving boundaries in 2D and 3D TLM simulations," *IEEE MTT-S*, pp. 791–792, June 1992.

[53] U. Mueller and A. Beyer, "Moving boundaries in 2D and 3D TLM simulations realized by recursive formulas," *IEEE Transactions on Microwave Theory and Techniques*, vol. 40, pp. 2267–2271, December 1992.

[54] J. Paul, C. Christopoulos, D. W. P. Thomas, and X. Liu, "Time-domain modeling of electromagnetic wave interaction with thin-wires using TLM," *IEEE Transactions on Electromagnetic Compatability, vol. 47, no. 3*, pp. 447–455, Aug. 2005.

[55] J. Paul, C. Christopoulos, and D. W. P. Thomas, "Correction to "time-domain modeling of electromagnetic wave interaction with thin-wires using TLM"," *IEEE Transactions on Electromagnetic Compatability, vol. 50, no. 2*, pp. 450–451, May 2008.

[56] L. Gaffour, "Analytical method for solving the one-dimensional wave equation with moving boundary," *Progress In Electromagnetics Research*, vol. 20, pp. 63–73, 1998.

[57] I. S. Grant and W. R. Phillips, *The Elements of Physics*. Oxford, UK: Oxford University Press, 2001.

[58] L. W. Couch II, *Digital and Analog Communication Systems*. Prentice Hall, 7th ed., 2007.

[59] D. Davidson, *Computational Electromagnetics for RF and Microwave Engineering*. Cambridge University Press, 2005.

[60] R. G. Manley, "Vibrations in aircraft: A series of articles covering the general principles for aeronautical engineers," *Aircraft Engineering and Aerospace Technology*, vol. 16, no. 2, pp. 38–49, 1993.

[61] T. Holt, K. Pahlavan, and J. Lee, "A graphical indoor radio channel simulator using 2D ray tracing," *Proceedings of Third IEEE International Symposium on Personal, Indoor and Mobile Radio Communications*, pp. 411–416, October 1992.

Appendix A

Sequences for Spread Spectrum Techniques

Direct sequence spread spectrum techniques use a spreading sequence in order to spread the bandwidth of the transmitted data. The types of codes that can be used for DSSS and CDMA and their propertiesare described in this chapter.

A.1 Maximal-Length Sequences

Maximal-length sequences (M-sequences) are generated using a shift register such as the one shown in Figure A.1.1. For a shift register of length N the codes created will have a length of $2^N - 1$, different sequences of codes are created depending on the maximal taps used in the shift register. The additions of binary bits are carried out using modulo-2 addition.

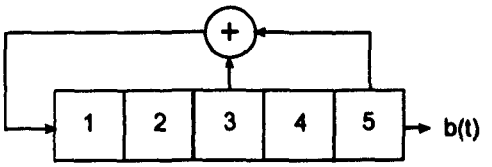

Figure A.1.1: A shift register used to create a 31 bit maximal length sequence

For the shift register shown in Figure A.1.1 with maximal taps at [5,3] and an initial state of 1,1,1,1,1 the output sequence b(t) is given by

$$b(t) = \{1,1,1,1,1,0,0,0,1,1,0,1,1,1,0,1,0,1,0,0,0,0,1,0,0,1,0,1,1,0,0\} \tag{A.1.1}$$

After the 31 bits shown the sequence repeats itself and is effectively a pseudo-random sequence. In order to be suitable for spread spectrum systems the code should have good auto-correlation properties. In this context good means that there is one definite auto-correlation peak so that the spread signal can be correctly synchronised and decoded at the receiver.

The auto-correlation of a sequence is defined by the integral

$$\psi(\tau)_{(auto)} = \int_{-\infty}^{+\infty} f(t)f(t-\tau)dt \tag{A.1.2}$$

and the cross-correlation of a pair of functions f and g is defined by the integral

$$\psi(\tau)_{(cross)} = \int_{-\infty}^{+\infty} f(t)g(t-\tau)dt \tag{A.1.3}$$

The sequence shown in Equation A.1.1, and indeed any m-sequence, has an auto-

correlation function given by

$$\psi(\tau) = \begin{cases} N & \tau = mN \\ -1 & \tau \neq mN \end{cases} \qquad m = 1, 2, 3... \tag{A.1.4}$$

The auto-correlation of a sequence can be directly related to the spectrum of the sequence [33]. The discrete correlation theorem states that discrete correlation of two real functions g and h is one member of the discrete Fourier transform pair

$$Corr(g, h)_j \Leftrightarrow G_k H_k* \tag{A.1.5}$$

and hence

$$AutoCorr(g)_j \Leftrightarrow G_k G_k* \;=\; |G_k|^2 \tag{A.1.6}$$

The auto-correlation of a m-sequence as given by A.1.4 is a single peak therefore A.1.6 shows that this corresponds to a flat spectral function. The m-sequence is therefore a suitable pseudo-random sequence that can be used to spread a signal in a DSSS system.

In terms of their auto-correlation properties the m-sequence codes cannot be surpassed, however they are not ideal for use in CDMA systems [34]. CDMA systems ideally require a large number of spreading codes with strong auto-correlation and bounded cross-correlation properties. Although m-sequences are ideal in terms of autocorrelation, their cross correlation is very variable between m-sequence pairs and is not well bounded. In addition there are only a limited number of codes that can be created from a given shift generator. For a five-stage shift generator there are only 6 available codes of length 31 that can be created. This means that in order to have a large number of users in CDMA system a large shift generator is required to create enough m-sequences. A solution to this problem was proposed by Gold in 1967 where a number of codes are generated from a pair of m-sequences.

Details of Gold codes can be found in the following section.

A.2 Gold codes

Maximal-length sequences are the most efficient spreading codes for use in a direct sequence spread spectrum system. However, for a given length of sequence there are only a limited number of sequences that possess cross-correlation properties that allow them to be used for orthogonal code based systems such as a CDMA system. For example, there exist only five 31 bit long maximal-length sequences that can be use simultaneously. Gold codes were developed by Gold to overcome this low limit and allow more codes to be used simultaneously. By reducing the auto-correlation properties of the codes Gold was able to enhance the cross-correlation properties of a number of codes. Gold codes are created from a pair of m-sequences which have a three level cross-correlation function; these sequences are called *preferred sequences*.

Gold codes are created using the modulo-2 sum of two preferred m-sequences where one sequence is progressively shifted by one for each gold code output. The result is that, for a pair of 31 bit m-sequences, it is possible to create 33 Gold codes. A generator for Gold codes is shown in Figure A.2.2.

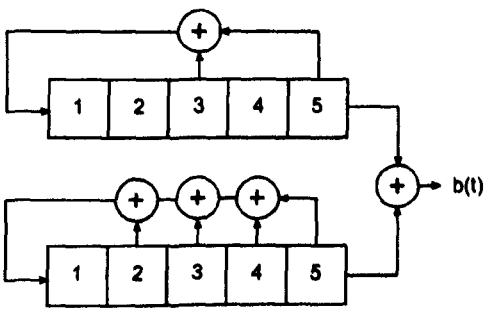

Figure A.2.2: A shift register system used to generate a 31 bit Gold code.

Gold codes offer the advantage that only a pair of feedback-tap generators are needed to produce a large number of codes. Each of these codes possesses good cross-correlation and auto-correlation properties, although auto-correlation is not as ideal as an m-sequence. Some auto-correlation cross-correlation properties of Gold codes are shown in Figure A.2.3 and Figure A.2.4.

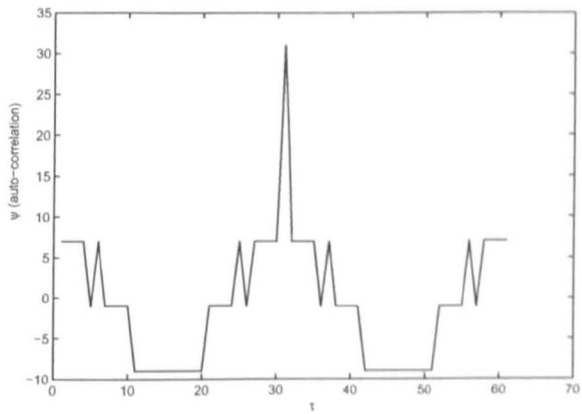

Figure A.2.3: Autocorrelation function of a 31 bit Gold code sequence.

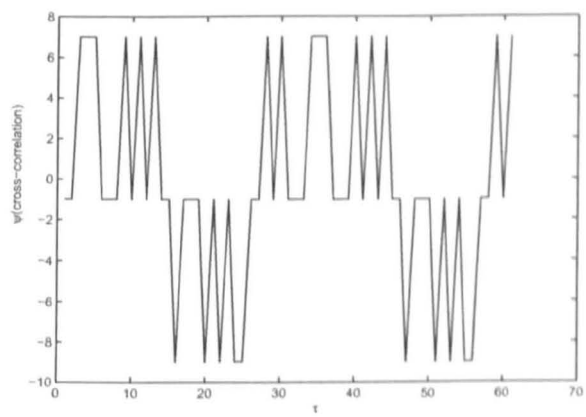

Figure A.2.4: Cross correlation function of a pair of 31 bit Gold code sequences.

The auto-correlation and cross-correlation of Gold codes make them suitable for use in spread spectrum techniques. Although their auto-correlation properties are not as perfect as m-sequences they provide a huge multi-code advantage over m-sequences when they are to be used in CDMA systems.

The cross-correlation of Gold codes is triple valued and well-bounded whilst the auto-correlation of the codes have a clear peak correlation as shown in Figure A.2.3. The peak is sufficient for use in CDMA systems where synchronisation of spreading sequence and received signal is necessary. These properties, along with the ability to create a large number of codes from simple shift registers, mean that Gold codes are ideally suited to CDMA multiplexing.

Appendix B

Cavity Resonance from Geometric Optics

The RLC model derived in Chapter 4 includes the resonant nature of an enclosed cavity channel and the resonance parameters are completely controllable. It is stated that the resonant behaviour is a result of periodic and low loss multipath propagation inside a cavity. If multipath propagation leads to resonant responses then conversely a resonant channel includes the multipath propagation behaviour and the two effects are closely related. This would mean that the multipath delay effect is included implicitly in the model. Furthermore, it is assumed that the differential propagation between the multiple received pulses is much smaller than the bit length being transmitted. Considered here is a modelling approach derived directly from the basis of multipath propagation rather than the electromagnetic and resonant behaviour of the cavity.

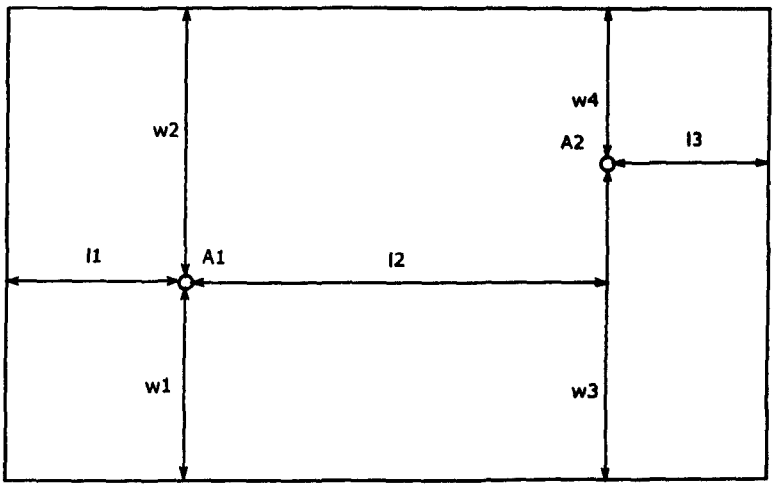

Figure B.1.1: 2D metal box geometries

B.1 A Geometric Optics Approach

It is accepted that resonant behaviour is owing to energy storage in a system and it is assumed that the energy in multiple propagation paths can be considered *stored*. Consider a perfectly electrically reflective chamber with a point-like transmit and receive antenna and the transmit antenna is excited with an impulse, propagating energy in all directions. Until the multiple paths reach the receiving antenna they continuously *bounce* around the box amassing varying phase delays. The delays combine when they reach the antenna and constructively or destructively interfere. The interference will produce patterns similar to resonances if mulitpath propagation and resonant behaviour in a small metallic cavity are closely linked.

Here the concept of geometric optics is applied to a relatively simple 2D metallic box with a point source at A_1 and a field measurement at A_2. The approach is to model the time delay phase shift due to multipath propagation. The geometry used is shown in Figure B.1.1 and it can be seen that the box has the length and

width dimensions

$$W = w_1 + w_2 = w_3 + w_4$$
$$L = l_1 + l_2 + l_3 \tag{B.1.1}$$

The aim is to measure all components of a field source at A_1 that are received at A_2 and include all paths from reflections on the sides of the box and a line of sight component. Sinusoidal field sources are to be used in this test. To do this the concept of images [14],[61] is used by expanding the box as shown in Figure B.1.2. The point A_2 is labeled in each box and using the geometries of the box the distance to each A_2 can be easily calculated. Each box is labelled with integers m and n corresponding to each path in the real system. Each boundary crossing causes a $\pi/2$ phase shift in the field and a wall loss.

The signal received $b(t)$ from a source $a(t)$ can be calculated in free space using the Green's function so that

$$b(r,t) = g(r;r')\, a(r',t) \tag{B.1.2}$$

where the function $g(r : r')$ tells us the field at r due to a source at r'. Here sinusoidal inputs are used of the form

$$a(0,t) = a_0 sin(\omega t + \phi) \tag{B.1.3}$$

The received signal can be calculated from all of the multipath components by summing the received components

$$B(r,t) = \sum_{m=0}^{\pm M} \sum_{n=0}^{\pm N} b(r,t)_{m,n} \tag{B.1.4}$$

where each received path component is given by

$$b(r,t)_{m,n} = \Gamma_{m,n}\, g(r;r')_{m,n}\, \phi_{m,n}\, a(0,t) \tag{B.1.5}$$

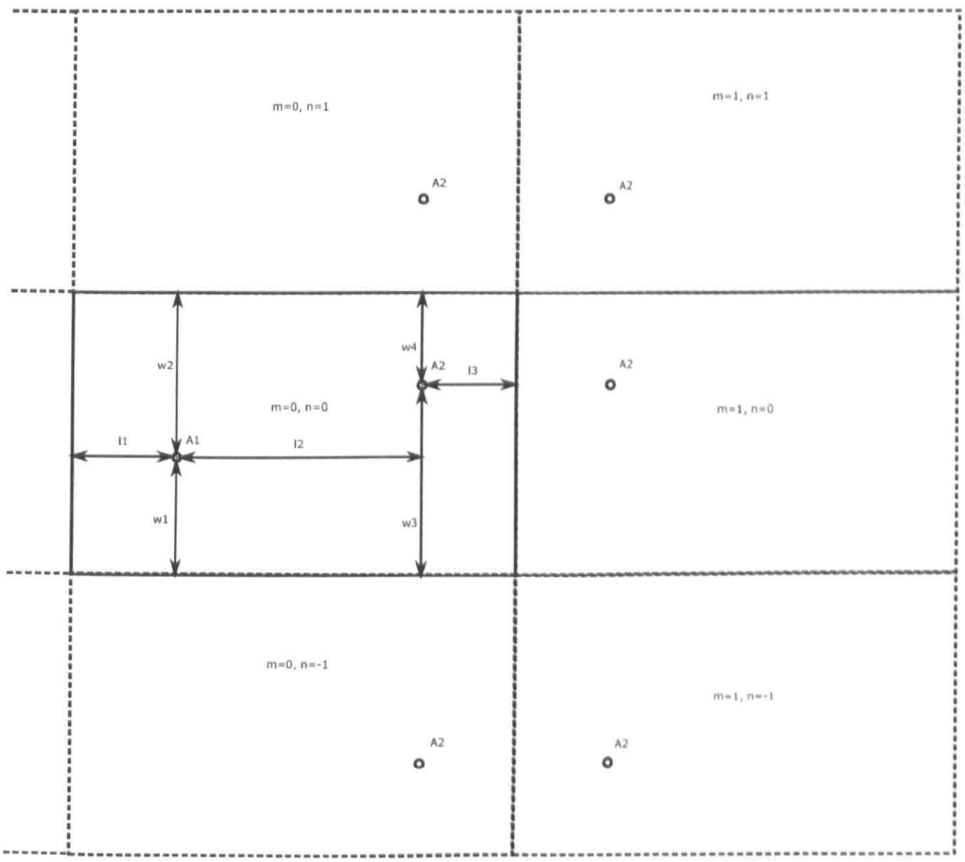

Figure B.1.2: Metal box reflections shown as images

Here $\Gamma_{m,n}$ is the reflection coefficient due to $m+n$ reflections and is given by

$$\Gamma_{m,n} = \Gamma'^{(|m|+|n|)} \tag{B.1.6}$$

The $\phi_{m,n}$ term accounts for the π phase shift due to a wall reflection and is given by

$$\phi_{m,n} = e^{j\frac{\pi}{2}(1-(-1)^{m+n})} \tag{B.1.7}$$

Finally the Green's function for free space[14], which also applies to cavities is given by

$$g(r;r')_{m,n} = \frac{e^{jkR_{m,n}}}{4\pi R_{m,n}} \tag{B.1.8}$$

for paths of lengths defined by $R_{m,n}$. The path lengths are simply calculated using

$$R_{m,n} = \sqrt{x_m^2 + y_n^2} \tag{B.1.9}$$

where using the geometries of the problem we can see that, with some manipulation, the path lengths in the x and y dimensions are given by

$$x_m = l_2 + m_1 l_3 + m_2(l_1 + l_2) \tag{B.1.10}$$

and

$$y_n = (w_3 - w_1) + n_1 w_4 + n_2 w_3 \tag{B.1.11}$$

Here the integers $m1, m2, n1, n2$ are given by

$$\begin{aligned} m_1 &= m + 1/2 - \tfrac{(-1)^m}{2} \qquad m = 0,\ \pm 1,\ \pm 2... \\ m_2 &= m - 1/2 + \tfrac{(-1)^m}{2} \qquad m = 0,\ \pm 1,\ \pm 2... \end{aligned} \tag{B.1.12}$$

where the expressions for n integers are equivalent to those for m. Negative integers are also included to account for paths initially travelling away from the receiver being reflected from the left wall of the box.

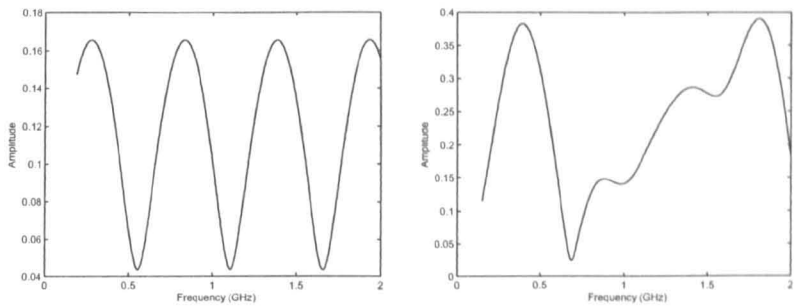

(a) (b)

Figure B.2.3: Multipath interference with (a) 2 paths and (b) 5 paths

B.2 Example Problem

In order to test the simple model derived above a 1m x 1m box is used to investigate the frequency response between 0.1GHz and 2GHz. The response is calculated in the frequency domain by stepping through sinusoid frequency and calculating the maximum field received. A plot of amplitude versus frequency gives the response of the box. The input and output positions were

Parameter	Length (m)
l_1	0.2
l_2	0.7
l_3	0.1
w_1	0.3
w_2	0.7
w_3	0.6
w_4	0.4

Table B.2.1: Geometries used for 2D box example

The number of paths included are modified by adjusting the maximum and minimum limits of m and n. Given only the line of sight path and one other path (m=0,n=1) the response of the system is given by Figure B.2.3(a).

It can be seen in Figure B.2.3(a) that there are narrow troughs and broad peaks;

these are well known phenomenon and occur in built up areas where signals bounce from large objects. Obviously it is likely there will be more paths but it can be seen with 5 paths, as in Figure B.2.3(b) there is a similar effect, only with a few more peaks.

This is the case for large (outdoor) systems, but they are not of concern here. In large systems there are large differences in path lengths of the multipath components and each path has high magnitude loss due to scattering, reflection, absorption etc. In addition a lot of energy is propagated in such a direction that it will never reach the antenna. These systems will have a high energy loss, hence low energy storage, no narrow resonances and low Q factor. The geometry of such an outdoor system tends not to be well defined or fixed.

In a small metal cavity there is little loss, high energy storage and high Q factor. Due to the enclosed electromagnetic reflecting structure a high amount of transmitted power will, at some point, reach the receiver; even if the paths are initially heading away from the receiver. As the environment is small the path differences are quite small also, and of very similar power to each other. The dimensions of the cavity lead to some regularity in the paths' lengths (discrete quanta) as the box dimensions are well defined and an element of regularity will be introduced into the results. The effect of this can be seen by progressively increasing the number of paths in the model to 121, 3721, and 10201.

It can be seen that as the number of paths increases resonant peaks start to appear and converge. They narrow further with increasing number of paths. Hence, the resonant behaviour is observed by only taking account of the multipath delays of sinusoids in a metal box. Figure B.2.4(d) has the first 6 theoretical resonances shown, it can be seen that these coincide very well with the resonant peaks produced in the multipath delay model.

Using this simple test for a 2D box the effect of the concepts of resonance and multipath propagation in a small resonant environment can be observed. This shows that the two concepts are closely related and a resonant cavity could be considered as a highly reflective, completely enclosed multipath environment.

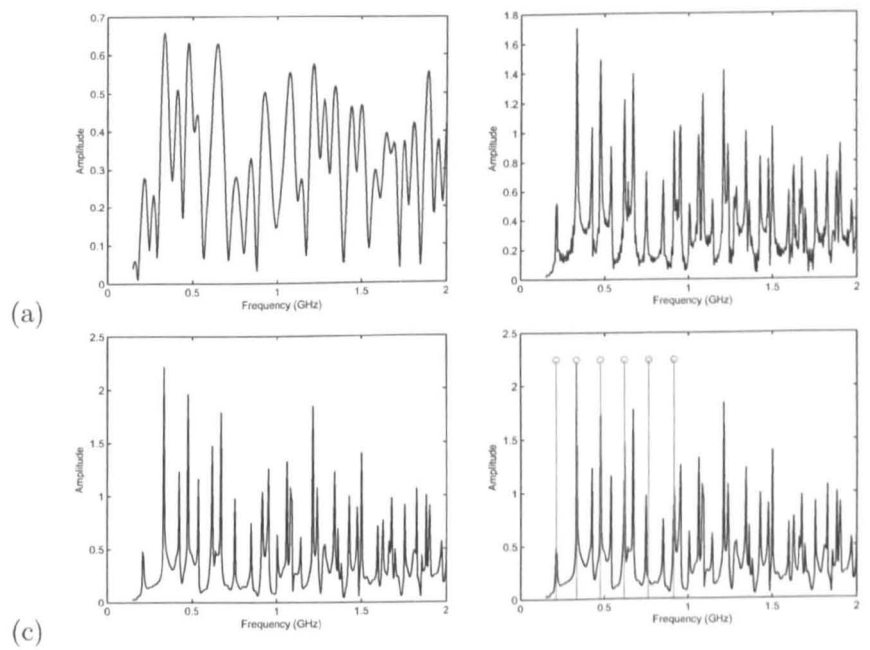

Figure B.2.4: Multipath interference with (a) 121 paths, (b) 3721 paths, (c) 10201 paths and (d) 10201 paths with first 6 analytical resonances shown

Appendix C

TLM Stub Calculations

In deriving the fractional boundary placement model it is necessary to model the inductance and capacitance deficit of the boundary region using transmission line stubs. In the models developed in this thesis the derivation of the properties of these stubs are definied in the following sections.

C.1 Stub Calculation in 2D

We choose the link-line characteristic impedance for the boundary line model to be Z_b as given in (6.3.30). Then the modelled capacitance is

$$C_b = \frac{\Delta t}{Z_b} = \frac{\varepsilon_0(\Delta\ell)^2}{\sqrt{2}d} \tag{C.1.1}$$

where Δt is the time-step used in the field mesh.

In order to model correctly the desired capacitance given by (6.3.26) we intro-

duce an additional capacitance in the form of a capacitive stub such that

$$C_b + C_s = \frac{\varepsilon_0(\Delta\ell)^2}{d} \tag{C.1.2}$$

Hence

$$C_s = \frac{\varepsilon_0(\Delta\ell)^2}{d}\left(1 - 1/\sqrt{2}\right) \tag{C.1.3}$$

and the capacitive stub impedance

$$Z_C = \frac{\Delta t}{2C_s} = \frac{Z_b}{2\left(\sqrt{2}-1\right)} \tag{C.1.4}$$

This impedance normalised to Z_b is equal to

$$\tilde{Z}_C = 1/\left(2\left(\sqrt{2}-1\right)\right) \tag{C.1.5}$$

Proceeding in a similar way we obtain the normalised impedance of the required inductive stub to be

$$\tilde{Z}_L = 2\left(\sqrt{2}-1\right) \tag{C.1.6}$$

We also need to calculate the time derivative $\frac{\partial i_{bx}}{\partial T}$ and $\frac{\partial V_b}{\partial T}$. The first is modelled by an inductive stub and the second by a capacitive stub as described in [54] so that

$$\frac{\partial i_{bx}}{\partial T} = 2V^i_{bLx} + i_{bx}\tilde{Z}_L \tag{C.1.7}$$

where

$$\tilde{Z}_L = 2\left(\sqrt{2}-1\right) \tag{C.1.8}$$

in normalised form, and

$$\frac{\partial V_b}{\partial T} = \frac{V_b - 2V^i_{bC}}{Z_C} \tag{C.1.9}$$

where

$$\tilde{Z}_C = \frac{1}{2\left(\sqrt{2}-1\right)} \tag{C.1.10}$$

Combining the respective terms we obtain (6.3.39) and (6.3.38).

C.2 Stub Calculation in 3D

As for the 2D case we choose the link-line impedance to be Z_b. Then the inductance modelled is

$$L_b = Z_b \Delta t = \frac{\mu_0 d}{2} \tag{C.2.11}$$

The required stub inductance is

$$L_b + L_s = \mu_0 d \tag{C.2.12}$$

hence

$$L_s = Z_b \Delta t = \frac{\mu_0 d}{2} \tag{C.2.13}$$

and

$$Z_s = 2\eta_0 \frac{d}{\Delta \ell} = 2Z_b \tag{C.2.14}$$

The capacitance modelled is

$$C_b = \frac{(\Delta \ell)^2 \varepsilon_0}{2d} \tag{C.2.15}$$

but the field sees the capacitance modelled by the two link lines i.e. $\frac{(\Delta \ell)^2 \varepsilon_0}{d}$ hence the required stub capacitance is

$$C_s = \frac{(\Delta \ell)^2 \varepsilon_0}{d} - \frac{(\Delta \ell)^2 \varepsilon_0}{d} = 0 \tag{C.2.16}$$